2013

Formation Mechanisms and Photocatalytic Properties of ZnO-Based Nanomaterials

Natalie Herring
Virginia Commonwealth University

Formation Mechanisms and Photocatalytic Properties of ZnO-Based Nanomaterials

A dissertation submitted in partial fulfillment of the requirements for the degree of Doctor of Philosophy at Virginia Commonwealth University

by

Natalie Paige Herring
M. S., University of North Carolina at Charlotte, North Carolina, 2009
B. S., The College of William and Mary, Virginia, 2007

Director: M. Samy El-Shall
Professor, Department of Chemistry

Virginia Commonwealth University
Richmond, Virginia
May 2013

Acknowledgement

My education at VCU has been helped by many individuals, to whom I would like to express thanks. I am most grateful to my research advisor, Dr. Samy El-Shall, for directing and encouraging me. I am extremely thankful for the support and guideance that you have given me. It has been a pleasure to share my research experience with the entire El-Shall group, including Leela Panchakarla, Khaled Abouzeid, Serial Almahoudi, Kwame Attah, Abdallah Zedan, Sherif Moussa, Parichehr Afshani, Sean Platt, Ahmed Hamid, Abdel Rahman Khedr and Hany El-Azab. I would like to especially thank Leela for useful discussions and sharing my interst and enthusiasm in ZnO based materials. I would also like to thank others, who spent time researching in the El-Shall lab, including Mona Mohamed, Chelsea Olson, Angeli Patel, John Pinsk, Kathleen Chocho, Ashley McDonald, and Fang Di. I am extremely thankful to Dr. Mona Mohamed for her guidance when I first started at VCU.

I appreciate the support given by my thesis committee: Dr. Collinson, Dr. Gupton and Dr. Terner. Each member has offered valuable suggestions and assistance. I am aslo appreciative of Dr. Turner for his help throughout my learning process ranging from help with instrumentation to proof reading.

In recognition of all of your help and support, I would like to mention the Department of Chemistry at Virginia Commonwealth University. The students, professors and staff have made the department a welcoming place to learn and explore science. I am grateful to many of you for

providing friendship, advice and encouragement. I would especially like to thank Dan Hudgins, Fernando Luna-Vera, Alberto Martinez, Alex Martin, Kendra Woodberry, Stevara Clinton, Minh Ho and Louis Franzel. I would also like to thank Dmitry Pestov for all of his help with instrumentation. I am grateful to Tim Carney for his help with XPS instrumentation and data analysis.

I am extremely grateful to my Maser's research advisor, Dr. Jordan Poler, for inspiring and encouraging me. I am extremely thankful for everything you have taught me as well as your continuted support.

I would like to express my sincerest thanks to those individuals whom have provided me with friendship and support. I would especially like to thank Brandon for his unwaivering support during my entire graduate career. I would also like to thank friends Heather, Kevin and Jeff for sharing the challenges and successes of graduate school with me. Each of you has made yourself available to listen and offer advice when I needed you, and for that I am truly grateful.

I would like to acknowledge Dr. and Mrs. Gerald and Sue Bass as well as Linda Vallarino for generous scholarship support, for which I am extremely grateful. I would like to offer thanks to Altria for providing generous fellowship support. I would also like to thank the National Science Foundation for financial support of this research.

Table of Contents

List of Figures

List of Tables

List of Abbreviations

2-D	2-dimensional
acac	acetylaceonate
BTB	borane tertbutylamine
CVD	chemical vapor deposition
DI	deionized
FTIR	Fourier transform infrared spectroscopy
GC	gas chromatography
GO	graphene oxide
MS	mass spectrometry
MUA	mercaptoundecanoic acid
MWI	microwave irradiation
OAC	oleic acid
OAM	oleylamine
PL	photoluminescence
RGO	reduced graphene oxide
SPR	surface plasmon resonance
TEM	transmission electron microscopy
TiO_2	titanium dioxide

UV	ultraviolet
XPS	X-Ray photoelectron spectroscopy
XRD	X-ray diffraction
ZnO	zinc oxide

Abstract

FORMATION MECHANISMS AND PHOTOCATALYTIC PROPERTIES OF ZNO-BASED NANOMATERIALS

By: Natalie Paige Herring

A dissertation submitted in partial fulfillment of the requirements for the degree of Doctor of Philosophy at Virginia Commonwealth University.

Virginia Commonwealth University, 2013

Director: M. Samy El-Shall, Professor, Department of Chemistry

Zinc Oxide (ZnO) is one of the most extensively studied semiconductors because of its unique properties, namely, its wide band gap (3.37 eV) and high excitation binding energy (60 meV).[1] These properties make ZnO a promising material for uses in a broad range of applications including sensors, catalysis and optoelectronic devices. The presented research covers a broad spectrum of these interesting nanomaterials, from their synthesis and characterization to their use as photocatalyts.

A new synthetic approach for producing morphology controlled ZnO nanostructures was developed using microwave irradiation (MWI). The rapid decomposition of zinc acetate in the presence of a mixture of oleic acid (OAC) and oleylamine (OAM) results in the formation of hexagonal ZnO nanopyramids and ZnO rods of varying aspect ratios. The factors that influence the morphology of these ZnO nanostructures were investigated. Using ligand exchange, the ZnO nanostructures can be dispersed in aqueous medium, thus allowing their use as photocatalysts for the degradation of malachite green dye in water. Photocatalytic activity is studied as a function of morphology; and, the ZnO nanorods show enhanced photocatalytic activity for the degradation of the dye compared to hexagonal ZnO nanopyramids.

After demonstrating the catalytic activity of these ZnO nanostructures, various ways to enhance photocatalytic activity were studied by modification of this MWI method. Photocatalytic activity is enhanced through band gap modulation and the reduction of electron-hole recombination. Several approaches were studied, which included the incorporation of Au nanoparticles, N-doping of ZnO, supporting ZnO nanostructures on reduced graphene oxide (RGO), and supporting N-doped ZnO on N-doped RGO.

ZnO-based nanostructures were studied systematically through the entire process from synthesis and characterization to their use as photocatalysis. This allows for a thorough understanding of the parameters that impact these processes and their unique photocatalytic properties.

Chapter 1: Introduction

Zinc Oxide (ZnO) is one of the most extensively studied semiconductors because of its unique properties, namely, its wide band gap (3.37 eV) and high excitation binding energy (60 meV).[1] These properties make ZnO a promising material for uses in a broad range of applications including sensors,[2-5] catalysis[6, 7] and optoelectronic devices.[8-10] The research detailed in this dissertation focuses on the development and understanding of ZnO-based nanomaterials, from synthesis and characterization to applications for photocatalysis.

Historically, ZnO has attracted interest for decades with characterization reports dating as far back as 1935.[11] With modern progress in nanomaterials and characterization techniques, ZnO has experienced a surge of renewed interest.[1, 11]ZnO nanomaterials exhibit new electrical, mechanical, chemical and optical properties as a result of size reduction and quantum confinement.[1] Furthermore, ZnO nanomaterials exist in a broad variety of m
orphologies including hexagonal pyramids,[12-15] rods,[16-21] wires,[4, 9, 22-26] tetrapods,[27, 28] disks,[29-31] cages,[32] combs[33] and rings.[31, 34, 35] Each morphology is synthesized through specific reaction conditions and results in interesting, morphology-specific properties.

This dissertation will focus mainly on the use of microwave irradiation (MWI) techniques for the formation of ZnO, but there exist a broad range of synthesis methods for the formation of ZnO. MWI was chosen as the primary synthesis route because it is fast and simple with minimal

thermal gradient effects.[49-54] MWI heating of a substance depends on dipole rotation and ionic conduction.[49-54] Thus, selective dielectric heating results from differences in solvent and reactant dielectric constants. The rapid transfer of energy directly to the reactants causes an instantaneous internal temperature rise with minimal thermal gradient. This also allows the rapid decomposition of the precursors thus creating highly supersaturated solutions where nucleation and growth can take place to produce the desired nanocrystalline products. This allows for a more rapid reaction, which requires less time compared to conventional heating.

Conventional, thermal heating methods have been reported for the formation of ZnO nanostructures. Zhou et al. report the formation of ZnO hexagonal micro-pyramids and micro-rods by thermal decompostion of zinc acetate in organic solvents including oleylamine and triocytlyamine.[15] There are several other reports in which ZnO hexagonal pyramids and rods have been synthesized through thermal decomposition of zinc acetate in organic solvents.[36, 37] Similar structures have also been reported by thermal decomposition of zinc acetate in mixtures of potassium hydroxide and methanol[38] as well as decomposition of zinc nitrate in N, N - dimethylformamide.[39]

Non-chemical, physical vapor deposition methods at high temperatures are more commonly used to synthesize unique one-dimensional zinc oxide structures.[22] High aspect ratio nanobelts are formed by heating ZnO powder to high temperatures (900 – 1300 ºC) in a tube furnace that contains a substrate for ZnO nanobelt growth in a lower temperature (500 – 600 ºC) region.[22] The polarity of the substrate can be changed, which results in rolled variations of the nanobelts, such as nanosprings and nanorings. There are a few chemical approaches for formation of one-dimensional zinc oxide structures. Most commonly, vertically aligned ZnO

nanorods are produced by chemical methods that utilize a catalyst deposited on a substrate to direct the growth.[22]

This dissertation focuses on formation mechanisms of unique ZnO nanomaterials and their application for photocatalysis. Through the systematic study of ZnO nanomaterials throughout the entire process from synthesis and characterization to their use as photocatalysts, a broad understanding of formation mechanisms and photocatalytic properties of these exceptional materials is gained.

1.1 Fundamental Principles of Semiconductor Photocatalysis

Semiconductors, especially ZnO and TiO_2, have been important materials throughout the history of chemistry, especially in the field of photocatalysis.[40, 41] Since the first discovery of photocatalysis on a TiO_2 electrode in 1972, semiconductor photocatalysis has emerged as a promising technology to utilize natural and artificial sunlight.[40] Progress has lead to photocatalysis being implemented in to a wide range of applications including: hydrogen fuel production through water splitting,[28, 42, 43] disinfection,[44] super-hydrophillic self-cleaning materials,[45] and the elimination of inorganic and organic pollutants.[19, 46-74]

Photocatalysis is a misleading term that refers to photoreactions that are accelerated by the presence of a catalyst; photocatalysis does not refer to reactions are catalyzed by light.[75] The majority of the work presented here focuses on heterogenous photocatalysis where the reactions occur on the surface of the catalyst nanoparticles. Heterogeneous photocatalysis reactions can be divided into two main categories: catalyzed photoreactions and sensitized photoreactions.[75] Catalyzed photoreactions are reactions in which the initial photoexcitiation occurs in the adsorbate molecule. This is different than the sensitized photoreactions where the initial

photoexcitation takes place on the surface of the catalyst. The majority of photocatalytic reactions, and those discussed here, refer to semiconductor-sensitized photoreactions.

As previously mentioned, decontamination of air and water polluted with toxic, non-biodegradable compounds is one application of photocatalysis and has been the focus of much research interest.[19, 46, 47, 50-74] It has been suggested that the majority of human contact with toxic chemicals is from groundwater contamination that leaks from hazardous waste sites.[76] Research focuses not only on methods to purify water by removing the contaminants but also on methods to degrade hazardous pollutants into innocuous compounds. Current waste management techniques include high temperature incineration, amended activated sludge digestion, anaerobic digestion and conventional physicochemical treatment of hazardous chemicals.[76] Research is currently focused on the use of photocatalytic methods for treatment of hazardous waste. Photocatalysis is an extremely promising solution for treatment of hazardous waste, because it has the ability to degrade pollutants into innocuous species *in situ* without the need to first separate contaminants.

Advanced physiochemical processes, like photocatalysis by semiconductor nanomaterials, are studied with the intention of being supplementary and complementary to conventional waste management techniques.[76] These methods are advantageous to conventional methods because they are able to completely degrade the toxic molecules into harmless compounds in relatively short reaction times.[77] Semiconductor materials such as TiO_2, ZnO, Fe_2O_3 CdS and ZnS are all suitable for photocatalysis reactions. Semiconductor materials are well suited as photocatalysts because of their high photosensitivity, stability, band gap and relatively low cost. Furthermore, many metal oxides are not environmental hazards and may be used for *in situ* degradation of organic pollutants. The semiconductor properties that determine

photocatalytic activity will be discussed in detail, as well as efforts to enhance photocatalytic activity by tuning these properties.

1.1.1 Mechanism of Semiconductor Photocatalysis

Photocatalytic reactions occur when irradiated semiconductors initiate specific oxidation and reduction reactions. A schematic diagram illustrating the mechanism for semiconductor photocatalysis is given in Figure 1.1. In general, when semiconductors are irradiated with light, photons with energies exceeding the band gap energy excite electrons from the valence band into the conduction band. This excitation leaves a hole in the valence band, which creates an electron-hole pair. The excited electrons and holes drive photocatalytic reactions.

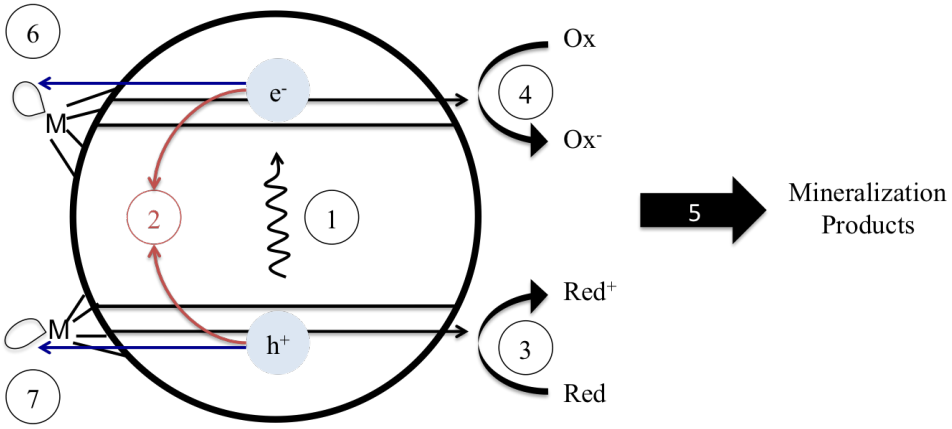

Figure 1.1. Schematic diagram of the photocatalytic mechanism. (1) Charge carriers are formed by a photon (from light irradiation). (2) Charge carriers recombine and release heat. (3) An oxidative pathway is initiated by valence-band holes. (4) A reductive pathway is initiated by conduction band electrons. (5) Additional thermal and photocatalytic reactions yield completely mineralized compounds. (6) Conduction band electrons are trapped in dangling surfacial bonds. (7) Valence band holes are trapped by surface groups.

After irradiation, the exited electron and hole pair either recombines to release heat, becomes trapped in a metastable surface state or migrates to the surface. Photocatalytic reactions occur when excited electrons and holes successfully migrate to the surface and react with

electron acceptors and donors adsorbed on the semiconductor surface. Electron-hole recombination, which inhibits photocatalytic reaction, occurs within nanoseconds unless electron and hole scavengers trap the electron-hole pair. Trapping occurs by scavengers as well as surface defect sites, which prevent recombination from occurring. Methods to prevent electron-hole recombination will be discussed in detail.

Excited electrons and corresponding holes promote chemical reactions that occur at the semiconductor surface. In semiconductors, conduction band electrons are highly reducing species and exhibit chemical potentials ranging between +0.5 to -1.5 V relative to normal hydrogen electrode.[40] Holes in the valence band are strong oxidizing species and exhibit chemical potentials ranging between +1.0 to 3.5 V relative to normal hydrogen electrode.[40] The reaction mechanism for ZnO photocatalysis occurs as follows. First, a photon, with energy greater than the band gap, excites an electron from the valence band to the conduction band

$$ZnO + h\nu \rightarrow ZnO\ (e^-_{CB} + h^+_{VB}) \quad 1.1$$

and an electron-hole pair is generated. If the electron-hole pair does not recombine, it reacts with nearby oxygen or water molecules adsorbed on the ZnO surface to form oxygen and hydroxyl radicals,[50, 52, 58] respectively:

$$e^-_{CB} + O_2 \rightarrow \bullet O^-_2 \quad 1.2$$

$$h^+_{VB} + H_2O \rightarrow \bullet OH + H^+. \quad 1.3$$

The produced oxygen and hydroxyl radicals are strong oxidizers and will promote oxidation of the organic molecules on the surface, hence the term advanced oxidation process is also given to these processes. Highly conjugated organic dyes are often used to study the photocatalytic activity of semiconductor materials because they are brightly colored and degradation is easily

monitored using UV-Visible absorbance spectroscopy. For the specific case of the removal of organic dye molecules, degradation occurs when hydroxyl radicals react with dye molecules:

$$\bullet OH + \text{dye} \rightarrow H_2O + \text{dye intermediate} \quad 1.4$$

$$\bullet OH + \text{dye intermediate} \rightarrow H_2O + CO_2 + \text{mineralization products.} \quad 1.5$$

The hydroxyl radical generated by valence band holes is the critical species for the degradation process. Final degradation of dye intermediates is crucial for environmental safety as the incomplete oxidation leads to intermediates that are often more toxic than the parent dye molecule. The exact mechanisms by which the organic dye molecules degrade are not reported, but previous studies report complete mineralization of organic dye molecules to innocuous compounds through semiconductor photocatalysis.

1.1.2 Semiconductor Photocatalysis Efficiency Challenges

In order for photocatalysis to be effectively implemented into practical applications, photocatalytic materials need to be enhanced to increase efficiency. Current efforts are focused on designing new semiconductor materials that are both efficient and stable. Approaches include: (1) tuning semiconductor surface energy, (2) energy band modulation and (3) construction of heterojunctions by combining photocatalytically active semiconductors with metals or other semiconductors.[40]

Tuning the surface energy of semiconductor particles enhances photocatalytic activity. Photocatalytic reactions occur at the particle surface, and higher surface energy yields higher activity. Therefore, photocatalytic activity is dependent on particle morphology. Tuning morphology and surface area of active sites has attracted attention due to advances in nanotechnology and nanomaterial synthesis methods.[40, 61, 62] Materials can now be developed to demonstrate a higher percentage of photocatalytically active surface facets. For example, certain

crystal faces are usually more active than others; therefore, particles are designed to have higher percentages of the active crystal face. Methods to control particle morphology are developed for the enhancement of photocatalytic activity.

Another fundamental aspect of enhancing photocatalytic activity is through energy band modulation.[40] Principally, the energy band of the semiconductor material determines the photon absorption, photoexcitation of electron-hole pairs, migration of charge carriers and redox potential of electrons and holes. Based on the mechanism, semiconductor nanoparticles catalyze photoreactions because of their band structure and their ability to absorb light in the solar spectrum. This requires the exciting photon to have an energy that is greater than or equal to the band gap energy of the semiconductor. Therefore, it is reasonable to expect that tuning the band gap will affect photocatalytic activity. Studies have shown that semiconductors with smaller band gaps, less than 3 eV, have a higher incidence of electron/hole pair recombination. At these energy gaps, the excited electron rapidly falls into holes and does not interact to form oxidative radical species. Semiconductors with larger band gaps, greater than 3.17 eV, light irradiation is not sufficient enough to excite an electron from the valence band in to the conduction band and therefore no radical species are formed. Therefore, semiconductors with a band gap between 3.1-3.17 eV are ideal for photocatalytic processes.[78]

Semiconductor band gap is modified through doping with different elements.[14, 28, 56, 79] In general, incorporating different elements into the semiconductor crystal lattice creates additional energy levels within the band gap, and therefore, changes the band gap and optical absorption. Methods to synthesize stable, semiconductors doped with different elements are studied to improve photocatalytic activity.

Another approach for enhancing photocatalytic activity is through designing composite materials that combine active semiconductors with metals or other semiconductors.[80, 81] In general, the addition of metal and certain semiconductors on the surface will behave as electron "sinks" or scavengers. When electrons are excited to the conduction band, they will migrate to the metal, which prevents recombination and allows the hole to migrate to the surface. Reducing recombination of electron-hole pairs increases photocatalytic activity.

The motivation for this research was the development and understanding of ZnO-based nanomaterials for use in photocatalytic applications. Hence, the research was divided into distinct chapters that fully incorporate design and synthesis of various ZnO-based nanomaterials as well as their photocatalytic applications. The specific projects were chosen to fully understand how photocatalytic properties were affected by various parameters. In subsequent chapters, formation and photocatalysis of ZnO-based nanomaterials will be discussed, including:

1. Synthesis and characterization of ZnO nanostrucutres
2. Investigation of the catalytic properties of ZnO nanostructures
3. Formation mechanisms of Au-ZnO heterostructures
4. Investigation of ZnO nanostructures supported on reduced graphene oxide
5. Synthesis of p-type N-doped ZnO nanostructures

Chapter 2: Characterization Techniques

2.1 UV-Visible absorption and photoluminescence spectroscopy

Nanostructured materials often exhibit unique optical properties that are not present in the bulk material. For example, gold nanoparticles appear red in color due to surface plasmon resonance compared to bulk gold, which appears gold in color. Optical properties of nanostructured materials often provide valuable information about particle size, shape and monodispersity as well as information about quality, impurities, defects and semiconductor band-gaps. Optical properties of the nanomaterials presented in this work are studied using UV-Visible absorption and photoluminescence (PL) spectroscopy.

In this work, nanoparticles are dispersed in an appropriate solvent (i.e. toluene, water, ethanol, etc.) by sonication. The absorbance spectra were measured using an Agilent 8453 UV-Visible Spectrophotometer operating with UV-Visible ChemStation software. Samples were measured using a quartz cuvette with a 1 cm pathlength. Prior to recording spectra, a background spectrum was recorded for the solvent. All solutions were adjusted to have an absorbance of one, which is an appropriate concentration for measuring PL. The PL spectra were recorded using a Varian Cary Eclipse Fluorescence spectrophotometer. Prior to recording spectra, the instrument was zeroed for the solvent. Typically, PL spectra were collecting using an excitation wavelength

that corresponds to the wavelength of maximum absorption. In general, ZnO PL spectra were collected using an excitation wavelength of 325 nm.

2.2 X-Ray diffraction

X-ray diffraction (XRD) is a valuable technique for identifying crystalline materials. Solids may either be described as amorphous or crystalline. Amorphous materials are those with atoms randomly arranged, whereas in crystalline materials the atoms are arranged in a regular pattern. Crystalline materials produce a unique XRD patterns that is like a fingerprint for each material and may be used for identification.

X-rays interacting with a solid may be scattered resulting in either destructive or constructive interference. The interaction between the incident X-rays and the sample results in constructive interference when the conditions satisfy Bragg's law. Bragg's law is written as

$$n\lambda=2d\sin\theta \qquad 2.1$$

where n is an integer, λ is the wavelength of the incident X-ray beam, d is the spacing between atomic layers in a crystal and θ is the scattering angle. A diffraction pattern is produced by collecting data for a range of 2θ angles.

In this work, XRD patterns of powder samples were measured using a Panalytical X'Pert Pro diffractometer with Cu Kα1 radiation. All measurements were carried out under ambient conditions. Diffraction patterns were analyzed using X'Pert Highscore Plus software and identied using the International Centre for Diffraction Data/Joint Committee on Powder Diffraction Standards (ICDD/JCPDS) diffraction pattern library.

2.3 Transmission electron microscopy

Transmission electron microscopy (TEM) is a powerful tool for characterizing nanoparticles allowing for evaluation of morphology and particle distribution through visualization.

In this work, particles are imaged using two microscopes: (1) Jeol JEM-1230 TEM equipped with a Gatan UltraScan 4000SP 4K x 4K CCD camera and (2) Carl Zeiss Libra 120 Plus Field Emission TEM. Both microscopes are operated at 120 kV.

Particles are supported on a substrate for imaging. In the case of TEM, support films are Formvar coated Cu grids in 200 mesh (Ted Pella). In a general sample preparation, particles are dispersed in an appropriate solvent (i.e. toluene, hexanes, methanol, etc.) by sonication. Following sonication, two drops of the dispersion are drop-cast onto a TEM grid placed on a piece of filter paper. The TEM grid is dried using an IR lamp for 1 hr to ensure complete evaporation of the solvent. Care must be taken during TEM sample preparation to ensure that an appropriate concentration of particles are supported on the TEM grid, because samples prepared using too high or too low a concentration are difficult to image. For samples prepared with too low a concentration, it is difficult to find particles on the substrate. For samples prepared with too high a concentration, aggregation of particles on the substrate makes it difficult to image distinct particles. UV-Visible absorption spectroscopy is useful for preparing dispersion of particles that absorb UV-Visible light. In general, a solution is an appropriate concentration if the absorbance of the solution is approximately one.

2.4 Raman spectroscopy

Raman spectroscopy is a sensitive tool for characterizing materials and providing information about defects and impurities. Raman spectroscopy is based on observing inelastic

scattering, or Raman scattering, of a monochromatic excitation source. Raman spectroscopy is often refereed to as being complementary to Infra-Red (IR) spectroscopy because both information regarding vibrational, rotational and other low-frequency modes. Selection rules are used to determine which modes are IR active and which are Raman active. Typically, a molecular vibration is IR active if it is asymmetrical and results in a change in the dipole moment. A molecular vibration is Raman active if there is a change in polarization of the electron cloud of the molecule.

A typical Raman experiment uses a laser source with an appropriate wavelength to irradiate a sample. Light is scattered by the sample, and a detector measures the frequency. Most of the light scattered will have the same frequency as the incident beam, elastic or Rayleigh scattering. However, inelastic scattering occurs when the laser interacts with the sample causing the frequency to be shifted from the incident beam. If the material absorbs the energy, lower frequency measured, it is referred to as a Stokes shift. If the material loses energy, higher frequency measured, it is referred to as an anti-Stokes shift.

Raman spectroscopy is used to study molecular compounds and crystalline solids. As mentioned previously, Raman spectroscopy is used to probe molecular vibrations. However, Raman spectroscopy probes phonon modes in solid materials. A phonon mode is Raman active based on the crystal symmetry. Therefore, this dissertation uses Raman spectroscopy to study defects and impurities in crystalline ZnO materials.

In general, the wavelength of the laser used for Raman spectroscopy has a strong impact on the experimental results. For Raman spectroscopy, laser wavelengths can range from UV through visible to near infra-red region. Sensitivity, spatial resolution and sample behavior are all

sensitive to the wavelength of the laser. Blue or green lasers, such as the 532 nm laser chosen for the experiments presented here, are best for inorganic and carbon (i.e. graphene) materials.

In this work, Raman spectra of powder samples were performed using a Thermo Scientific DXR SmartRaman Spectrophotometer with an excitation laser at 532 nm operating at 5 mW. Powder samples were supported using a standard sample holder designed for pressing powder samples into a small pellet. In some cases, samples exhibited significant fluorescence, in which case, photo-bleaching of the sample was performed for 5 min prior to data collection.

2.5 X-Ray photoelectron spectroscopy

X-ray photoelectron spectroscopy (XPS) is a surface sensitive technique used to study chemical composition, chemical states and charge transfer effects. In general, a sample is irradiated with photons in the X-ray region. Upon irradiation, the photon interacts with electrons in the atomic orbital, which results in the emission of photoelectrons. Photoelectrons emitted near the surface, ~ 10 nm, are able to escape into the vacuum chamber to be measured by a detector. Emitted photoelectrons are then separated according to kinetic energy (KE) and counted. The energy of the photoelectrons is related to the atomic and molecular environment, and therefore provides chemical information about the material. This process is described by a modified Einstein equation:

$$KE = h\nu - (BE + \phi + d) \qquad 2.2$$

where KE is the kinetic energy of the photoelectron, hν is the energy of the X-ray source, BE is the binding energy of the photoelectron, ϕ is the work function of the spectrometer and d is positive charge on the sample (if charging). The binding energy is used to describe how electrons are bound to the nucleus of an atom. Different elements have different nuclear charges, which result in varying binding energies. Further, the types of atoms bound to the atom of emitted the

photoelectron also effect the binding energy. Overall, the binding energy of the electrons is used to describe the chemistry.

The XPS spectra shown in this dissertation were collected using a Thermo Scientific ESCALAB 250 with a focused monochromatic Al Kα X-ray (1486.6 eV) source and a 180° hemispherical analyzer with a six-element multichannel detector. During data collection, charge compensation was performed using an internal flood gun with 2 eV electrons, and a low energy Ar^+ external flood gun. Charge compensation reduces sample charging as described by d in equation 2.2. For data collection, dry powder samples were pressed into indium foil that was attached to a sample holder with carbon tape. This method is utilized to reduce sample charging as well as eliminate additional carbon signal from the carbon tape.

XPS spectra were analyzed using CasaXPS processing software. All binding energies were corrected to the aliphatic hydrocarbon C 1s peak at 284.5 eV. Correction is required to account for slight variations in binding energies from sample to sample. Peak fitting was performed to analyze various components present in each spectrum. In general, similar peaks in different samples were fit to have binding energies within 0.2 eV of the reference sample and full width half max (FWHM) within 0.2 eV of the reference sample.

2.6 Evaluation of photocatalytic activity

Photocatalytic activity was evaluated by studying the degradation of malachite green, which is easily observed by following the absorbance of the dye solution. Photodegradation experiments were carried out in 100 mL Erlenmeyer flasks. A UV lamp operating at 365 nm was used as the light source. The experiments were performed at ambient conditions in a box designed to block any ambient light. Dye solution was prepared using deionized water and malachite green oxalate salt (Aldrich, technical grade). Catalyst particles were dispersed in

deionized water by bath sonication. Solutions were prepared with final concentration of $3x\ 10^{-5}$ M malachite green and 0.25 mg/mL catalyst nanoparticles. The dye-particle solution was stirred (using magnetic stirring) in the dark for 30 minutes to insure adsorption of dye molecules onto the catalyst surface. Immediately following 30 minutes of dark, the absorbance was measured, t=0. Then, the mixture was continuously top-irradiated with a UV lamp (365 nm) for 90 minutes and the absorbance was measured at 10-minute intervals. Full spectrum measurements were recorded to allow for baseline correction. Nanoparticle catalysts were not maintained after photocatalytic evaluation.

Absorbance spectra were baseline corrected using Origin Pro 8 software. Baseline correction was completed to ensure that all spectra had an absorbance of zero in the long-wave region. Next, the maximum absorbance value for each spectrum (absorbance at 617 nm) was recorded for studying the kinetics. According to the Beer-Lambert Law, absorbance (A) is related to concentration (C) by the relationship

$$A = \varepsilon \cdot l \cdot C \qquad 2.3$$

where ε is the molar aborbtivity and l is the pathlength of the cell. Therefore, we are able to use the absorbance as a measure of concentration.

For the photocatalytic studies, the kinetics of degradation of malachite green is calculated by plotting $\ln(C/C_0)$ as a function of irradiation time where C_0 is the concentration at t=0. Since the molar absorbtivity and the cell pathlength remain the same, C/C_0 is equivialent to A/A_0 where A_0 is the absorbance at t=0. A linear plot indicates that the photodegradation follows first order reaction kinetics $\ln(C/C_0) = kt$. Thus, the rate constant, k, may be calculated for each system by fitting a line to the data and taking the slope. Linear regression is carried out using the entire

region (10-90 min) using Origin Pro 8. Experiments were repeated in triplicate and the average values were taken for percent dye degraded in 90 minutes as well as rate constant, k.

Chapter 3: Synthesis and Characterization of Zinc Oxide Nanostructures

3.1 Introduction

Certain metal oxides, especially ZnO and TiO_2, have been extensively studied for their unique properties and photocatalytic activity. Through size and shape control, it is possible to finely tune the physical and chemical properties of metal oxide nanostuctures.

There are numerous methods for ZnO nanoparticle formation; each synthesis method provides particular advantages and challenges. Synthesis methods for ZnO nanostructures include: chemical vapor deposition,[4, 30] chemical bath deposition,[82] pulse laser deposition[83] and other high temperature methods,[12, 33, 84, 85] as well as, thermal[7, 15, 37, 39, 86, 87] and microwave[88] assisted synthesis methods. Each of these methods utilizes different starting materials and proceeds via different reaction pathways. For these reasons, each method produces particles with unique morphologies as well as physical and chemical properties.

Wet chemical synthesis and bottom up methods provide the most control and offer the best options for the production of small particles. The most established methods for ZnO nanoparticle synthesis involve the thermal decomposition of zinc precursors in the presence of stabilizing molecules. Adsorption of molecules onto the nanoparticles surface directs the growth and electrostatically stabilize the particles.

Thermal decomposition occurs as a result of heating; however, the manner in which the precursor is heated influences the final product. Microwave irradiation is an efficient and selective heating process used for nanoparticle synthesis. Compared to conventional heating methods, microwave irradiation significantly enhances reaction rates and allows reactions to proceed at lower temperatures.[89, 90] If the reactant requiring the most heat has the greatest ability to absorb microwaves, selective dielectric heating results in less overall energy required for synthesis.[90] Previous reports show that microwaves enhance organic reactions and lower activation energies.[88] The use of microwave irradiation allows for rapid and uniform heating as well as the ability to control nanoparticle size and shape.

Non-aqueous routes, which use non-polar stabilizing molecules, offer exceptional control and yield high quality ZnO nanostructures. Non-aqueous routes to form metal oxides proceed through simultaneous organic and inorganic pathways. Formation of the inorganic particles is possible through the organic chemical reactions, which are responsible for supplying oxygen to form the metal oxide.[88] These organic reactions have strong influences on particle size, shape and composition.[88] Thus, an understanding of the reaction will allow for the particle to be tailored to their specific application. For example, it is well known that metal oxides with a higher number of oxygen vacancies at the surface are more effective gas sensors[91] and catalysts. Thus, particles intended for use as catalysts or in gas sensing applications should have the greatest number of O-vacancies. Particles intended for use in optoelectronic devices may require a lower number of vacancy sites.

The basic challenge to any nanoparticle synthesis is the development of rational synthesis methods that allow for control of both the size and shape of the particles. This process produces homogeneous ZnO nanoparticles with controlled morphology through a non-aqueous, single-pot,

microwave synthesis method. Through this technique, hexagonal nanopyramids and nanorods are synthesized by varying the concentration of zinc acetate in a mixture of oleic acid and oleylamine.

3.2 Synthesis of ZnO Nanostructures

A single-pot, microwave synthesis method was developed to systematically study the formation of ZnO nanostructures. In a typical synthesis, anhydrous zinc acetate (Aldrich, 99.99%) was added to a 50 mL round bottom flask and dissolved in a mixture of oleic acid (Aldrich, technical grade, 90%) and oleylamine (Aldrich, technical grade, 70%). The reaction mixture was heated, to dissolve the zinc acetate and remove any residual water, in a hot oil bath with magnetic stirring to 120 °C, and the temperature was maintained for 1 hour. After heating, the flask was removed from the oil bath and immediately microwaved; the reaction mixture was not cooled to room temperature prior to microwave irradiation (MWI). The majority of the solutions were microwaved in a conventional 1000 W microwave at full power. For the mechanism study, solutions were microwaved using a CEM Discover microwave reactor operating at 250 W with a control temperature of 250 °C. To systematically study nanoparticle formation, the concentration of zinc acetate and proportions of oleic acid (OAC) and oleylamine (OAM) were varied as reported in Table 3.1.

Table 3.1: Summary of experimental conditions for ZnO synthesis.

Zinc acetate (mmol)	Oleic acid (mmol)	Oleylamine (mmol)	Mole ratio oleic acid : oleylamine	Temperature (°C)
2	20	20	1:1	280
2	10	30	1: 3	233
2	0	40	oleylamine only	184
5	10	25	1: 2.5	250
10	10	25	1: 2.5	259
20	10	30	1: 3	268
20	20	20	1:1	260
20	10	25	1: 2.5	255
30	10	25	1: 2.5	235
40	10	25	1: 2.5	241

Immediately following MWI, the solution temperature was measured using a temperature probe (IKA ETS-D5). This method provides an estimate of the reaction temperature. For the formation of ZnO nanostructures, reaction temperatures ranged from 184-280 °C. Variations in reaction temperatures are attributed to microwave fluctuations as well as variations in solvent composition. For example, ZnO formed in OAM only reached 184 °C, and ZnO formed in a 1:2.5 mixture ranged from 260-280 °C.

This synthesis has several benefits. First, it is a one-pot method, which allows for a straightforward production of monodisperse particles. Second, oleic acid and olyelamine act as both solvent and stabilizing molecules, which are also known as capping agents, because they "cap" the particle surface. Figure 3.1 illustrates a ZnO nanoparticle stabilized with oleic acid and

oleylamine ligands. Lastly, the use of microwave irradiation allows for the reaction to be completed quickly and at relatively low temperatures.

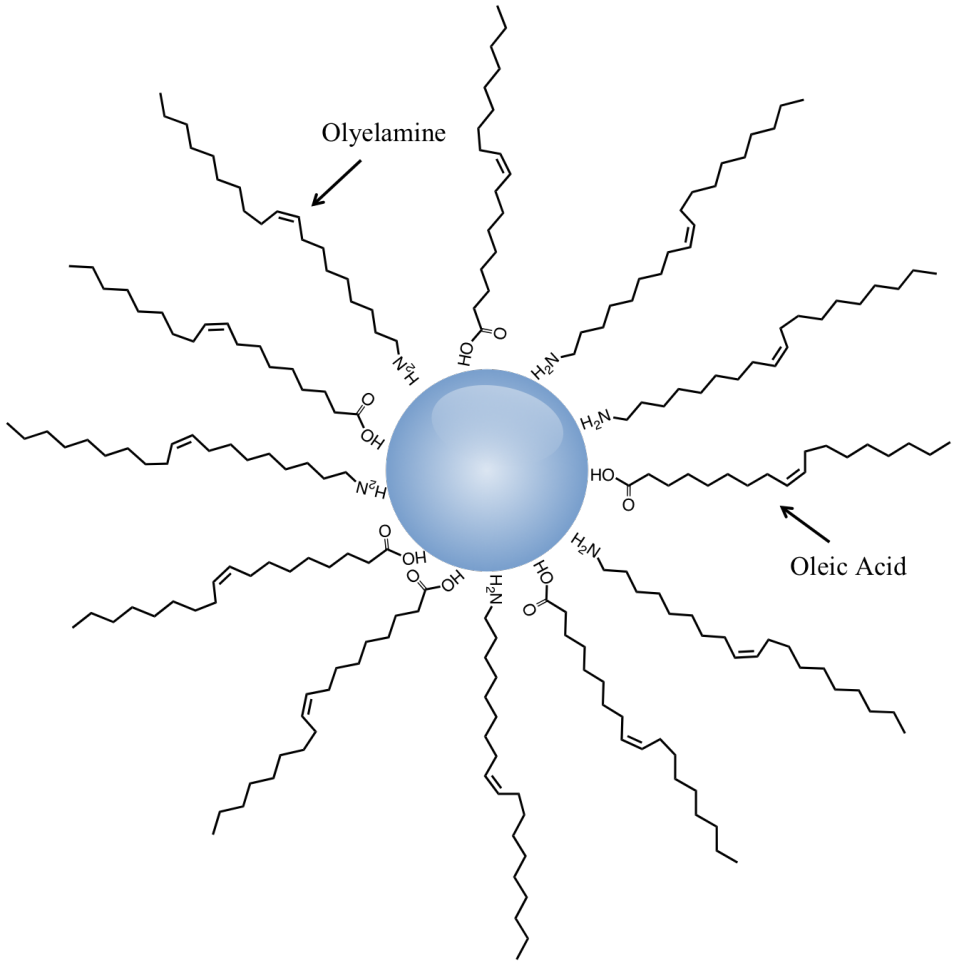

Figure 3.1. Illustration of a ZnO nanoparticle stabilized with oleic acid and oleylamine. The long carbon chains are bound to the surface, and the bulkiness of the carbon chains provides stability in solution. Note that this is an illustration and is not drawn to scale.

3.3 Growth and shape evolution

This synthetic approach utilizes microwave irradiation to thermally decompose anhydrous zinc acetate to ZnO in the presence of OAC and OAM. ZnO nanostructure size and shape are controlled by varying the reaction conditions. Two approaches for controlling nanoparticle morphology were studied: (a) varying the proportions of capping agents OAC and

OAM and (b) varying the concentration of the precursor, zinc acetate. Detailed structural and optical studies were performed on each sample. Figure 3.2 summarizes the synthetic strategies.

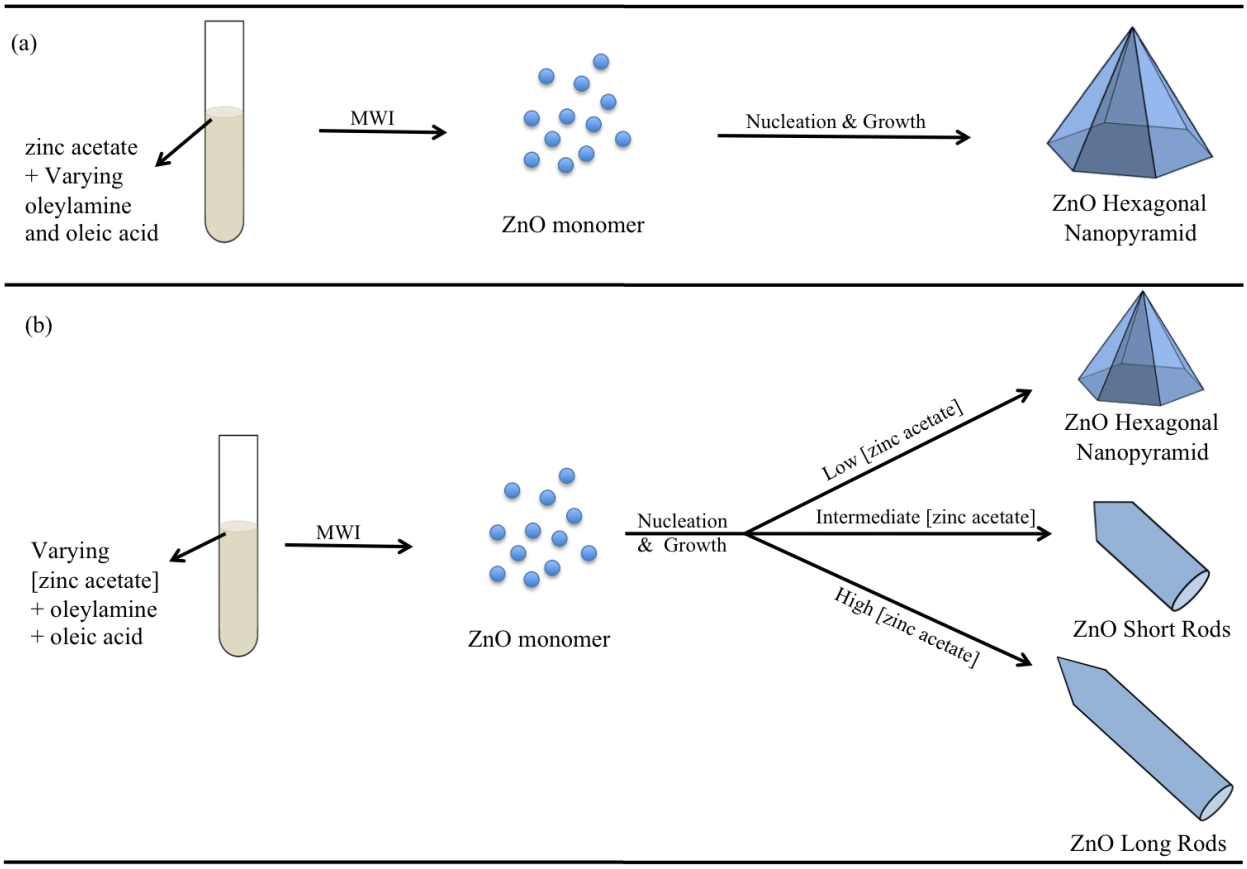

Figure 3.2. Schematic of nucleation and growth of ZnO nanopyramids and rods.

In the first approach (Fig. 3.2-a) the effect of varying the proportions of capping agents OAC and OAM on ZnO nanostructure formation was studied. Previous reports have demonstrated that varying these proportions results in strong shape control, and it is well known that ligands selectively adsorb to particular crystal faces of ZnO.[92] Organic capping ligands direct the growth of the nanostructures. Polar capping ligands preferentially adsorb onto polar crystal faces, while non-polar capping ligands tend to adsorb onto non-polar crystal faces. Therefore, by controlling the proportions of capping ligands, the growth in the direction of certain crystal faces is either hindered or enhanced.

The resulting morphology of the ZnO nanostructures was observed to be slightly dependent on the molar ratios of OAC and OAM. At a fixed concentration of zinc acetate (2 mmol), all of the nanostructures have hexagonal nanopyramid morphologies, but varying the proportions of OAC and OAM results in a range of particles sizes. As the proportion of OAM relative to OAC increases, the average particle diameter increases. Figure 3.3 shows typical TEM micrographs of the nanostructures produced with different proportions of OAC and OAM. The TEM images indicate that the average diameter of the nanopyramids range from 60-250 nm. The average diameters for the nanopyramids are 61, 242, and 100 nm for particles prepared using 1:1, 1:3 OAC/OAM and olyelamine only, respectively.

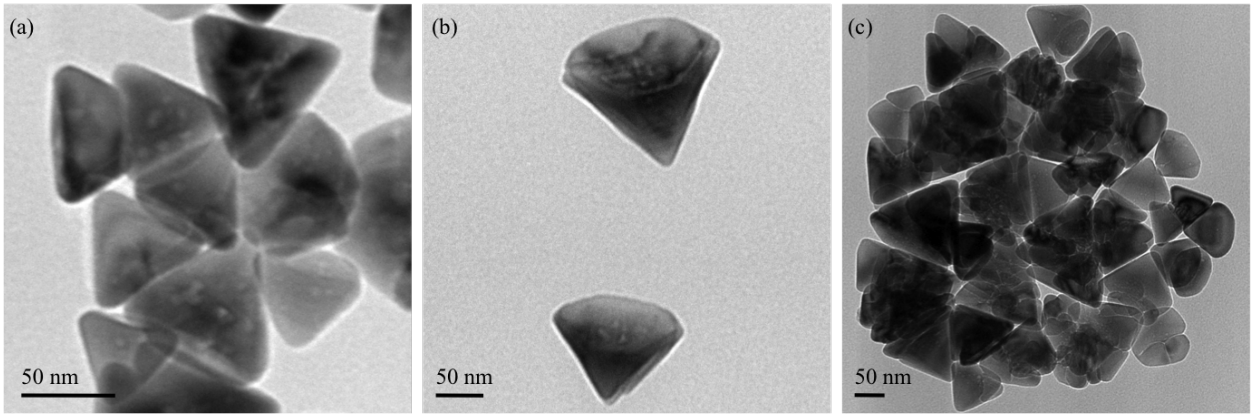

Figure 3.3. TEM images of ZnO nanopyramids prepared using 2 mmol of zinc acetate in the presence of (a) 1:1, (b) 1:3 molar ratio of oleic acid to oleylamine, and (c) oleylamine only.

The crystallinity of the resulting ZnO nanopyramids is studied through X-ray diffraction (XRD), and XRD patterns are given in Figure 3.4. The XRD pattern of each ZnO product shows peaks indicative of the hexagonal wurtzite crystal structure of bulk ZnO crystals (JCPDS Refrence # 36 – 1451). A slightly enhanced (101) peak, relative to (002), is observed in the pattern obtained from particles prepared using 1:3 OAC/OAM. This enhancement is attributed to a more defined facet present at the base of the pyramid that is not present in the other hexagonal pyramids.

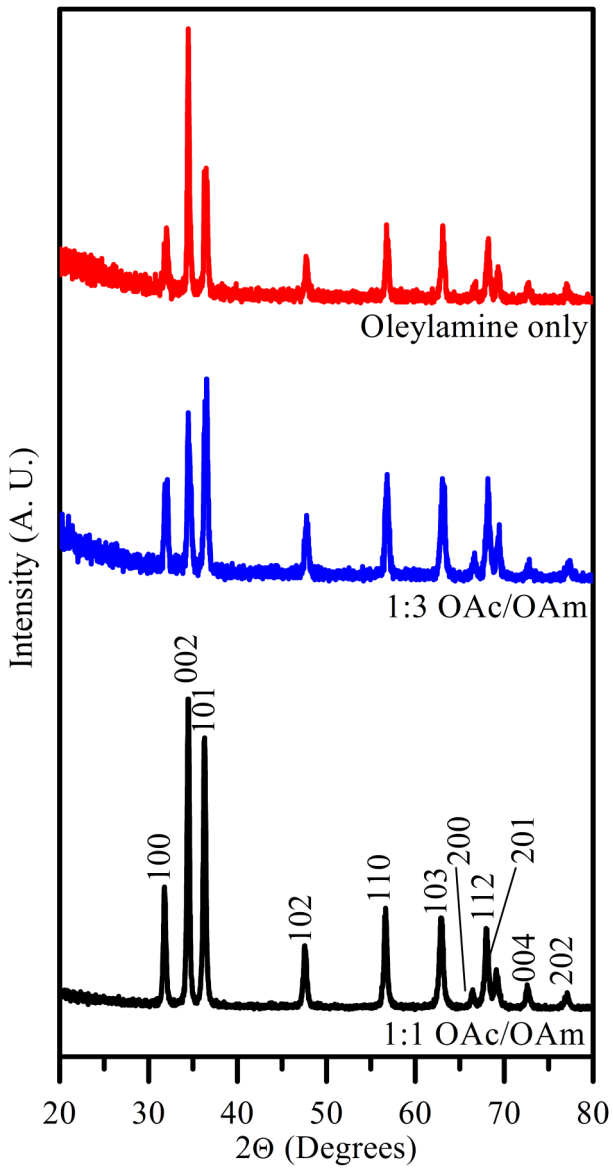

Figure 3.4. XRD patterns of ZnO nanopyramids prepared using 2 mmol of zinc acetate in the presence of (a) oleylamine only, (b) 1:3, and (c) 1:1 molar ratio of oleic acid to oleylamine. XRD data were obtained after 15 min MWI (1000W).

In the second approach (Fig. 3.2b), the concentration of the zinc acetate precursor was varied. Previous reports[37, 93] have shown that the starting concentration has a strong impact on the particle size and shape. The resulting morphology of the ZnO nanostructures was observed to be strongly dependent on the zinc acetate concentration. Low concentrations of zinc acetate produced hexagonal nanopyramids as seen in Figure 3.3, but increasing the concentration yielded rod shaped particles, Figure 3.5.

At low concentrations, 2 mmol and 5 mmol zinc acetate, particles have hexagonal pyramid morphologies. The increase from 2 to 5 mmol results in much larger particles. Upon further increasing the zinc acetate to 10 mmol (c), the formation of pencil shaped rods is evident. Increasing the zinc acetate to 20 mmol (d) results in pencil shaped rods with a larger aspect ratio. The average length of the rods increases from 29 to 292 nm for 10 mmol and 20 mmol zinc acetate, respectively. The base of the rods slightly increases from 57 to 76 nm for 10 mmol and 20 mmol, respectively. Finally, increasing the zinc acetate to 30 and 40 mmol results in the formation of high aspect ratio rods. These rods have lengths of 280 and 436 nm and widths of 61 and 45 nm for 30 and 40 mmol, respectively. As the concentration of zinc acetate increases, the length of the rods increases and the width of the rod decreases, which results in an overall increase in aspect ratio. The relationship between concentration and aspect ratio is given in Figure 3.6.

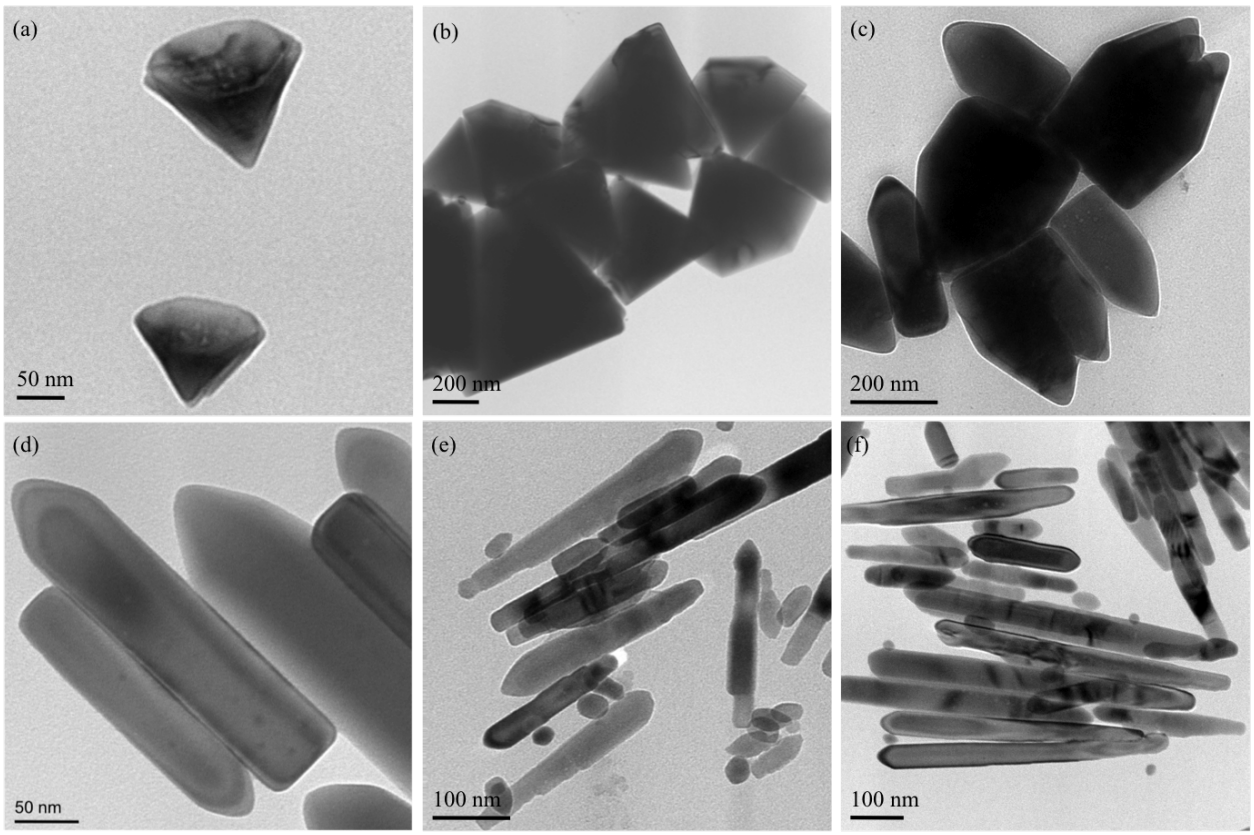

Figure 3.5. TEM images of ZnO rods prepared using (a) 2, (b) 5, (c) 10, (d) 20, (e) 30 and (f) 40 mmol of zinc acetate in the presence of 1:2.5 molar ratio of oleic acid to oleylamine. Micrographs were obtained after 15 min MWI (1000 W).

Nanoparticle morphology is directed by the capping ligands, or more specifically, the ratio of capping ligands relative to zinc acetate. During particle formation, the dipole moment of OAC results in a strong electrostatic interaction with the polar surfaces of the growing ZnO nanostructure. The carboxylic acid group binds to the surface of the ZnO nanostructure, and prevents growth in that direction.[94] In the presence of high concentrations of zinc acetate, OAC binds selectively to the polar surfaces and inhibits growth in those directions, which results in nanorods with higher aspect ratios. At lower concentrations of zinc acetate, OAC is present in excess and inhibits growth in all directions. Therefore, as the concentration of zinc acetate is increased, the aspect ratio of the nanorods increases. Studies were not carried out to see if

increasing beyond 40 mmol zinc acetate would result in higher aspect ratio nanorods because of solubility limitations.

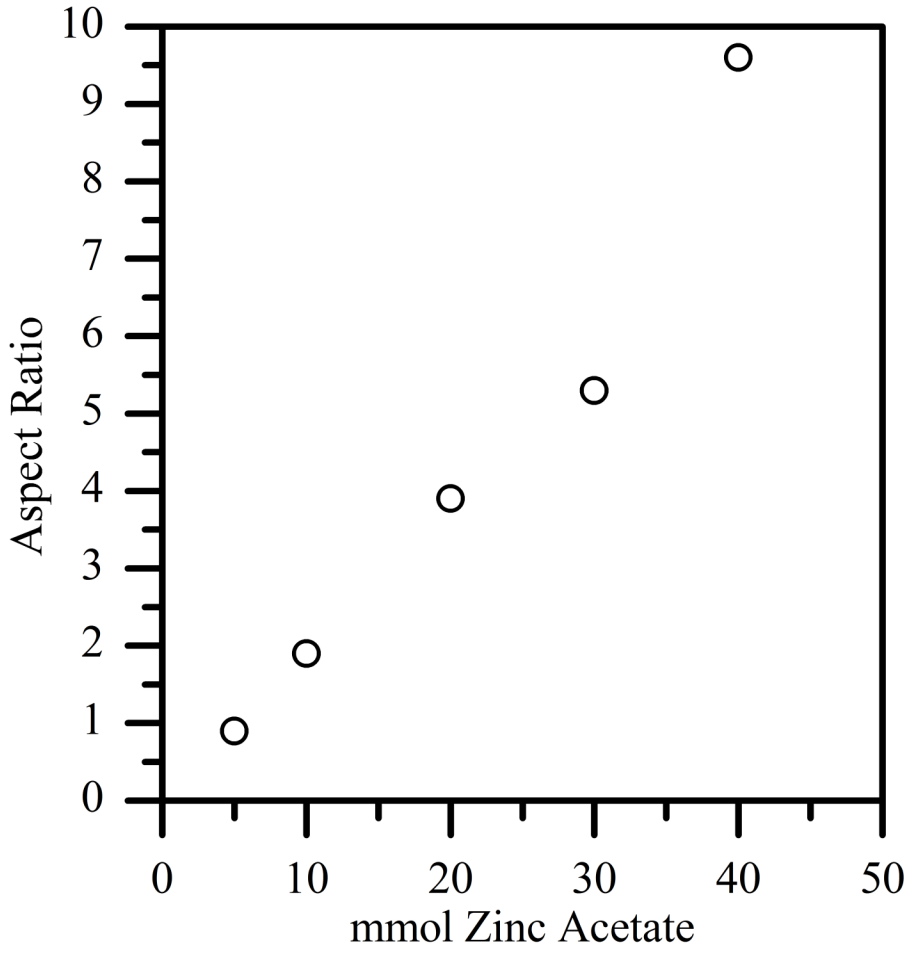

Figure 3.6. Plot showing the relationship between the aspect ratio of the ZnO nanoparticles as a function of the moles of zinc acetate used in the reaction.

The crystallinity of the rods was studied using XRD, and XRD patterns are displayed in Figure 3.7. Each pattern indexes to hexagonal wurtzite crystal structure of bulk ZnO, but the rods show the (110) peak significantly enhanced. For bulk ZnO, it is expected that the intensity of the (110) peak be 30% compared to the (101) peak.[95, 96] The rods prepared using 40 mmol zinc acetate, which have an aspect ratio of 10, have a (110) peak with an intensity of 89% relative to the (101) peak. This enhancement implies that growth of the length of the rod is along the (100) crystal face.

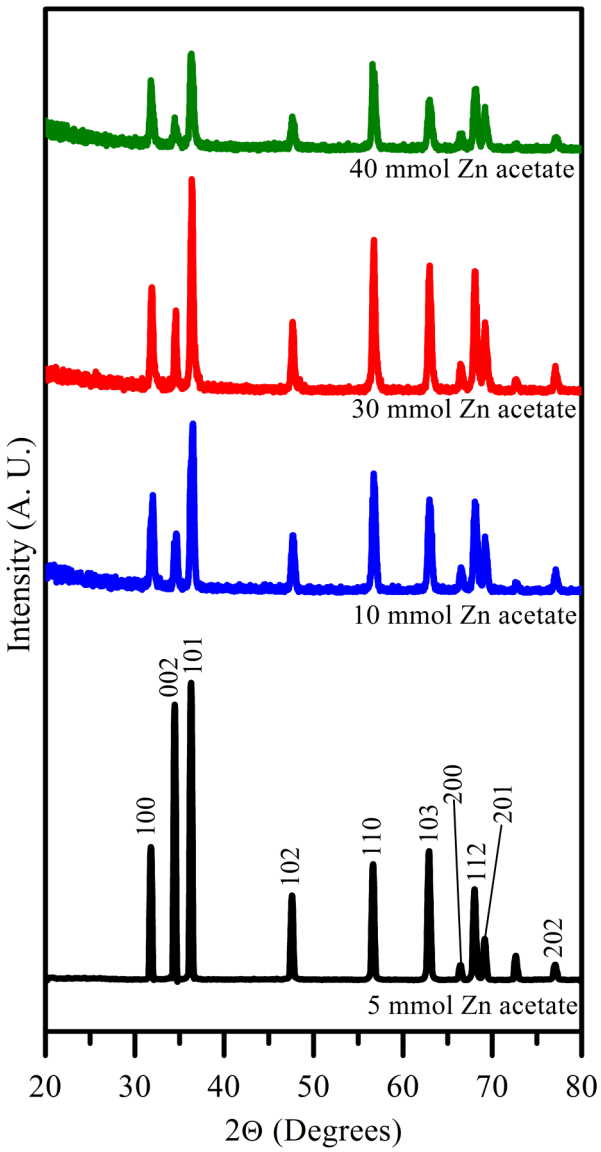

Figure 3.7. XRD patterns of ZnO nanopyramids prepared using varying amounts of zinc acetate in the presence of 2:5 molar ratio of oleic acid to oleylamine. XRD data were obtained after 15 min MWI (1000W).

Finally, a higher concentration of zinc acetate (20 mmol) with different ratios of OAC relative to OAM was studied. Figure 3.8 shows typical TEM micrographs of the nanostructures produced from mixtures of 20 mmol zinc acetate prepared using 3 different compositions of OAC and OAM. For nanorods prepared from 20 mmol zinc acetate, the aspect ratio varied from 2 to 4 depending on the ratio of OAC to OAM. From TEM, the nanorods range from 200-300 nm

in length with the hexagonal base ranging from 70-125 nm in diameter. In this case, a mixture of 1:2.5 OAC/OAM produced rods with higher aspect ratios than those produced in either 1:1 or 1:3 mixtures. The 1:2.5 mixture is considered the optimum mixture for producing rods.

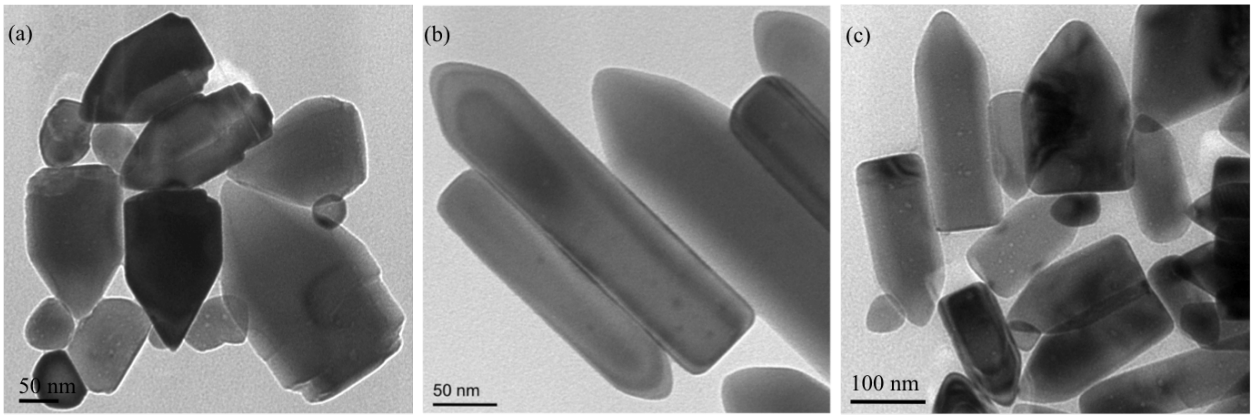

Figure 3.8. TEM images of ZnO rods prepared using 20 mmol of zinc acetate in the presence of (a) 1:1, (b) 1:2.5, and (c) 1:3 molar ratio of oleic acid to oleylamine. TEM images were obtained after 15 min MWI (1000W).

The XRD patterns for the rods prepared using 20 mmol zinc acetate in varying ratios of OAC to OAM, Figure 3.9 shows enhancement of the (100) and (110) peaks. (110) is the most significantly enhanced direction, and therefore, the growth of the length of the rods occurs along the (110) crystal face. This is consistent with all particles showing an aspect ratio above 1.

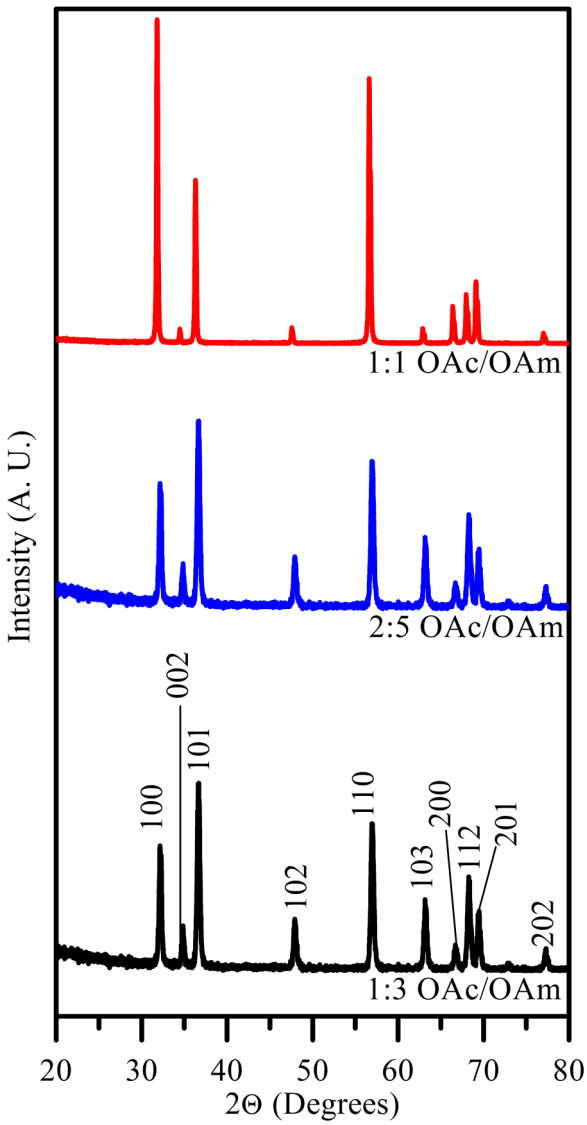

Figure 3.9. XRD patterns of ZnO nanopyramids prepared using 20 mmol of zinc acetate in the presence of varying molar ratios of oleic acid to oleylamine. XRD data were obtained after 15 min MWI (1000W).

Based on the results from both synthetic approaches, it can be concluded that the starting concentration of zinc acetate and solvent composition are critical for the shape control of ZnO nanostructures. Low concentrations of zinc acetate produced hexagonal pyramids, and high concentrations of zinc acetate produced rods. The final morphology is finely tuned by controlling the solvent composition.

3.4 Optical Properties

Optical properties of ZnO nanostructures were studied using UV-Visible absorption spectroscopy and photoluminescence (PL) spectroscopy. Optical properties are sensitive to experimental conditions and nanoparticle morphology.

3.4.1 UV-Visible absorption spectroscopy

Zinc oxide has a strong absorbance band, which appears in the UV region due to its wide band-gap (3.3 eV). The position of the absorbance peak is directly related to the band-gap energy. It is well known that particle size affects band gap at the nanoscale; smaller particles have increased band gap energies. Therefore, UV-Visible absorption spectroscopy can be used to study particle growth and characterize ZnO nanoparticles. UV-Visible absorbance of nanopyramids and nanorods provides valuable information regarding particle size, shape and sample homogeneity.[97]

The UV-Visible absorption spectra of ZnO nanostructures are displayed in Figure 3.10. All spectra were recorded after 15 minutes MWI time using as prepared particles dispersed in toluene. Each spectrum shows a strong absorbance peak at 370 nm. The absorption edge at 370 nm corresponds to the electronic transitions between the valence and conduction bands, which are slightly blue-shifted from bulk ZnO that appears at 385 nm (3.2 eV).[98] The blue-shifted absorbance is attributed to quantum confinement that results in an increased band gap with decreasing particle size. The largest particles are the main contributors to the absorbance edge, but all particles contribute to the maximum absorbance peak. The sharpness of the edge indicates sample homogeneity and suggests a narrow size distribution.[98] The absorbance spectra also demonstrate a broad absorbance tail at longer wavelengths that is a result of light scattering from the nanostructures, which appear white in solution.

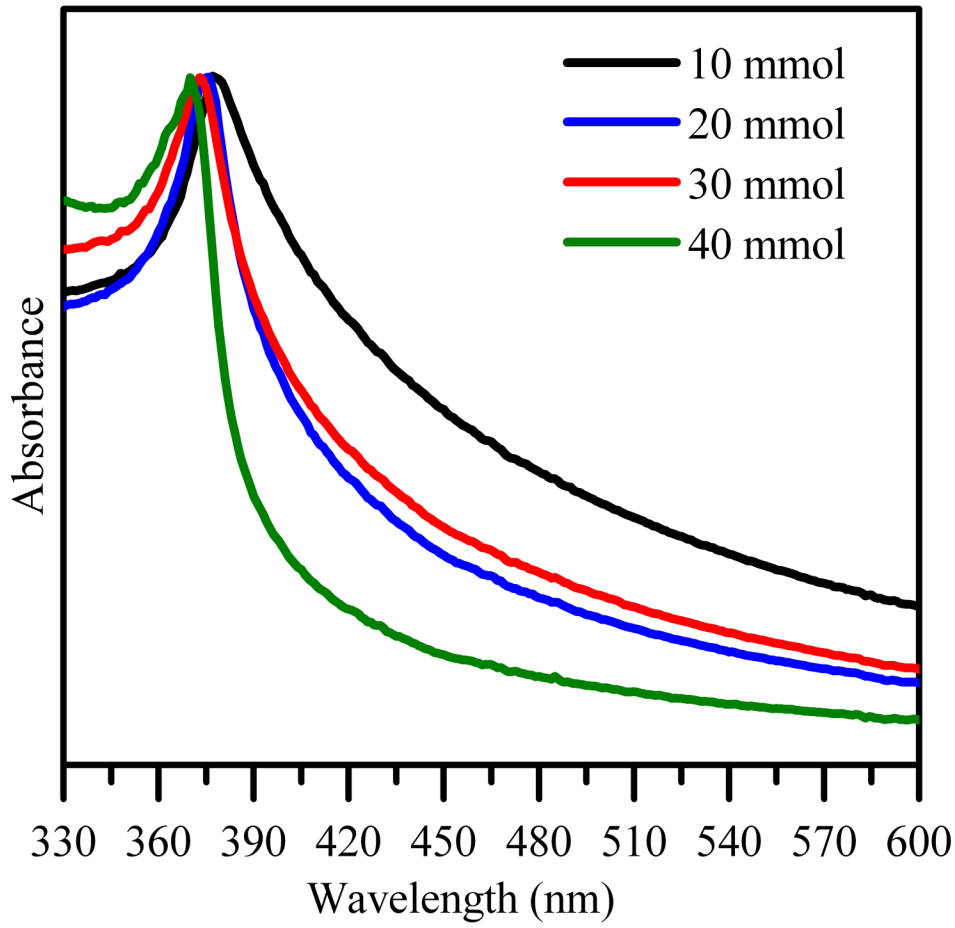

Figure 3.10. UV-Visible absorbance spectra for ZnO nanostructures prepared using varying amounts of zinc acetate in the presence of 1:2.5 molar ratio of oleic acid to oleylamine. Absorbance data were obtained after 15 min MWI (1000W).

3.4.2 Photoluminescence spectroscopy

ZnO nanostructures are studied using photoluminescence (PL) spectroscopy. In general, room temperature PL of ZnO consists of 2 emission bands: a UV emission band and a visible emission band. The visible emission band is attributed to defects and impurities within the crystal lattice. The position and intensities of these bands are dependent on the experimental conditions, crystallinity, and morphology.

PL spectroscopy of ZnO is strongly dependent on temperature. Both room temperature and low temperature PL for ZnO nanostructures have been previously reported. Low temperature

PL spectra show peaks that correspond to bound-exciton, donor-acceptor pair transitions, longitudinal optical phonon replicas, and free-exciton emission. The bound-exciton peaks are dependent on donor/acceptor concentrations and their capture cross sections. The exact chemical identity of donors and acceptors responsible for bound exciton peaks remains controversial. As the temperature increases, the intensity of the emission bands decreases. The free-exciton emission red-shifts with increasing temperature and is the only emission band observed at room temperature.

Studies have reported PL peak shifts for different morphologies of ZnO nanostructures measured at room temperature.[99] The position of the UV-emission band ranges from 377 to 397 nm depending on the particle shape. There are two possible explanations for these shifts: quantum confinement and native defects. For nanoparticles of different sizes, quantum confinement has been reported to cause a blue-shift of band-edge emission with decreasing size. For nanostructures of similar size, shifting of the emission band amongst particles with varying morphologies is attributed to different concentrations of native defects. Nanoparticles have a higher concentration of defects on the surface compared to bulk material because of increased surface area. Different particle morphologies have different surface area to volume ratios, and the defect levels vary with morphology. These variations affect the position and shape of the PL emission band. Therefore, the position and shape of the emission band is dependent on both particle morphology and preparation method.

Room temperature PL of ZnO may also exhibit a second emission band in the visible region, which is attributed to defects. The ratio of intensity the UV-band relative to the defect band depends on the excitation density and area. This ratio is useful for comparing crystalline quality from sample to sample if measurements are carried out using identical excitation

conditions. The most common visible emission for ZnO is green emission, but yellow, red, and blue-violet defect emission have also been reported.

Several explanations exist for the presence of green emission. The most common explanation attributes the emission to singly ionized oxygen vacancies. However, other explanations include oxygen vacancies and zinc interstitials, intrinsic defects, zinc vacancies, and surface defects. Regardless of the origin, it is widely believed that the defects responsible for green emission are located on the surface. Studies have confirmed this hypothesis by using surfactant to coat ZnO and suppress green emission.

Similarly, the less common defect emission peaks are attributed to specific defects either on or within the ZnO. Yellow defection emission is attributed to oxygen interstitials. The deep levels for green and yellow emission are different, because the defect for the yellow emission is not located on the surface. Orange-red emission is attributed to oxygen-rich ZnO. Blue-violet emission is attributed to zinc vacancies. Despite these claims, the exact origin of the defect emission remains unclear.

PL spectra for various morphologies of ZnO prepared in OAM and OAC are shown in Figure 3.11. A strong UV-band is observed around 380 nm, and there is little shifting for various morphologies. A second visible emission band is observed in each sample, which is attributed to defect emission. The defect emission band is slightly blue-shifted for the highest aspect ratio rods.

Furthermore, the ratio of the defect band relative to the UV-band increases with increasing aspect ratio. This is consistent with an increase in the surface area to volume ratio. It is reasonable to assume that ZnO rods with higher aspect ratios have a greater concentration of defects on the surface. This is observed by the increase in defect emission.

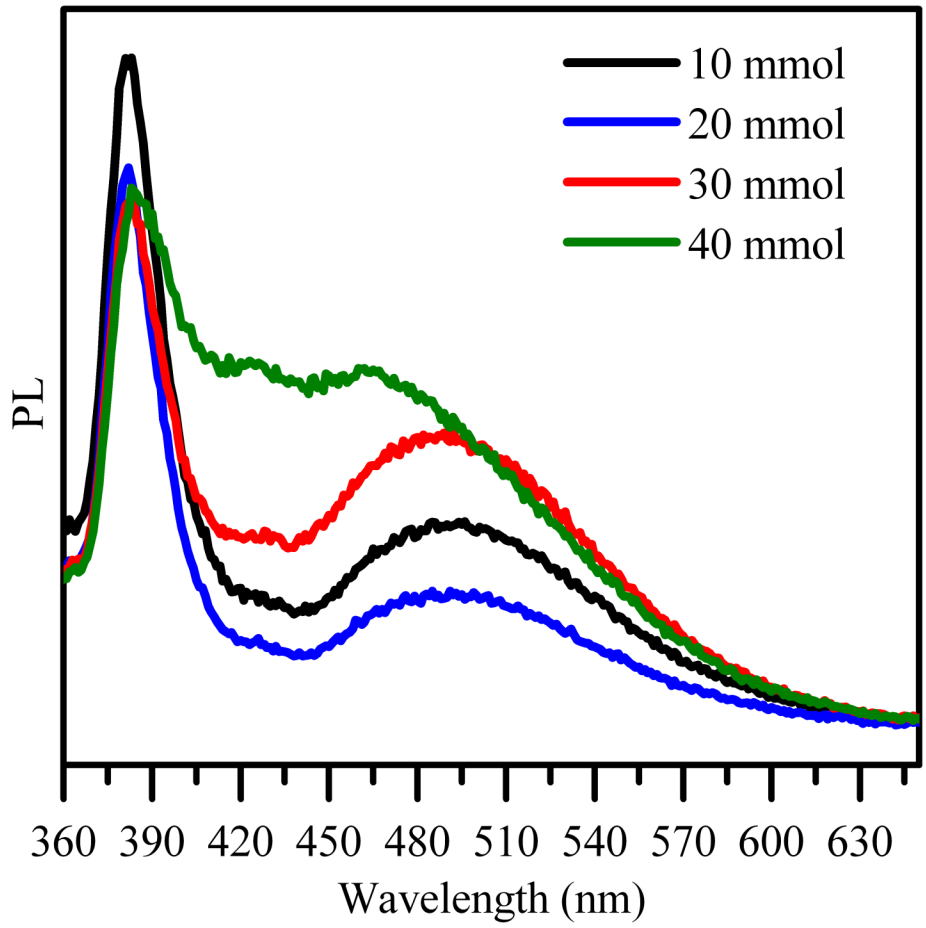

Figure 3.11. Photoluminescence spectra for ZnO nanostructures prepared using varying amounts of zinc acetate in the presence of 2:5 molar ratio of oleic acid to oleylamine. PL data were obtained after 15 min MWI (1000W).

3.5 Raman Spectroscopy

Raman spectroscopy is a powerful tool to characterize ZnO. ZnO has several distinct Raman bands, and the appearance of additional bands provides information about oxygen vacancies and impurities in the crystal lattice. Raman spectra for pure ZnO prepared with different concentrations of zinc acetate are shown in Fig. 3.12. Raman analysis of pure ZnO has been previously reported.[100-102] ZnO shows characteristic bands at 330, 380 and 437 cm^{-1} with the peak at 437 cm^{-1} being the most intense. Therefore, all spectra have been normalized with respect to the peak at 437 cm^{-1}. The peaks at 330 and 437 cm^{-1} are attributed to vibration modes

2E2(M) due to multiple-phonon-scattering processes and E2(high) from O atom, respectively. The peak at 380 cm^{-1} is attributed to A1(TO) vibration mode. The Raman spectra are not dependent on morphology of the ZnO, and there are no spectral changes observed.

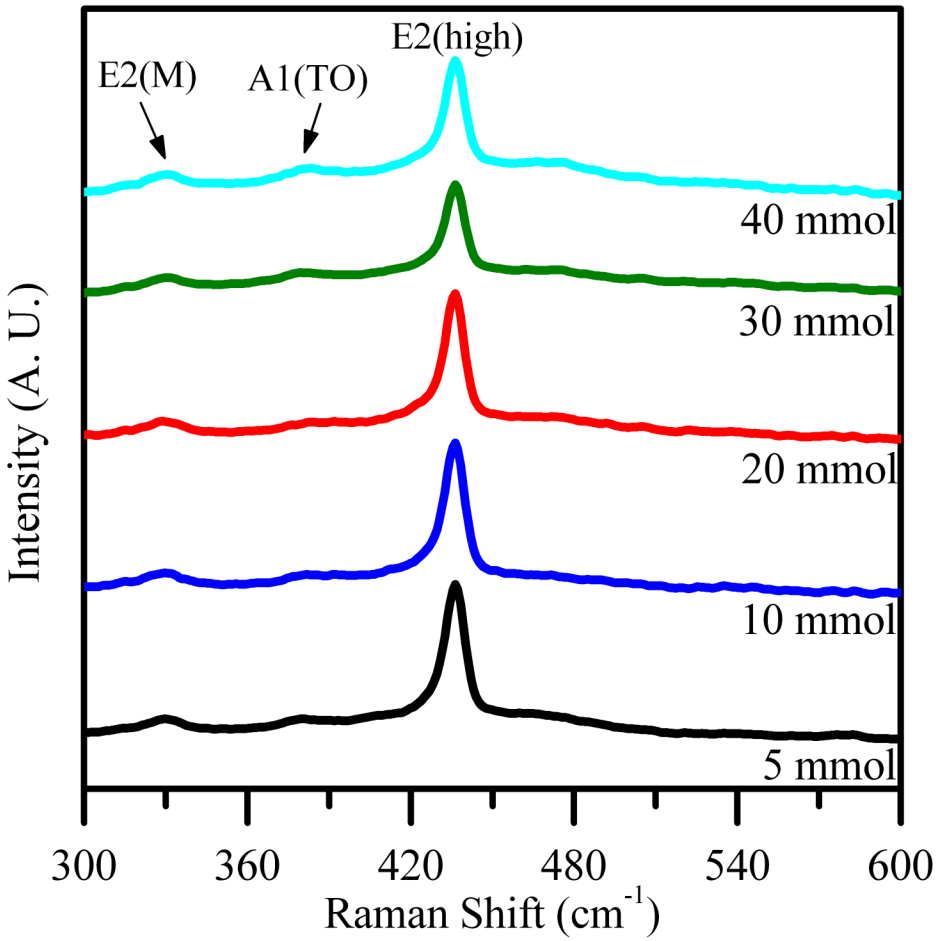

Figure 3.12. Raman spectra for ZnO nanostructures prepared using varying amounts of zinc acetate in the presence of 2:5 molar ratio of oleic acid to oleylamine. Raman data were obtained on solid samples prepared by 15 min MWI (1000W).

The appearance of additional Raman bands that arise as a result of oxygen vacancies and other defects are not observed in these samples. Raman spectroscopy of ZnO with defect bands will be discussed in more detail in Chapter 6.

3.6 ZnO Nanoparticle Surface

3.6.1 X-Ray Photoelectron Spectroscopy

The surface of prepared ZnO nanoparticles was characterized using X-Ray Photoelectron Spectroscopy (XPS). XPS provides valuable information about the composition of the nanoparticle surface. It is well known that metal-oxide surfaces contain a large number of point defects, the most predominant of which are oxygen vacancies.[91] Defects have a strong affect on the electronic band structure and therefore the catalytic and other properties. Oxygen vacancies are responsible electronic structure surface band bending. High concentrations of O-vacancies leave extra electrons at the surface, which change the surface carrier concentration. This change has a strong influence on the electronic conductivity. Surface defects also influence the chemisorption of gases, resulting in a change of the surface conductivity, a requirement for ZnO gas sensors. Therefore, the amount of surface defects, namely O-vacancies, is directly related to the use of ZnO in electronic, catalytic and sensor applications.

XPS spectra for ZnO hexagonal pyramids are given in Figure 3.13. The binding energy associated with 2 regions, Zn 2p and O 1s, was studied. It should be noted that O 1s is more sensitive to the chemical environment compared to Zn 2p.[103] All samples were calibrated to the carbon peak at 285 eV (not shown) to correct for sample charging and instrument variations, which cause slight shifts in the binding energies.

First, the Zn 2 p region was studied; this region includes two peaks: 2 $p_{1/2}$ and $2p_{3/2}$. Zinc oxide is reported to have binding energies of 1044 and 1021 eV for the Zn $2p_{1/2}$ and $2p_{3/2}$ electrons, respectively.[104] Similar results were observed for the ZnO hexagonal pyramids as shown in Figure 3.13a, which correspond to the expected binding energies for the Zn atoms in ZnO.

Second, the O 1s region was studed. For ZnO hexagonal pyramids, the oxygen 1s region (Figure 3.13-b) shows a peak around 530 eV with a shoulder at higher binding energies, which is consistent with ZnO.[104] The spectrum is fit with 3 peaks at 530, 531 and 532 eV. The predominant oxygen peak at 529.9 eV is attributed to Zn-O species.[105-107] The shoulder at higher binding energies is attributed to several subspectral components[4] including adsorbed oxygen species. There is a peak at 531 eV attributed to O^{2-} in oxygen group vacancies in the ZnO structure.[105-107] A third peak at 532 eV is also present and is correlated to O in adsorbed –OH species.[105-107] Binding energies for ZnO hexagonal pyramids prepared using different ratios of OAC/OAM are given in Table 3.2.

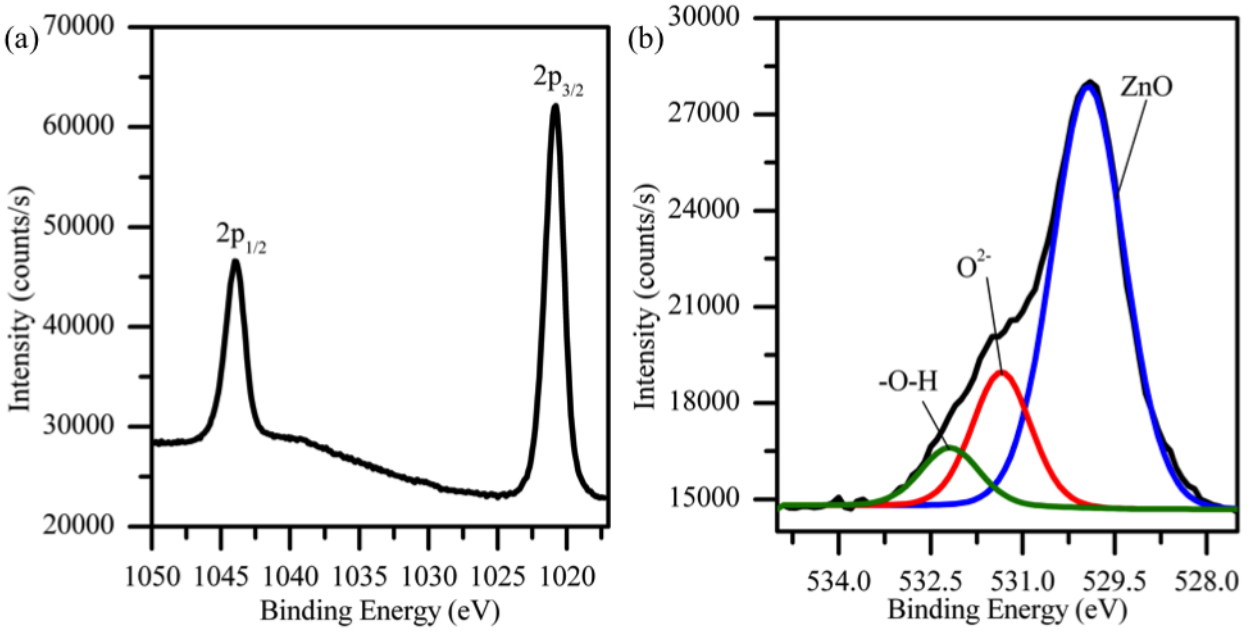

Figure 3.13. XPS spectra of the (a) Zn 2p and (b) O 1s regions of particles prepared using 2 mmol zinc acetate in a 1:3 mixture of OAC/OAM.

Furthermore, the surfaces of the various morphologies of ZnO are also studied. XPS spectra of varying morphologies of ZnO are given in Figure 3.14. Each morphology shows Zn peaks with binding energies of 1044 and 1021 eV for the $2p_{1/2}$ and $2p_{3/2}$ electrons,[104] respectively. No peak shifting is observed for the Zn peaks upon varying the morphology

reaction conditions. The observed line widths for the ZnO rods (FWHM = 1.7 eV) are in good agreement with previously reported results for ZnO rods.[4] The predominant oxygen peak at 529.9 eV is attributed to Zn-O species. The shoulder at higher binding energies is attributed to O^{2-} in oxygen group vacancies in the ZnO structure and adsorbed –OH species. No previous work reports XPS data for these novel shapes. Overall, there was no significant differences between the surfaces of the ZnO hexagonal nanopyramids and nanorods; therefore, any differences in the catalytic properties of the ZnO nanostructures are attributed to the morphology rather than the chemical composition.

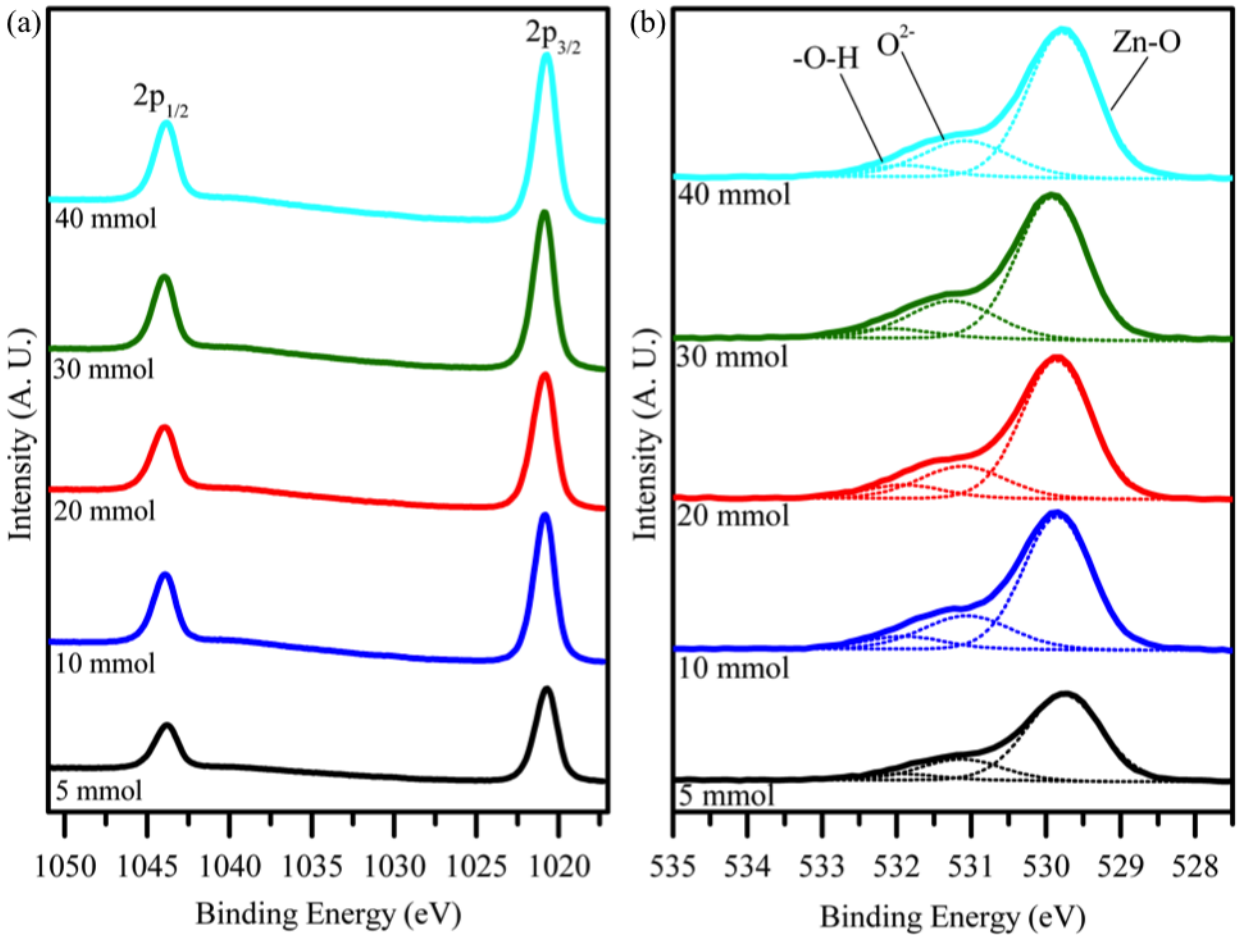

Figure 3.14. XPS spectra of the (a) Zn 2p and (b) O 1s regions of particles prepared using varying amounts of zinc acetate in a 1:2.5 mixture of OAC/OAM.

Table 3.2: Summary of XPS binding energies for ZnO produced under various reaction conditions.

Zinc acetate (mmol)	Mole ratio oleic acid : oleylamine	Oxygen Binding Energy (eV)			Zinc Binding Energy (eV)	
		Zn-O	O^{2-}	-O-H	Zn $2p_{3/2}$	Zn $2p_{1/2}$
2	1: 3	529.9	531.3	532.2	1020.9	1044.0
2	oleylamine only	529.7	531.0	531.9	1020.7	1043.8
5	1: 2.5	529.8	531.1	531.9	1020.8	1043.9
10	1: 2.5	529.8	531.1	531.9	1020.9	1044.0
20	1: 2.5	529.9	531.1	531.9	1020.9	1044.0
20	1:3	529.9	531.1	531.9	1020.9	1044.0
20	1: 1	529.8	531.0	532.0	1020.9	1044.0
30	1: 2.5	529.9	531.3	532.1	1020.9	1044.0
40	1: 2.5	529.7	531.0	531.9	1020.8	1043.9

3.6.2 FTIR

FTIR of the powder provides some insight regarding the nanoparticles surface and the nature of the binding of the stabilizing ligands. FTIR spectra of zinc acetate, oleic acid, oleylamine and ZnO prepared from different ratios of oleic acid and oleylamine were compared (Figure 3.15). All spectra for zinc acetate, oleic acid and oleylamine are similar to previously reported spectra. Oleylamine shows a broad peak between at approximately 1450 cm^{-1}, which may be attributed to the unsaturated bond in oleylamine as well as the amine moiety (CH_2-N).[108] A similar, but more defined, peak appears in each of the ZnO spectra. Therefore it is reasonable to assume that the capping material retains some unsaturation. This is consistent with the presence of the green emission band from the PL spectra. After transforming zinc acetate to ZnO via MWI, a new peak appears around 1550 cm^{-1} for all of the ZnO nanoparticles.

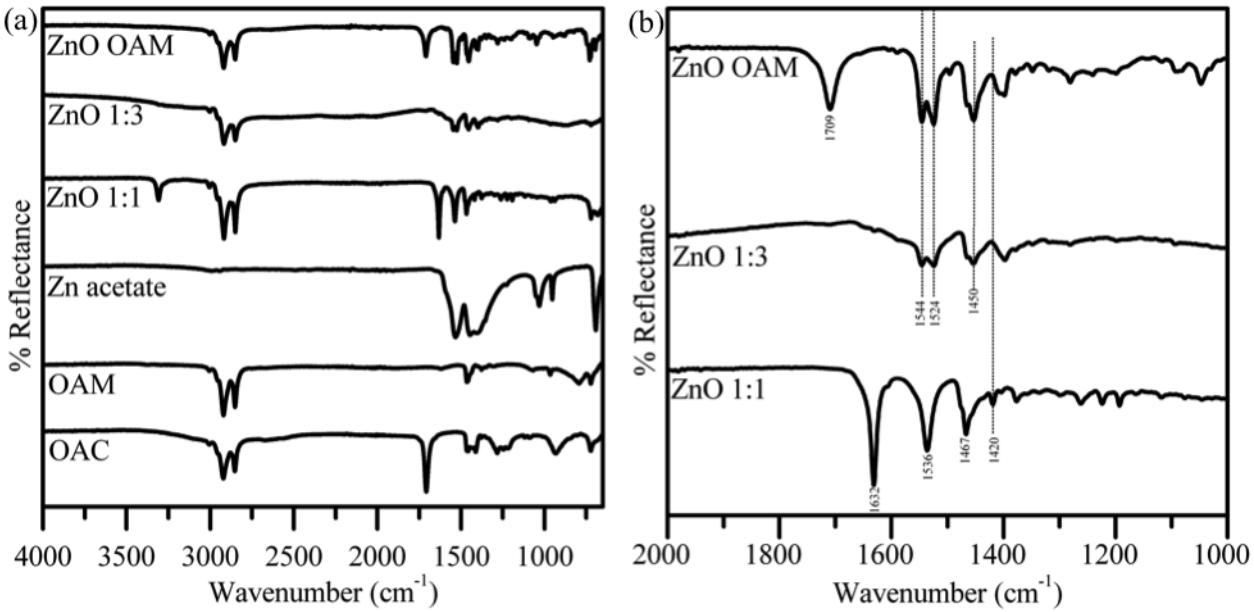

Figure 3.15. FTIR spectra in the full range (top) and magnified region (bottom) of oleic acid, oleylamine, zinc acetate, and ZnO nanoparticles prepared using different ratios of oleic acid to oleylamine varied from 1:1, 1:3, and pure oleylamine.

3.7 Mechanism Studies

In order to fully eludicate the reaction mechanism, GC-MS was used to study the organic reaction that was occurring simultaneously during the formation of ZnO. Since the organic reaction is responsible for supplying oxygen to the metal oxide particles, these organic reactions have a strong influence on particle composition, size and morphology.[88, 109] Understanding the reaction mechanism increases control of the system. Forming ZnO particles in the presence of oleylamine was used to study the reaction mechanism. Zinc acetate was dissolved in oleylamine, and the solution was exposed to MWI for various amounts of time; any particles formed were removed by centrifugation. Supernatant was preserved and diluted in toluene for GC-MS characterization.

Figure 3.16 shows the GC data for reactions after 5, 10, 15 and 20 minutes MWI. After 5 minutes MWI, GC-MS of the supernatant solution revealed that only oleylamine was present in solution. No precipitate was present in solution. After 10 minutes MWI the solution was cloudy

and a small amount of precipitate was present. The cloudy solution coincided with GC-MS results showing the appearance of a new peak at 14.15 minutes. MS identified the peak as dodine, which shown in Scheme 3.1. Increasing microwaving time resulted in increased dodine abundance. Therefore, reaction Scheme 3.1 is proposed as the possible organic reaction that occurs to facilitate particle formation. Previous reports[87] have proposed similar reaction mechanisms where the amine group attacks the zinc acetate carbonyl group, but have reported different end products other than dodine. This result shows that oleylamine acts as a stabilizing molecule whilst promoting the decomposition reaction.

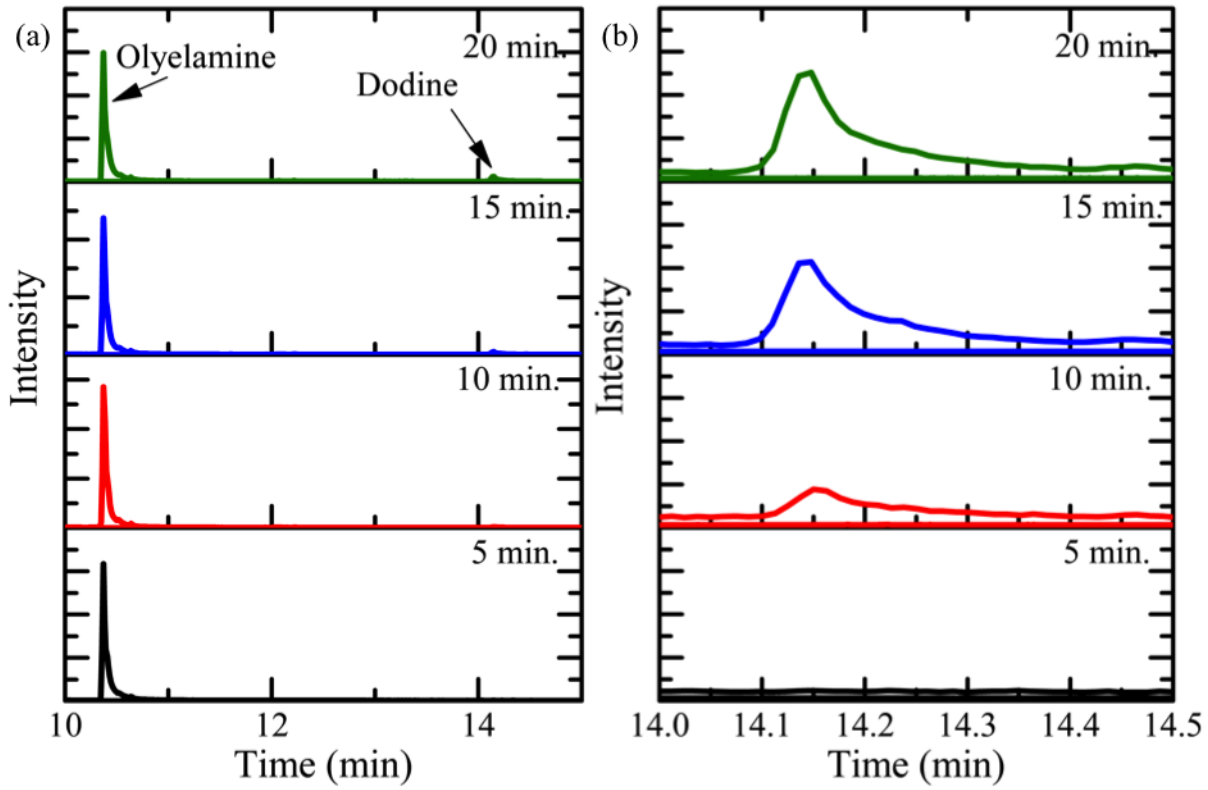

Figure 3.16. Gas chromatogram of ZnO reaction mixture after 5, 10, 15 and 20 minutes of MWI. Notice that after 5 minutes, a peak appears around 14.1 minutes (retention time). This peak increases as microwave irradiation time increases, which indicates that it is a product of the zinc acetate decomposing in the presence of oleylamine.

Adding oleic acid to the reaction mixture and microwaving showed similar results. In this case, dodine appears at microwaving times just before precipitate appears. However, no

additional components other than oleic acid, oleylamine and dodine appeared in the reaction mixture. From this, it appears that when both oleic acid and oleylamine are present, oleylamine acts as the dominant promoter for the decomposition reaction. Microwaving zinc acetate in oleic acid only resulted in the appearance of only 9E-octadecanoic acid, which correlates with a conformational change of oleic acid. Microwave heating isomerizes the *cis* bond of oleic acid (9Z-octadecanoic acid) into a *trans* bond (9E-octadecanoic acid). It is interesting to note that no new compounds appear. Control studies were conducted to ensure that microwaving of oleylamine, oleic acid, and mixtures of the two did not produce any foreign compounds.

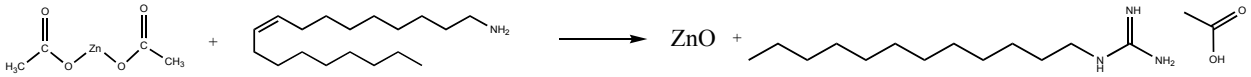

zinc acetate oleylamine dodine

Scheme 3.1: Reaction scheme for ZnO formation in the presence of oleylamine only.

3.8 Ligand Exchange

In order to investigate the photocatalytic properties of the ZnO nanostructures, the particles should be dispersible in water. As prepared, the ZnO particles are coated with oleic acid and oleylamine ligands, which makes them dispersible in non-polar solvents. Therefore, the surface ligands to be replaced with a polar ligand, which will make the particles stable in water. To obtain biocamptible and water dispersible particles, ligand exchange was performed using mercaptoundecanoic acid (MUA).

3.8.1 Ligand Exchange Procedure

To make the ZnO nanoparticles dispersible in aqueous solutions, they are transformed to water-soluble nanoparticles by changing the surface ligands. In a typical ligand exchange, 10 mg of ZnO was dispersed in a mixture of OAC (2.5 mL) and OAM (2.5 mL). Separately, 1 g of MUA was dissolved in 5 mL chloroform. The two solutions (ZnO and MUA) were mixed together and gently stirred for 5 hours. Finally, 25 mL ethanol, 15 mL chloroform and 0.01 g

MUA are added to the particles. Particles were removed from solution using centrifugation at 5000 rpm for 10 min. The particles are washed with ethanol and dried at 60 °C overnight.

The ligand exhange process is extremely sensitive to concentration and solvents. ZnO particles are dispersed in a mixture of OAM and OAC to prevent agglomeration and degradation of particle morphology during the ligand exchange process. Dispersing ZnO particles in a non-ligand solvent, such as hexanes, results in large ZnO aggregates. The presence of excess amounts of ligand in solution prevents agglomeration. Chloroform is utilized to disperse MUA for two reasons. First, it is miscible with both non-polar and polar solvents. Second, chloroform facilitates removal the OAC and OAM ligands from the ZnO surface, and therefore allows for the adsorption of the MUA to the ZnO surface.

3.8.2 Characterization of water-soluble ZnO

Figure 3.17 shows dispersions of ZnO nanoparticles in hexanes and water. In Figure 3.17 (left), the organic capped ZnO nanoparticles dispersed in hexanes are at the top, whereas water is on the bottom. After ligand exchange, Figure 3.17 (right), the ligand-exchanged ZnO particles dispersed in water stay at the bottom of the vial and the hexane at the top stays clear.

Figure 3.17. Organic capped ZnO particles are suspended in hexanes (left). MUA capped ZnO, after ligand exchange, are suspended in water (right).

Furthermore, TEM was utilized to study ZnO nanoparticle morphology after the ligand exchange process. Figure 3.18 shows TEM images of the ZnO particles after ligand exchange. The morphology of the particles is well maintained and they are easily dispersed into water. Through TEM, it was observed that hexagonal pyramids remain hexagonal pyramids, and rods remain rods. Improper ligand exchange conditions resulted in aggregated ZnO particles with non-defined shapes (not shown). Generally, synthetic procedures to obtain high quality, monodisperse nanoparticles involve organic reactions, but ligand exchange allows for the production of high quality, water-soluble nanoparticles.

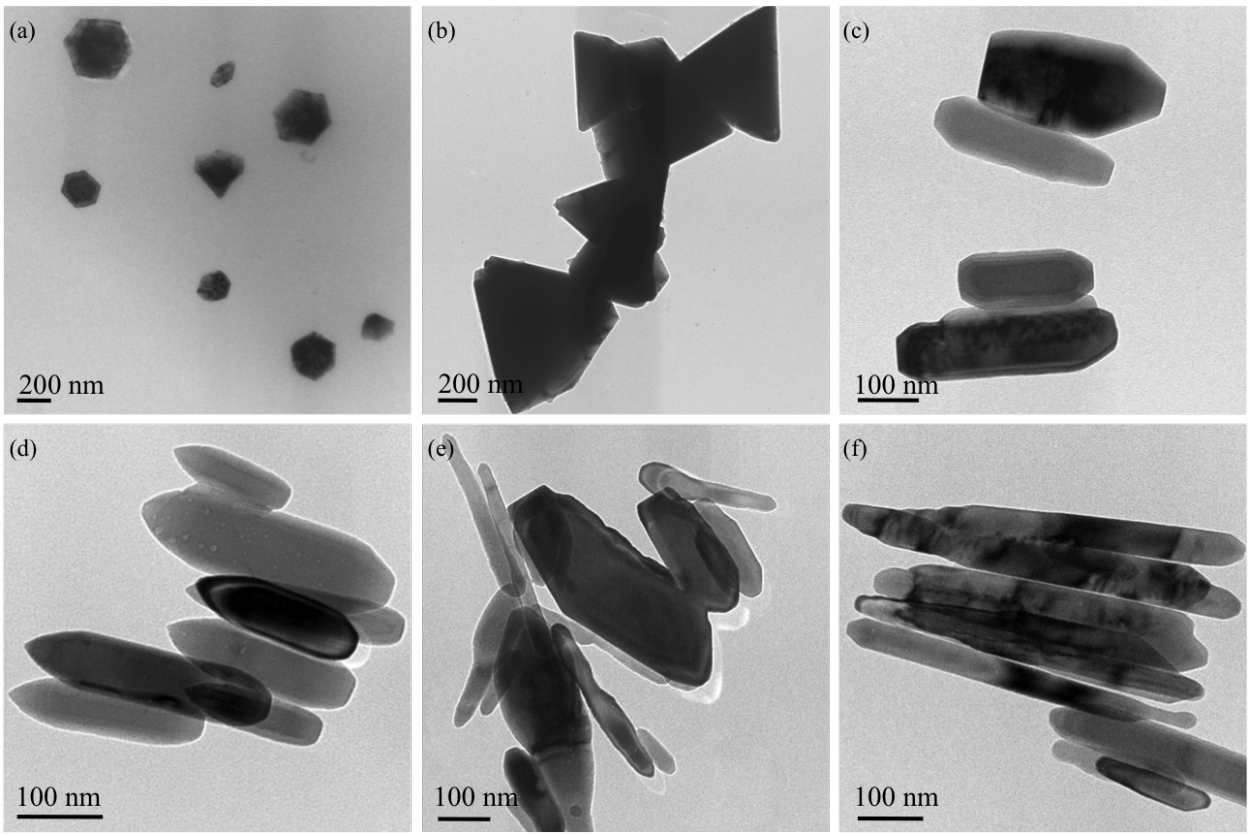

Figure 3.18. TEM images of ZnO nanoparticles after ligand exchange experiment. Starting conditions are (a) 2 mmol 1:3 OAc/OAm, (b) 5 mmol, (c) 10 mmol, (d), 20 mmol, (e), 30 mmol, and (f) 40 mmol 2:5 OAc/OAm. After the surface ligands are exchanged with MUA, the ZnO particles maintain the originally morphology and are water soluble.

3.9 Photodegradation of malachite green

As previously mentioned, semiconductor nanoparticles are of great interest for the degradation of organic dyes.[50, 52, 53, 58, 60, 65, 72, 76-78, 110-121] Industrial processing and manufacturing of textiles and paper as well as printing and photography has resulted in a significant amount of brightly colored wastewater that is polluted with non-biodegradable organic dyes.[52, 53, 77] This pollution is hazardous to the environment by damaging stream ecosystems as well as consumers of contaminated fish. Therefore, a way to reduce the pollution of organic dyes from contaminated water is desirable.

The most widely used dyes are aromatic organic compounds. Many of these dyes are known to degrade into highly carcinogenic aromatic amine compounds; therefore, they must be removed from industrial waste.[77, 122] Unfortunately, their high solubility makes them difficult to remove and enhances their contamination potential.[77] Current removal techniques include chemical coagulation, airflotation and adsorption methods.[77] These methods simply remove the hazardous dyes from the water and do not reduce the toxicity or the compounds. An additional step is needed to degrade the hazardous compounds once they are removed from the water. Degrading the organic dyes into nontoxic species is a more appealing solution offered by photodegradation on semiconductor surfaces.

Experimentally, observing degradation of organic dyes is quite simple. Organic dyes have high molar absorbtivities and form brightly colored solutions, which means they can be easily observed by UV-Visible absorbance spectroscopy measurements. The decoloration of the solution, which is easily observable by UV-Visible spectroscopy, indicates degradation of malachite green into benign products. However, other methods such as high performance liquid chromatography and total organic content analysis are sometimes used for more exact quantitative studies.

Photocatalytic activity of ZnO nanostructures is studied through the photodegradation of malachite green. Malachite green is a highly conjugated organic dye molecule, shown in Figure 3.19, that absorbs strongly at 617 nm. The absorbance of malachite green is utilized to study photodegration of malachite green in the presence of ZnO nanostructures.

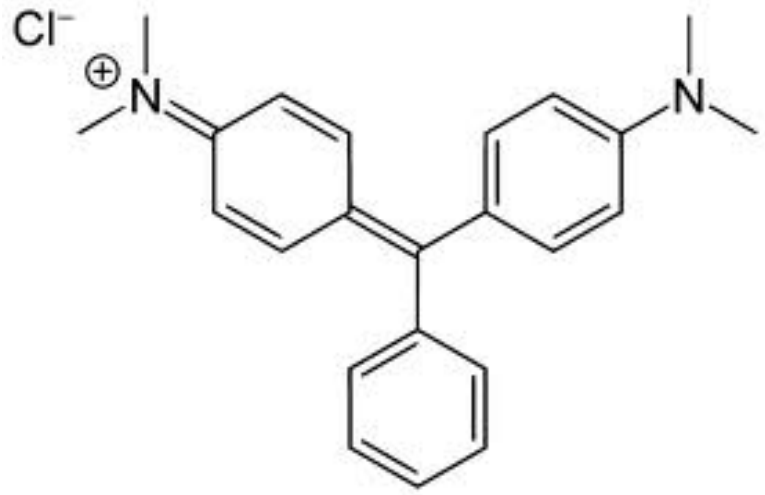

Figure 3.19 Structure of malachite green.

3.9.1 Photodegradation measurements

Photodegradation experiments were carried out in 100 mL Erlenmeyer flasks. A UV lamp operating at 365 nm was used as the light source. The experiments were performed at ambient conditions in a box designed to block any ambient light. Dye solution was prepared using deionized water and malachite green oxalate salt (Aldrich, technical grade). Aqueous ZnO particles were dispersed in deionized water by bath sonication. Solutions were prepared with final concentration of 3 x 10^{-5} M malachite green and 0.25 mg/mL ZnO nanoparticles. The dye-particle solution was stirred in the dark for 30 minutes to insure adsorption of dye molecules onto the catalyst surface. Immediately following 30 minutes of dark, the absorbance was measured, t=0. Then, the mixture was continuously top-irradiated with the UV lamp (365 nm) for 90 minutes and the absorbance was measured at 10-minute intervals. Photodegradation studies were repeated and average values are reported.

3.9.2 Photocatalytic activity

The photocatalytic behavior of the ZnO nanostructures was studied in order to understand the relationship between photocatalytic activity and particle morphology. Ligand exchanged ZnO nanostructures show that the photocatalytic activity for the degradation of malachite green is

strongly dependent on the particle morphology. Several other studies comparing photocatalytic activity to particle morphology have been reported,[29-32] but these utilize various synthesis methods to produce a range of morphologies.

Figure 3.20 displays typical absorption spectra of malachite green after various times of constant UV irradiation in the presence of ZnO nanostructures prepared from 2 mmol zinc acetate in the presence of (a) 1:1, (b) 1:3 OAC/OAM, and (c) OAM only. The green curve shows the absorbance of malachite green only at 3 x 10^{-5} M. Malachite green has a strong absorption band at 617 nm; this peak is used to calculate the concentration of malachite green. Immediately after the ZnO particles are added to the dye solution, there is a reduction in the intensity of the peak. The peak continues to decrease as the irradiation time increases.

ZnO nanostructures degrade 49, 79 and 76% of malachite green in 90 minutes for ZnO nanostructures prepared from 2 mmol zinc acetate in the presence of (a) 1:1, (b) 1:3 OAC/OAM, and (c) OAM only. Note that degradation is measured relative to the concentration calculated at time t=0. Recall from section 3.3, that the average diameter for these particles is 61, 242 and 100 nm, respectively. Therefore it is observed that as the average diameter of the ZnO hexagonal nanopyramids increases, the percent degradation also increases. There is little difference between the two larger particles.

The kinetics of degradation of malachite green is also studied. Plotting $\ln(C/C_0)$ as a function of irradiation time is linear (Fig. 3.20-d and f), which indicates that the photodegradation follows first order reaction kinetics $\ln(C/C_0) = kt$. Thus, the rate constant, k, may be calculated for each system by fitting a line to the data and taking the slope. Larger rate constants correspond to higher photocatalytic activity.

ZnO nanostructures degrade at a rate of 0.0074, 0.017 and 0.017 s^{-1} for ZnO nanostructures prepared from 2 mmol zinc acetate in the presence of (a) 1:1, (b) 1:3 OAC/OAM, and (c) OAM only. This further demonstrates that as average diameter of the ZnO hexagonal nanopyramids increases, rate of degradation also increases. Again, there is no difference in rate between the two larger samples of hexagonal nanopryamids.

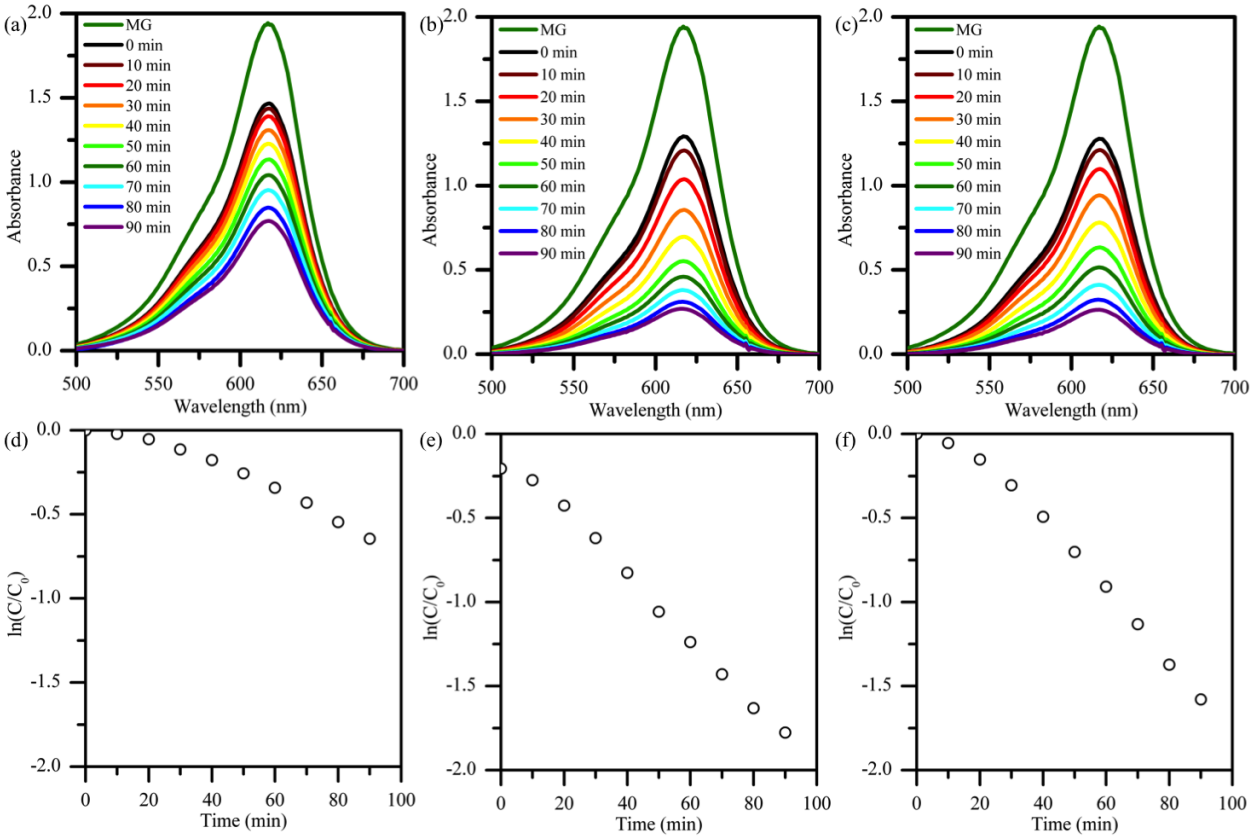

Figure 3.20. Absorption spectra of malachite green after various times of constant UV irradiation in the presence of ZnO nanostructures prepared from 2 mmol zinc acetate in the presence of (a) 1:1, (b) 1:3 OAC/OAM, and (c) OAM only. Graphs showing the degradation of malachite green plotted as $\ln(C/C_0)$ as a function of UV irradiation time corresponding to (e) 1:1, (f) 1:3 OAC/OAM, and (g) OAM only.

Next, the correlation between particle morphology and degradation of malachite green was studied. Typical absorbance spectra obtained from photodegradation experiments for ZnO nanoparticles prepared in 2:5 OAc/OAm from (a) 5 and (b) 20 and (c) 40 mmol zinc acetate are shown in Figure 3.21. Typical graphs showing the degradation of malachite green plotted as

$\ln(C/C_0)$ as a function of UV irradiation time corresponding to (d) 5, (e) 20, and (f) 40 mmol zinc acetate. Table 3.3 summarizes the amount degraded and rate constants for all of the ZnO nanostructures. In is observed that the photocatalytic degradation of malachite green is related to the ZnO morphology. As the aspect ratio of the ZnO nanorod increases, both the precent degraded and the rate of degradation increase.

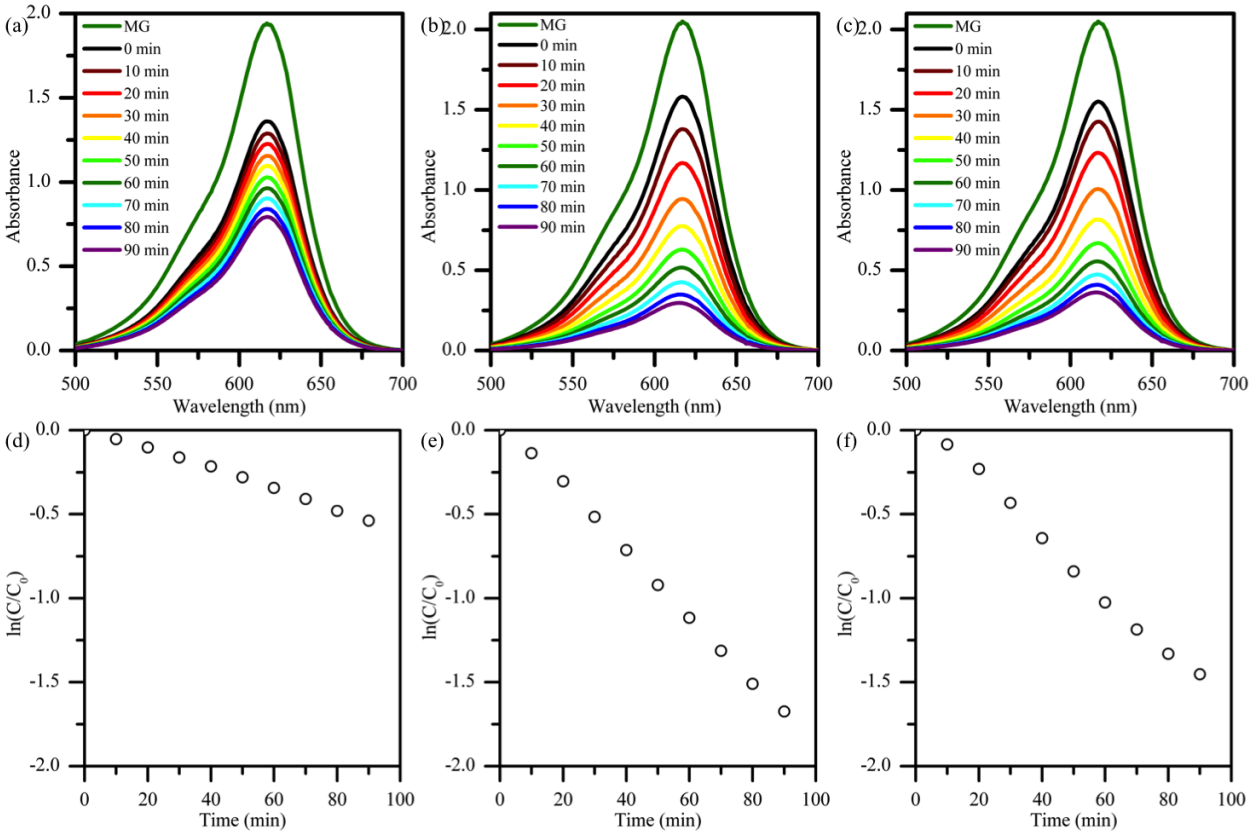

Figure 3.21. Absorption spectra of malachite green after various times of constant UV irradiation in the presence of ZnO nanostructures prepared from 2:5 OAC to OAM using (a) 5, (b) 20, and (c) 40 mmol zinc acetate. Graphs showing the degradation of malachite green plotted as $\ln(C/C_0)$ as a function of UV irradiation time corresponding to (d) 5, (e) 20, and (f) 40 mmol zinc acetate.

In order to visualize how photocatalytic activity correlates to the shape, the percent degraded and rate constants are plotted as a function of the aspect ratio in Figure 3.22. This graph includes only data from the ZnO structures prepared in the presence of 2:5 OAC/OAM. This shows that as the aspect ratio increases, the photocatalytic activity also increases up to aspect ratio 5. Thereafter, the photocatalytic activity slowly declines. The overall trend of

increasing photocatalytic activity with increasing aspect ratios is attributed to preferential adsorption of dye molecules onto the (110) crystal face. In the rod structures, the length of the rod is comprised of the (110) crystal face and therefore, there is more surface area of this crystal face exposed for dye adsorption.

Photocatalytic activity slowly declines as the aspect ratio increases above 5. This may be attributed to the width of the nanostructures. For the rods with aspect ratio 5, the average width is 61 nm; as the aspect ratio increases, the width decreases to 45 nm for rods with aspect ratio of 10 nm. The decrease in photocatalytic activity with decreasing aspect ratio is attributed to steric hindrance. Rods with smaller diameters have less room for dye molecules to adsorb around the sides of the rods.

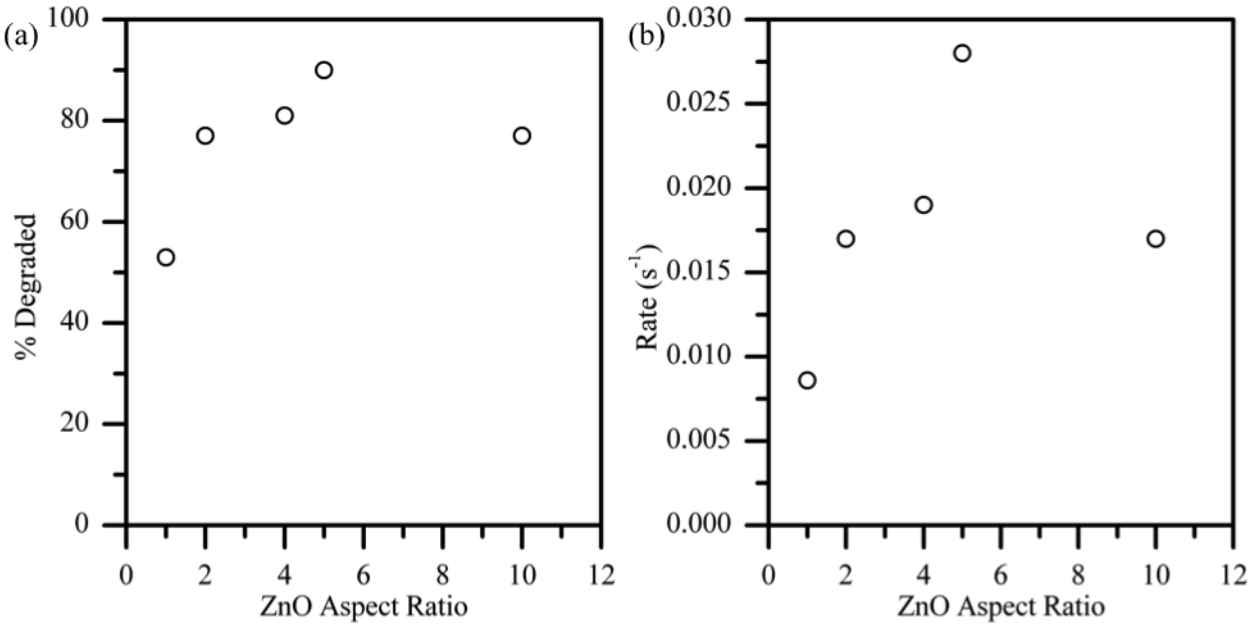

Figure 3.22. Plot showing the relationship between the photoactivity of ZnO nanoparticles as a function of aspect ratio for particles prepared in 2:5 OAc/OAm reaction mixture. (a) shows the percent malachite green degraded (a) after 90 minutes of UV irradition. (b) shows the rate of degradation as calculated by the slope of plotting $\ln(C/C_0)$ as a function of time.

Table 3.3. Summary of photocatalytic degradation of malachite green in the presence of ZnO nanostructures produced under various reaction conditions.

Zinc acetate (mmol)	Mole ratio oleic acid : oleylamine	Aspect Ratio	% Degraded in 90 min	Average Slope ($\ln C/C_0$ v t)
2	1:1	1	49	0.0074
2	1: 3	1	79	0.017
2	oleylamine only	1	76	0.017
5	2: 5	1	53	0.0086
10	2: 5	2	77	0.017
20	2: 5	4	81	0.019
20	1:3	2	76	0.017
20	1: 1	2	82	0.020
30	2: 5	5	90	0.028
40	2: 5	10	77	0.017

3.10 Conclusions

In this chapter, the formation of ZnO nanostructures with controlled morphology was studied by the decomposition of zinc acetate using MWI in the presence of OAC and OAM. By varying the reaction conditions, ZnO nanostructures with various morphologies were synthesized. The formation of ZnO nanoparticles is strongly dependent on the concentration of zinc acetate. The presence of high concentrations of zinc acetate results in selective electrostatic interaction between OAC and the polar surfaces of the ZnO nanocrystals. It was found that high concentrations of zinc acetate in mixtures of OAC and OAM produce ZnO rods.

This work demonstrates the use of ligand exchange to transform high quality ZnO nanostructures prepared in organic media to water-dispersible particles. The use of ligand exhange provides direct evidence for the effect of morphology on the photocatalytic degradation of malachite green. It was further found that photocatalytic degradation of malachite green is enhanced for ZnO particles with higher aspect ratios.

Chapter 4: Au-ZnO structures

4.1 Introduction

Hybrid nanostructured materials consisting of metal and semiconductor nanocrystals and their assemblies have attracted great attention from both fundamental basic science and technological points of view.[1-5] These hybrid semiconductor-metal nanocrystals not only combine the unique properties of the metal and the semiconductor but also generate collective new phenomena based on the intraparticle interaction between the metal and the semiconductor at their interface.[4,6,7] The presence of the metal-semiconductor interface can promote effective charge separation and can enhance light absorption in the semiconductor and the overall carrier transfers which can increase the light-harvesting efficiency and improve photocatalysis.[2,6,8-11]

Due to the unique properties of gold-semiconductor hybrid nanostructures, many studies have focused on the controlled synthesis and optical properties of these nanostructures. Hybrid structures consisting of gold and group II-VI semiconductors have received extensive attention mostly due to their applications in solar energy harvesting and conversion.[1-9] Au-ZnO represents another important class of hybrid gold-semiconductor nanostructures because of the interesting properties of ZnO, which includes a wide band gap semiconductor, high excitation energy, unique catalytic and electrical properties.[12,13] These features make ZnO attractive for use in sensors,[14,15] electronics[16] and photoelectronics.[17,18] Furthermore, the hexagonal wurtzite structure

of ZnO and its polar crystal surface have resulted in the formation of a large number of nanocrystals encompassing a variety of sizes, shapes and assemblies including nanowires, nanobelts, nanocages, nanosprings, nanorings, nanocombs, nanobows, nanodisks and complex structures.[13-28] These different nanostructures exhibit enhancement of the optical, electronic and catalytic properties of ZnO. For example, ZnO nanowires and nanobelts have demonstrated potential applications as UV lasers, LEDS, gas sensors, UV photodiodes and photocatalysis.[14-18,29-32]

Several studies have reported the synthesis and applications of Au-ZnO nanocomposites.[10, 33-47] The majority of the reported methods include techniques for depositing gold nanoparticles onto ZnO supports using thermal[33-36], sputtering[37], and laser ablation[38] methods. Some Au-ZnO core-shell composites have also been reported as water-soluble particles.[39-42] ZnO nanowires decorated with Au nanoparticles have shown improved response as photodetectors.[43] Gold nanoparticles can enhance both the light absorption efficiency of ZnO by particles-induced scattering and the band gap emission of ZnO nanorods by the gold surface plasmon resonance.[44]

Although the formation of Au-ZnO hybrid nanostructures has been reported, the rational design and synthesis of more complex structures and understanding the growth mechanisms have not been achieved. Very recently, the formation of Au-ZnO hybrid nanopyramids has been reported using a two step seed-mediated growth process at relatively high temperatures (180 °C).[48] Here, a fast and simple, one-pot route is presented for the synthesis and assembly of Au-ZnO nanopyramids by stepwise binary nucleation involving both Au and Zn ions using microwave irradiation (MWI) without the need of high temperature or high pressure. The binary nucleation approach is compared with the heterogeneous nucleation of ZnO on preformed Au

nanoparticles. Focus is given to understanding the mechanism of formation of the hybrid nanopyramids and the factors that control the assembly and growth of these complex structures. Furthermore, the optimized assembly and growth conditions are repored and new insights are offered into the binary and heterogeneous nucleation processes along with plausible mechanisms.

MWI provides a simple and fast route to the synthesis of nanomaterials particularly for a controlled large-scale synthesis that minimizes the thermal gradient effects.[49-54] Heating of a substance by MWI is based on dipole rotation and ionic conduction, that is, by reversal of solvent dipoles and the resulting replacement of charged ions of a solute.[49-54] Due to the difference in the solvent and reactant dielectric constants, selective dielectric heating can provide significant enhancement in reaction rates. The rapid transfer of energy directly to the reactants causes an instantaneous internal temperature rise. Thus, the activation energy is essentially decreased as compared with conductive heating and the reaction rate increases accordingly. This also allows the rapid decomposition of the precursors thus creating highly supersaturated solutions where nucleation and growth can take place to produce the desired nanocrystalline products. In the nucleation stage, the number and size of the nuclei formed are controlled by the degree of the supersaturation. According to classical nucleation theory, the larger the supersaturation, the smaller the critical size of the nucleus and the smaller the nanocrystals that can grow.[55] This work demonstrates the application of MWI not only for the synthesis of high quality hybrid Au-ZnO nanopyramids, but also to provide direct evidence for the catalytic effect of Au nanocrystals on the assembly and growth of the ZnO nanopyramids, and to obtain new insights on the binary and heterogeneous nucleation processes in these systems.

4.2 Synthesis

4.2.1 Synthesis of gold nanoparticles

Gold nanoparticles were prepared by MWI of a mixture of $HAuCl_4$ (Aldrich, 30 wt% in dilute HCL, 99.99%), oleic acid (Aldrich, technical grade, 90%) and oleylamine (Aldrich, technical grade, 70%) until a red color appears, approximately 40 seconds. Additional MWI time increases gold nanoparticles size. A 1:1 ratio of oleic acid to oleylamine was used to create spherical particles. Varying the ratio of OAC to OAM results in non-spherical anisotropic shapes of gold nanoparticles.[123]

4.2.2 Synthesis of Au-ZnO heterostructures

Two methods were used for the preparation of Au-ZnO nanoparticles. In both methods, anhydrous zinc acetate (Aldrich, 99.99%) was dissolved in a mixture of oleic acid and oleylamine. The reaction mixture was heated in a hot oil bath with magnetic stirring to 120 °C, and temperature was maintained for 1 hour. Heating for is necessary to dissolve the zinc acetate and remove any residual water. In one method, gold nanoparticles, as prepared above, were added to the zinc reaction mixture and stirred vigorously until homogeneous in color. Then, the solution was microwaved. Microwaving time was varied between 8 and 15 minutes. In the second method, $HAuCl_4$ was added to the zinc reaction mixture. The solution was stirred until homogeneous in color and microwaved. Following the microwave reaction, the precipitate was separated from the liquid phase by centrifugation and dried at 60 °C overnight.

For all the syntheses described here, a conventional microwave oven (2.45 GHz) operating at 600 – 1000 W was used.

For characterization, as prepared Au-ZnO particles were diluted in toluene and mixed by vigorous pipetting. UV-Visible absorbance spectra were recorded using a HP-8453

spectrophotometer. The particles size and morphology were studied using transmission electron microscopy (TEM). TEM images were obtained using a JEOL JEM-1230 TEM operating at 120 kV. Samples for TEM imaging were prepared by suspending a Formar carbon-coated, 300 mesh copper grid (Ted Pella) in toluene diluted samples for approximately 2 minutes. Particles were centrifuged from solution and powder X-ray diffraction (XRD) patterns of the particles were collected at room temperature using an X'Pert Philips Materials Research Diffractometer with $CuK_{\alpha}R$ radiation.

4.3 Au-ZnO nanopyramids

4.3.1Nucleation and growth mechanisms

Figure 4.1 summarizes the synthetic strategies and the nucleation and growth mechanisms involved in each strategy.

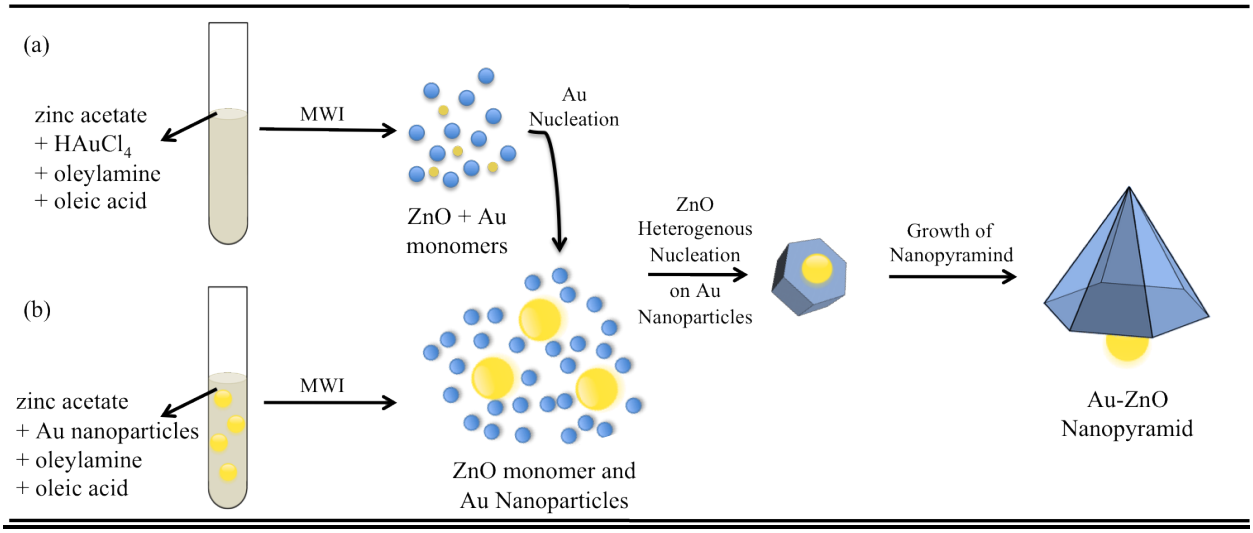

Figure 4.1 Schemes of nucleation and growth mechanisms of Au-ZnO nanopyramids.

The first approach (Fig 4.1-a) studies the sequential homogeneous–heterogeneous nucleation process under similar conditions to those previously discussed for ZnO in Chapter 3. Under these conditions, the reduction of the Au ions and the subsequent formation of Au nanoparticles are expected to be much faster than the formation of ZnO nanocrystals since the

reduction of the Au ions using oleylamine does not require higher temperatures unlike the decomposition of zinc acetate. Therefore, it is expected that the newly formed Au nanoclusters would act as in situ heterogeneous nuclei for the growth of ZnO nanopyramids. Since heterogeneous nucleation involves a lower free energy barrier as compared to homogeneous nucleation,[124] the nucleation rate is expected to be faster, and therefore, the growth of the ZnO nanopyramids around the Au nuclei should occur at a shorter time than that observed in (a) in the absence of Au ions. If the formation of Au nanoparticles is significantly faster than that of ZnO nanoparticles, then approach (a) would represent a stepwise sequential nucleation process where the initially formed clusters from the most stable phase (Au, fcc) act as heterogeneous nuclei for the formation of the less stable phase (ZnO, wurtzite).[124]

The second approcah (b) considers the conventional heterogeneous nucleation mechanism by introducing Au nanoparticle seeds during the decomposition of zinc acetate in the presence of OAC and OAM. To achieve appropriate heterogeneous nucleation conditions, the concentration of zinc acetate must be kept low so nucleation of ZnO nanocrystals will not take place in the absence of the Au seed. Since growth is usually thermodynamically favored over nucleation,[124] ZnO nanopyramids can be grown monodispersely on the Au surface. The following sections describe the results obtained from these two approaches.

4.3.2 Sequential homogeneous-heterogeneous nucleation mechanism

As indicated earlier, two approaches, one-step and two-step, for the formation of Au-ZnO nanopyramids were studied. For the single step approach, Au^{+3} ions (0.007 M) and zinc acetate (0.17 M) in the presence of 1:1 molar ratio of OAC/OAM were combined in a single test tube prior to microwave irradiation for 8 min (using a 1000 W MW oven). The TEM images of the resulting nanocrystals (Figure 4.2) indicate the formation of Au-ZnO nanopyramids, each

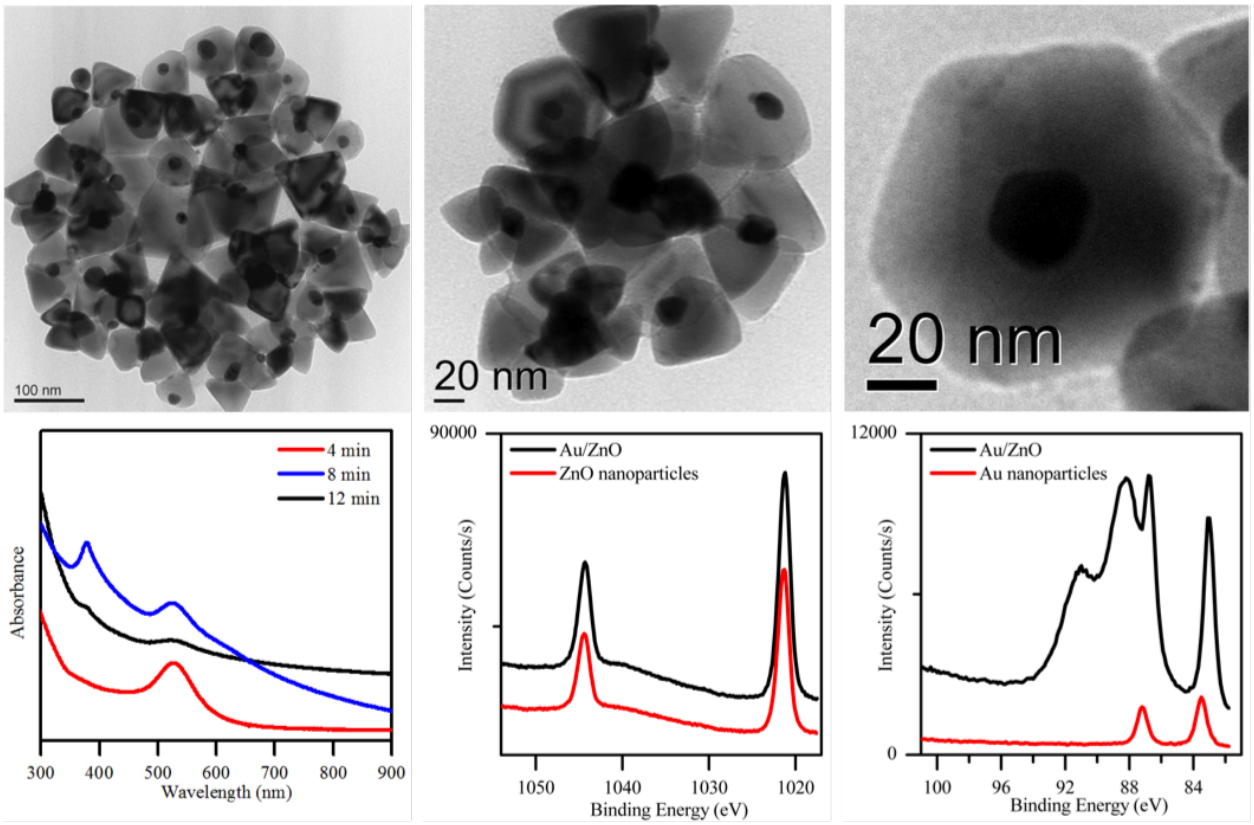

Figure 4.2. (a) TEM images of Au-ZnO nanopyramids prepared using 0.17 M Zn acetate and 0.007 M $HAuCl_4$ in the presence of 1:1 molar ratio of oleic acid to oleylamine and 8 min MWI time (1000 W). (b) Absorption spectra obtained at different MWI times. (c) XPS binding energy of the Zn 2p electron in ZnO (red) and Au-ZnO nanopyramids (black). (d) XPS binding energies of the Zn 3p and Au 4f electrons in Au-ZnO nanopyramids (black), and of the Au 4f electrons in Au nanoparticles (red).

consisting of a gold nanoparticle occupying the center of the hexagonal base of the ZnO nanopyramid. To understand the formation mechanism of these hybrid nanopyramids, the absorption spectra of the reaction mixture were recorded following MWI for different times as shown in Figure 4.2-b. As expected, the formation of Au nanoparticles is much faster than the growth of the ZnO nanocrystals. The gold nanoparticles form during the first minute of MWI, and the ZnO pyramids require additional MWI (~7 minutes) for formation. This is confirmed by the TEM image obtained after 1 minute of MWI, which shows predominately Au nanoparticles (Figure 4.3). Even after 4 minutes of MWI, only the SPR (surface plasmon resonance) band of

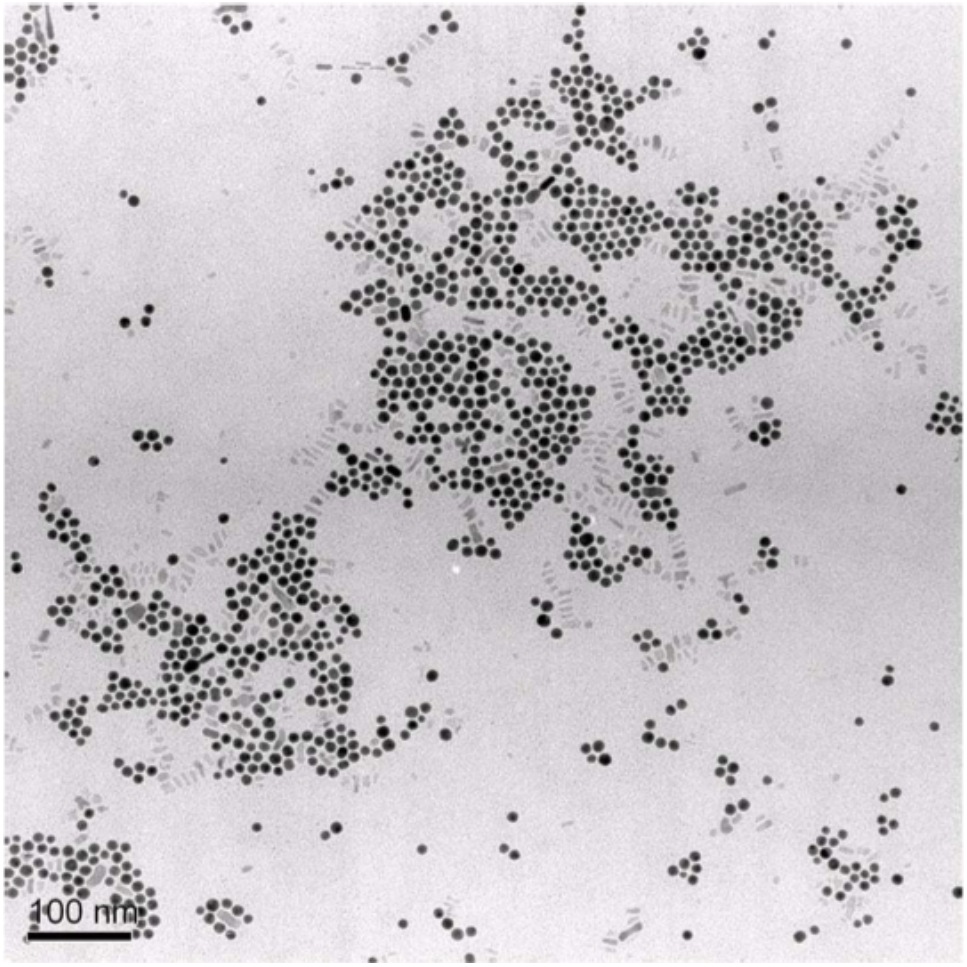

Figure 4.3. TEM image of nanoparticles (mostly Au nanoparticles) prepared using 0.17 M Zn acetate and 0.007 M $HAuCl_4$ in the presence of 1:1 molar ratio of oleic acid to oleylamine and one minute MWI time (1000 W).

Au nanoparticles at 530 nm[123] is observed with no evidence of the formation of ZnO nanocrystals as indicated by the absence of the ZnO absorption at 370 nm. After 8 minutes of MWI, the ZnO absorption is observed simultaneously with the SPR of Au, and after 12 minutes both bands become much weaker probably due to the continuous growth of Au-ZnO nanopyramids. The rapid formation of the Au nanocrystals is attributed to the presence of OAC, which is known to enhance the growth rate of Au nanocrystals formed by the reduction of the Au^{+3} ions by OAM.[123] The Au-ZnO hybrid nanocryatals were also characterized by powder XRD (Figure 4.4) and XPS (Figure 4.2). The XRD of the resulting nanocrystals clearly show the

presence of both the Au fcc and ZnO wurtzite crystal patterns as shown in Figure 4.4. The XPS binding energy of Au-ZnO nanopyramids (Figure 4.2c) show the Au $4f_{7/2}$ peak at 83.1 eV and the $4f_{5/2}$ at 86.8 eV shift to significantly lower values than in pure Au nanoparticles (83.5 and 87.2 eV, respectively) which suggests possible transfer of electrons from the Au nanoparticle to the ZnO nanopyramid. A similar result has been reported for Ag-ZnO nanocomposites.[71] The observed Zn $3p_{1/2}$ and $3p_{3/2}$ at 91.7 and 89.1 eV are slightly higher than the Zn standard values of 91 and 89 eV, respectively. However, the peak positions of Zn $2p_{1/2}$ and $2p_{3/2}$ in ZnO (1045 and 1020 eV, respectively) and Au-ZnO (1045 and 1020 eV, respectively) have nearly the same values confirming that the Zn exists mainly in the Zn^{2+} state in both the ZnO and Au-ZnO nanoparticle surfaces.[18, 71]

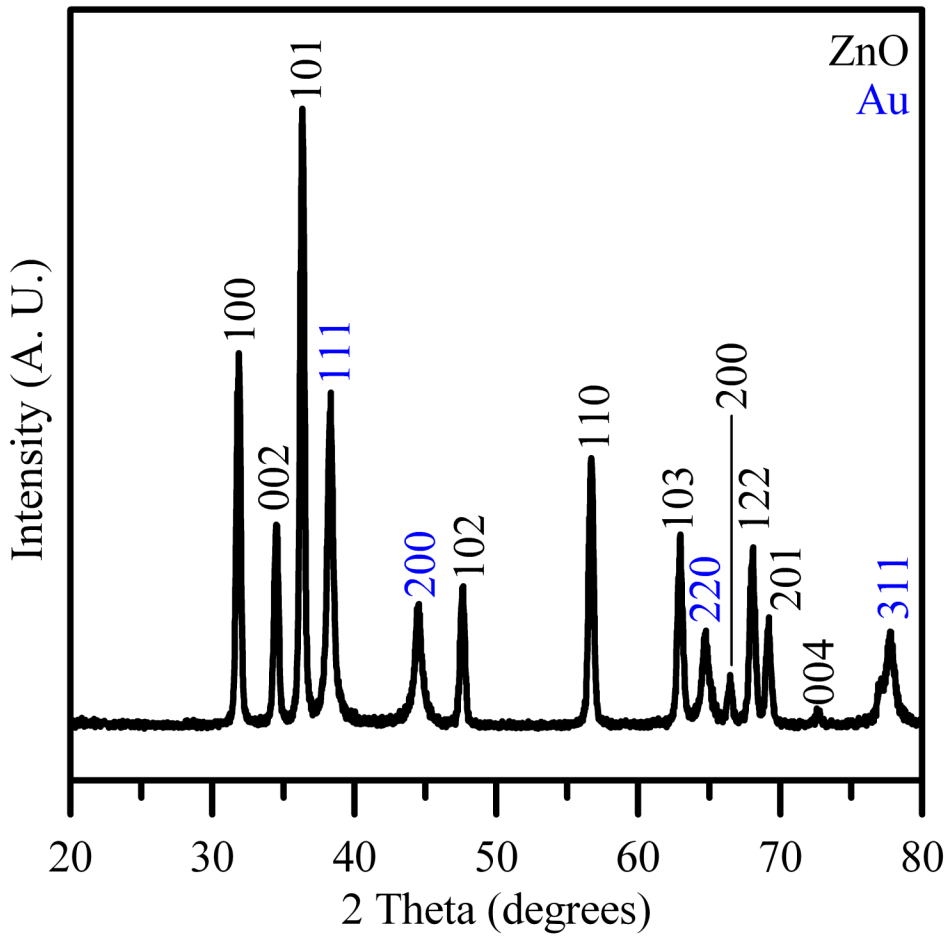

Figure 4.4. XRD for the Au-ZnO nanopyramids prepared using 0.17 M Zn acetate and 0.007 M HAuCl4 in the presence of 1:1 molar ratio of OAC to OAM and 8 minutes MWI time (1000 W).

Au nanoparticles, which are assumed to forme during the early stage of the reaction, catalyze the formation of the hexagonal base of the ZnO nanopyramids.[19,36,48] Once the base is formed, six nucleation sites along the edges of the hexagon are created thus resulting in the growth of the side facets of the pyramid. Therefore, the one-step approach should be considered as a stepwise binary nucleation process where the *in situ* formation of Au nuclei catalyzes the heterogeneous nucleation of ZnO to form the Au-ZnO nanopyramids. As expected, the concentration of the Au^{+3} ions plays a major role in the formation of the Au-ZnO nanopyramids with narrow size and composition distributions. Decreasing the concentration of the Au^{+3} ions from 7 mM (Figure 4.2) to 4 mM results in the formation of Au-ZnO nanopyramids containing

smaller Au nanoparticles (Figure 4.5). Increasing the concentration of the Au^{+3} ions to 0.014 M results in the formation of free Au nanoparticles in addition to the ones incorporated within the ZnO nanopyramids (Figure 4.5).

These results indicate that the formation of the Au-ZnO hybrid nanopyramids requires the early formation of Au nanoparticle catalysts in a small concentration (with respect to zinc acetate) to act as heterogeneous nuclei for the growth of the ZnO nanopyramids. Under these conditions, the growth rate of the ZnO nanopyramids is enhanced and therefore, the MWI time required for the formation of the Au-ZnO nanopyramids is decreased. This is consistent with results shown in Chapter 3 and Fig. 4.2 where the MWI times required for the formation of the ZnO nanopyramids, under otherwise similar experimental conditions, were found to be 15 and 8 minutes in the absence and presence of the Au^{+3} ions, respectively.

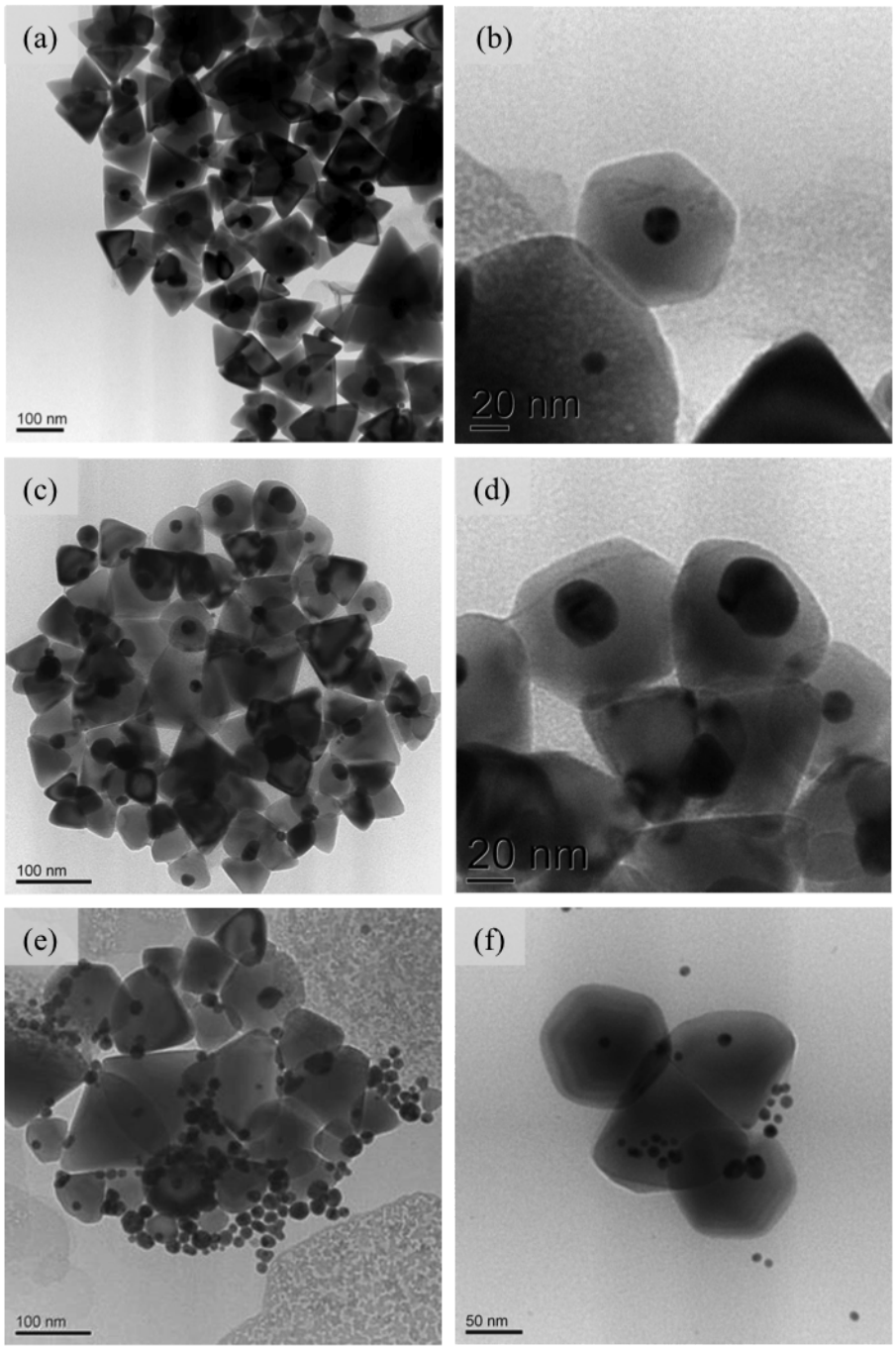

Figure 4.5 TEM images of Au-ZnO nanopyramids prepared using 0.17 M Zn acetate in the presence of 1:1 molar ratio of oleic acid to oleylamine and 8 minutes MWI time (1000 W) with different concentrations of HAuCl4: (a-b) 0.004 M, (c-d) 0.007 M, (e) 0.014 M and (f) 0.014 M HAuCl4, 12 min MWI time.

4.3.3. Heterogeneous Nucleation of ZnO Nanopyramids on Preformed Au Nanocrystals

To confirm the stepwise sequential nucleation mechanism, the formation of ZnO nanopyramids is studied in the presence of preformed Au nanoparticles under conditions comparable to those used in the binary nucleation approach. For the two-step process, MWI was first used to synthesize nearly monodisperse gold nanoparticles (approximately 14 nm in diameter) using a 1:1 OAM/OAC mixture as a solvent, reducing and capping agent (Figure 4.6a). Next, the gold nanoparticles were added into the zinc acetate reaction mixture followed by MWI. It was found that, for the formation of high-quality Au-ZnO nanpyramids, the concentration of zinc acetate precursor and the temperature of the reaction must be adjusted to avoid the formation of free independent ZnO nanopyramids that did not grow on the Au nanoparticles. Figure 4.6b shows the SPR band of the preformed Au nanoparticles and the absorption spectrum of the zinc acetate reaction mixture containing 0.05 M zinc acetate after MWI for 10 min in the presence of the Au nanoparticles. It is clear that, following MWI, the SPR of Au nanoparticles nearly disappears and the ZnO absorption at 370 nm appears indicating the formation of Au-ZnO nanocrystals. The TEM images displayed in Figure 4.6c and d clearly indicate the formation of Au-ZnO nanopyramids containing smaller Au nanoparticles with a narrow size distribution.

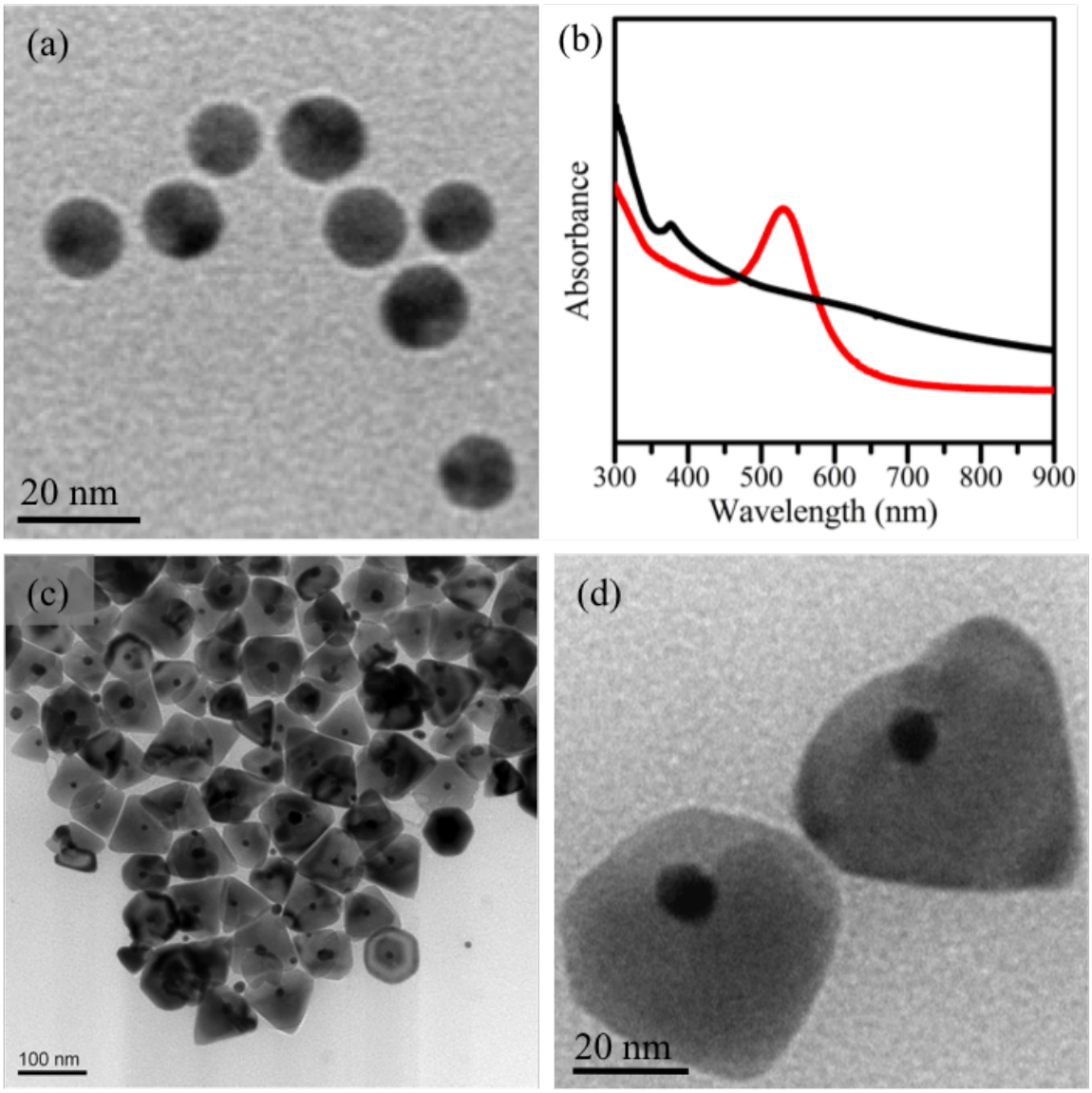

Figure 4.6. (a) TEM image of preformed Au nanoparticles. (b) Absorption spectra of preformed Au nanoparticles (red) and Au-ZnO nanopyramids obtained from a reaction mixture containing preformed Au nanoparticles, 0.05 M Zn acetate, and a 1:1 molar ratio OAc/OAm after 10 min MWI time (1000 W). (c,d) TEM images of Au-ZnO nanopyramids.

The similarity of the results obtained from the heterogeneous nucleation of ZnO on preformed Au nanocrystals (Figure 4.6) and those obtained from the one-step process involving a mixture of Au^{+3} ions and zinc acetate (Figure 4.2) indicates that in both cases, the formation of Au nanoparticle catalyst is crucial for the growth of Au-ZnO nanopyramids. As indicated earlier, in the absence of Au nanoparticles, the formation of ZnO nanopyramids requires longer MWI

times (Chapter 3) as compared to formation in the presence of Au ions or nanoparticles as shown in Figures 4.2 and 4.6, respectively. In the absence of Au nanoparticles, the formation of ZnO nanopyramids is consistent with a homogeneous nucleation mechanism, which requires higher supersaturation than in the heterogeneous mechanism. Since the growth of ZnO nanopyramids on the preformed Au nanoparticles occurs at low ZnO supersaturation, the formation of free ZnO nanocrystals can be avoided in the two-step approach. Similarly, the concentration of the preformed Au nanoparticles must be adjusted with respect to the concentration of zinc acetate in order to avoid the presence of free Au nanoparticles. At lower concentrations of Au nanoparticles, the incorporation of Au nanoparticles within the ZnO nanopyramids is not complete and free ZnO nanopyramids not containing Au nanoparticles are observed (Figure 4.7). At the optimum concentration ratio of Au nanoparticles to zinc acetate, almost all the ZnO nanopyramids are observed to encapsulate Au nanoparticles within their basal planes (Figures 4.6-c and 4.7-c). By increasing the concentration of Au nanoparticles, free Au nanoparticles are adsorbed on the surface of the Au-ZnO nanopyramids (Figures 4.7-e and 4.7-f). Thus, the appropriate concentration ratio of gold nanoparticles to the zinc acetate precursor provides the highest likelihood of having most of the ZnO nanopyramids grown on the Au nanoparticle catalysts. The same trend was observed for the concentration of Au^{+3} ions with respect to zinc acetate in the one-step binary nucleation approach (Figure 4.5).

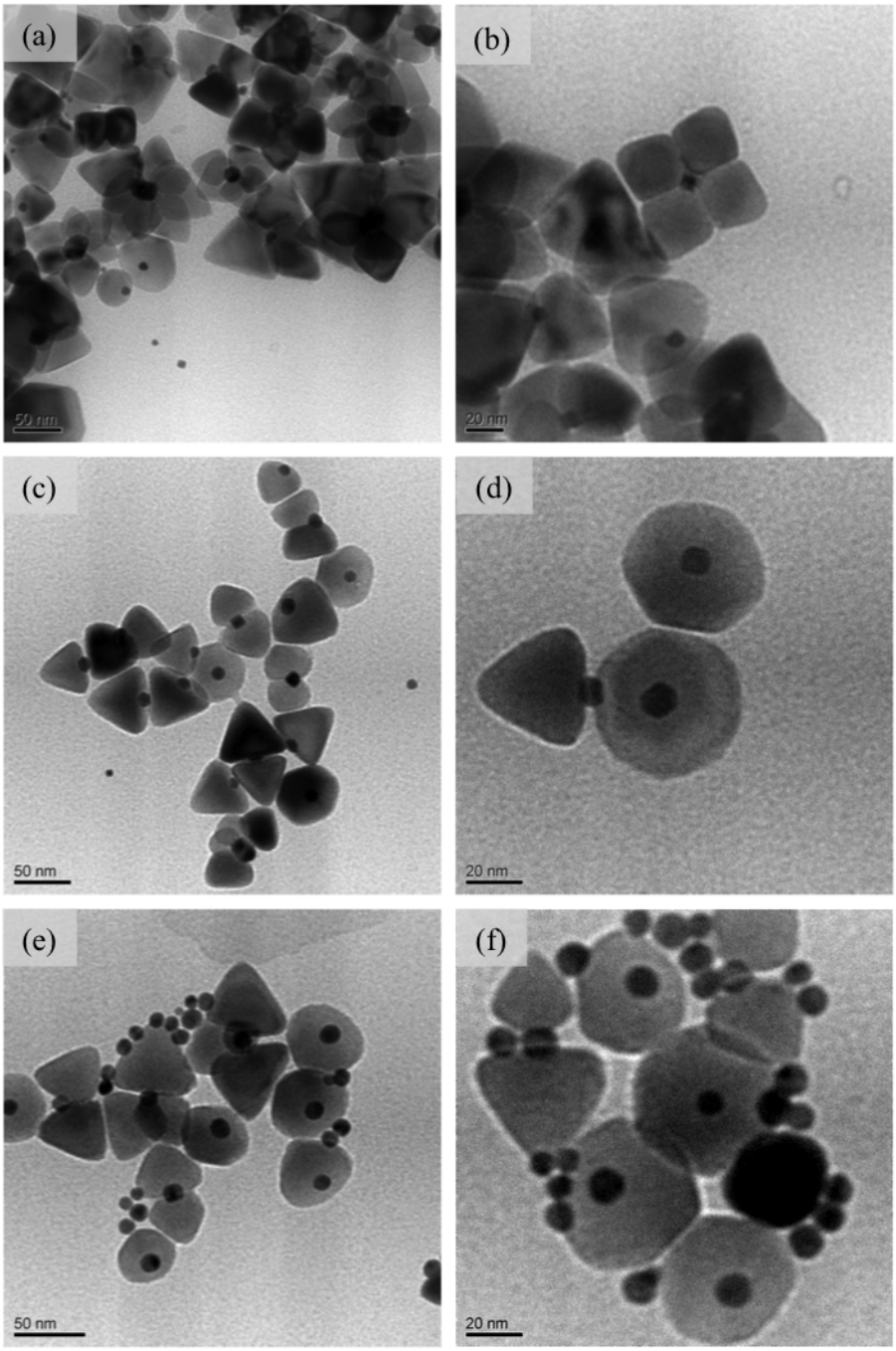

Figure 4.7 TEM images of Au-ZnO nanopyramids prepared using 0.25 M Zn acetate in the presence of 1:1 molar ratio of oleic acid to oleylamine (4 mL) and 10 minutes MWI time (1000 W) with different added volumes of preformed Au nanoparticles: (a-b) 0.5 mL, (c-d) 1 mL, (e-f) 2 mL.

The effect of the molar ratio of OAC/OAM on the size, shape and composition of the Au-ZnO hybrid nanostructures prepared by the two-step approach was investigated. Samples were prepared using the optimum concentration ratio of preformed gold nanoparticles to zinc acetate and various ratios OAC/OAM under similar MWI conditions (1000 W for 10 minutes). It is interesting to note that the optimum range of the OAC/OAM molar ratio (50%-75% OAm) for the formation of Au-ZnO nanopyramids is similar to the range observed for the formation of pure ZnO nanopyramids. As shown in the TEM images displayed in Figures 4.8-a and 4.8-b, the use of OAC/OAM molar ratios of 1:2 and 1:3, respectively, produces high yield of a narrow size distribution of the Au-ZnO nanopyramids. Under these conditions, most of the Au-ZnO nanopyramids produced are symmetric, with a gold core centered in the basal plane of the pyramid.

In pure OAC, the growth of ZnO nanopyramids appears to be fast but does not result in the formation of well-defined nanopyramid shapes as shown in Figure 4.8-c. This may be a result of polar oleic acid preferentially binding to the (001) ZnO plane. In pure OAM (Figure 4.8-d) the formation of the ZnO nanopyramids is slow and the majority of particles formed are ZnO nanocrystals not containing a gold core. Increasing the mole ratio of oleylamine above 75% does not produce as uniform Au-ZnO nanopyramids. The gold cores of the ZnO nanopyramids are offset from the center of basal plane similar to the composites formed in the presence of oleylamine only (Figure 4.8-d). These results confirm that both oleic acid and oleylamine must be present within the optimum molar ratio range (50-75% OAM) in order to produce uniform hybrid Au-ZnO nanopyramids.

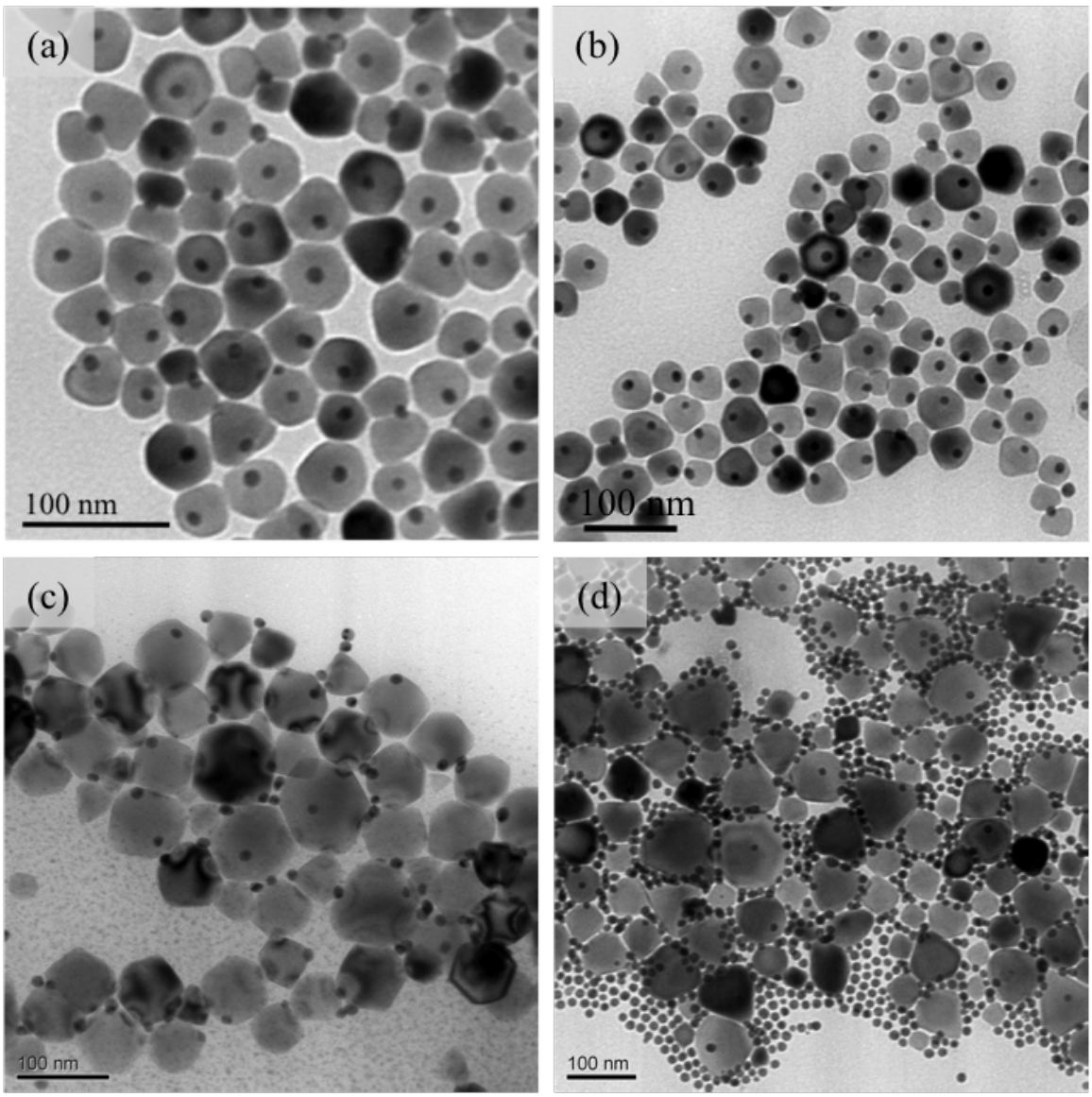

Figure 4.8. TEM images of Au-ZnO nanocrystals obtained from a reaction mixture containing 0.05 M Zn acetate and 0.5 mL solution of preformed Au nanoparticles after 10 min MWI time (1000 W) using different molar ratios of OAC/OAM: (a) 1:2, (b) 1:3, (c) pure OAC, and (d) pure OAM.

In order to confirm the shape of the Au-ZnO nanopyramids, high-resolution electron tomography measurements were carried out on the Au-ZnO nanparticles using a TECNAL G2-Twin HR-TEM operated at 200 kV and equipped with a ±45 degree α-tilting and ±29 degree β-tilting stages and a Gatan UltraScan 4000SP 4k × 4k CCD camera.[125] This allowed the rotation of TEM grid along a fixed axis as shown in Figure 4.9. Images for topographic reconstruction

were taken using a 2° interval, over the largest possible angle. A reference image taken at 0° tilt was taken before and after image acquisition. The tilting experiments show that Au nanoparticle integrated within the ZnO nanopyramid is clearly exposed in the center of the basal plane.

The tilting experiments show that a Au nanoparticle integrated within the ZnO nanopyramid is clearly exposed in the center of the basal plane. They symmetrical hexagonal base and the smooth nature of the pyramid sides are clearly evident. Also, it appears that the Au nanoparticle is embedded within the body of the pyramid and is not just being adsorbed on the outside surface. This feature could provide an interesting possibility of forming metallic contact point within the hybrid nanopyramid structure. These gold particles could serve not only as ohmic electrical contacts, but also as an anchor points for bottom-up assembly of Au-ZnO devices. Furthermore, the gold nanoparticles could facilitate charge separation of the photogenerated electron-hole pairs within the ZnO pyramid for solar energy conversion and photocatalysis. In fact, the Au-ZnO nanopyramid could represent a unique design of a supported Au catalyst with a large surface area and strong catalyst-support interaction. These emerging directions are currently investigated in the El-Shall laboratory.

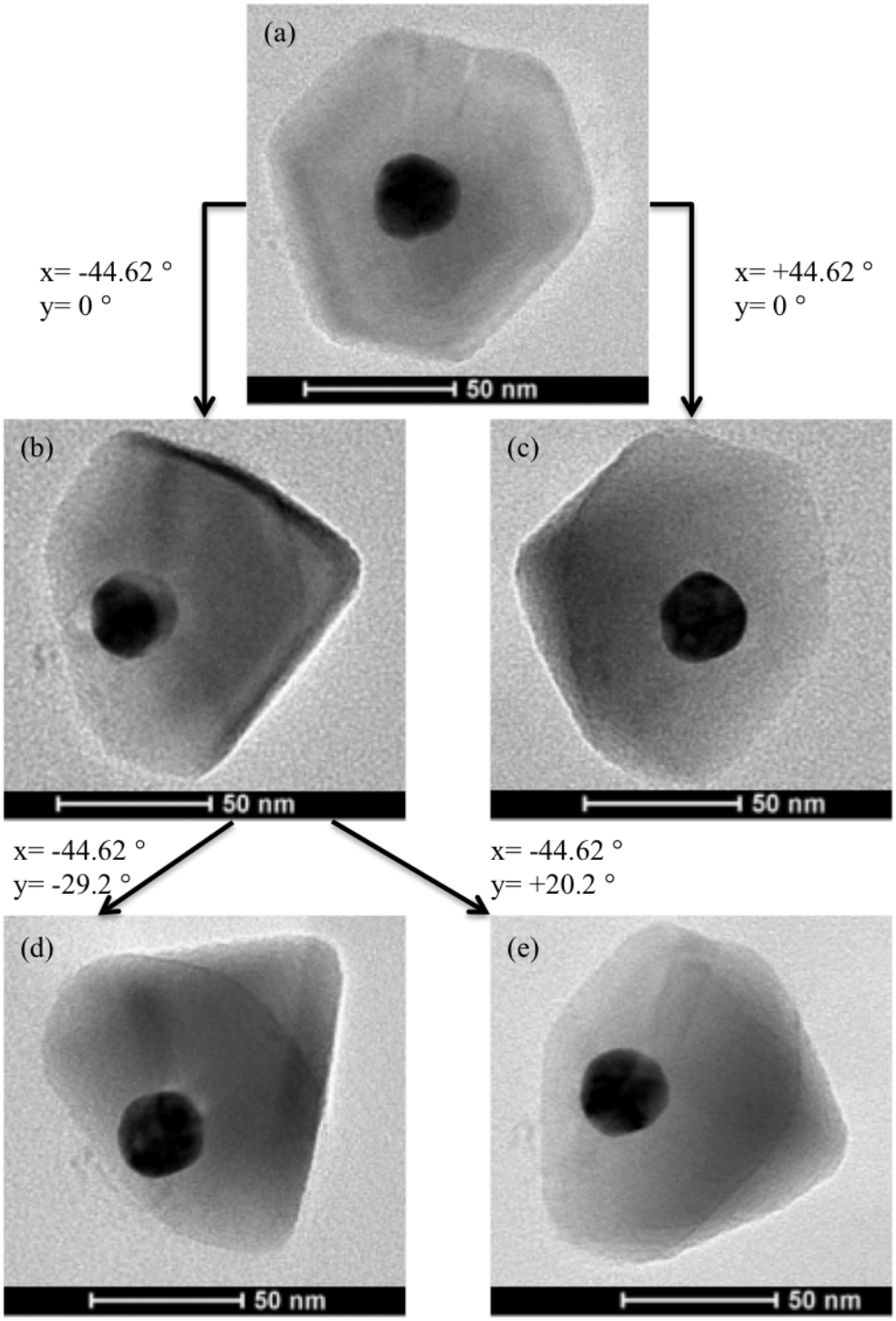

Figure 4.9 TEM images of the Au-ZnO hexagonal nanopyramid obtained by rotation of the TEM grid along a fixed axis.

4.3.4 Growth and shape evolution of Au-ZnO nanopyramids

The growth and shape evolution of the Au-ZnO nanopyramids have been investigated by changing the microwave power for the same reaction mixture over a fixed reaction time (10 min). It has been previously reported that the final structure of ZnO nanoparticles is strongly dependent on the decomposition temperature of zinc acetate.[85] Since MWI provides a rapid decomposition of the zinc acetate precursor, controlling the microwave power plays a key role in determining the degree of heating, and consequently the degree of ZnO supersaturation. Figure 4.10 displays representative TEM images of the Au-ZnO nanocrystals formed by various MWI powers of a mixture containing 0.05 M zinc acetate in a 1:1 molar ratio of OAC/OAM in the presence preformed Au nanoparticles following MWI using different powers. Microwave irradiation of the reaction mixture for 10 min with power ranging from 100 to 500 W resulted in no ZnO growth, and only the preformed Au nanoparticles were present, with no sign of ZnO formation. This indicates that, at power less than 600 W, not enough heat was transferred to the zinc acetate precursor to effectively decompose to produce ZnO. It should be noted that the final temperatures of the reaction mixtures measured immediately following the 10 min MWI were found to be 109, 126, 149, 160, 184, and 214 °C at the MW power of 500, 600, 700, 800, 900, and 1000 W, respectively.

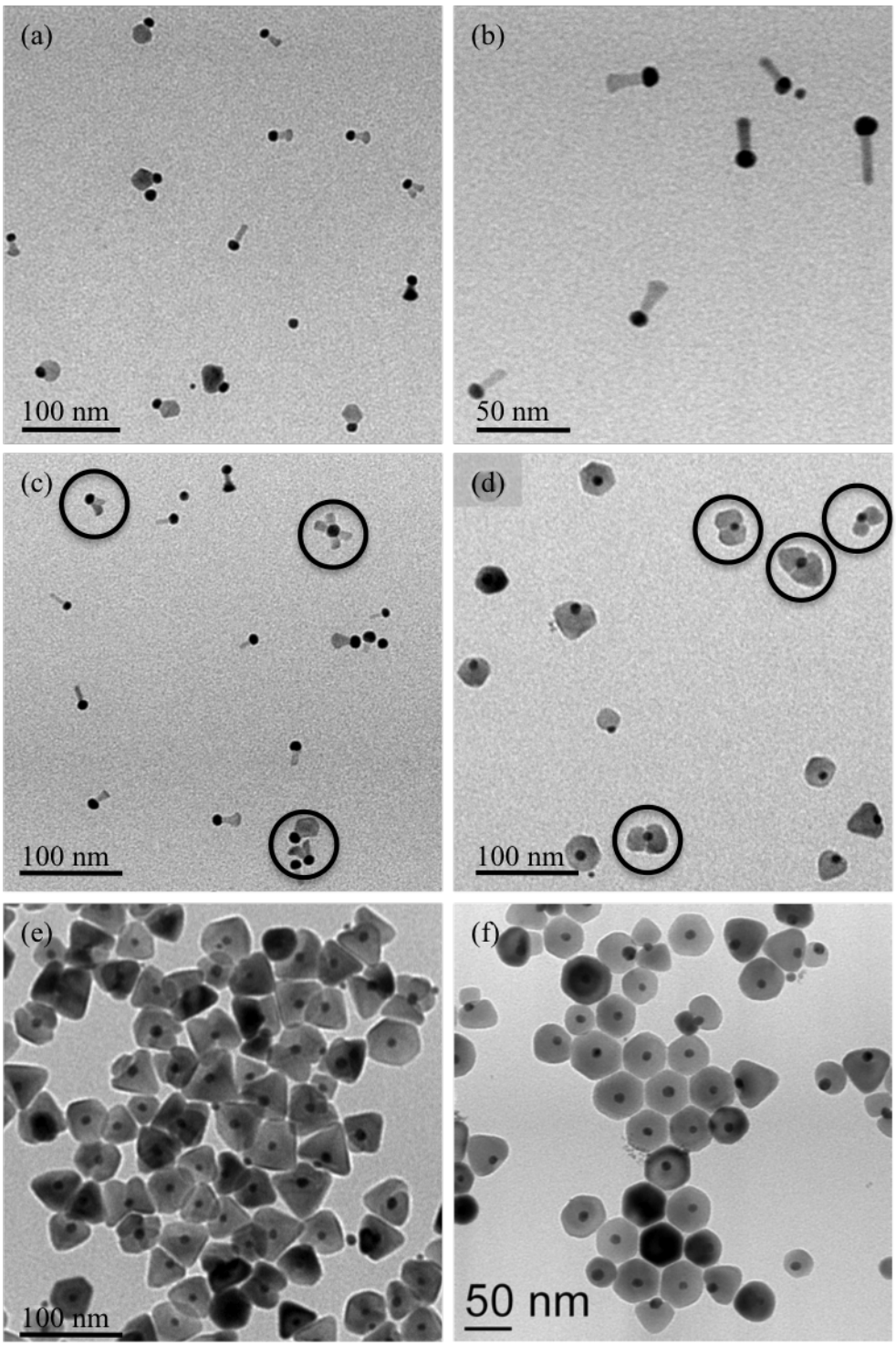

Figure 4.10 TEM images of Au-ZnO nanocrystals obtained from a reaction mixture containing 0.05 M Zn acetate, 0.5 mL solution of preformed Au nanoparticles, and a 1:2 molar ratio of OAC/OAM after 10 min MWI time using different MW powers: (a,b) 600 W, (c) 700 W, (d) 800 W, (e) 900 W, and (f) 1000 W.

The first sign of ZnO growth was observed after 10 minutes of MWI at a power of 600 W 126 °C). As shown in Figures 4.10-a and 4.10-b, ZnO spindles begin to grow from gold nanoparticles resulting in interesting Au-ZnO composites that consist of a spherical gold nanoparticle attached to a small ZnO rod. This observation is consistent with previous work which reported the role of gold nanoparticles as a catalyst for the growth of ZnO nanostructures.[19, 36, 48] The spindles growing from each gold nanoparticle are approximately 20 nm in length and only a few nm in diameter (Figure 4.10-b). It is interesting to note that the diameter of the hexagonal basal plane of the final Au-ZnO nanopyramid is about 50-60 nm, i.e. one Au nanoparticle attached to two ZnO spindles, one on each side. Therefore, additional MWI must not increase the length, but rather the diameter of the ZnO spindles.

As the MWI power is increased to 700 W (149 °C), the ZnO spindles attached to gold nanoparticles increase in size as shown in Figure 4.10-c. The Au-ZnO composite particles created in this case resemble a single gold nanoparticle attached to a ZnO particle. Several gold nanoparticles show attachments to more than one ZnO particle as indicated in Figure 4.10-c. By increasing the MWI power to 800 W (160 °C), the ZnO spindles begin to encapsulate the gold nanoparticle in the center of the hexagonal base and the development of the ZnO nanopyramid can be clearly observed as shown in Figure 4.10-d. Interestingly, several nanopyramids form pairs through interactions between the basal planes as indicated in Figure 4.10-d. Further increase of the MWI power to 900 W (184 °C) results in a sudden increase in the number density of the Au-ZnO nanostructures, and most of the nanopyramids appear to be fully developed as shown in Figure 4.10-e. Lastly, MWI power of 1000 W (214 °C) yields well-defined hexagonal pyramids with a narrow size distribution and with each pyramid containing a single Au nanoparticle in the center of its hexagonal base as shown in Figure 4.9-f. Based on the changes in

particles size, shape and morphology observed at different MWI powers, the growth sequence illustrated in Figure 4.11 is proposed. The gradual increase in MWI power scales with the reaction temperature, which determines the composition rate of the zinc acetate precursor and thus the degree of supersatruation of the ZnO monomer. Increasing the temperature increases the growth evolution of the ZnO nanocrystal on the surface of the Au nanoparticles until the full development of the hexagonal nanopyramid. It is clear that, as the ZnO nanopyramid is fully developed, the Au nanoparticle becomes more embedded within the hexagonal base of the pyramid.

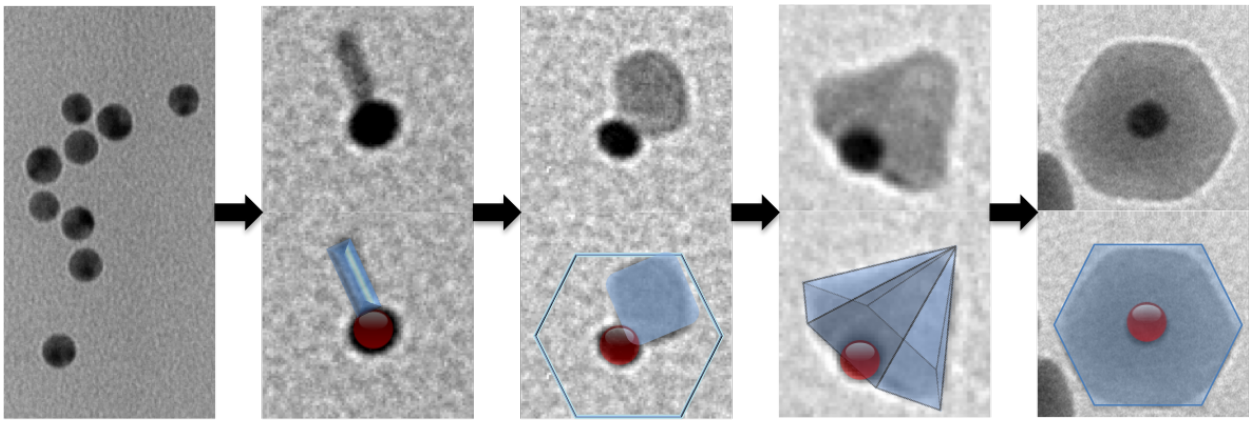

Figure 4.11. TEM images showing the growth sequence of the Au-ZnO hexagonal nanopyramids starting from preformed Au nanoparticles (left) and illustrative drawings of the growth sequence.

4.4 Conclusions

In this chapter, the formation of ZnO nanopyramids by the decomposition of zinc acetate using microwave irradiation (MWI) in the presence of a mixture of OAC and OAM was studied. The rapid decomposition of zinc acetate by MWI in the presence of the mixture of OAC and OAM results in nucleation and subsequent formation of a hexagonal ZnO plate which continues to grow to form the nanopyramid. ZnO hexagonal nanopyramids were produced at good yield using 0.1 M zinc acetate and a 1:3 molar ratio of OAC/OAM.

In the presence of Au^{3+}, the initially formed Au nanocrystals act as heterogeneous nuclei for the nucleation and growth of the ZnO nanopyramids. The Au nanoparticles promote the formation of the hexagonal base of the ZnO nanopyramids. Using preformed Au nanoparticles instead of Au ions results in a narrow size distribution of uniform Au-ZnO nanopyramids, each consisting of a gold nanoparticle embedded in the center of the hexagonal base of the ZnO nanopyramid. The formation of the Au-ZnO nanopyramids is strongly dependent on the molar ratios of OAC to OAM. The presence of OAC with a considerable dipole moment results in strong electrostatic interaction with the polar surfaces of the growing ZnO nanocrystals, thus resulting in slowing the growth rate of the polar planes and allowing the formation of well-developed facets. In the absence of Au nanoparticles, a high concentration of zinc acetate precursor and longer MWI times are required for the production of the nanopyramids.

This work demonstrates the use of MWI not only for the synthesis of high quality Au-ZnO nanopyramids, but also to provide direct evidence for the effect of Au nanocrystals on the assembly and growth of the ZnO nanopyramids, and to obtain new insights on the sequential homogeneous–heterogeneous and conventional heterogeneous nucleation processes in this system. The growth of the ZnO nanocrystals on the surface of the Au nanoparticles is followed by gradually increasing the effective reaction temperature by increasing the MWI power. This allows for observation of the evolution of the Au-ZnO nanostructures until the full development of the hexagonal nanopyramids. The gold nanoparticles could provide the metallic contact points within the heterostructured nanopyramids, which could facilitate the bottom-up assembly of Au-ZnO devices. Furthermore, the Au-ZnO nanopyramids may present improved performance in solar energy conversion and photocatalysis.

Chapter 5: Nitrogen-Doped Zinc Oxide Nanostructures

5.1 Introduction

ZnO is one of the most interesting and important materials because of its unique properties; namely, wide band gap (~3.37 eV), large exciton binding energy (60 meV at room temperature) and bio-compatibility. As a result, ZnO has been exploited for a wide range of applications. Substitutional doping with a non-metal allows for fine-tuning of these unique properties to make ZnO more effective for various applications including optoelectronics, sensors, and catalysis.[1, 126-131]

Numerous strategies for substitutional doping of ZnO are reported in the literature, which include doping with Li, P, As, B, and N. Electronic and optical properties are modified through substitution of these atoms for oxygen atoms in the ZnO lattice. The type and amount of doping are varied based on the intended application.

As previously discussed, ZnO is a very active material for UV-photocatalysis. However, the wide band gap of ZnO deems it inactive for visible photocatalysis, because visible photons do not have enough energy to overcome the band gap. Modifying the ZnO bandgap by doping with non-metals, such as nitrogen, is one approach for improving the visible response of ZnO. Through N-doping, the range of light absorption is increased to include UV and visible light. In

general, N-doping ZnO is shown to have more advantages for field emssion, photoelectrochemical water splitting, and photocatalysis.[42, 132]

The character of the charge carriers, n or p-type, produced through doping is also important for different applications, mainly optoelectronics. Both n-type and p-type ZnO is needed to expand their applications. There is significant interest for replacing GaN with ZnO for use in optoelectronic devices due to lower toxicity and production costs.[11, 133] In order to use ZnO, there is a need for a reliable and reproducible method for p-type ZnO of high quality.[11, 133] This is extremely challenging because of the difficulty associated with p-type doping in ZnO.[11, 133] Naturally, ZnO exhibits n-type conductivity due to oxygen vacancies and Zn interstitials as well as hydrogen atoms present in the host material. The concentration of n-type carriers in ZnO can be further increased by doping with different elements.[134] Different approaches have been proposed to synthesize p-type ZnO among which nitrogen doping is shown to be the most effective.[14, 135-139]

Different chemical and physical methods have been reported for the preparation of N-doped ZnO nanostructures including hydrothermal synthesis,[20, 132, 140] combustion,[14] low temperature ammonolysis of ZnO_2,[133] metal organic chemical vapor deposition,[100, 141-143] magentron sputtering[144-147] and post annealing of ZnO with a nitrogen source.[148] At present, very few solution phase synthesis methods have been reported for the preparation of N-doped ZnO nanostructures.[20, 140, 149, 150] The previously reported solution phase synthesis methods require high temperatures and/or long reaction times. Currently, no rapid, solution phase synthesis method has been reported for N-doping of ZnO. Several procedures for the facile synthesis of doping ZnO with other metals have been reported,[151, 152] but N-doping is more challenging. Moreover, there is an increase in interest of a microwave method for synthesizing various

nanomaterials due to unique advantages such as rapid volumetric heating, short reaction time, high reaction rates as well as energy efficiency.[153-156] ZnO synthesis with controlled morphology by MWI has previously been demonstrated in Chapter 3. Currently, no microwave method has been reported for the preparation of N-doped ZnO with morphology control. Here, a simple MWI method for the preparation of p-type N-doped ZnO with morphology control using urea as the nitrogen source is presented. The role of concentration of zinc acetate and urea on morphology and N-doping level is investigated.

5.2 Microwave synthesis of N-doped ZnO

A simple microwave irradiation method was developed to systematically study the formation of N-doped ZnO nanostructures. In general, a zinc precursor was decomposed to ZnO in the presence of urea, which serves as the nitrogen source. Two zinc-based starting materials were studied: preformed ZnO_2 and zinc acetate.

First, the formation of N-doped ZnO nanoparticles from preformed ZnO_2 nanoparticles was studied. ZnO_2 nanoparticles were prepared following a method by Uekawa et al.[157, 158] In a typical synthesis, 100 mL of 0.1 M zinc nitrate was mixed with 100 mL of 0.1 M NaOH. The solution was gently mixed using magnetic stirring for 5 minutes. After mixing, a white precipitate formed and was removed from solution by centrifugation (3000 RPM for 5 minutes) followed by three washings with water. The precipitate was dispersed in 50 mL 1 M H_2O_2 and heated in a closed vessel at 70 °C for 2 hours. The gelatinous solution was then uncapped and dried at 70 °C until a dry, white powder remained. The resulting ZnO_2 powder was used as the starting material. ZnO_2 and urea were dissolved in oleylamine, which acts as the capping agent and solvent. The reaction mixture was heated in a hot oil bath with magnetic stirring to 110 °C and the temperature was maintained for one hour to assist dissolving and removal water. After

heating, the reaction mixture is pale yellow in color. Microwave irradiation was applied at ambient pressure in an open test tube, which resulted in the solution becoming pale pink and opaque indicating the formation of ZnO. Following the microwave reaction, the precipitate was separated from the liquid phase by centrifugation with ethanol and dried at 80 °C overnight.

Second, the formation of N-doped ZnO from anhydrous zinc acetate was studied. The second approach is similar to the method described above. This method utilizes zinc acetate as the starting material, urea as the N source, and oleylamine as the solvent and capping agent. Zinc acetate is a more preferable starting material because it does not require any prior processing and allows for morphology control. In a general synthesis procedure, zinc acetate and urea are dissolved in oleylamine by magnetic stirring in a hot oil bath (110 °C) for 1 hour. The solution is transparent yellow in color. Next, the solution was heated by MWI until the solution turned from transparent yellow to opaque pink. The intensity of the pink color was dependent on the amount of N-doping, which will be discussed in more detail in the remainder of this chapter. Following the microwave reaction, the precipitate was separated from the liquid phase by centrifugation with ethanol and dried at 80 °C overnight. After microwave irradiation, solution temperatures ranged from 178.4 °C to 229.6 °C.

The synthesis method for N-doped ZnO is similar to that for ZnO presented in Chapter 3. The main differences are the addition of urea and removal of oleic acid from the reaction mixture. Many hydrocarbon acids, including oleic acid, are known to readily form urea-adduct complexes.[159, 160] Therefore, if both urea and oleic acid are present in solution, an oleic acid-urea adduct forms, which prevents the formation of N-doped ZnO. It should be noted that formation of ZnO in the presence of oleylamine only without oleic acid does result in minimal amounts of N-doping.

For characterization, particles were centrifuged from solution and used either as a powder or particles were diluted in toluene and mixed by vigorous pipetting. UV-Visible absorbance spectra were recorded using an HP-8453 spectrophotometer. The particle size and morphology were studied using transmission electron microscopy (TEM). TEM images were obtained using a JEOL JEM-1230 TEM operating at 120 kV. Samples for TEM imaging were prepared by drop casting toluene diluted samples on a Formar carbon-coated, 300 mesh copper grid (Ted Pella). Powder X-ray diffraction patterns of the dried particles were collected at room temperature using an X'Pert Philips Materials Research Diffractometer with CuKαR radiation. Raman spectra were obtained using a Thermo Scientific DXR SmartRaman Spectrometer operating at 532 nm on dried particles.

5.3 Optical properties

The synthesis of N-doped ZnO nanostructures by the decomposition of ZnO_2 and zinc acetate using microwave irradiation (MWI) in the presence of urea and oleylamine (OAM) was studied. Chavillon, et al. previously demonstrated that ZnO_2 nanoparticles were a suitable starting material for thermal synthesis of N-doped ZnO with p-type conductivity.[133] Furthermore, it has been previously reported that ZnO nanopyramids are formed by MWI of zinc acetate in a mixture of OAM and oleic acid (OAC).[13] In this reaction mixture, OAM acts as both capping agent and solvent, while the OAC acts mainly as a capping agent and allows for additional morphology control. N-doping in ZnO is achieved by the addition of urea, which acts as a nitrogen source, to a reaction mixture containing OAM in the absence of OAC. As previously discussed, OAC must not be present when nitrogen doping with urea because the urea reacts with OAC and forms urea complex crystals and the formation of ZnO is inhibited.[159, 160] Different

amounts of nitrogen are incorporated in ZnO by changing the concentration of urea in the reaction mixture with respect to zinc precursor.

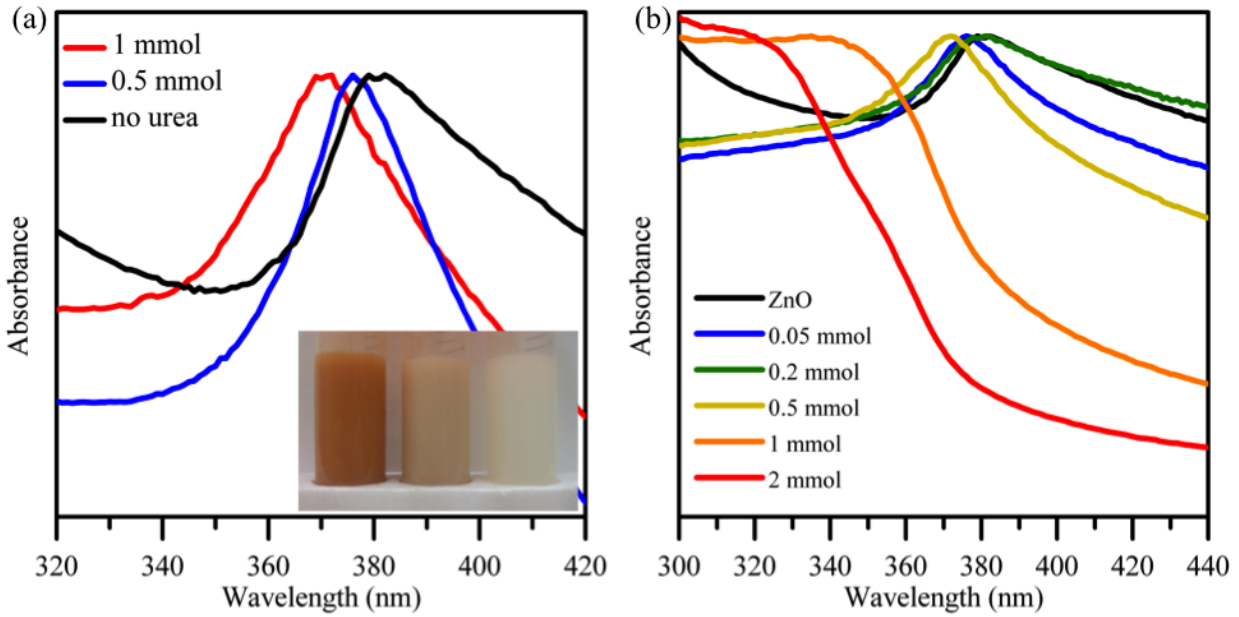

Figure 5.1. Absorbance spectra of ZnO nanoparticles and N-doped ZnO nanoparticles prepared using (a) 5 mmol zinc acetate and (b) 0.5 mmol ZnO_2. In spectra (a), ZnO particles were prepared using 5 mmol of zinc acetate and the amount of urea was varied from no urea (black) to 0.5 mmol (blue) to 1 mmol (red). All solutions were microwaved for 3 minutes. Burstein-Moss shift is observed with increasing doping. In spectra (b), ZnO particles were prepared using 0.5 mmol ZnO_2 and urea was varied from no urea (ZnO) to 2 mmol.

Figure 5.1 displays the optical absorption spectra of ZnO and nitrogen doped ZnO (N-ZnO) prepared by MWI with different urea concentrations. Both ZnO and N-ZnO nanostructures show the characteristic excitonic band for ZnO around 375 nm, which is attributed to electronic transitions between the valence and conduction bands. These bands are slightly blue-shifted compared to that of bulk ZnO that is observed at 385 nm.[98, 161] The sharpness of the absorption edge indicates the sample is monodisperse with a narrow size distribution.[98] Additionally, as nitrogen doping increases in the ZnO lattice, there is an increasing blue shift in the absorption band. Similar blue shifting of the absorption edge as a result of doping has been previously reported for N-doped TiO_2 nanostructures[56] and various doped ZnO nanostructures.[42, 162-166] Several explanations for blue shifting as a result of doping have been previously proposed

including additional strain,[56] conversion of crystal structure from one phase to another,[167] quantum size effect,[168] and banding filling mechanism (Burstein-Moss effect).[56, 169] The blue shifting observed is most likely a result of band filling on the photoexcitation threshold energy. This apparent increase in the semiconductor band gap is known as the Burstein-Moss effect where the generation of a blue shift of the fundamental absorption edge results from the creation of a high density of electrons in the conduction band (n-type) or valence band (p-type). For n-type doping, electrons fill the conduction band near the bottom and optical transitions then have to involve higher energy band states, and therefore a blue shift is observed.[169] Burstein-Moss shifts have been observed in semiconductor colloids with high doping density.[169-171]

Furthermore, doping ZnO with N results in a visible color change of the ZnO material (Fig 5.1 inset). Pure wurtzite ZnO is white in color. However, the addition of low amounts of N doped in the ZnO lattice results in a pale pink product as seen in the inset in Fig. 5.1. Increasing the N-doping results in a more intense pink color that appears orange/red in solution. It is interesting that the pink color is not observed in the visible region of the absorbance spectrum.

In some instances, a broad absorption band was observed in the visible region, as demonstrated in Figure 5.2. This broad absorption band was not observed in every N-ZnO sample, and the appearance showed no relationship with urea concentration nor with reaction temperature. Similar broad absorption has been reported for N-ZnO.[172]

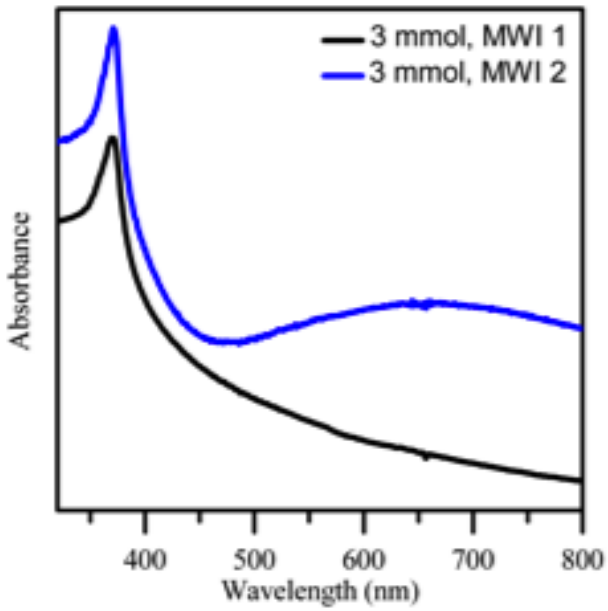

Figure 5.2. Broad absorption band observed from N-doped ZnO.

5.4 X-Ray Diffraction

The crystallinity of the preformed ZnO_2 nanoparticles and ZnO nanostructures was studied using XRD. Zinc peroxide (ZnO_2) nanoparticles were studied as a starting material for synthesis of N-doped ZnO. The XRD pattern for ZnO_2 nanoparticles is given in Figure 5.3. Figure 5.3 demonstrates that the diffraction pattern corresponds to ZnO_2. The broadness of the peaks is consistent with the formation of small particles. No ZnO appears to have formed during the ZnO_2 synthesis.

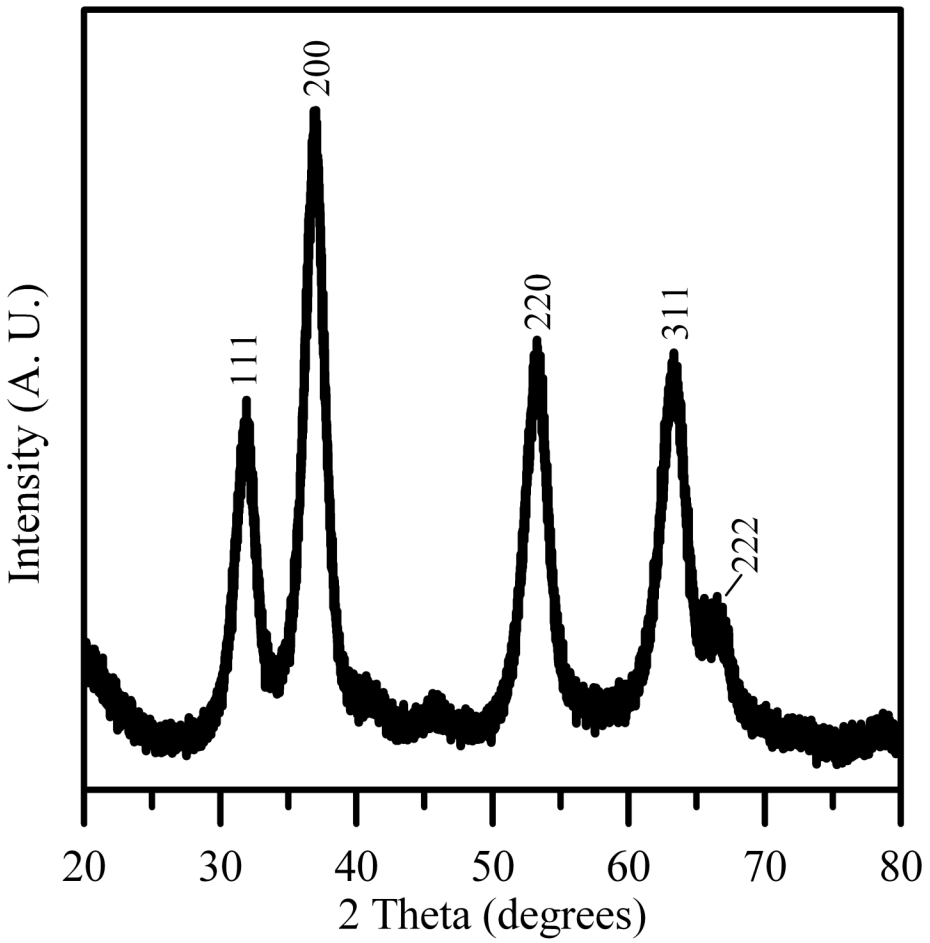

Figure 5.3 Powder X-Ray diffraction pattern of preformed ZnO_2 nanoparticles.

Typical XRD patterns of pure and nitrogen-doped ZnO nanostructures are shown in Figure 5.4. Each diffraction pattern indexed to the hexagonal wurtzite ZnO crystal structure (JCPDS Reference # 36-1451).

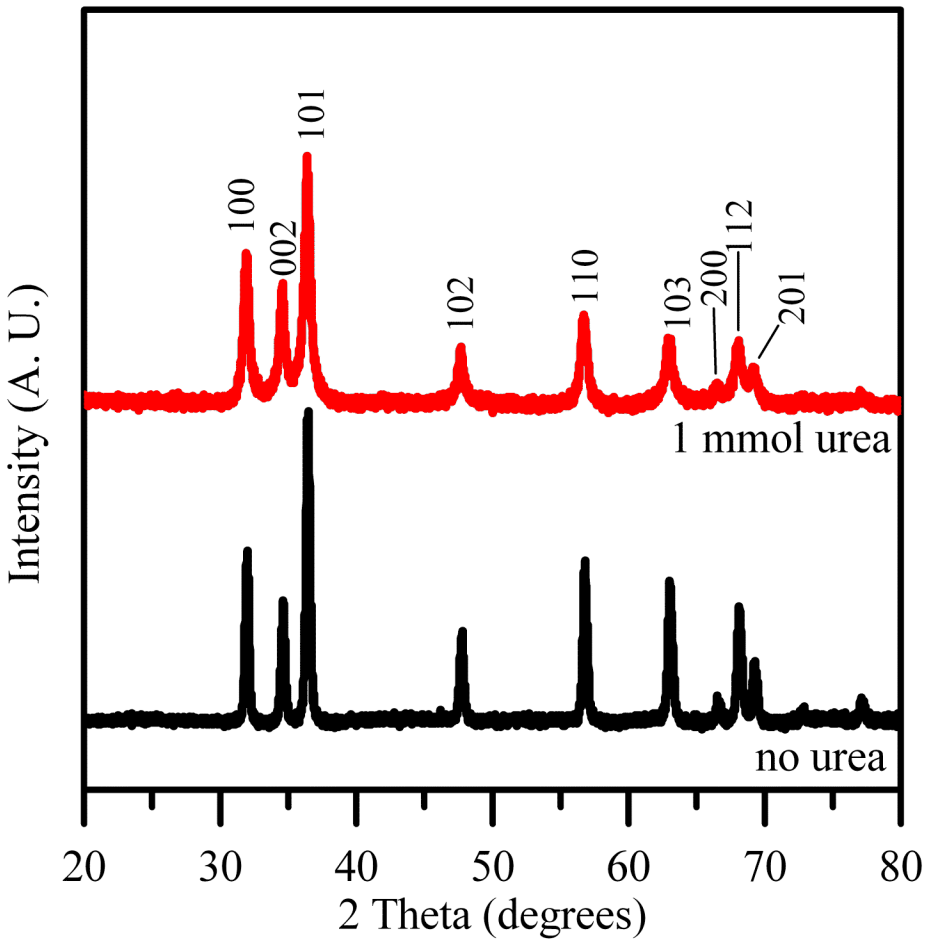

Figure 5.4 Powder X-Ray diffaction patterns of ZnO and N-doped ZnO samples prepared by MWI. All ZnO particles were prepared using 0.5 mmol of zinc acetate and the amount of urea was varied from no urea (black) to 1 mmol (red). Both XRD diffraction patterns show wurtzite ZnO.

XRD is a useful tool for studying doping within the crystal lattice, because dopants alter the crystal structure. It is expected that doping will alter the crystal structure of the ZnO and result in peak shifting. XRD patterns of the N-doped ZnO nanostructures were similar to that of the pure ZnO. Previous reports in the literature have shown that incorporating N into the ZnO lattice will result in peak shifting to either higher or lower degrees. Shifts are attributed to compression of the crystal structure or excess tensile stress for higher or lower degree shifts, respectively. Ye et al. studied the structural properties of N-doped ZnO prepared by chemical

vapor deposition using NO as the nitrogen source and reported shifting of the 002 plane from 34.36 to 34.26 degrees with nitrogen doping.[173] Shifting is attributed to tensile stress caused by N-doping. Shifting is not reported for other peaks in the ZnO spectrum. Therefore, the 002 peak for as prepared ZnO and N-ZnO was studied. Doping N into the ZnO lattice induces a shift of 0.1 degrees (resolution 0.001). This peak shift is consistent with the literature shifts to lower degrees upon incorporation of N into the ZnO lattice.

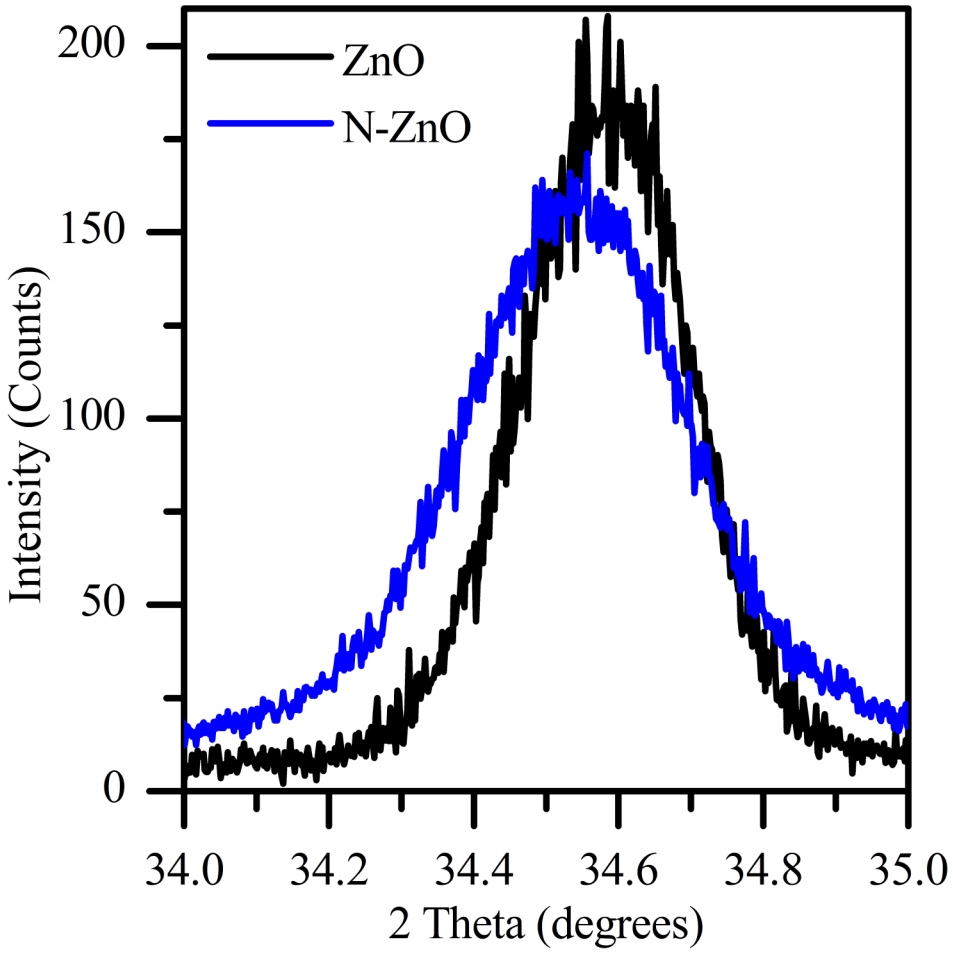

Figure 5.5 (002) X-Ray diffaction peak of ZnO and N-doped ZnO samples prepared by MWI.

5.5 Raman Spectroscopy

Raman spectroscopy is utilized to characterize the doping of ZnO, which is recognized through the presence of nitrogen related features that appear in the Raman spectra. Raman

spectra for ZnO_2, pure ZnO, and N-doped ZnO are shown in Fig. 5.6. Raman analysis of pure and N-doped ZnO has been previously reported.[100-102] ZnO shows characteristic bands at 330, 380 and 437 cm^{-1} with the peak at 437 cm^{-1} being the most intense. Therefore, all spectra have been normalized with respect to the peak at 437 cm^{-1}. The peaks at 330 and 437 cm^{-1} are attributed to vibration modes 2E2(M) due to multiple-phonon-scattering processes and E2(high) from O atom, respectively. The peak at 380 cm^{-1} is attributed to A1(TO) vibration mode. When ZnO is doped with N, additional bands at 275, 508, 578 and 642 cm^{-1} are observed in the Raman spectrum. These additional vibrational modes in N-doped ZnO are attributed to breakdown of the translational crystal symmetry by doping in wurtize-ZnO. Furthermore, Kaschner et al. observed that the N-related local vibrational modes demonstrate a linear dependence to N concentration.[100] It is interesting to observe that as the amount of urea in the reaction mixture is increased, the

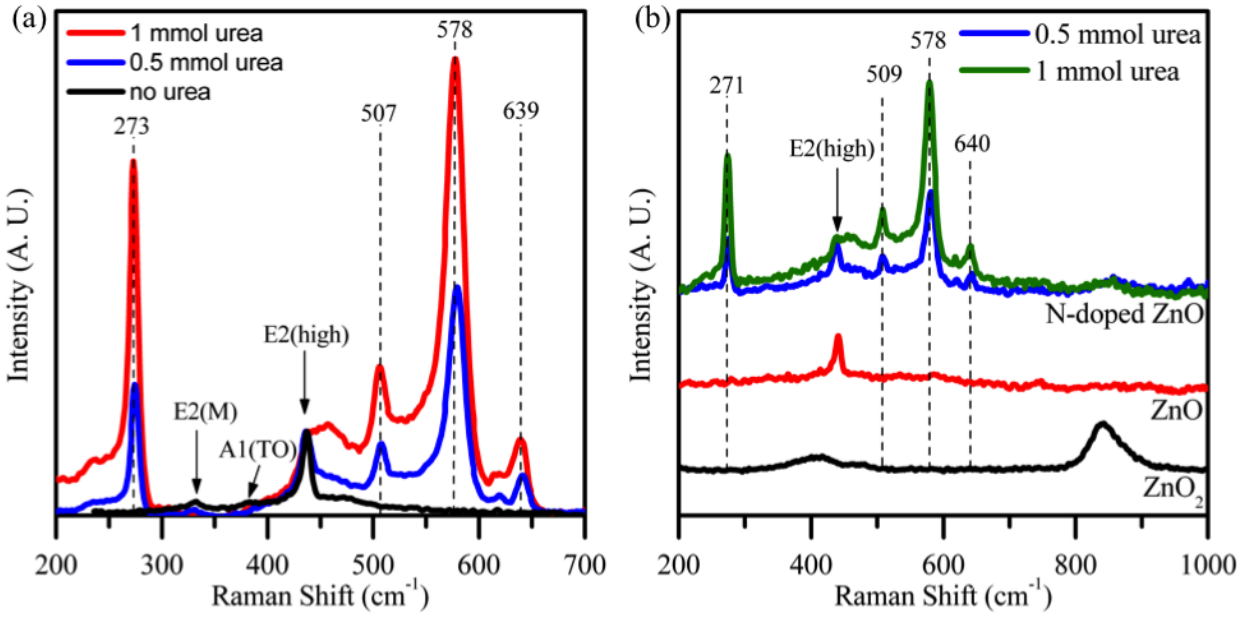

Figure 5.6 Raman spectra of pure ZnO and N-ZnO prepared from (a) zinc acetate and (b) ZnO_2. In spectra (a), ZnO particles were prepared using 5 mmol of zinc acetate and the amount of urea was varied from no urea (black) to 0.5 mmol (blue) to 1 mmol (red). In spectra (b), ZnO particles were prepared using 0.5 mmol ZnO2 and the amount of urea was varied from no urea to 1 mmol. All solutions were microwaved for 3 minutes. The additional local vibrational modes of N in ZnO appear for the N-ZnO particles.

relative intensity of the additional vibrational bands increase in intensity. The measured intensities and peak positions are given in Table 5.1. Thus, increasing the amount of urea in the reaction mixture results in increased N-doping in the ZnO crystal lattice.

Table 5.1. Relative Raman intensities (compared to ZnO 437 cm^{-1}) for N-related features for all samples. Each relative Raman intensity is given with its respective peak position in parenthesis.

	273 cm^{-1}	507 cm^{-1}	578 cm^{-1}	639 cm^{-1}
ZnO_2				
0.5 mmol urea	1.14 (276)	0.75 (508)	2.15 (581)	0.37 (643)
1 mmol urea	2.80 (274)	1.62 (508)	4.40 (579)	0.82 (641)
Zn Acetate Particles				
0.5 mmol urea	1.56 (274)	1.77 (506)	2.72 (579)	0.48 (641)
1 mmol urea	4.21 (273)	0.85 (507)	5.43 (578)	0.91 (639)
Zinc Acetate Prisms				
2 mmol urea	0.11 (276)	0.10 (510)	0.33 (581)	0.06 (643)
10 mmol urea	0.65 (275)	0.39 (509)	1.17 (581)	0.22 (643)
Zinc Acetate Rods				
2 mmol urea	0.12 (276)	0.12 (509)	0.36 (581)	0.08 (644)
10 mmol urea	0.22 (276)	0.15 (509)	0.41 (581)	0.09 (643)

5.6 X-ray photoelectron spectroscopy

To gain more insight into the chemical species present in the N-doped ZnO samples, they were examined by X-ray photoelectron spectroscopy. Figure 5.7 displays the XPS spectra for ZnO and N-doped ZnO prepared using 0.5 mmol urea and 1 mmol urea. The Zn 2p region reveals 2 peaks that are typical for Zn $2p_{1/2}$ and $2p_{3/2}$. For pure ZnO, the $2p_{1/2}$ peak appears at

1021.3 eV, which is consistent with ZnO. The addition of urea into the reaction mixture results in a shift of the Zn 2p peaks to lower binding energies. Similar shifts are observed by Chavillon in N-doped ZnO, and are attributed to preparation conditions.

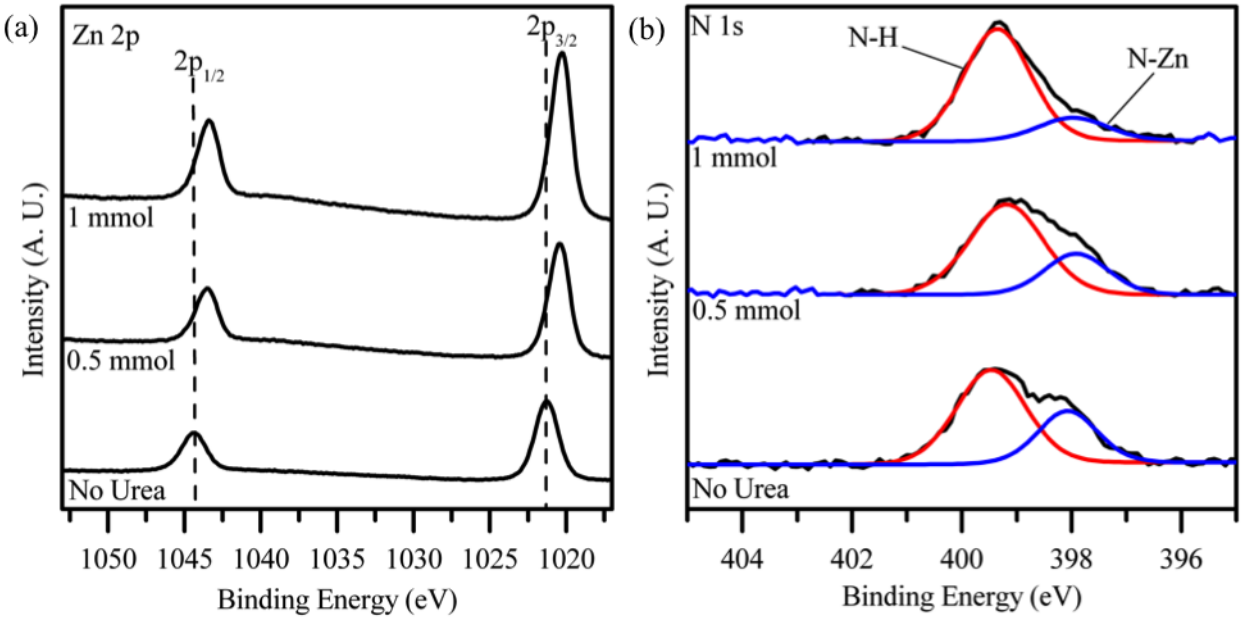

Figure 5.7 XPS spectra of ZnO and N-ZnO samples prepared by MWI of zinc acetate in the presence of oleylamine with and without urea, respectively. XPS spectra are shown for (a) Zn 2p and (b) N 1s regions.

The incorporation of N into the ZnO lattice can occur in more than one chemical state; either by incorporation of N_2 into the ZnO lattice or a N atom can be incorporated substitutionally at an O site. Inspection of the N 1s region shows the presence of 2 peaks. The peak at 399 eV is typical of N 1s binding energy in amines.[18] Since OAM is used as both the capping and reducing agents, it is reasonable to expect the presence of N-H compounds on the nanoparticle surface. The second peak is observed at 398 eV, which is within the region for zinc nitride compounds, and thus, this peak is attributed to oxynitride (O-Zn-N).[18,40] This result suggests that N is doping substitutionally at O sites on the surface of the ZnO structure. It is important to note that this peak is also present for ZnO nanoparticles produced in the absence of

urea. Keeping in mind that XPS is a surface sensitive technique, this peak is attributed to the binding of OAM as a capping agent on the surface of the particles. Note that Raman spectroscopy does not show any Raman peaks for N-related features for ZnO prepared in the absence of urea.

Table 5.2. Binding energies (eV) for Zn 2p and N 1s peaks obtained by XPS.

	Zn 2p	Zn 2p	N 1s	N 1s
ZnO; no urea	1021.3	1044.4	399.5	398.1
N-ZnO; 0.5 mmol urea	1020.5	1043.5	399.2	397.9
N-ZnO; 1 mmol urea	1020.3	1043.4	399.4	398.0

Table 5.3. Peak fitting for N 1s region of XPS spectra.

	Position	Area	FWHM	% Conc.
ZnO; no urea	399.5	1503.7	1.48	68
	398.1	711.8	1.27	32
N-ZnO; 0.5 mmol urea	399.2	1542.1	1.58	72
	397.9	601.2	1.35	28
N-ZnO; 1 mmol urea	399.4	1718.9	1.42	82
	398	376	1.5	18

5.7 Nanostructure morphology

TEM was utilized to further investigate the morphology of the ZnO structures formed by MWI and the effect of N-doping on nanoparticles structure. Figure 5.8 shows the TEM images of ZnO prepared in the absence of and with increasing amounts of urea. The ZnO nanoparticles

prepared in the absence of urea are hexagonal pyramids. Upon the addition of urea to the reaction mixture, the particles produced are spherical in shape and range from 100 to 200 nm in diameter. Increasing the concentration of urea in the reaction mixture does not result in a change in particle morphology. The particle morphology appears to be independent of N-doping.

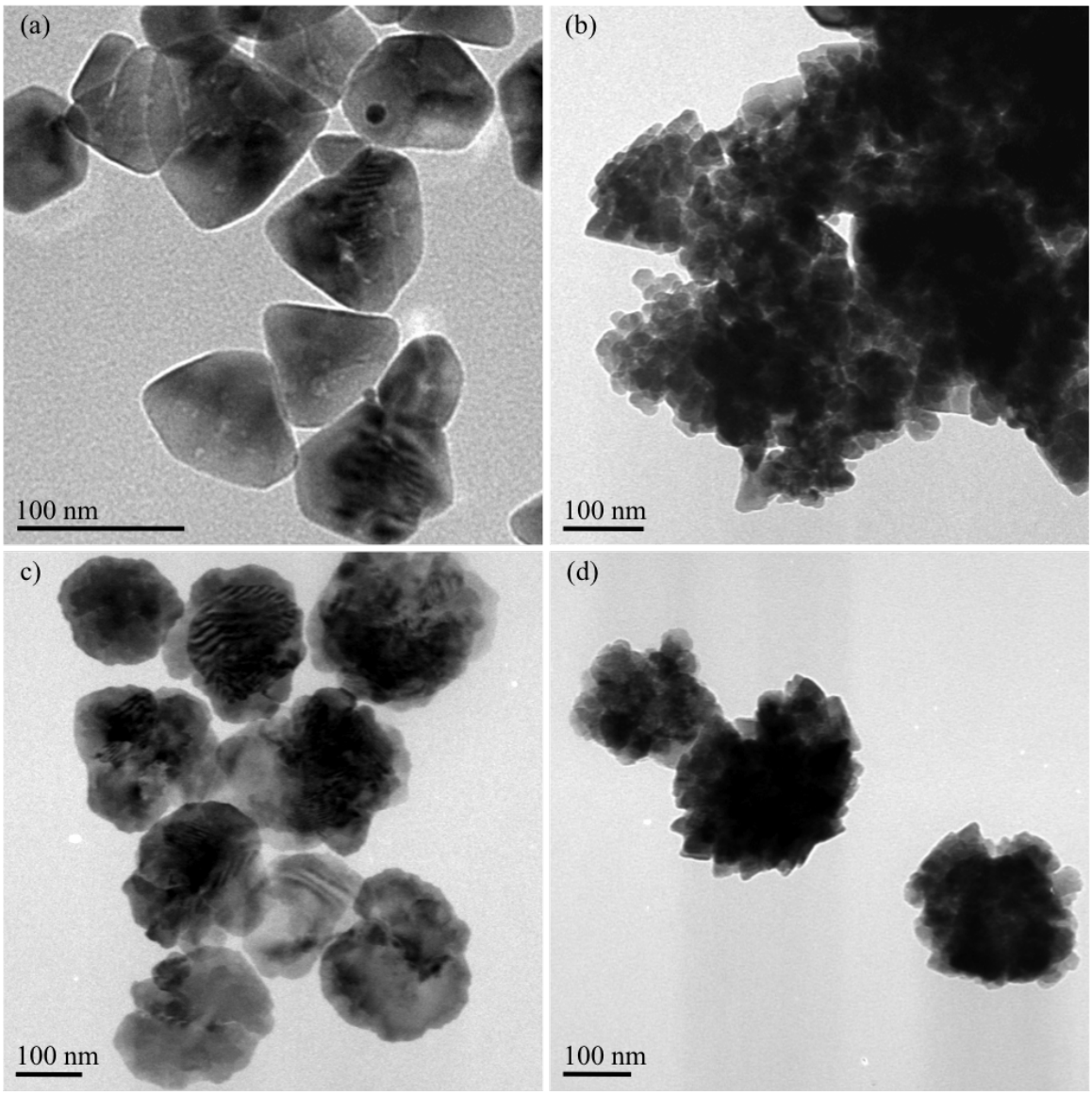

Figure 5.8 TEM comparing different levels of N doping and starting materials. (a) no urea, (b) 0.5 mmol ZnO_2, (c) 5 mmol Zn acetate with 0.5 mmol urea (d) 5 mmol Zn acetate with 1 mmol urea.

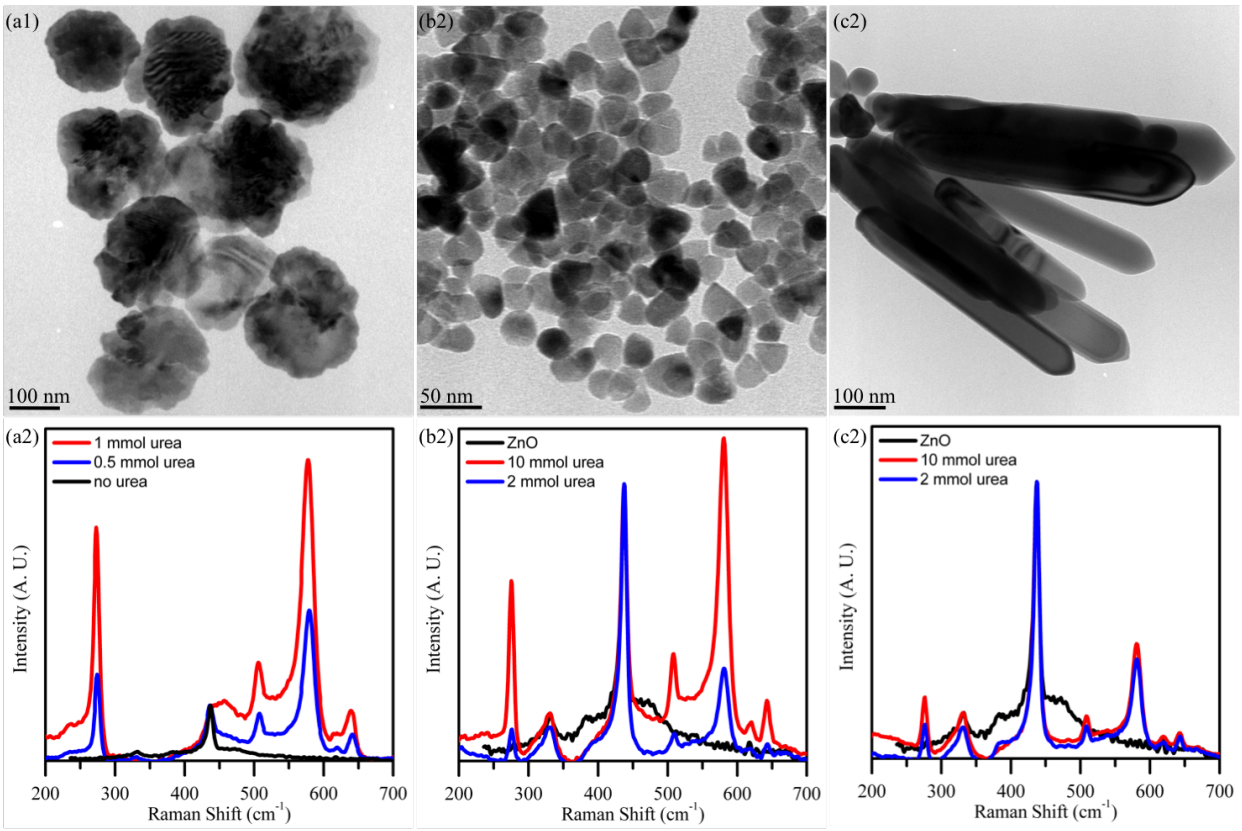

Figure 5.9 TEM and Raman comparing different morphologies and controllable levels N-doping for each. Nanoparticles (a1) are prepared using low concentration of Zn acetate and are able to achieve high levels of N-doping (a2). Prisms (b2) are formed at high concentrations with reduced MWI power and are able to achieve high levels of N-doping (b2). Rods (c1) are formed at high concentrations will full MWI power and have a threshold for N-doping (c2).

The solution route allows for the synthesis of large-scale quantities of homogeneous nanoparticles. Furthermore, this synthetic method allows for N-doping at various concentrations as well as control of morphology of ZnO nanostructures. The morphology of the products was studied by TEM and the N-doping of the three morphologies was studied by Raman spectroscopy. Figure 5.9 shows transmission electron micrographs demonstrating the morphological control of doped ZnO nanoparticles. As previously demonstrated in Chapter 3, morphology of ZnO prepared by MWI is controlled by varying the starting concentration of zinc acetate. The growth of ZnO starting with low concentrations of zinc acetate results in small, nearly spherical ZnO nanoparticles (Fig 5.9A). Increasing the concentration of urea in the

reaction mixture results in an increase in N-doping as previously discussed and the resulting morphology remains consistent (Fig. 5.8). The morphology is not changed by the concentration of urea added to the reaction mixture. At higher concentrations of zinc acetate, the resulting morphology is either prisms (Fig. 5.9-b) or rods (Fig. 5.9-c). Oleylamine acts as a capping agent for ZnO nanoparticles formation. When there is an excess of oleylamine, it caps all surfaces equally and spherical or prism-like particles are formed. Upon increasing the concentration of zinc acetate, oleylamine selectively caps more polar surfaces and rod-shaped particles form. This trend persists in conditions with the addition of urea to the reaction mixture as shown in Figure 5.9. For this experiment, spherical particles form at low concentrations and rod-shaped particles form at high concentrations. Prism-shaped particles are formed at high concentrations when the microwave power is reduced (power 5), and particle formation is slowed. Furthermore, this method allows for the synthesis of three different morphologies of ZnO nanoparticles with controllable N-doping. It is interesting to note that for the rod-shaped particles there is a N-doping threshold that is lower than other two morphologies.

5.8 Characterization of charge carriers via Mott-Schottky measurements

Electrochemical measurements are used generally to find out the type of carriers in resistive systems where Hall measurements are known to give unreliable results. When semiconductor is kept in electrolyte solutions, there is a net charge transfer at interface between electrolyte and semiconductor in order to equilibrate the (electrochemical potential of the both) redox potential of the electrolyte and Fermi level of the semiconductor. In general, for n-type semiconductors at open circuit, Fermi level energy lies above the redox potential of the electrolyte, thus electrons moves form semiconductor to solution where as for p-type semiconductors, electrons moves from electrolyte to semiconductor. Thus, the excess charge on

the surface of the semiconductor extends large distance into the semiconductor (10-1000 nm), and resulting band bending occurs. This region is called as space charge region and has an associated electric field, also called as depletion region due to removal of majority charge carriers. Now this region is considered to be space charge double layer.[174]

Fermi level of the n-type and p-type semiconductors lies just below the conduction band and just above the valence band respectively whereas for intrinsic semiconductors, it lies mid of the band gap. The applied potential alters the Fermi level of the semiconductors and it rises by negative potentials. At a certain applied potential, flat band potential (V_{FB}), there is no net charge transfer between electrolyte and semiconductor. Positive potential of V_{FB} in n-type semiconductors and negative potential of V_{FB} in p-type semiconductor creates the depletion region. Negative potential of V_{FB} in n-type semiconductors and positive potential of V_{FB} in p-type semiconductor creates the accumulation of carriers in semiconductors where it behaves like a metal. The type and number of carriers in the semiconductors are determined by calculating the capacitance as a function of potential in the depletion region.

5.8.1 Mott-Schottky measurements

The electrochemical capacitance were measured (CH instruments electrochemical workstation/ potentiostat software CH660) by using a standard three-electrode configuration with a Pt wire as a counter electrode and Ag/AgCl as a reference electrode and pressed and 300 ^{o}C annealed ZnO pellet as a working electrode with 0.076 cm^2 exposed area. All potentials are reported relative to Ag/AgCl and the electrolyte is a 0.5 M lithium perchlorate in distilled water. CHI potentiostat was used for the measurements and the capacitance is plotted as a function of potential under depletion conditions using Mott-Schottky relationship. Frequencies are used in 3-7 KHz and an AC current of 5 mV.

5.8.2 Mott-Schottkey analysis

Electrochemical impedance studies were carried out in the dark coupled with Mott-Schottky analysis to determine the intrinsic electronic properties, which include type of carriers, carrier density and capacitance in the electrolyte solution in N-ZnO nanostructures. The electrochemical cell used here is a standard three-electrode configuration with a Pt wire as a counter electrode and Ag/AgCl as a reference electrode and pressed and 300 ^{o}C annealed ZnO pellet as a working electrode and $LiClO_4$ is used as an electrolyte. The space charge capacitance can be estimated by Mott–Schottky relationship:

$$1/C^2 = 2/e_0\varepsilon\varepsilon_o N_D[(V-V_{FB})-KT/e_0] \quad 5.1$$

where C is the space charge capacitance, e_0 is the electron charge, N_D the carrier density, ε is the dielectric constant of ZnO**,** ε_o is the permittivity of vacuum, K is the Boltzman constant, T the absolute temperature, V_{FB} is the flat band potential and V is the potential difference across the semiconductor space charge region.

Mott-Schottky plots of bulk ZnO, ZnO nanoparticles and N-ZnO nanoparticles, nanoprisms and nanorods prepared by MWI are given in Figure 5.11. The positive slope in bulk ZnO and ZnO nanoparticles prepared by microwave synthesis confirms the n-type character where as negative slope in the nitrogen doped ZnO nanostructures prove the p-type character. The carrier density of the materials can be calculated from the slope of the Mott-Schottky plot using the following equation:

$$N_D = 2/e_0\varepsilon\varepsilon_o A^2[d(1/C^2)/dv] \quad 5.2$$

from the area of the pellet (A), permittivity of vacuum (ε_o= 8.85 × 10^{-14} F/cm) and known dielectric constant of ZnO (ε = 8.5) carrier density was estimated at 3KHz frequency. The carrier density of ZnO bulk, ZnO nanoparticles, N-ZnO nanoparticles, N-ZnO nanoprisms and N-ZnO

nanorods are respectively $8.5x10^{21}$, $8.4\ x10^{21}$, $3.7\ x10^{23}$, $5.9x10^{19}$ and $1.8\ x10^{21}\ m^{-3}$. Carrier density is comparable to typical ZnO where as carrier density is very low in N-ZnO nanorods due to less nitrogen doping in these structures.

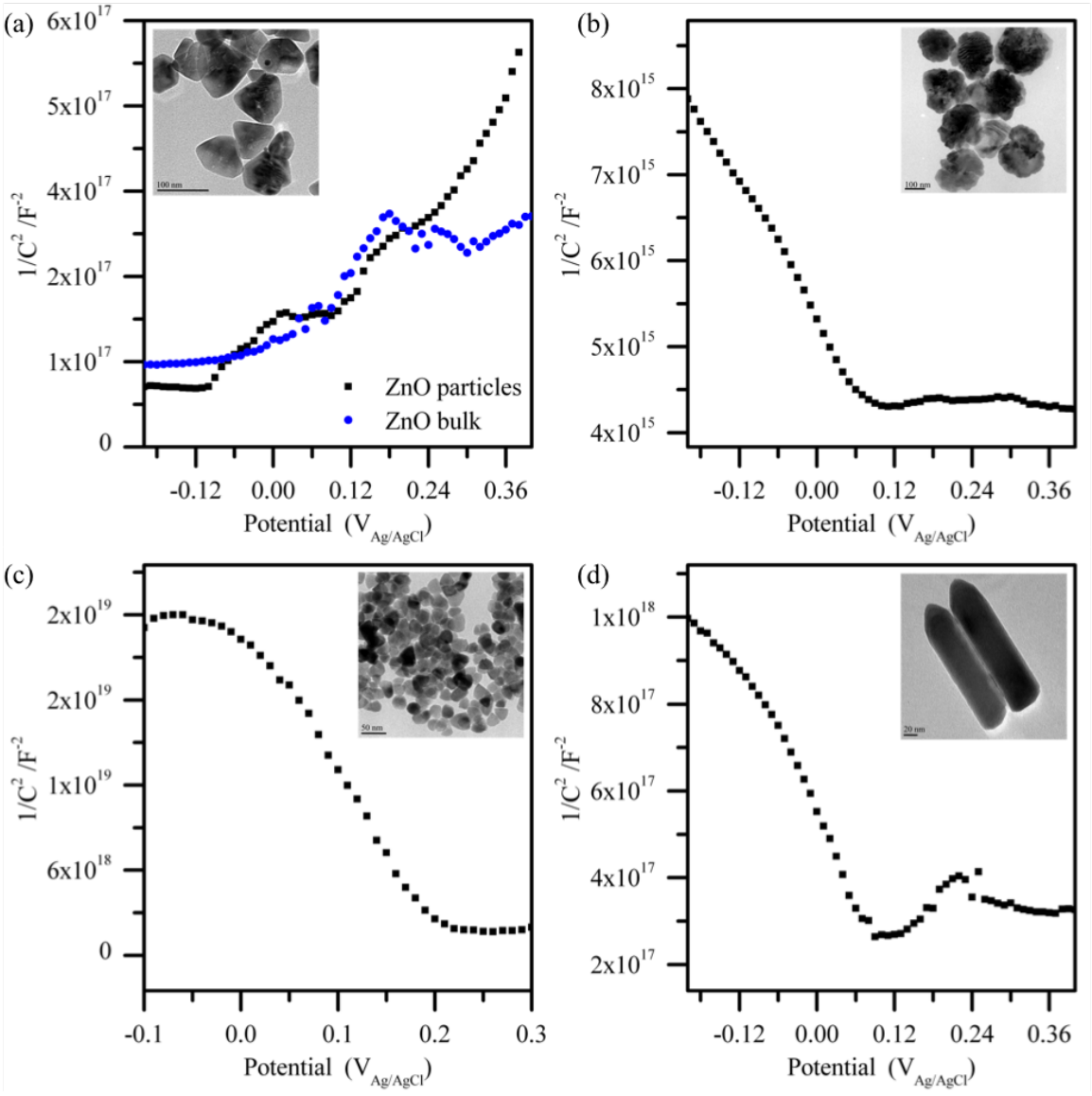

Figure 5.10 Mott−Schottky plots (a) pure ZnO, (b) N-doped ZnO nanoparticles, (c) N-doped ZnO prisms, and (d) N-doped ZnO rods measured in the dark at frequencies of 3 kHz and an AC current of 5 mV.

5.9 Conclusions

This work demonstrates a simple one-step synthesis of N-doped ZnO nanostructures through decomposition of zinc acetate using MWI in the presence of a mixture of OAC, OAM and urea. The rapid decomposition of different concentrations of zinc acetate by MWI in the presence of OAC and OAM results in the formation of ZnO hexagonal nanopyramids or ZnO nano rods. Urea has a high affinity for absorbing MWI, which results in increased reaction temperatures. Therefore, the formation of ZnO nanostructures in the presence of urea requires less MWI times than in the absence of urea under identical reaction conditions. Incorporating urea into the reaction mixture results in N-doping of the ZnO nanostructures. By increasing the concentration of urea, an increase in N-doping is observed using Raman spectroscopy. The N-doped ZnO nanostructures show p-type conductivity as measured by Mott-Schottky measurements. This is of significant importance due to the difficulty of producing stable, p-type ZnO. The N-ZnO may present improved performance in photocatalytic and electronic applications.

Chapter 6: ZnO Supported on Reduced Graphene Oxide

6.1 Introduction

Graphene consists of a hexagonal monolayer network of sp^2-hybridized carbon atoms.[175] The unique properties of this 2-D material include the highest intrinsic carrier mobility at room temperature of all known materials and very high mechanical strength and thermal stability.[176-179] Most of the outstanding electronic properties of graphene can only be observed in samples with high perfection of the atomic lattice since structural defects, which may appear during growth or processing, deteriorate the performance of graphene electronic devices.[176-179]

In addition to the unique electronic properties of graphene, other properties such as high thermal, chemical and mechanical stability as well as high surface area also represent desirable characteristics as 2-D support layers for metallic and bimetallic nanoparticles in heterogeneous catalysis.[180-183] The large surface area (2600 m^2g^{-1}, theoretical value) of graphene and its high thermal and chemical stability make it an excellent candidate for catalyst support applications.[180-183] The high surface area of graphene makes it an excellent candidate as a nanoparticle support that helps prevent aggregation effects. Strong van der Waals interactions between particles lead to aggregation, but particles anchored on graphene remain dispersed on the graphene sheet. Therefore, it is advantageous to support catalytically active nanoparticles on graphene sheets. In addition to reducing catalyst poisoning that occurs by nanoparticle aggregation, catalytic activity

may also be enhanced by catalyst-support interactions. In these cases, structural defects can be useful as they make it possible to tailor the localized properties of graphene to achieve new surface functionalities, which enhance the interactions with the anchored metal nanoparticles.[184, 185]

Several recent reports have demonstrated unusual catalytic activity for metallic and bimetallic nanoparticles supported on the defect sites of the graphene nanosheets.[47, 48, 182, 183, 186-188] In addition to catalysis, other interesting applications of metal and semiconductor nanoparticles supported on graphene include light harvesting,[181, 189] charge separation,[190, 191] H_2 storage and production, biosensing, chemical sensing[192] and electronics.[193, 194]

The study of ZnO nanoparticles deposited on two-dimensional graphene is particularly interesting for understanding the interaction between semiconductor nanoparticles and graphene. It has been suggested that ZnO-graphene composites will have enhanced photocatalytic degradation of organic dyes as a result of electronic interaction between the ZnO and graphene support.[188] Photocatalytic degradation of organic dyes by semiconductor materials occurs though light absorption. In composite materials, when electrons in ZnO are excited by UV light, the graphene support can act as an efficient electron acceptor and hinder the recombination of the charge carriers thus enhancing the redox properties of the nanocompsite in solution. Recent studies have further shown that the electronic properties of the graphene support also play an important role in the photocatatlytic activity of semiconductor nanoparticles supported on graphene.[59]

Microwave irradiation has been demonstrated for the efficient, low temperature synthesis of ZnO nanoparticles.[13, 195, 196] Compared to conventional heating methods, microwave irradiation significantly enhances reaction rates and allows reactions to proceed at lower

temperatures.[89, 90] If the reactant requiring the most heat has the greatest ability to absorb microwaves, selective dielectric heating results in less overall energy required for synthesis.[90] Previous reports show that microwaves enhance organic reactions and lower activation energies.[88] The use of microwave irradiation allows for rapid and uniform heating as well as the ability to control nanoparticle size and shape.[13, 123, 191, 196-200] Furthermore, the use of microwave irradiation in conjunction with organic capping ligands allows for exceptional control over the formation of ZnO nanoparticles.[13, 196, 197]

In this chapter, a simple one-step synthesis of ZnO nanostructures supported on graphene nanosheets via MWI reduction of graphene oxide (GO) in the presence of zinc acetate is studied. In this method, ZnO nanoparticles are formed directly on the graphene nanosheets by the simultaneous reduction of GO and thermal decomposition of zinc acetate in the presence of OAC and OAM by MWI. The high affinity of GO for absorbing MWI results in strong local heating around the graphene oxide nanosheets dispersed in solution.[198] The defect sites created in the reduced graphene oxide (RGO) act as heterogeneous nucleation sites for the nucleation and growth of the ZnO nanoparticles. The photocatalytic activity of the resulting ZnO-RGO nanocomposites for the degradation of malachite green dye is studied and the effect of using RGO as a catalyst support is evaluated in order to understand the enhancement mechanism of the photocatalytic activity of ZnO-RGO nanocomposites.

6.2 ZnO-RGO Composite Synthesis

There are numerous methods for preparation of graphene and chemically modified graphene from graphite derivatives.[201] One approach for the direct growth of a single layer of graphene on a metal substrate is by chemical vapor deposition (CVD).[201, 202] CVD methods result in high quality graphene with few defects but are not practical for synthesizing a large quantity

of material.[201, 202] In order to produce large quantities of graphene with a high number of defects, the method presented here utilizes GO as a starting material for graphene.

GO is typically synthesized by the oxidization of graphite using strong acids and oxidizing agents, which functionalize each graphite layer with oxygen containing functional groups such as esters, carboxylic acids, hydroxyl and carbonyl groups.[201] Graphite oxide is extremely hydrophilic and is readily exfoliated to form suspensions of GO in solution. Dispersions of GO are chemically reduced to removed oxygen moieties resulting in RGO.

In a typical synthesis, GO was prepared from graphite powder using Hummers' method[203] by treatment with strong oxidizing agents ($KMnO_4$ in H_2SO_4), washing with water and drying. A complete preparation method for GO is given in Appendix A. The dried product was suspended in oleylamine (Aldrich, technical grade, 70%) and sonicated using a bath sonicator to disperse GO sheets in OAM.

For the preparation of the supported ZnO nanopyramids supported on RGO, 2 reaction mixtures were prepared: (1) GO reaction mixture and (2) zinc acetate reaction mixture. A reaction mixture of GO dispersed in OAM was prepared by sonication for 1 hour. GO will disperse in OAM only and not a mixture of OAM and OAC. A reaction mixture containing anhydrous zinc acetate dissolved in a mixture of OAC and OAM was was heated in a hot oil bath with stirring at 120 °C. The reaction mixture was heated to dissolve the zinc acetate and remove any residual water from solution. After heating the zinc acetate reaction mixture was cooled to room temperature and the mixture of GO dispersed in OAM was added. Cooling to room temperature was necessary before the addition of GO to prevent the reduction of GO before the formation of the ZnO nanoparticles. Adding the GO prior to heating the reaction mixture to 120 °C results in the reduction of graphene oxide before MWI and formation of ZnO

nanoparticles. The room temperature solution containing zinc acetate in a mixture of OAC and OAM was stirred until a homogeneous light-brown dispersion was obtained, and then MWI was applied using a conventional microwave oven (2.45 GHz) operating at 1000 W. Following MWI for a few minutes, the solution turned black in color indicating the reduction of GO. By continuing the microwave irradiation for 5-10 more minutes, the black color changed to light grey indicating the formation of the white ZnO nanoparticles on the black RGO nanosheets. The dispersion was centrifuged (10,000 rpm for 10 minutes) and the precipitate was separated from the liquid phase and dried at 60 °C overnight.

To make the ZnO-RGO composites dispersed in aqueous solutions, they are transformed to water-soluble composites by changing the surface ligands. Ligand exchange was performed by dissolving 1 g of 11-mercaptoundecanoic acid (MUA) in 5 mL chloroform and adding 10 mg of ZnO-graphene dispersed in OAC and OAM to the chloroform solution. The solution was stirred for 5 hours. 25 mL ethanol, 15 mL chloroform and 0.01 g MUA are added to the particles and centrifuged at 5000 rpm for 10 min. The particles are washed with ethanol and dried at 60 °C overnight. For additional details on ligand exchange, refer to Chapter 3, Section 3.8.

6.3 Reduction of GO by microwave irradiation

First, the reduction of GO by microwave irradiation in the presence of a 1:1 mixture of OAC/OAM was studied. A facile and convenient method for the synthesis of chemically converted graphene sheets from exfoliated GO has been developed using hydrazine hydrate as a reducing agent and microwave heating in an aqueous medium.[198] Liu et al. have previously reported the reduction and functionalization of GO using non-polar organic solvents including oleylamine.[204] In their study, GO was reduced to graphene after heating the GO in the presence of OAM for 24 hours at temperatures up to 100 °C. However, in our experiments, using a

mixture of OAM and OAC in combination with microwave irradiation resulted in a complete reduction of GO in a few minutes.

The first indication that GO is reduced, is a color change from brown to black. A color change was observed following microwave irradiation of the dispersed GO in the OAM/OAC mixture, as demonstrated in Figure 6.1. The resulting black solid indicates the removal of oxygen moieties from GO and formation of the RGO nanosheets. For GO dispersed in water, the absorbance spectrum shows two absorbance bands for π to π^* and n to π^* transitions. Upon reduction, the n to π^* transition is no longer present, which is observed as a color change. This cannot be observed when GO and RGO are dispersed in organic solvents because solvents also absorb in that region. GO is not typically dispersible in non-polar solvents such as hexanes, but following sonication in OAM and stirring in the presence of oleic acid, the GO becomes coated with the fatty acid and hence it can be dispersesd in hexanes.

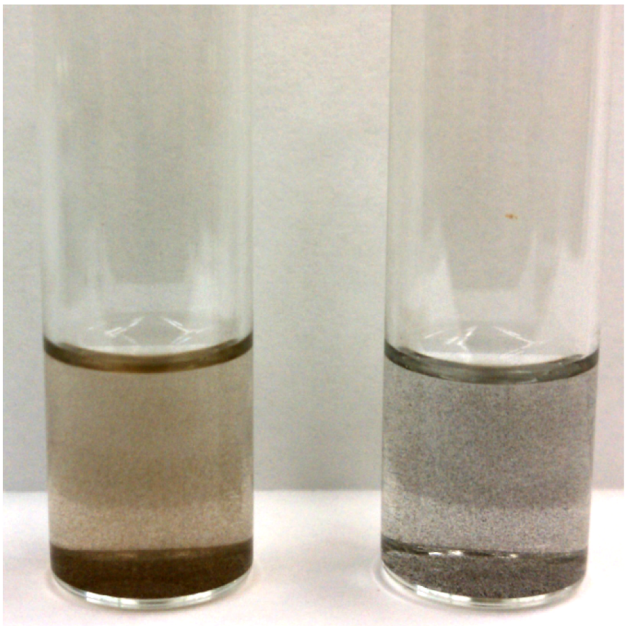

Figure 6.1. GO dispered in OAM and diluted with hexanes (left). RGO dispersed in hexanges (right).

Further detailed analysis of the nature of the RGO is studied through Raman spectroscopy. Raman spectroscopy is a well-known sensitive tool for characterizing graphene. Few layer graphene typically show two Raman bands: G band and D band. Single layer graphene shows a third Raman band, 2D. In single layer graphene, the 2D band arises due to double resonance processes. The Raman G band at ~1580 cm^{-1} is due to the doubly degenerate zone center E2g and is characteristic of the sp^2 carbon network.[205] The Raman D band at ~1350 cm^{-1} arises as a result of defects in the graphene structure and only appears in samples with a significant amount of defects or on the edges of pristine graphene sheets.[205] Therefore, the ratio of the intensity of the Raman D and G bands is used to compare the relative number of defects in each sample. The Raman spectra of GO and RGO are given in Fig. 6.2. The ratio of intensities of the D band with respect to the G band increases slightly with the reduction of GO, from 0.96 to 1.0, which implies that the reduction using OAM leads to a higher number of defects in the graphene structure.

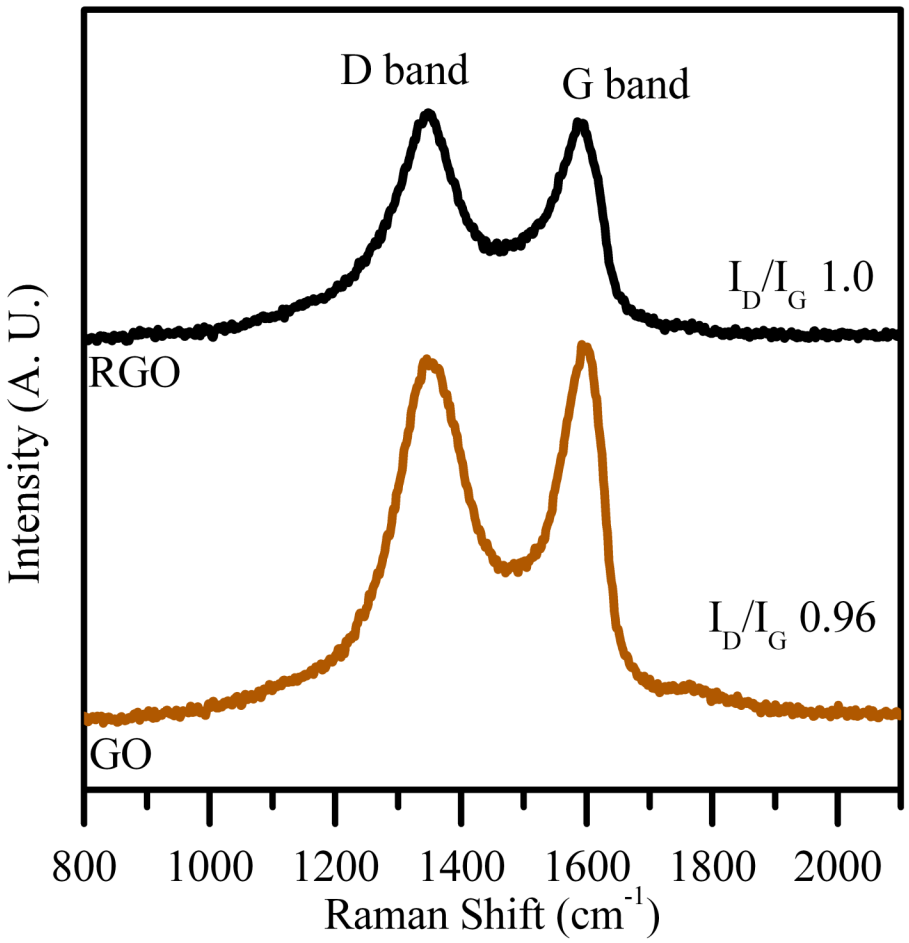

Figure 6.2. Raman spectra of GO and RGO prepared by MWI in the presence of OAM. Both spectra show the D-band and G-band for graphene.

X-ray diffraction is utilized to confirm the reduction of GO to RGO prepared by MWI in the presence of OAM, Figure 6.3. XRD of GO shows a strong peak at 12 degrees, which is consistent with d-spacing of 7.43 Å of the 001 diffraction peak.[206] XRD of RGO after MWI shows a broader peak with reduced intensity at 20 degrees, which corresponds to a decrease in the interlayer spacing. Thus, the shift of the diffraction peak to higher degrees is consistent with decreased interlayer spacing as a result of removal of oxygen moieties.

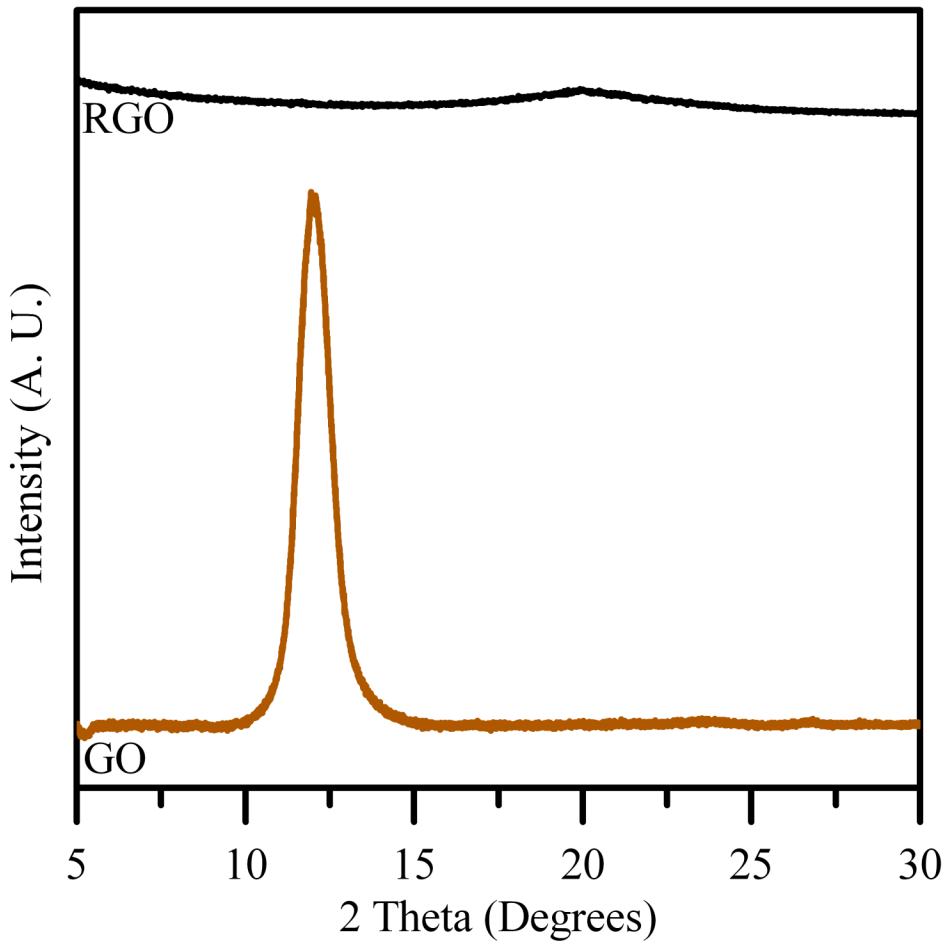

Figure 6.3. XRD of GO and RGO prepared by MWI in the presence of OAM.

6.4 ZnO-reduced graphene oxide composites

The formation of ZnO nanoparticles supported on RGO (ZnO-RGO) was studied through the simultaneous reduction of GO and the decomposition of zinc acetate via MWI. In this approach, zinc acetate and GO in the presence of 1:1 molar ratio of OAC/OAM were combined in a single test tube prior to MWI (using a 1000 W MW oven). GO has a high affinity for absorbing MWI, and therefore, the reaction mixture heats up rapidly in the presence of GO. As a result, there is a significant local heating around the GO sheets in solution, and therefore, it is hypothesized that the nucleation and growth of the ZnO nanoparticles are more likely to take place on the defect sites created in the RGO nanosheets. This is further supported by the

observation that the majority of the ZnO nanoparticles are found directly adsorbed on the RGO nanosheets. The near absence of free ZnO nanoparticles indicates that most of the nanoparticles are preferentially attached to the RGO sheets. Chapter 3 previously demonstrated that ZnO nanoparticles synthesized by this method in the absence of GO require long microwave times of 10-15 min MWI and reach temperatures of 214 °C (after 10 min MWI at 1000 W).[13] Upon the addition of GO, ZnO nanoparticles form after 5 min MWI and the solution temperature exceeds 250 °C (after 10 min MWI at 1000 W). This temperature is similar to the temperature of 246 °C recorded for the GO solution in the absence of zinc acetate after 10 min MWI at 1000 W. Therefore, the affinity for GO to absorb microwaves is responsible for increasing the temperature of the solution, which enhances the nucleation and growth of the ZnO nanoparticles on the surface defects of the RGO nanosheets.

The UV-Visible absorption spectra of the resulting ZnO-RGO composites at different MWI times are shown in Figure 6.4(a). The ZnO-RGO has a strong absorbance band at 370 nm similar to the free ZnO nanoparticles prepared in the absence of GO as shown in Chapter 3. There is also a low-energy tail observed in all spectra, which is attributed to a combination of light scattering from ZnO nanoparticles as well absorbance of the RGO, which is black in solution. The absorption band of the ZnO slightly red-shifts with increasing microwaving time consistent with the formation of larger ZnO nanoparticles on the RGO sheets with increasing MWI times. Note that at shorter MWI times (5 min or less), the absorption band of ZnO nanoparticles is not observed since the particles' size is too small to exhibit significant absorption of the ZnO crystals.

The XRD data of the ZnO-RGO nanocomposite prepared after 10 min MWI, shown in Figure 6.4(b), display the typical hexagonal wurtzite crystal structure of bulk ZnO crystals.[13, 196]

There is also a broad peak at 2θ value of 20 °, which is attributed to the presence of a few graphene layers. This peak appears broader, less intense and at lower 2θ compared to the XRD pattern of graphite.[198] This is attributed to van der Waals forces causing uneven disordered stacking of the graphene layers.[204]

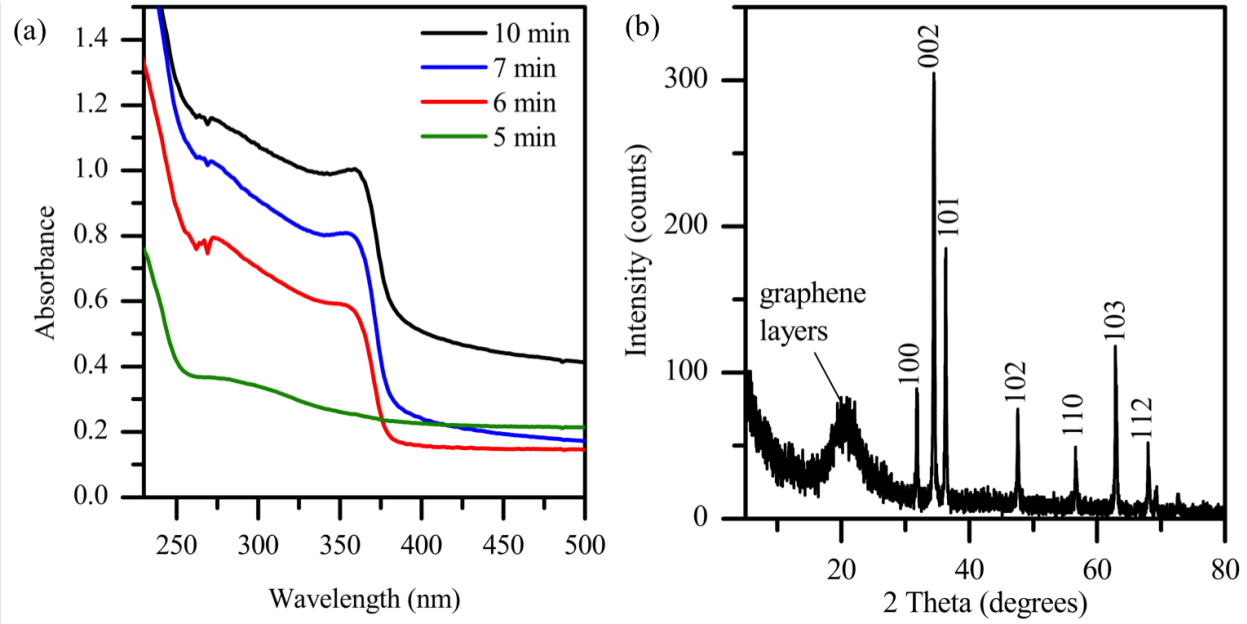

Figure 6.4. (a) Absorption spectra of ZnO supported on RGO obtained at different MWI times. (b) XRD for ZnO supported on RGO after 10 minutes of microwave irradiation.

It was observed that the size of the resulting ZnO nanoparticle is dependent on the microwave time. Shorter microwave time results in smaller particles, whereas increasing the microwave time increases the particle size, which is analogous to conventional heating methods. The effect of increased particle size with increasing MWI times is further supported by TEM images of the particles after 6 and 10 min MWI as shown in Figure 6.5. Figure 6.5(a) shows that the ZnO nanocrystals supported on the RGO sheets after 6 min MWI have an average particle size in the range of 25-30 nm. A significant increase in the particle size is observed after 10 min MWI as shown in Figure 6.5(b) where the average particle size is around 60 nm. It should be noted that using 0.05 M zinc acetate with a 1:1 molar ratio of OAC/OAM produces ZnO

nanoparticles with hexagonal pyramidal shapes at all MWI times.[13] Therefore, MWI times only affect the particle size, but have no impact on the particle morphology.

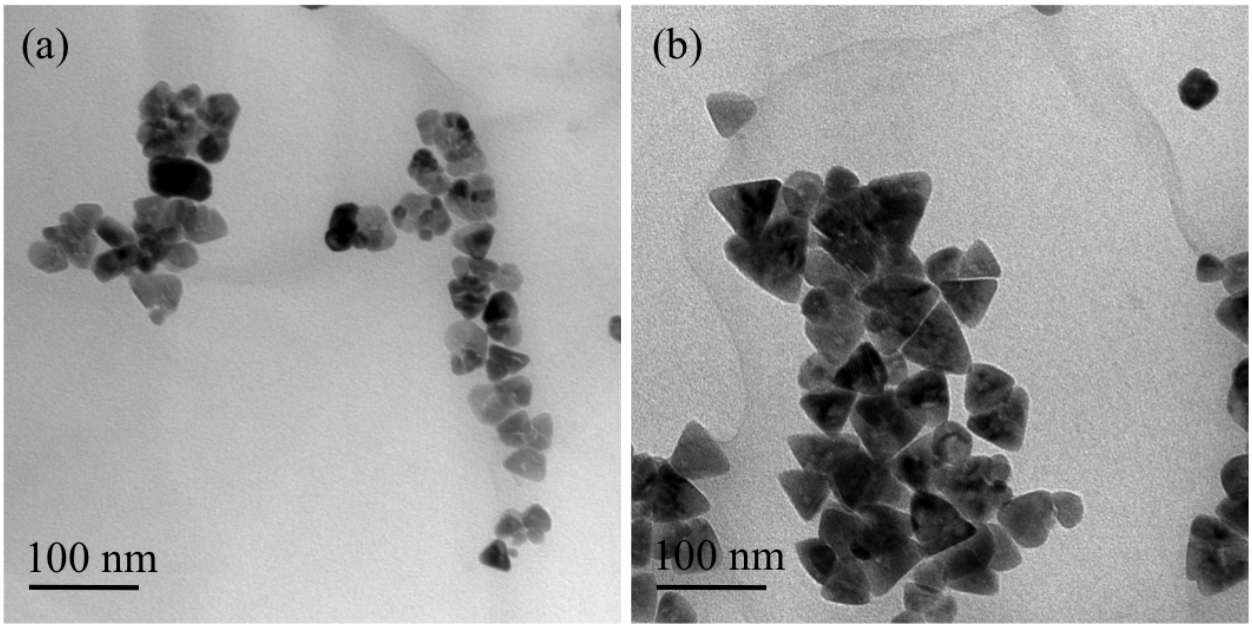

Figure 6.5 TEM images of ZnO supported on RGO from a reaction mixture containing1 mg/mL GO and 0.05 M zinc acetate using 1:1 molar ratio of OAC/OAM after various MWI times (1000 W): (a) 6 min and (b) 10 min.

The growth evolution of the ZnO nanopyramids on the RGO nanosheets has been investigated by changing the MWI power for the same reaction mixture over a fixed reaction time (10 min). The strong dependence of the final ZnO nanoparticle morphology on decomposition temperature of zinc acetate has been previously reported.[13, 85] Since MWI rapidly decomposes zinc acetate, the degree of ZnO supersaturation is strongly dependent on MWI power. Figure 6.6 displays representative TEM images of ZnO-RGO after MWI at various powers. It should be noted that the final temperatures of the reaction mixtures immediately following the 10 min MWI were found to be 138, 209, 220, 227, 235 and 250 °C at the MWI powers of 500, 600, 700, 800, 900 and 1000 W, respectively.

The first sign of ZnO growth, after 10 min of MWI at a power of 600 W is shown in Figure 6.6(a). This TEM image shows that there are only few fully formed ZnO hexagonal

nanopyramids, and many very small aggregates of ZnO nanoparticles exist. At low MWI powers, small flower-shaped ZnO clusters appear on the RGO sheets. As shown in Fig. 6.6(a), the overall ZnO nanoflowers are smaller than 50 nm in diameter, and they consist of several smaller segments. Increasing MWI power slightly, Fig. 6.6(b), to 700 W results in a high density of ZnO nanoflowers, but does not lead to a significant increase in the size of the overall nanoflower or to a change in the morphology of the petals. The observation of very small ZnO nanoparticles forming at lower MWI powers is consistent with our hypothesis that there regions of localized heating (hot spots) on the surface of the RGO. As MWI powers increases, the ZnO nanoclusters continue to grow to form ZnO nanopyramids as shown in Figs. 6.6(c) and 6.6(d). At intermediate MWI power of 800 W, Fig. 6.6(c), the ZnO nanoparticles begin to take on a more pyramidal shape, but the edges of the pyramids remain undefined. After 10 minutes MWI at full power (1000 W), the ZnO nanopyramids show a well-defined structure with a hexagonal base. On the basis of these observed changes in particle size and morphology, the degree of heating, which can be controlled by the MWI power, has the most significant effect on determining the growth rate, size and morphology of the ZnO nanoparticles.

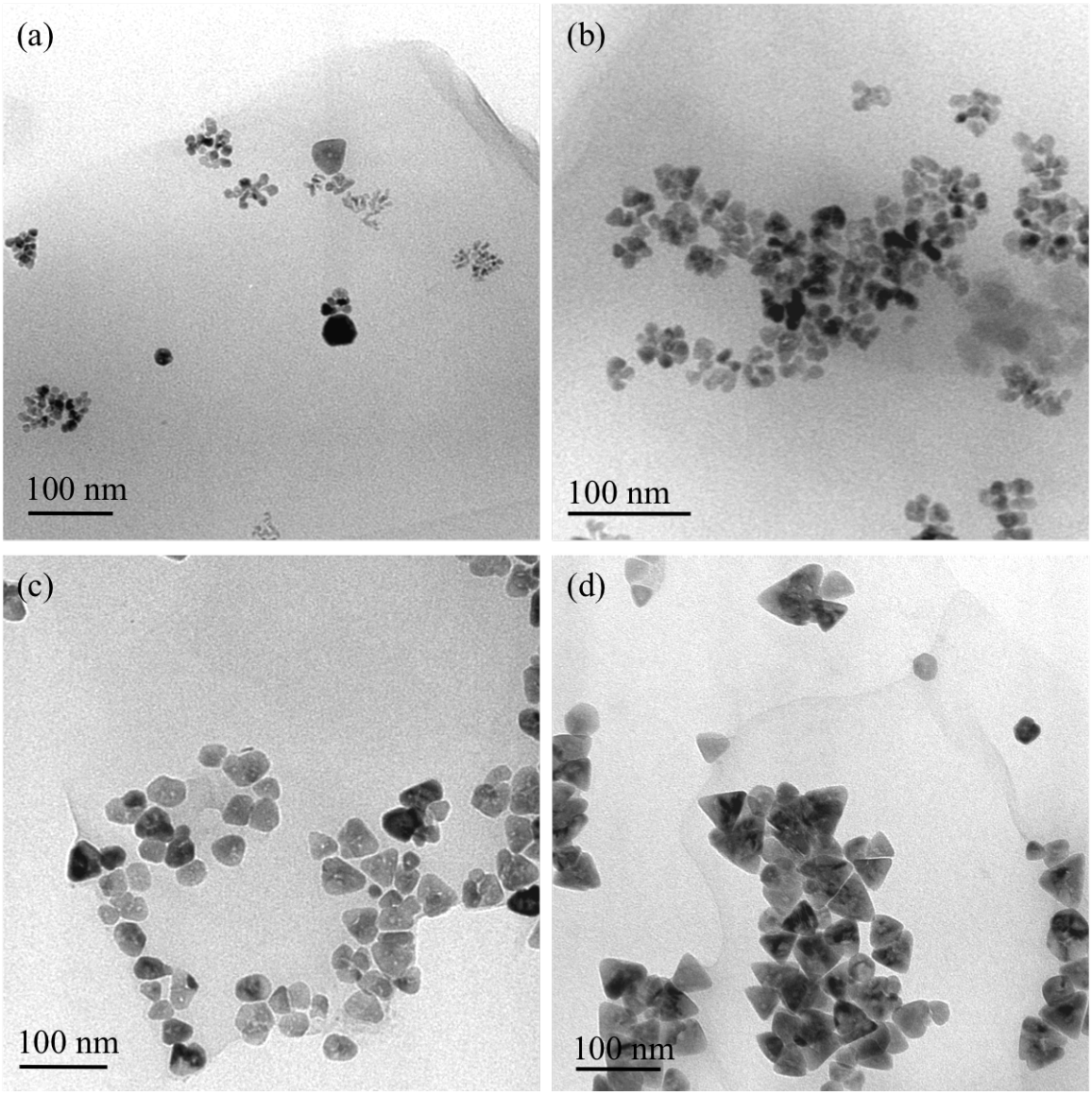

Figure 6.6 TEM images of ZnO supported on RGO from a reaction mixture containing 1 mg/mL GO and 0.05 M zinc acetate using a 1:1 molar ratio of OAC/OAM after 10 min MWI at different MW powers (a) 600 W (209 °C), (b) 700 W (220 °C), (c) 800 W (227 °C), and (d) 1000 W (250 °C).

To obtain information on the number of RGO layers supporting the ZnO nanopyramids, analysis was carried out on several TEM images of the supported ZnO nanoparticles as shown in Fig. 6.7. The image analysis indicates that most of the particles are supported on a few RGO nanosheets with bilayers and five or more layers representing the majority of the sample. The analysis reveals that the overall distribution of RGO nanosheets ranges from one to eight layers.

The TEM images also show that most of the RGO layers are folded on one edge and that the ZnO nanoparticles are more concentrated around the edges of the layers. These results are consistent with a previous report on the microwave synthesis of RGO using hydrazine hydrate as a reducing agent for GO.[198]

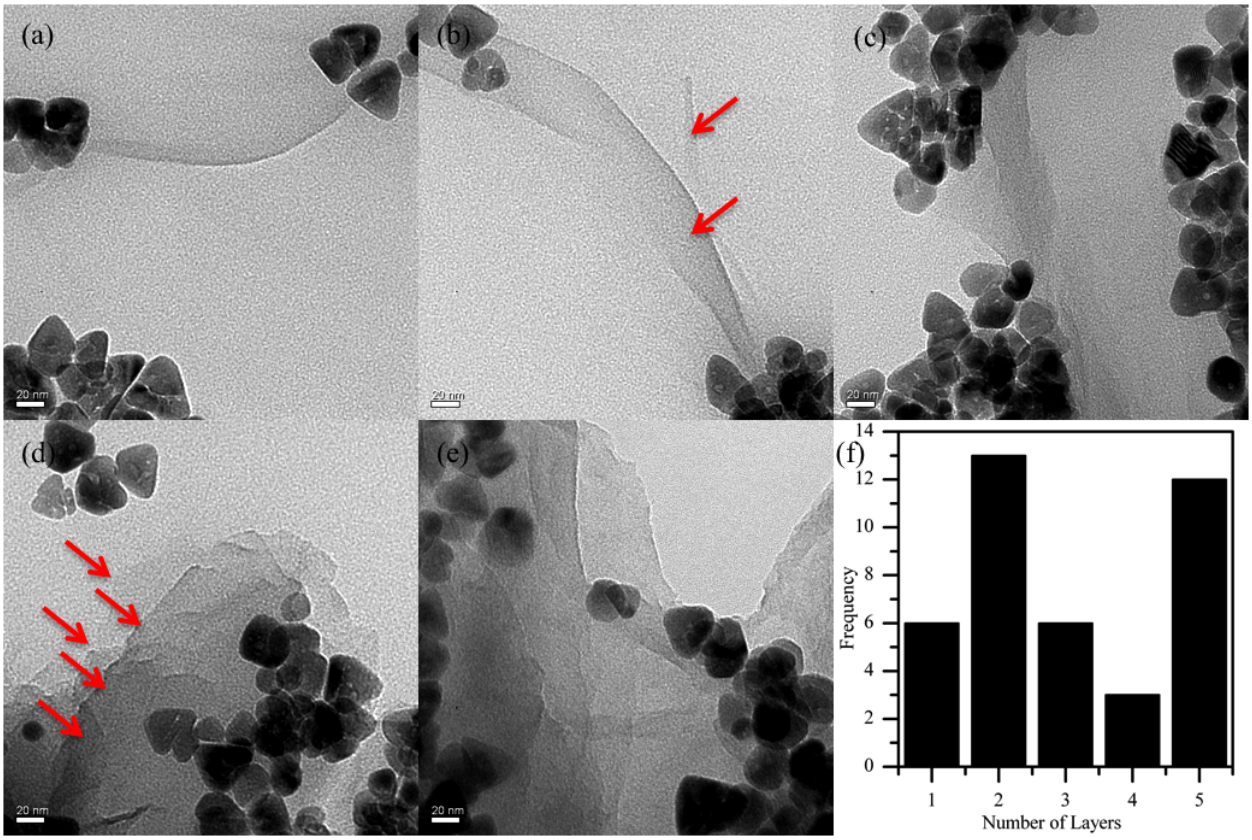

Figure 6.7 TEM images of ZnO supported on a few layers RGO nanosheets. The red arrows indicate individual RGO nanosheets.

To study the reduction of GO to RGO and the formation of the ZnO nanoparticles, the XPS binding energies for the C 1s, O 1s and Zn 2p regions were measured as shown in Figure 6.8. For the C 1s region, Figure 6.8(a), there is a single peak at 285 eV that can be assigned to the C 1s electron in C-C species.[207] There are no additional peaks at higher binding energies that would indicate the presence of carbon associated with oxygen on the composite surface. Therefore, MWI in the presence of the OAM/OAC mixture reduces the oxygen moieties on the surface of GO resulting in RGO. The oxygen 1s region, Figure 6.8(b), shows a peak at 530 eV

attributed to O^{2-} species with a shoulder at higher binding energy consistent with the O 1s in ZnO.[104] The appearance of this peak is a result of O^{2-} in oxygen group vacancies in the ZnO structure The shoulder at higher binding energies is attributed to several subspectral components including ZnO, and oxygen deficiencies.[4] The observed shoulder at 531.5 eV is attributed to Zn-OH from adsorbed OH groups on the surface. The peak positions of Zn $2p_{1/2}$ and $2p_{3/2}$, Figure 6.8(c), in the ZnO-RGO composite are consistent with the standard values and those of ZnO nanoparticles alone.[13] The XPS data thus confirms that the Zn exists mainly in the Zn^{2+} state in both the ZnO nanoparticles and in the ZnO nanoparticles supported on the RGO nanosheets.

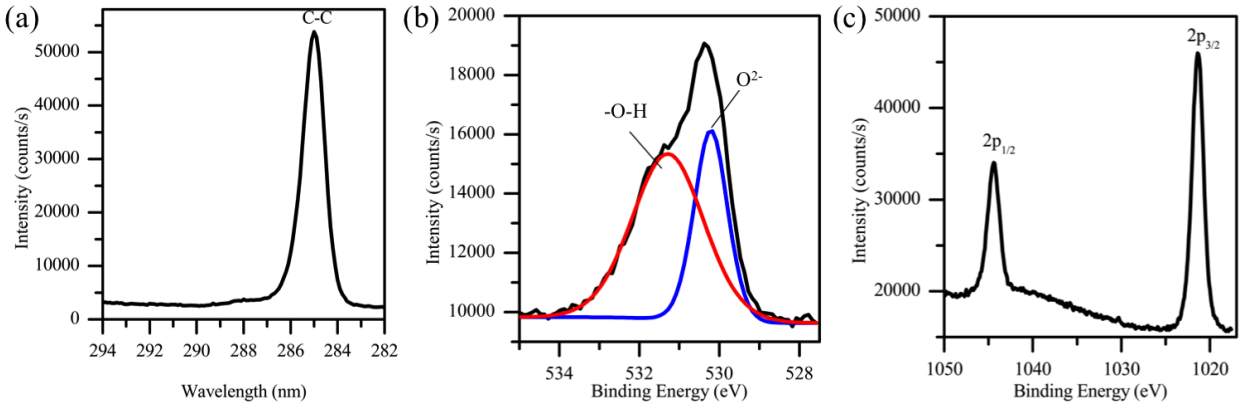

Figure 6.8 XPS binding energies of the C 1s, O 1s and Zn 2p electrons in the ZnO-RGO nanocomposites prepared using a reaction mixture containing 1 mg/mL GO and 0.05 M zinc acetate in a 1:1 molar ratio of OAC/OAM after 10 min MWI.

Raman spectroscopy is used to further characterize the ZnO-RGO composites because both ZnO and graphene exhibit Raman bands. Few layer graphene typically shows 2 Raman bands, G band and D band, as discussed previously. Figure 6.9 shows Raman spectrum for ZnO-RGO nanocomposites. In this spectrum, D and G bands are observed from few layer graphene and the appearance of new peaks at lower wavenumbers, which is attributed to ZnO. ZnO shows characteristic bands at 330 and 437 cm^{-1} with the peak at 437 cm^{-1} being the most intense.[102] The peaks at 330 and 437 are attributed to vibration modes 2E2(M) due to multiple-phonon-scattering processes and E2(high) from O atom, respectively.[102] Thus, both the ZnO

Raman signal and the RGO Raman signal are observed. For the carbon region, a I_D/I_G ratio of 1.3 was observed. This compares to a ratio of 1.0 for RGO, which indicates a large number of defects in the RGO lattice.

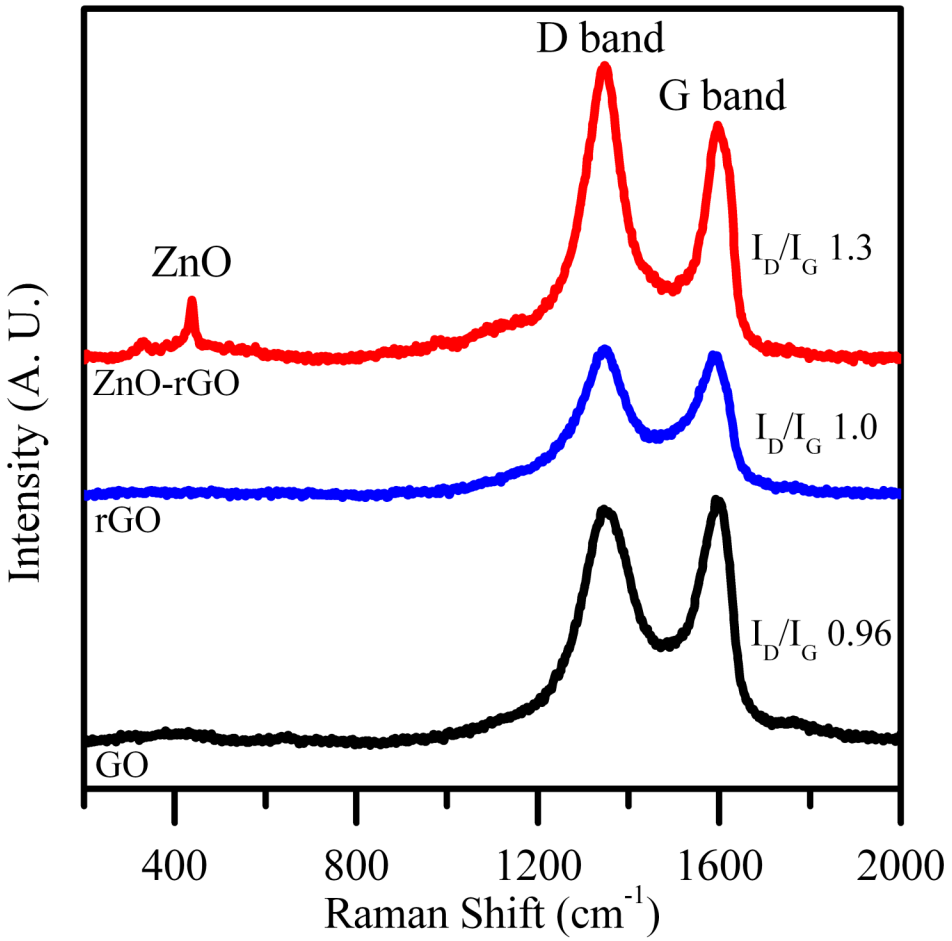

Figure 6.9 Raman spectra for GO, rGO and the ZnO-RGO nanocomposites prepared using a reaction mixture containing 1 mg/mL GO and 0.05 M zinc acetate in a 1:1 molar ratio of OAC/OAM after 10 min MWI.

The photocatalytic degradation of malachite green (MG) under UV irradiation was used to evaluate the photocatalytic performance of ZnO-RGO, as shown in Figure 6.10. Malachite green is a strongly absorbing organic dye with an absorption band in the visible region at 617 nm. Since absorbance is related to concentration, absorbance is used to follow degradation of malachite green in solution as a function of UV irradiation time. It was observed that the

concentration of malachite green is not reduced under UV light irradiation in the absence catalyst (results not shown). As shown in Fig. 1.10(a-b), when the photocatalyst is present, the UV-Visible absorption peak of malachite green at 617 nm decreases in intensity as the UV light irradiation is applied to the solution. Prior to UV irradiation, the dye solution is stirred with the catalyst particles to allow dye molecules to adsorb onto the catalyst surface and to achieve

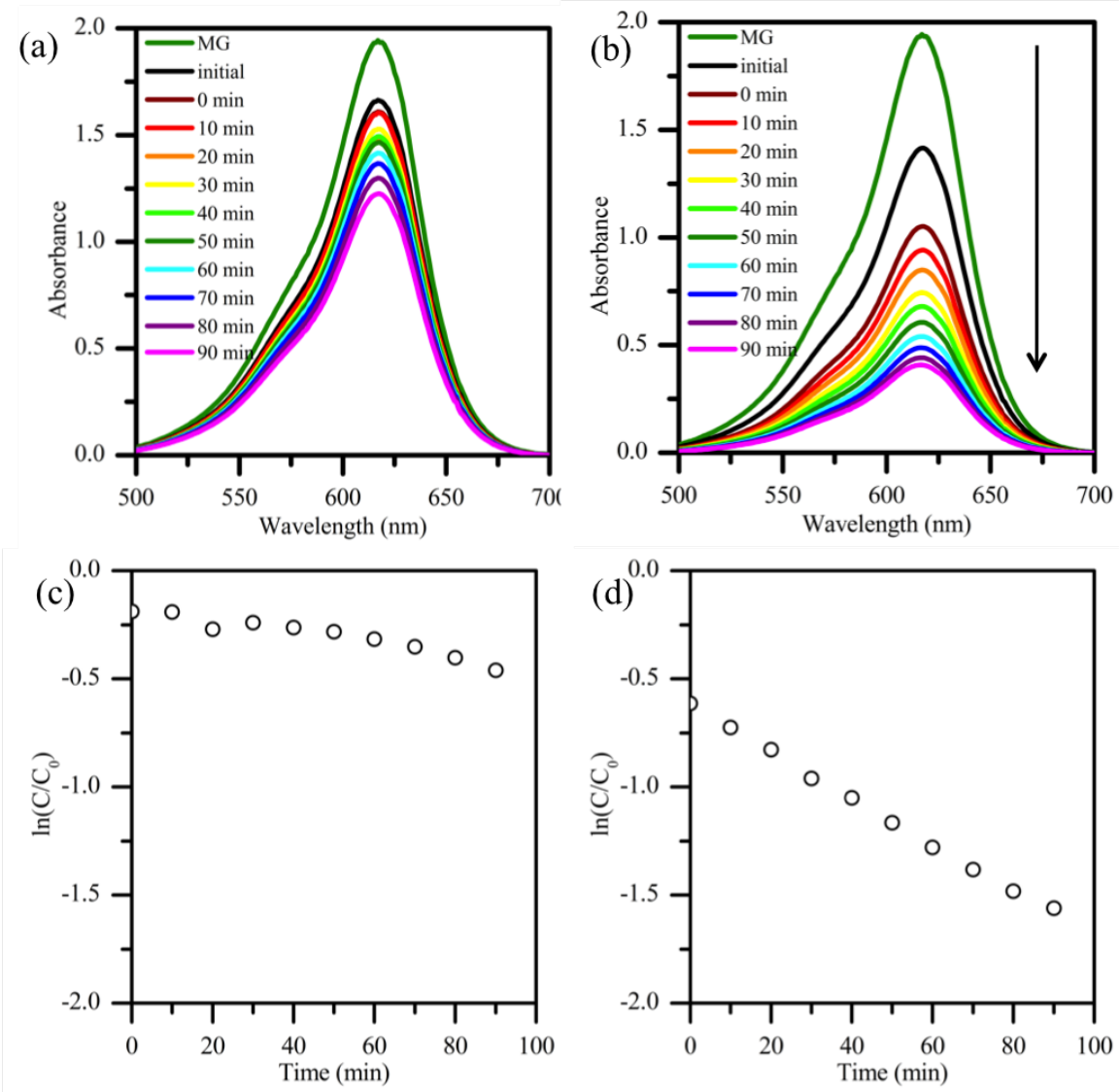

Figure 6.10 Absorption spectra of malachite green after various times of constant UV irradiation in the presence of (a) ZnO nanoparticles and (b) ZnO supported on RGO prepared by MWI. Graphs showing the degradation of malachite green plotted as $\ln(C/C_0)$ as a function of UV irradiation time using (c) ZnO nanoparticles and (d) ZnO-RGO nanocomposites.

adsorption-desorption equilibrium; this step resulted in a decrease of the dye concentration. ZnO nanopyramids, Fig. 6.10(a), have a degradation efficiency of 49% after 90 min. This compares to a degradation efficiency of 78% after 90 min for the ZnO nanopyramids supported on the RGO nanosheets as shown in Fig. 6.10(b).

The photocatalytic degradation of MG dye by ZnO obeys pseudo-first-order kinetics. The rate expression for MG dye concentration is given by $\frac{-d[C]}{dt} = k'[C]$ where k' is the pseudo-first-order rate constant. Integration of the rate expression gives $\ln\frac{C}{C_0} = -k't$ where C_0 is the initial concentration of dye and C is the concentration at time t. Plot of $\ln(C/C_0)$ as a function of t for photodegradation using both ZnO and ZnO-RGO photocatalysts are shown in Figs. 6.10(c) and 6.10(d). A linear relationship between the dye concentration and irradiation time was observed where the slope was taken to be the rate constant. ZnO nanopyramids supported on the RGO nanosheets have an increased rate constant over the free ZnO nanopyramids for the photodegradation of the MG dye.

The enhanced photocatalytic activity from supporting the ZnO on RGO can be attributed to both the fixed placement of the ZnO particles and the electronic structure of the composite. As mentioned earlier, ZnO has the ability to transfer photogenerated electrons to graphene upon irradiation with UV light. Therefore, the photogenerated electron has a lower incidence of recombining with the hole left in the valence band. This hole then initiates an oxidative pathway that leads to the degradation and mineralization of the MG. Thus, supporting ZnO directly on RGO enhances the photocatalytic activity.

The transfer of photogenerated electrons from ZnO nanoparticles to carbon materials such as carbon nanotubes and graphene (Figure 6.11) has been reported by mixing prepared ZnO

nanoparticles with carbon materials.[188] This transfer of electrons from ZnO to graphene prevents electron-hole recombination and thereby increases photocatalytic activity.

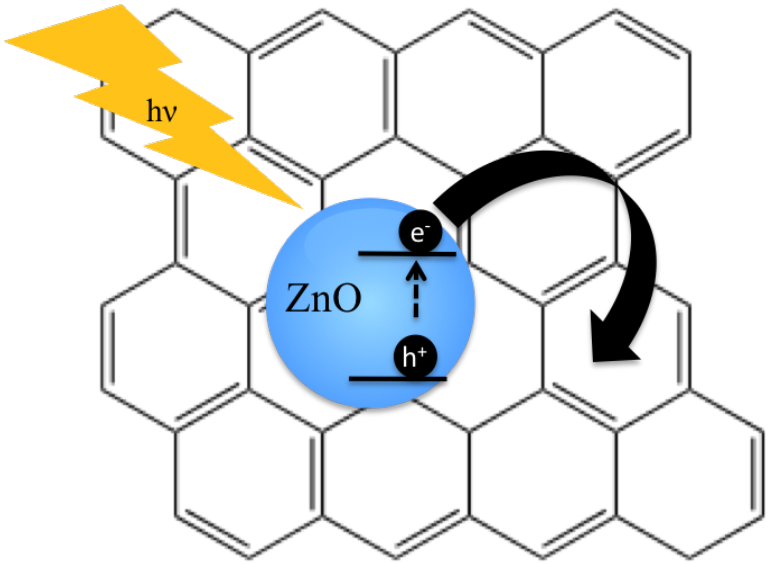

Figure 6.11 Charge separation and transfer of the photogenerated electrons in ZnO to graphene following the bandgap excitation of ZnO nanoparticles.

6.5 Shape controlled ZnO supported on RGO

Thus far it has been demonstrated that photocatalytic activity is enhanced when ZnO is supported on RGO. It has been demonstrated in Chapter 3 that photocatalytic activity is also dependant on ZnO morphology with rods showing the greatest activity for the degradation of MG. Therefore, it is expected that photocatatlytic activity should be further enhanced using ZnO rods supported on graphene. In this section, MWI synthesis and characterization of shape controlled ZnO supported on RGO is studied. Photocatalytic degradation of MG as a function of morphology of ZnO-RGO is also studied.

As previously reported in Chapter 3, ZnO morphology is strongly dependant on the concentration of zinc acetate relative to OAC and OAM. Low concentrations of zinc acetate produce hexagonal nanopyramids, and higher concentrations of zinc acetate yield rod-like

nanostructures. Thus, preparing the ZnO-RGO nanocoposities using varying concentrations of zinc acetate allows for morphology of the ZnO nanoparticles supported on RGO. The reaction conditions of shape controlled ZnO supported on RGO are given in Table 6.1. According to Xu et al., 2 wt% graphene with ZnO is the best condition for photocatalysis.[48] Therefore, the amount of GO in the reaction mixture was varied to produce composites with 2 wt% RGO assuming 100% decomposition of zinc acetate to ZnO.

Table 6.1 Summary of experimental conditions for synthesis of shape controlled ZnO supported on RGO.

Zinc acetate (mmol)	GO (mg)	Oleic acid (mmol)	Oleylamine (mmol)	Temperature (°C)
5	8	10	25	283
10	16	10	25	309
20	33	10	25	329
30	45	10	25	331
40	65	10	25	333

The UV-Visible absorption spectra of the resulting ZnO-RGO composites prepared using varying amounts of zinc acetate are shown in Figure 6.12. As expected, the ZnO-RGO displays a strong absorbance band at 370 nm. All spectra also display a low-energy tail, which is corresponds to a combination of light scattering from ZnO nanoparticles and absorbance of the black RGO.

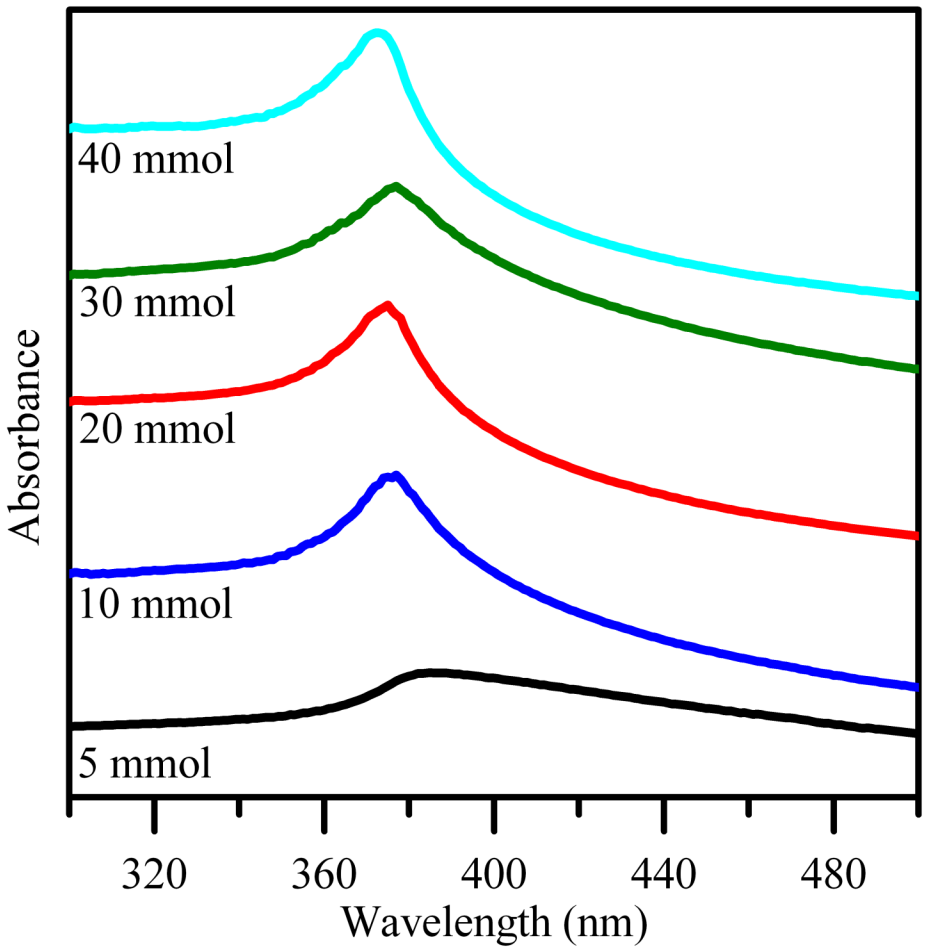

Figure 6.12. Absorption spectra of ZnO supported on RGO prepared using varying amounts of zinc acetate.

XRD data of the shape controlled ZnO-RGO nanocomposites prepared using varying concentrations of zinc acetate are shown in Figure 6.13. Each spectrum indexes to the typical hexagonal wurtzite crystal structure of bulk ZnO crystals.[13, 196] For ZnO-RGO nanocomposites prepared using 5 mmol of zinc acetate, a broad peak at 2θ value of 20 ° is observed. This broad peak corresponds to the presence of a few layers of RGO. This peak appears broader, less intense and at lower 2θ compared to the XRD pattern of graphite.[198] This is attributed to van der Waals forces causing uneven disordered stacking of the graphene layers.[204] For ZnO-RGO

nanocomposites prepared using more than 5 mmol of zinc acetate, no diffraction peak for RGO is observed. This is consistent with the reduction of GO and no restacking of the RGO sheets.

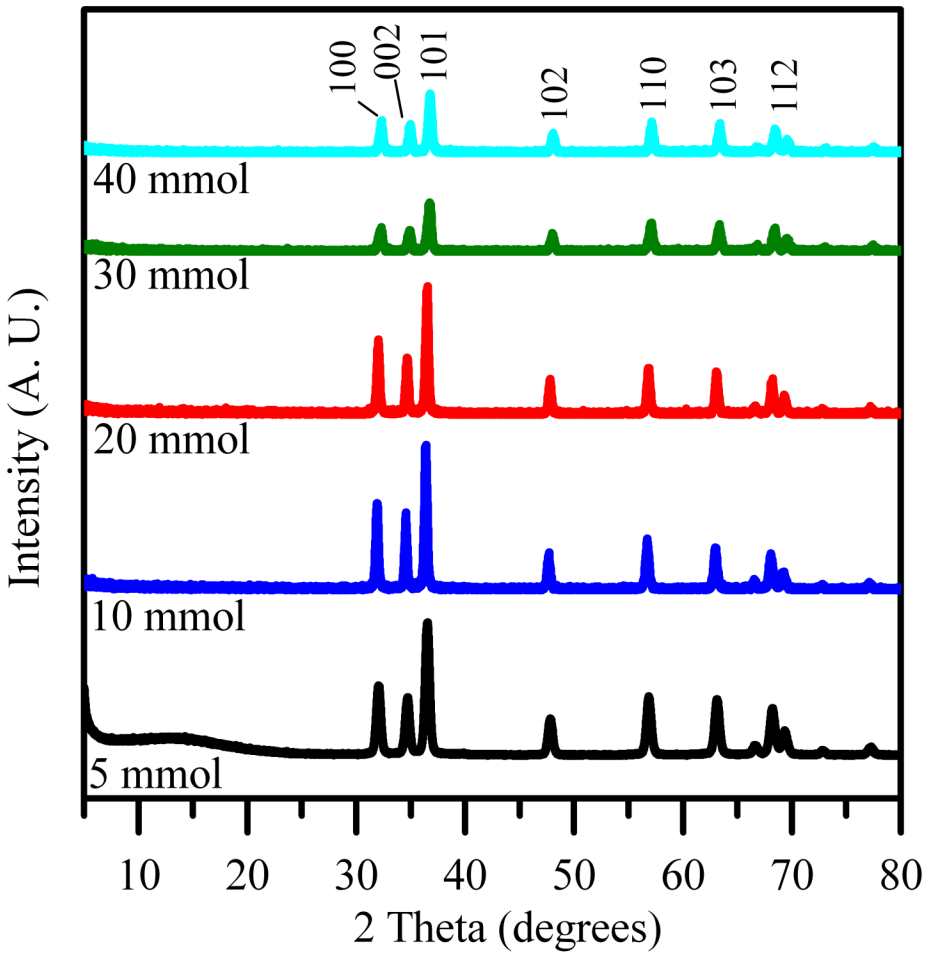

Figure 6.13 XRD for ZnO supported on RGO prepared using varying concentrations of zinc acetate.

The ZnO-RGO composites were further characterized by Raman spectroscopy, which has characteristic bands for both ZnO and RGO. Raman spectra for ZnO-RGO composites prepared with zinc acetate concentrations ranging from 5-40 mmol are presented in Figure 6.14. The ZnO-RGO composites prepared using different concentrations of zinc acetate exhibit 4 Raman bands. ZnO peaks are observed at 330 and 437 cm^{-1}, which are attributed to vibration modes 2E2(M) due to multiple-phonon-scattering processes and E2(high) from O atom, respectively.[102] This

further confirms the formation of ZnO. RGO exhibit the expected G and D bands. Each ZnO-RGO composite shows a strong D band relative to the G band, indicating a large number of defects are present in the RGO of each sample.

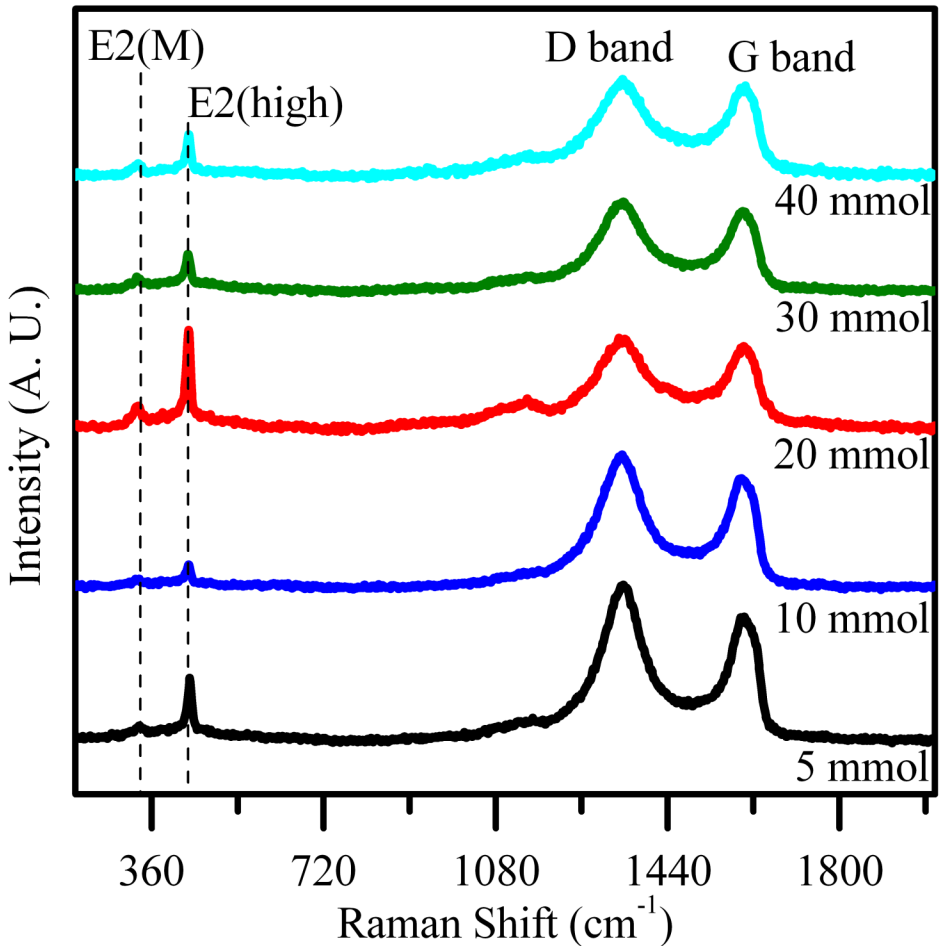

Figure 6.14 Raman spectra for ZnO supported on RGO prepared using varying concentrations of Zn acetate.

Morphology control of the ZnO nanostructures on the RGO nanosteets has been investigated by changing the concentration of zinc acetate. The strong dependence of the final ZnO morphology on zinc acetate concentration has previously been reported in Chapter 3. Lower concentrations of zinc acetate result in nanopyramids, whereas increases the zinc acetate concentration results in rod-shaped nanoparticles. Since the nanostructure growth is controlled

through the use of capping agents, OAC and OAM, the morphology is strongly dependent on the concentration of zinc acetate relative to OAC and OAM.

The effect of particle morphology with Zn acetate concentration is further supported by TEM images of the particles prepared from 5-30 mmol zinc acetate as shown in Figure 6.15. Figure 6.15(a) shows that ZnO nanocrystals supported on the RGO sheets prepared using 5 mmol zinc acetate with an average particle size in the range of 50-60 nm. At intermediate zinc

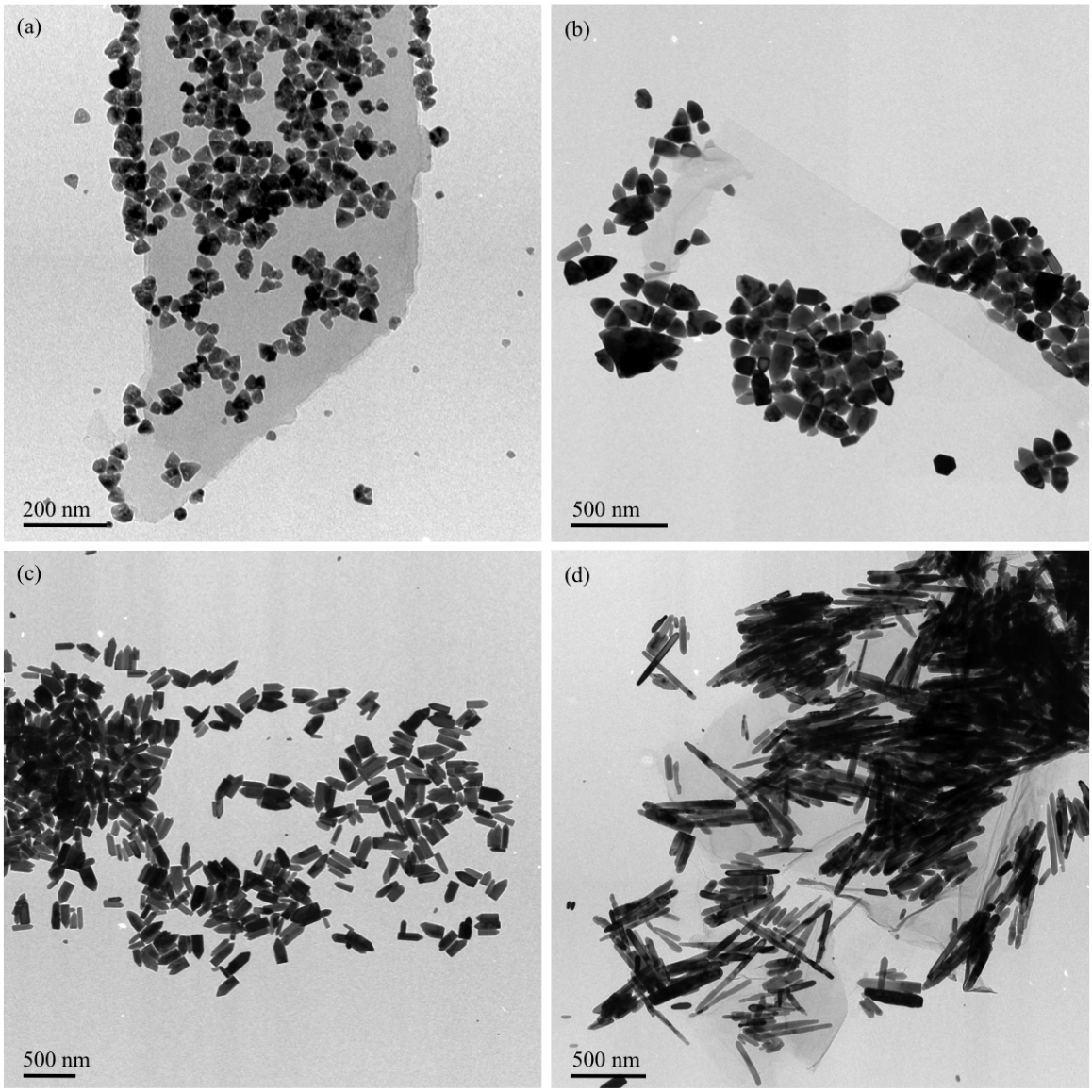

Figure 6.15 TEM images of ZnO supported on RGO from a reaction mixture containing (a) 5, (b) 10, (c) 20 and (d) 30 mmol zinc acetate using a 1:2.5 molar ratio of OAC/OAM after 10 min MWI at full power.

acetate concentration of 10 mmol, Figure 6.15(b), the ZnO nanoparticles begin to take on a more rod-like morphology. At higher concentrations of zinc acetate, 20 and 30 mmol, the ZnO nanostructures show a well-defined rod structure, Figure 6.15(c-d). The aspect ratio of the ZnO nanorods is significantly increased upon increasing the concentration of zinc acetate from 20 to 30 mmol. On the basis of these observed changes in particle morphology, the concentration of zinc acetate has a significant effect on controlling ZnO nanoparticle morphology.

The photocatalytic degradation of MG under UV irradiation was used to evaluate the photocatalytic performance of ZnO-RGO in order to determine the effect of ZnO morphology. The strong dependence of photodegradation of MG on ZnO morphology was reported in Chapter 3. Photodegradation experiments were carried out as described previously. All ZnO-RGO composites showed good photocatalytic activity and degraded 90%, 94%, 82% and 88% for composites prepared using 10, 20, 30 and 40 mmol zinc acetate, respectively. Figure 6.16 graphs $\ln(C/C_0)$ as a function of time for photodegradation using ZnO-RGO photocatalysts prepared with 10-40 mmol of zinc acetate. The average rate for degradation was found to be 0.026, 0.030, 0.019, and 0.024 s^{-1} for ZnO-RGO composites prepared using 10, 20, 30, and 40 mmol zinc acetate, respectively. Therefore, there is a slight enhancement in the photocatalytic activity of the ZnO nanorods supported on RGO compared to the ZnO nanopyramids supported on RGO. The enhanced photocatalytic activity from varying the morphology of the ZnO on RGO can be attributed to more surface area of the active crystal present in the ZnO nanorods.

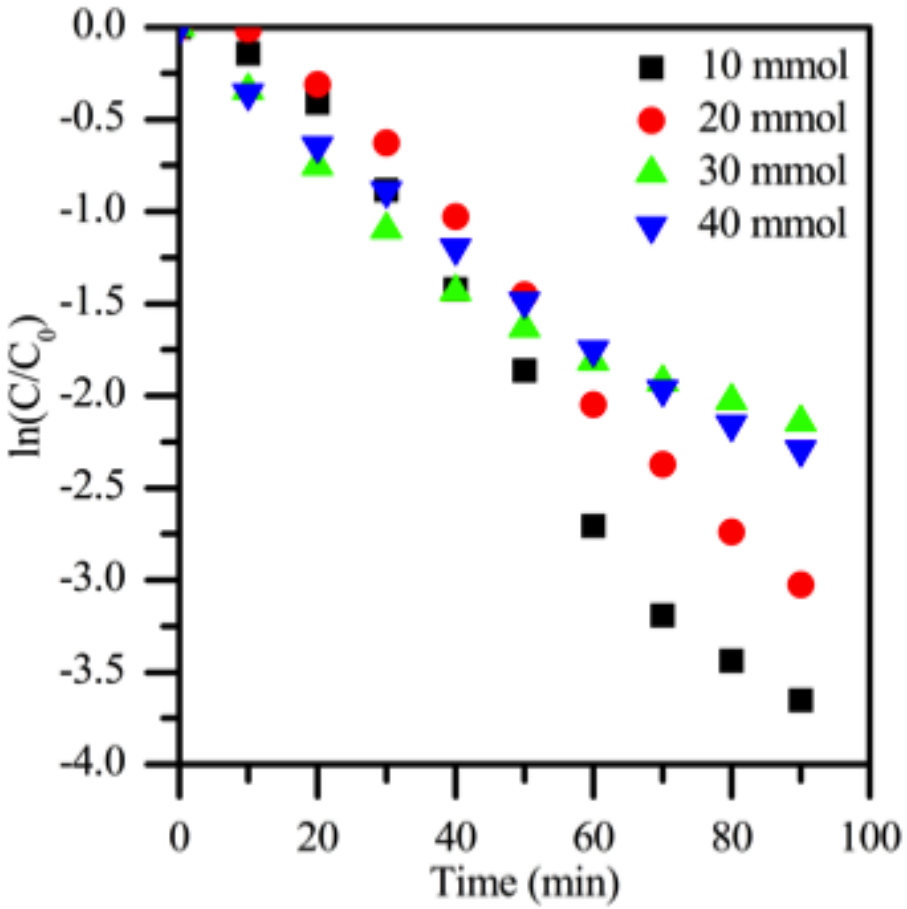

Figure 6.16 Graph showing the degradation of MG plotted as $\ln(C/C_0)$ as a function of UV irradiation time using ZnO-RGO nanocomposites prepared using 10, 20, 30 and 40 mmol zinc acetate.

6.6 Conclusions

This work demonstrates a simple one-step synthesis of ZnO nanopyramids supported on RGO nanosheets through MWI of zinc acetate and GO in the presence of a mixture of OAC and OAM. The rapid decomposition of zinc acetate by MWI in the presence of the mixture of OAC and OAM results in the formation of hexagonal ZnO nanopyramids or ZnO nanorods depending on the starting concentration of zinc acetate. GO has a high affinity for absorbing microwave irradiation, which results in a high local heating effect around the GO nanosheets and facilitates the reduction of GO by the OAM. The RGO nanosheets act as heterogeneous surface sites for nucleation and growth of the ZnO nanostructures. Therefore, the formation of ZnO

nanostrucutres in the presence of GO requires less MWI times than in the absence of GO under identical reaction conditions. Using ligand exchange with MUA, the ZnO-RGO nanocomposites can be dispersed in an aqueous medium thus allowing their use as photocatalysts for the degradation of the MG dye in water. The ZnO-RGO nanocomposites show enhanced photocatalytic activity for the degradation of the dye over the unsupported ZnO nanopyramids. The enhanced activity is attributed to efficient charge transfer of the photogenerated electrons in the conduction band of ZnO to graphene. This enhances the oxidative pathway of the holes generated in the valence band of ZnO, which can effectively lead to the degradation and mineralization of MG. The ZnO nanostructures supported on RGO could have improved performance in other photocatalytic reactions and also in solar energy conversion.

Chapter 7: Nitrogen-doped Zinc Oxide Supported on Nitrogen-doped Reduced Graphene Oxide

7.1 Introduction

Zinc oxide nanostructures exhibit extraordinary electronic and photocatalytic properties that can be tuned for various applications.[24-26, 208] As discussed in previous chapters, ZnO is a wide band gap semiconductor (3.7 eV), which makes it photocatalytically active under UV irradiation, and therefore a promising material for photoelectrochemical water splitting[42] and the photodegradation of organic contaminants.[14] Upon irradiation, electron-hole pairs are produced and initiate a series of desirable reactions, but recombination of photogenerated electron-hole pairs reduces photocatalytic efficiency. Therefore, efforts to reduce electron-hold pair recombination are beint studied.

Approaches to enhance semiconductor photocatalyst performance by reducing recombination and increasing light absorption include ion doping, noble metal loading and anchoring semiconductor nanoparticles to an electron-accepting support. Ion doping changes the electronic properties by modifying the band gap. The incorporation of N in the crystal lattice has been shown to enhance the properties of ZnO nanostructures.[14, 28, 42, 132] It has been reported that nitrogen doping in ZnO results in visible light absorption[172] and enhances photoelectrochemical water splitting[42] and photocatalytic degradation of organic dyes.[14]

Graphene has attracted wide interest because of its fascinating properties and applications.[175, 177, 209] Experimental and theoretical reports confirm that doping is an effective way to tailor the properties of graphene to produce novel nanomaterials and expand its potential applications.[210-213] Nitrogen and boron doping in graphene results in n-type and p-type conductivity, respectively.[214] Furthermore, nitrogen doping has been shown to enhance sensing[215] and catalytic[73] properties.

Many studies have reported the synthesis of ZnO supported on graphene with enhanced photocatalytic activity.[47, 48, 57, 66, 67, 69, 74, 81, 193, 216-220] The addition of graphene enhances both light absorption and charge separation as well as increasing organic dye adsorptivity. Although it is well known that the electronic properties of each component can be tuned to improve catalytic performance, few reports have studied tuning the electronic properties of the ZnO or the graphene in these composites.[51, 59, 221] It has recently been reported that the electronic structure of the nanocarbon support plays an important role in photocatalytic activity.[59] It was reported that doped graphene showed selectivity towards different organic dyes depending on the type of doping. Thus, it is expected that nitrogen doping of both the ZnO and the graphene would further enhance photocatalytic degradation of organic dyes. In this work, a single-step synthesis method for N-doped ZnO nanoparticles supported on N-doped reduced graphene oxide (RGO) was developed and its superior photocatalytic activity for the degradation of malachite green was studied.

7.2 Combustion Synthesis

A graphical illustration of the synthetic strategy for anchoring N-ZnO nanoparticles on N-doped reduced graphene oxide (N-RGO) sheets is presented in Figure 7.1. This approach studies the simultaneous formation of ZnO nanoparticles by the thermal decomposition of zinc

nitrate with the reduction of GO in the presence of urea. The high surface area of GO and RGO make it an excellent support for ZnO nanoparticles. It is expected that GO plays a major role in the formation of ZnO nanoparticles rather than bulk ZnO through combustion synthesis. In order to achieve a uniform distribution of ZnO supported on rGO, a uniform gel was prepared for combustion, which yields a homogeneous dispersion for combustion. Furthermore, N-doping is achieved by carrying out the reaction in the presence of urea, which acts as a N source for N-doping both the ZnO and RGO simultaneously. In this chapter, the synthesis of N-doped ZnO supported on N-doped RGO and its application for the photocatalytic degradation of malachite green will be discussed. Each component, N-ZnO and N-RGO, will be studied separately to confirm N-doping of each.

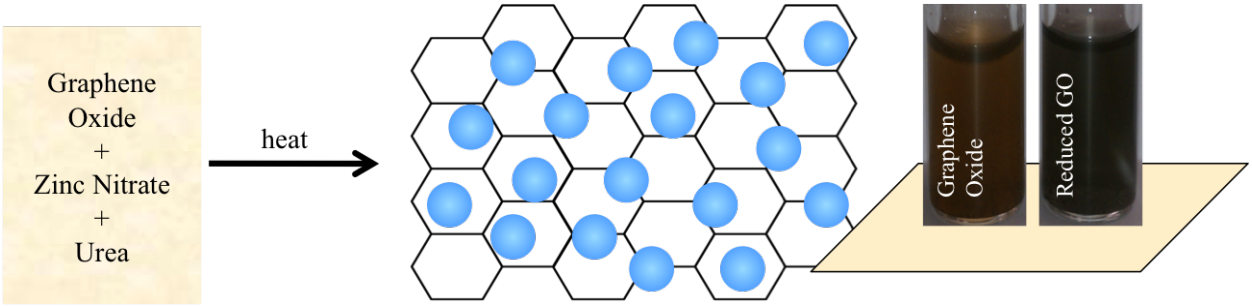

Figure 7.1. Pictorial illustration of the synthetic strategy for anchoring ZnO nanoparticles on RGO.

7.2.1 Combustion Synthesis of N-ZnO

N-doped ZnO was prepared following a method by Mapa et al.[14] In a typical synthesis, 0.04 mol zinc nitrate hexahydrate (Alfa Aesar, 99%) and 0.04 mol urea (Alfa Aesar, ACS grade) were dissolved in approximately 5 mL DI water. The mixture was stirred with magnetic stirring at room temperature until completely dissolved. The solution was heated in a muffle furnace at 80 °C until a uniform gel formed, which required approximately 2 hours. Heating the solution facilitated the evaporation of water and created a gel suitable for combustion. The formation of

the gel was required to evenly disperse the urea and zinc nitrate, which allows for uniform doping of ZnO upon combustion.

For combustion, the aforementioned gel was placed in a muffle furnace preheated to the desired temperature (250-450 °C). Combustion occurred within the first minute, as indicated by a plume of smoke escaping the furnace. The temperature is maintained for 2 hours, and then the solid product is collected. A pink colored solid indicates N-ZnO formation.

Pure ZnO is formed through modification of this method. The previous synthesis procedure carried out in the absence of urea results in the thermal decomposition of zinc nitrate to ZnO. For the formation of pure ZnO, there is no need to form a gel, because only one precursor material is used for the formation of ZnO. A yellow/white colored solid indicates ZnO formation.

7.2.2 Combustion synthesis of N-ZnO supported on N-RGO

For synthesis of N-ZnO supported on N-RGO, the combustion method is modified to integrate the simultaneous thermal decomposition of zinc nitrate alongside reduction of GO.

GO was prepared from graphite powder following Hummers' method[203] by treatment with $KMnO_4$ in H_2SO_4, washing with water and drying. A complete preparation method for GO is given in Appendix A.

Next, a gel was prepared for combustion. First, 0.04 mol zinc nitrate hexahydrate (Alfa Aesar, 99%) and 0.04 mol urea (Alfa Aesar, ACS grade) were dissolved in approximately 5 mL DI water. The mixture was stirred using magnetic stirring at room temperature until completely dissolved. Second, GO was dispersed in DI water by sonication using an ultrasonic bath for 1 hour. For both reaction mixtures, only enough DI water was used to completely dissolve or disperse the reagents. Once all reagents were completely dissolved or dispersed, they were

combined in a small beaker and stirred until homogeneous. The solution was then heated in a muffle furnace at 80 °C until a uniform gel formed, approximately 2 hours.

For combustion, the aforementioned gel was placed in a porcelain boat. The boat was placed in a quartz tube under the flow of argon. The mixture was inserted into a tube furnace with a constant temperature and kept under constant flow of argon. Note that the gel was maintained in the quartz tube under the flow of argon, but outside of the furnace until it reached the desired temperature. During the first minute, water in the gel evaporates. Then, the mixture ignites yielding N-ZnO-N-RGO product. The product is kept at constant temperature and argon flow is maintained for 2 hours. The solid product is then collected. The produce is gray in color indicating a reduction from GO (brown) to RGO (black) and formation of ZnO. ZnO-RGO composites were prepared following the above procedure in the absense of urea.

Reactions containing GO were carried out in a tube furnace under the flow of argon rather than ambient conditions in a muffle furnace. This is to prevent the oxidation of thermally reduced GO, which occurs at higher temperatures during the reaction process.

7.3 N-doped ZnO

First, N-doping of ZnO by the combustion of zinc nitrate in the presence of urea was studied using Raman spectroscopy. Raman spectroscopy is a powerful tool for characterizing ZnO, and the appearance of new Raman bands suggests N-doping in the ZnO crystal lattice. Raman spectra for pure ZnO and N-ZnO are given in Figure 7.2. As will be shown in section 7.5.2, when ZnO is coupled to RGO, the Raman signal from ZnO is quenched. Similar quenching is observed in other ZnO-graphene composites. Therefore, ZnO prepared using this method needs to be characterized separately than ZnO-RGO composites.

Figure 7.2 shows the Raman spectra for pure ZnO and N-ZnO. ZnO has three characteristic bands at 330, 380 and 437 cm^{-1}. The peaks at 330 and 437 cm^{-1} are assigned to vibration modes 2E2(M) due to multiple-phonon-scattering processes and E2(high) from O atom, respectively. The peak at 380 cm^{-1} is assigned to A1(TO) vibration mode. In the pure ZnO sample, there is a peak around 578 cm^{-1}, which is attributed to a large number of oxygen vacancies. Upon incorporation of N into the ZnO lattice, additional bands at 275, 508, 578 and 642 cm^{-1} are observed in the Raman spectrum. These additional vibrational modes in N-doped ZnO are attributed to breakdown of the translational crystal symmetry by doping in wurtize-ZnO. The appearance of these new peaks in the Raman spectrum confirms successful N-doping of ZnO by combustion of zinc nitrate in the presence of urea.

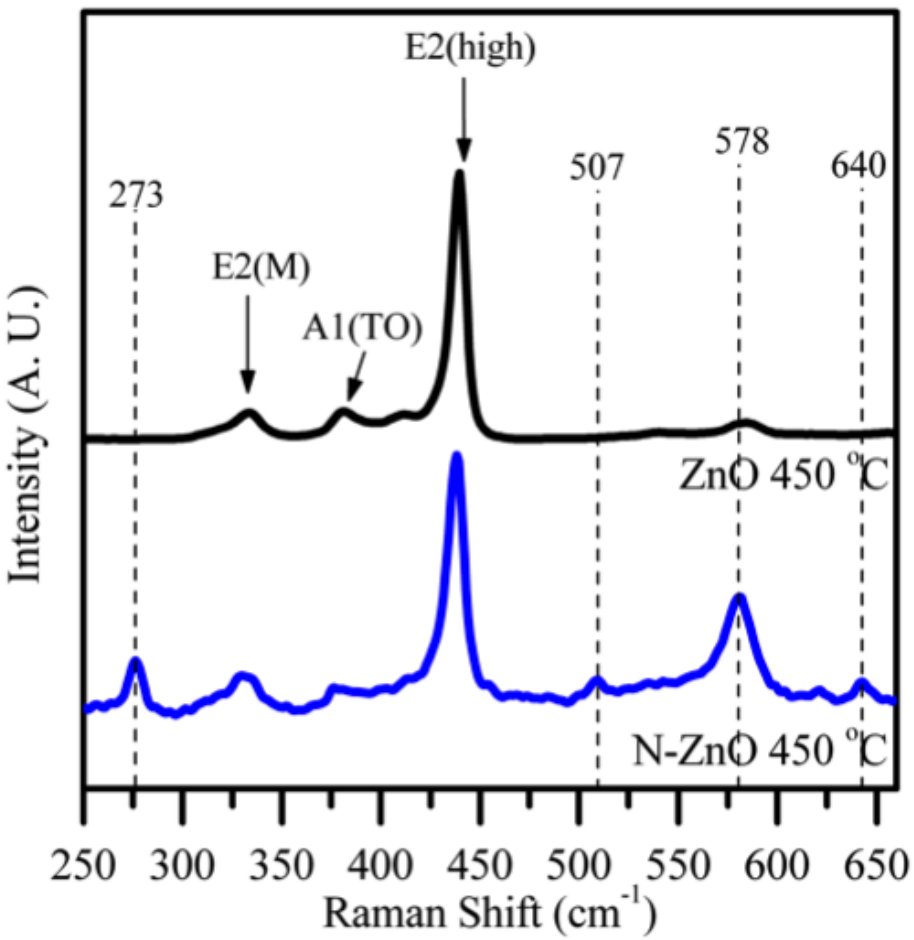

Figure 7.2 Raman spectra of ZnO and N-ZnO prepared at 450 °C.

7.4 N-doped RGO

The thermal reduction and N-doping of GO are studied using XRD, Raman spectroscopy and XPS.

The crystallinity of RGO and N-RGO were characterized using powder XRD. Figure 7.3 shows the XRD patterns for GO, rGO and N-rGO as prepared at 250 °C. GO has a characteristic diffraction peak at 12 degrees, which corresponds to a d-spacing of 7. 43 Å of the 001 diffraction peak.[206] Thermal reduction of the graphene oxide results in the disappearance of the peak at 12 degrees and the appearance of a new, broad peak at 26 degrees. The peak at 26 corresponds to the 002 diffraction peak of graphite and indicates that the d-spacing is reduced.[222] This is

expected because the oxygen moieties on the graphene oxide increase spacing between the graphene layers, and upon reduction, the oxygen moieties are removed and the layer spacing is able to return to that similar of graphene. This confirms that GO is thermally reduced during this process.

Similar results are observed for the formation of N-RGO in the presence of urea. The peak at 12 degrees for GO disappears, and a new peak appears at 26 degrees. In this case, the peak at 26 degrees is more intense for RGO formed in the absence of urea. There are two possible explanations for this increase in peak intensity. First, this may indicate increased stacking of the N-RGO compared to undoped RGO, which means the N-RGO is closer to well-ordered graphite. Previous reports have demonstrated that GO may be thermally reduced to form N-RGO in the presence of urea.[223, 224] Second, the peak at 26 degrees may also indicate formation of graphitic carbon nitride, which is readily formed during thermal treatment of urea.[225-227] Graphitic carbon nitride has a structure very similar to N-doped graphene and is an active photocatalyst.[225, 227] XRD peaks around 26 degrees are characteristic of inter-planar stacking of conjugated aromatic systems,[227] and therefore, it is difficult to use distinguish between N-doped graphene and carbon nitride.

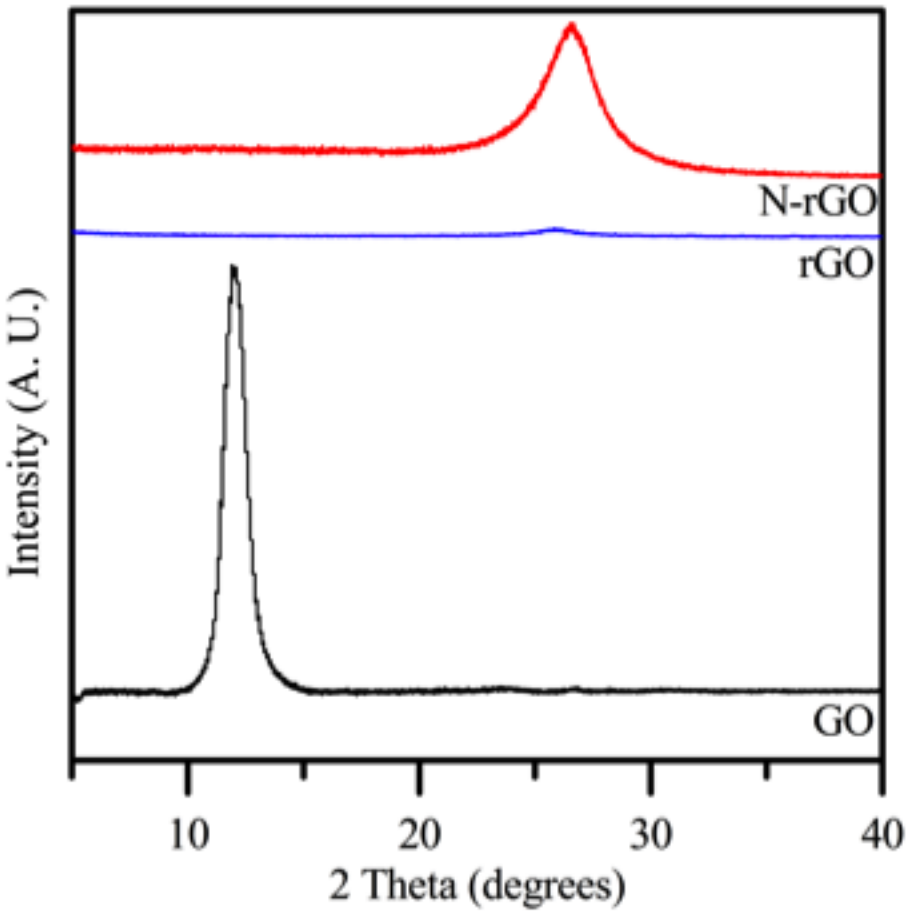

Figure 7.3 XRD patterns of GO, RGO prepared at 250 °C and N-RGO prepared at 250 °C.

The nature of RGO and N-RGO is further studied using Raman spectroscopy. Few layer graphene typically show two Raman bands: G band and D band. Single layer graphene shows a third Raman band, 2D. The Raman G band at ~1580 cm^{-1} is due to the doubly degenerate zone center E2g and is characteristic of the sp^2 carbon network.[205] The Raman D band at ~1350 cm^{-1} arises as a result of defects in the graphene structure and only appears in samples with a significant amount of defects or on the edges of pristine graphene sheets.[205] Thus, the ratio of the intensity of the Raman D and G bands is used to compare the relative number of defects in each sample. Raman spectra of GO, RGO and N-RGO are presented in Fig. 7.4.

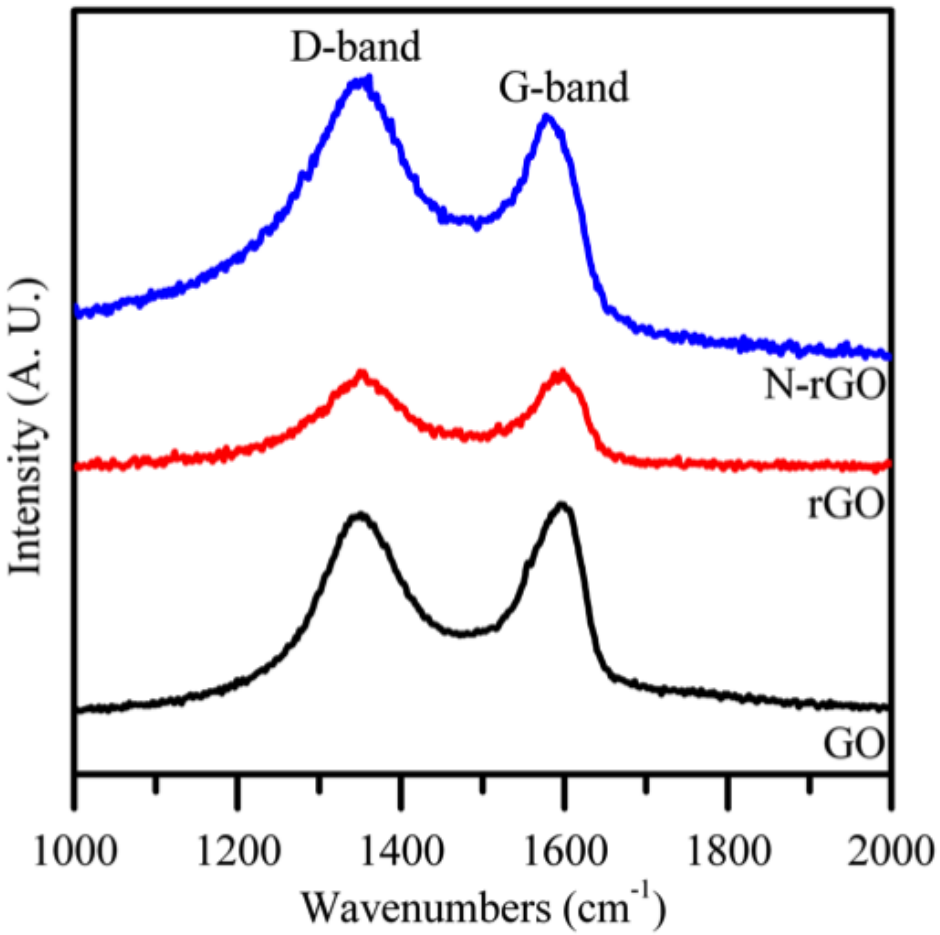

Figure 7.4 Raman spectra of GO, RGO prepared at 250 °C and N-RGO prepared at 250 °C.

7.5 N-doped ZnO-reduced graphene oxide composites

The previous sections demonstrated that the combustion method is successful towards the synthesis of both N-ZnO and N-RGO separately. Combining zinc nitrate and GO in the presence of urea is expected to result in the formation of N-doped ZnO supported on N-doped RGO (N-ZnO-RGO). The resulting composites are studied using XRD, Raman spectroscopy, XPS and TEM.

7.5.1 X-ray diffraction

The crystallinity of unsupported N-ZnO, ZnO supported on RGO prepared at 250 °C and N-ZnO supported on N-rGO prepared at 250 and 450 °C are given in Figure 7.5. N-ZnO results

in a pattern consistent with wurtzite ZnO. ZnO supported on RGO prepared at 250 °C results in a pattern consistent with ZnO as well as a small broad peak at 26 degrees, which is corresponds to RGO. Similar results are observed for N-ZnO supported on N-rGO prepared at both 250 and 450 °C. The N-ZnO peaks for the sample prepared at 450 °C are more narrow and sharp compared to those of the sample prepared at 250 °C, which indicates a more crystalline structure is produced at higher temperatures. These results provide strong evidence for the formation of ZnO-RGO composities prepared both with and without urea. In the composites, a more pronounced peak for N-RGO compared to that of RGO is also observed at 26 degrees. This may be a result of stronger interactions between the N-RGO sheets that initiate restaking, or may be a result of graphtitic carbon nitrides.

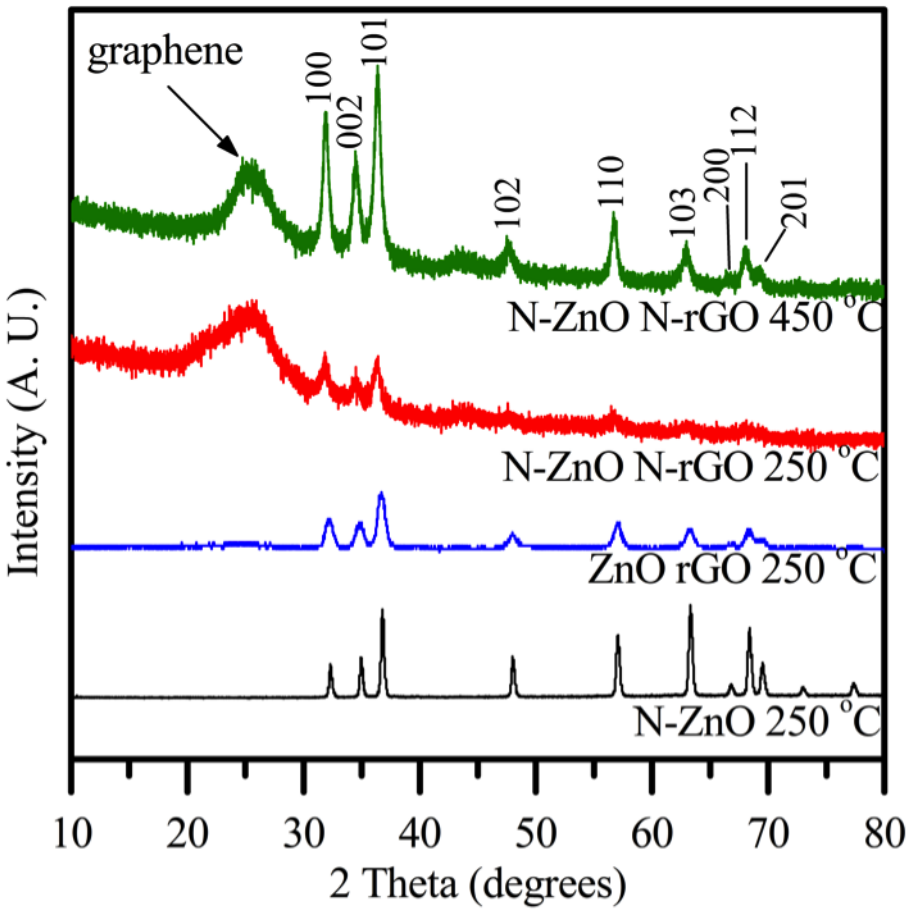

Figure 7.5. XRD of N-ZnO, N-ZnO supported on N-rGO prepared at 250 and 450 ºC.

7.5.2 Raman spectroscopy

Raman spectroscopy was used to further characterize the ZnO-graphene composites. Figure 7.6 shows Raman spectra for N-ZnO supported on N-RGO prepared at 2 temperatures, 250 and 450 °C. When the composite is prepared at 250 °C, the graphene is only partially reduced, and therefore still maintains some semiconductor properties. Thus, both the ZnO Raman signal and the RGO Raman signal are observed. Additional peaks indicative of N-doping are observed in this spectrum. For the carbon region, an I_D/I_G ratio of 1.1 was observed, which indicates a large number of defects in the rGO lattice. For N-ZnO supported on N-RGO prepared at 450 °C, the Raman signal for the ZnO is quenched by the RGO. In this spectrum, a I_D/I_G ratio

of 1.1 was observed. Therefore, both samples have resulted in either partially reduced or fully reduced GO with a high number of defects.

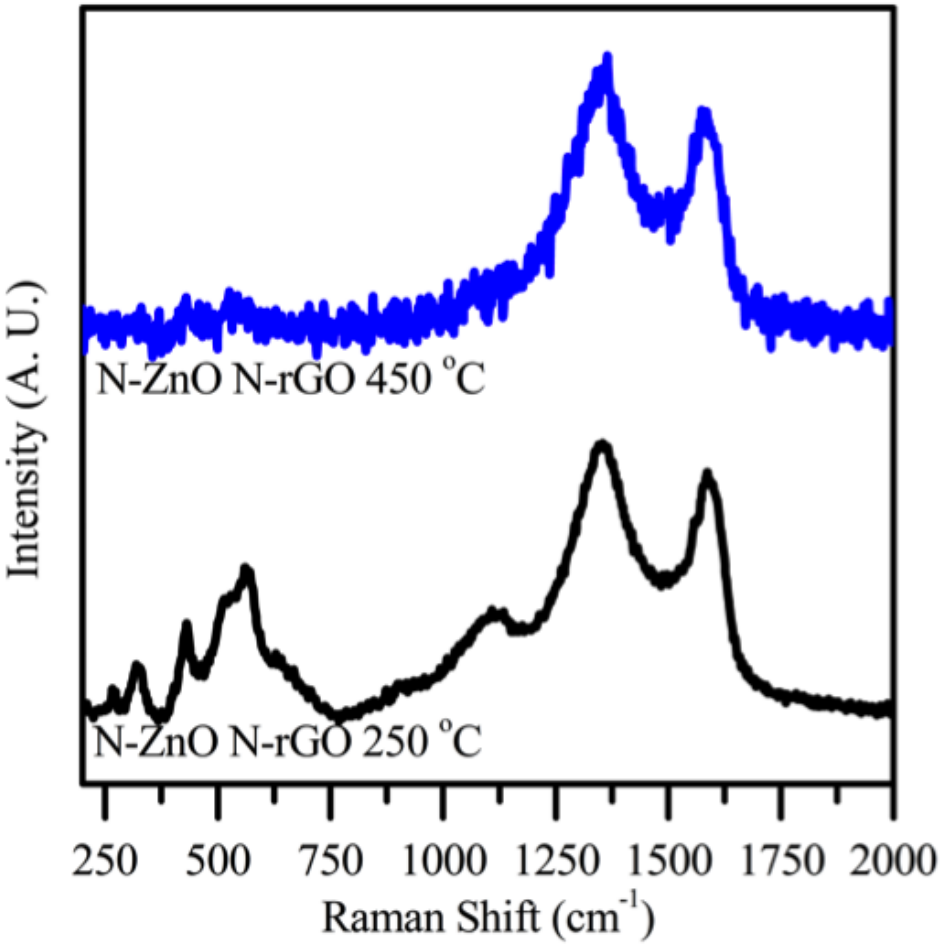

Figure 7.6. Raman spectra of N-ZnO supported on N-rGO prepared at 250 and 450 ºC

7.5.3 X-ray photoelectron spectroscopy

In order to further understand the chemical species present, the surfaces of our composites were studied using X-ray photoelectron spectroscopy, as shown in Fig 7.7. Figure 7.7-a shows the C 1s region for GO, RGO, N-RGO and N-ZnO supported on N-RGO. For graphene oxide, the biding energy of the C-C and C-H bonding are assigned at 284.5 eV with additional peaks at higher binding energies assigned for chemical shifts of +1.5 and +4.0 eV for C=O and O=C-OH functional groups, respectively. After reduction of the GO at 250 °C, the

intensity of the C=O and O=C-OH peaks are greatly reduced, indicating the removal of the oxygen containing moieties. Upon addition of urea to the reaction mixture, the C 1s spectrum for N-RGO displays an additional peak with a chemical shift of +1 eV is fitted for N bound to sp^2 C. This C-N peak is fitted for N-ZnO supported on N-RGO. Both N-rGO and N-ZnO N-RGO show decreased intensity of the C=O and O=C-OH peaks indicating the reduction of GO. Although the C 1s region provides important information for the graphene, N-doping must be confirmed by studying the N 1s region.

Nitrogen is incorporated into both ZnO and graphene lattice, therefore several different types of N are expected to be present. The incorporation of N into the ZnO lattice can occur in more than one chemical state; either by incorporation of N_2 into the ZnO lattice or a N atom can be incorporated substitutionally at an O site. The peak at 399 eV is typical of N 1s binding energy in amines.[133] Since urea is used as a nitrogen source, it is reasonable to expect the presence of N-H compounds to be present in the sample. However, this peak is also within the region for zinc nitride compounds, and may be attributed to oxynitride (O-Zn-N).[133, 172] A second peak centered at 405 eV indicates the incorporation of molecular N_2 on the oxygen sublattice.[172, 228] This result suggests that N is doping substitutionally at O sites in the ZnO structure.

Nitrogen also incorporates into the graphene lattice. In GO, the N peak is absent, but in N-doped RGO, the N 1s peak may be fitted to 3 components, which suggests three different bonding configurations for N in the graphene lattice. The bonding configurations for N in the graphene lattice are termed pyridinc, pyrrolic and graphitic N, which appear at 398, 400 and 402 eV, respectively.[222, 229-231] Pyridinic and pyrrolic N refer to N that incorporated into the π–conjugated system bound to 2 C atoms within 6 and 5 membered rings, respectively. Whereas

graphitic N refers to N atom replacing a C atom in the graphene sheet, or a N attached to 3 C atoms. For N-RGO, a broad peak centered ~400 eV is observed, and it is fitted with 3 peaks. This confirms that this method is successful for doping N into the graphene lattice. Furthermore, XPS is used to study N-ZnO supported on N-RGO. Here, a broad peak with binding energy centered at ~400 eV is observed. This peak is fitted to 3 peaks and it is assumed that the peak at 399 is the overlap of the N component in the ZnO and the pyridinic C-N component. However, it is interesting to notice that the molecular N_2 (405 eV) is not present in the composite material.

The Zn region shows 2 peaks for Zn representing electrons from $2p_{1/2}$ and $2p_{3/2}$ orbitals. For ZnO these peaks appear at binding energies 1045 and 1020 eV. Comparing ZnO and N-doped ZnO prepared by this method, no shift is observed in the Zn peaks. However, once graphene is present, the peaks shift to higher binding energies. The most probable explanation for this shift is a strong interaction between the ZnO and the RGO.[220, 232]

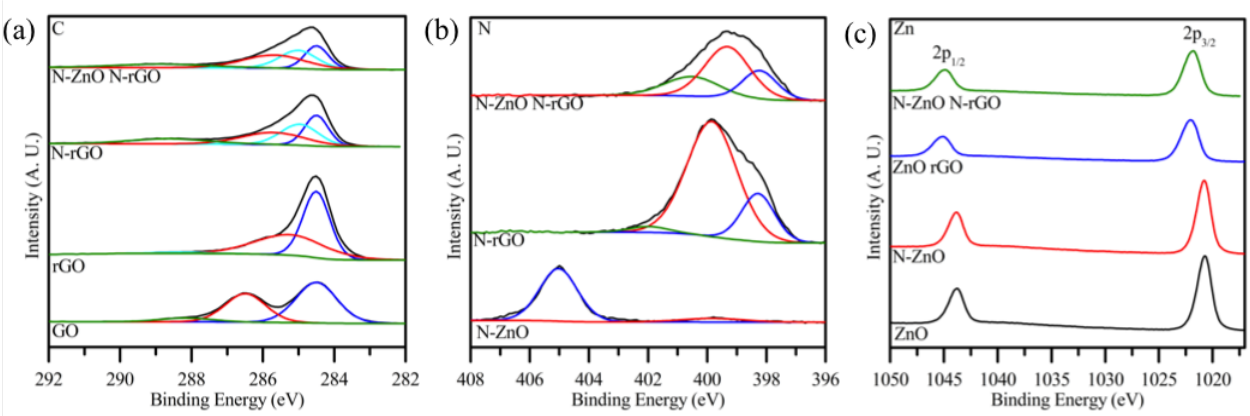

Figure 7.7. XPS spectra of C 1s, N 1s and Zn 2p regions.

7.5.4 Morphology

Morphology of as prepared ZnO supported on RGO and N-ZnO supported on N-RGO was studied using TEM. It is expected that defects sited on GO sheets will serve as nucleation sites for the formation of ZnO nanoparticles. TEM images of N-ZnO, ZnO-RGO and N-ZnO-RGO are shown in Fig 7.8. Fig 7.8-a demonstrates that N-ZnO prepared in the absence of

graphene is a bulk ZnO with no definite structure or individual particles observed. ZnO supported on RGO, Fig. 7.8-b, shows few ZnO nanoparticles, that are well defined, distributed on an RGO sheet. ZnO nanoparticles were slightly aggregated and few particle aggregates were observed without RGO supports. N-ZnO-RGO is shown in Fig. 7.8-c. The N-RGO sheet is heavily decorated with very distinct N-ZnO nanoparticles with little aggregation. Furthermore, there were no N-ZnO particles not attached to N-rGO observed. Thus, it is assumed that the use of RGO as a catalyst support will act as nucleation sites for the formation of ZnO nanoparticles, prevent aggregation of ZnO nanoparticles and enhance catalytic activity. This distribution of N-ZnO on N-RGO (Fig. 7.8-c) further indicates that there is a strong interaction between the N-ZnO and the N-RGO. In is expected that the strong interaction between the ZnO and RGO support will provide enhanced catalytic activity.

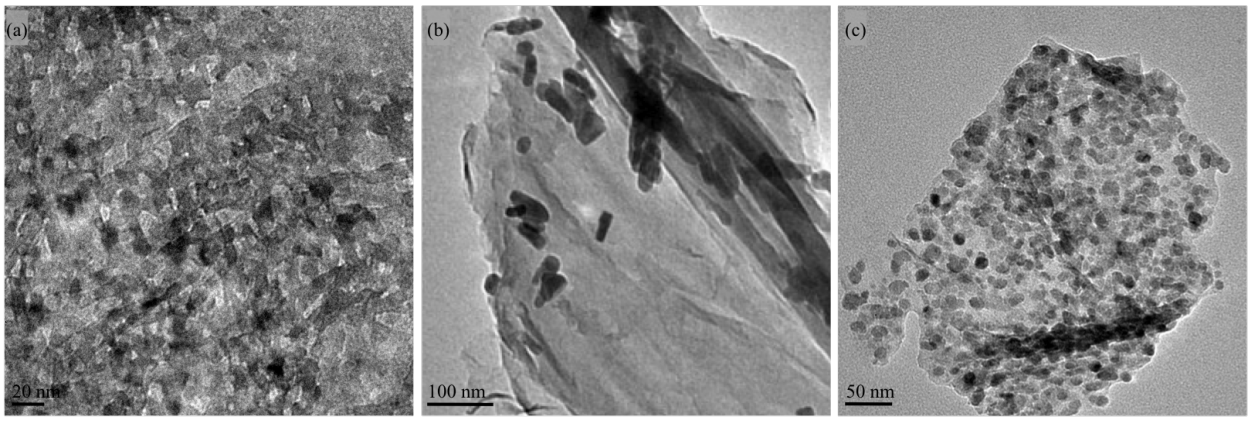

Figure 7.8. TEM (a) N-ZnO, (b) ZnO supported on rGO, (c) N-ZnO supported on N-rGO

7.5.5 Photocatalytic degradation of malachite green

In order to evaluate the photocatalytic performance of each material, the photocatalytic degradation of malachite green under UV irradiation was studied, as shown in Fig. 7.9. Malachite green is a commonly used organic dye that has a strong absorption band at 620 nm, which was used to follow the photocatalytic degradation as a function of UV irradiation time.

Malachite green does not degrade under UV irradiation without the presence of a catalyst material (results not shown). However, when a catalyst material is present, the absorption peak at 620 nm decreases in intensity under UV light irradiation, as shown in Fig. 7.9. The kinetics of dye degradation were studied by examining the change in concentration of the dye as a function of irradiation time. The kinetics are fitted to pseudo-first order reactions by $\ln(C/C_0)=kt$ where k is the rate constant. Figure 7.10, shows the time variation of the natural log of C/C_0 of malachite

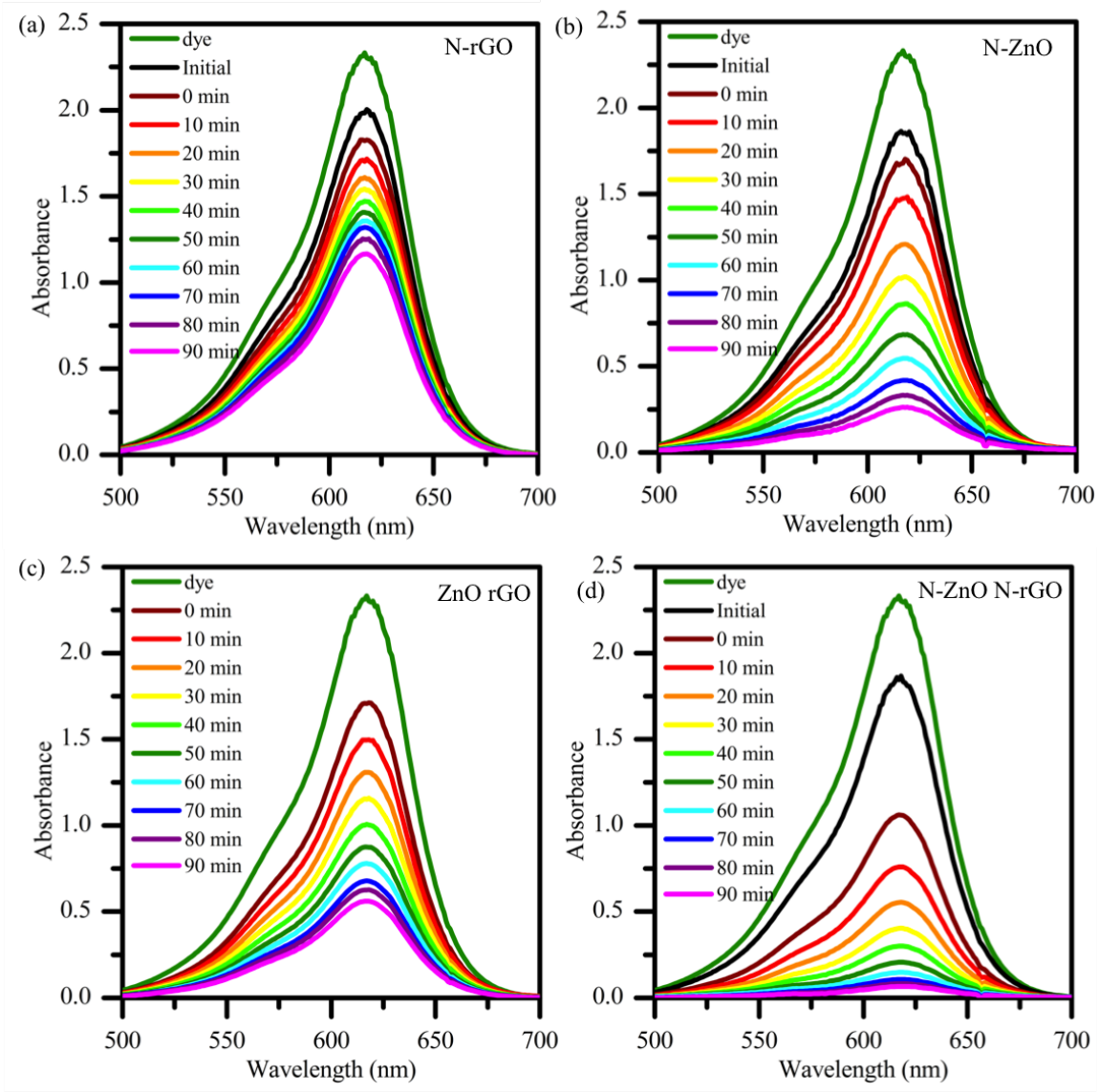

Figure 7.9 Absorbance spectra showing the degradation of malachite green by UV irradiation.

green plotted as a function of time. N-ZnO-RGO has the highest rate constant. The rate constant for N-ZnO supported on N-RGO is nearly three times greater than unsupported N-ZnO and undoped ZnO supported on RGO. The degradation rate varies as N-ZnO-RGO > ZnO-RGO > N-ZnO > N-RGO. It is expected that N-RGO shows little photocatalytic activity because it is not the active catalyst in this system. The percentage of dye degraded after 90 minutes of UV irradiation as well as the rate constants are given in Table 7.1.

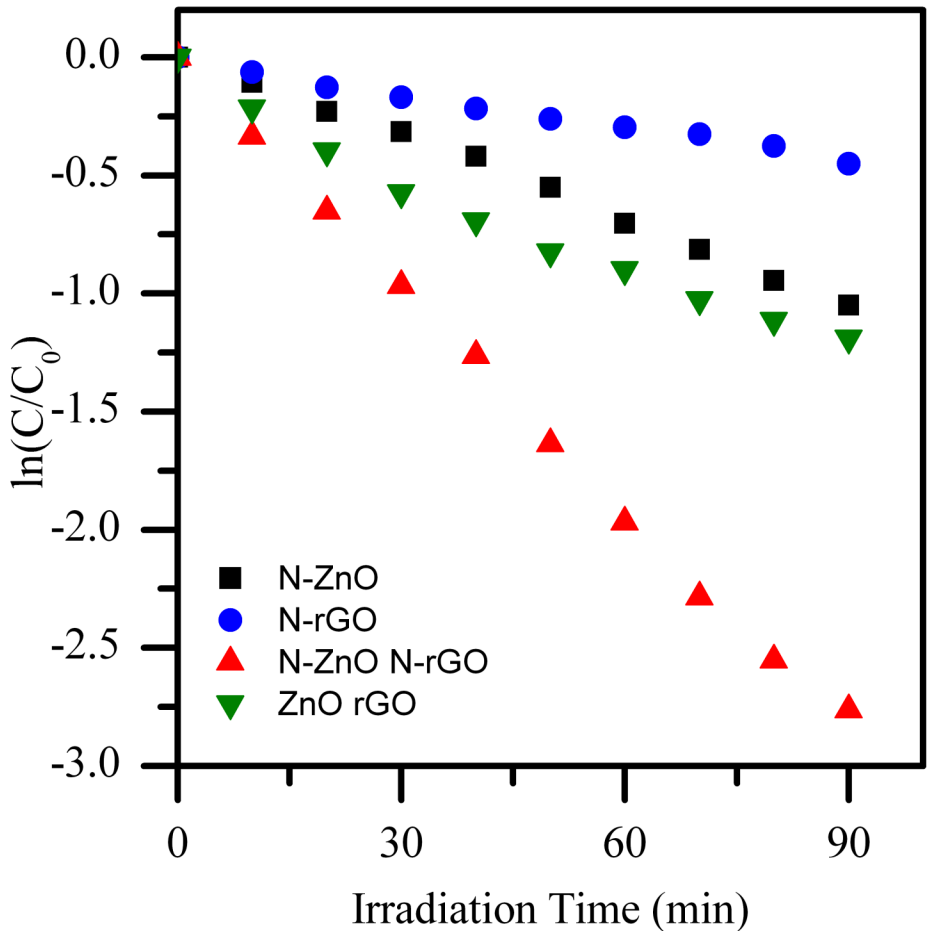

Figure 7.10 Photocatalytic degradation of malachite green by irradiation with UV light.

Table 7.1. Summary of photocatalytic degradation of malachite green

Sample	**% Degraded in 90 min**	**Rate (min^{-1})**
N-RGO	36	0.005
N-ZnO	65	0.012
ZnO-RGO	68	0.013
N-ZnO – N-RGO	94	0.031

Further, the effect of reaction temperature on the photocatalytic degradation of malachite green was studied. Figure 6.11 displays the catalytic activity for N-ZnO supported on N-RGO prepared at 250, 350, 450 and 800 ºC. The highest photocatalytic activity was observed for catalysts prepared at 250 ºC.

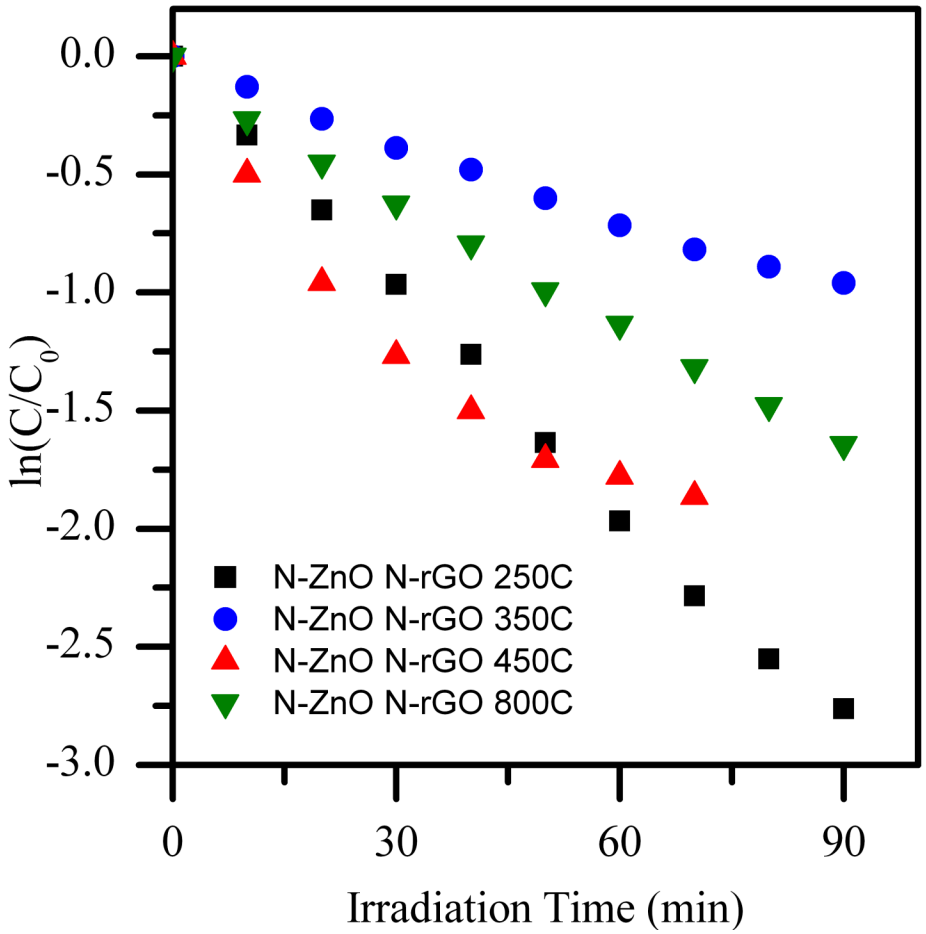

Figure 7.11 Photocatalytic degradation of malachite green by irradiation with UV light for N-ZnO-RGO prepared at 250, 350, 450 and 800 ºC.

7.6 Conclusions

In conclusion, this chapter demonstrates a simple synthesis method for the formation of N-doped ZnO nanoparticles supported on N-doped RGO nanosheets using combustion of zinc nitrate and GO in the presence of urea. The thermal decomposition of zinc nitrate in the presence of urea results in the formation of ZnO nanoparticles that are N-doped. Furthermore, the reduction of GO in the presence of urea results in the incorporation of N into the graphene lattice. The nanocomposites are dispersible in aqueous medium allowing their use as photocatalysts for the degradation of the malachite green dye in water. The N-ZnO supported on

N-RGO nanocomposites show three-fold enhancement in photocatalytic activity for the dye degradation compared to unsupported N-ZnO nanoparticles and undoped ZnO-RGO. Enhanced activity is attributed to efficient charge transfer of photogenerated electrons in the conduction band of ZnO to graphene.

Chapter 8: Non-ZnO Based Nanomaterials

8.1 Introduction

There has been considerable research interest focused on metal and bimetallic nanoparticles. Historically, metal nanoparticles were exploited for unique optical properties and were used in decorative glass as seen in the Lycurgus Cup.[233] The Lycurgus Cup is a fasinating Roman artifcat made of gold nanoparticles, which causes it appear green in reflected light and red in transmitted light.[233] More recently, metal nanoparticles have been studied to understand the unique optical and electronic properties that arise from quantum confinement at the nanoscale. This has lead to the use of metal nanoparticles in practical applications, which include catalysis,[197, 234-238] sensors,[239] biomedical applications, and biomass conversion.[240]

Bimetallic nanoparticles are of great interest because of new properties that may arise as a result of varying the composition of metal nanoparticles by combining two or more metals.[241] The term bimetallic encompases many possible mixing patterns, whereas the term alloy implies mixing of metal ions rather than segregation.[241] The work presented in this chapter will focus on the MWI assisted synthesis of alloy nanoparticles. In order for alloys to form, experimental conditions must result in binary nuleaction events, which includes both metal precursors.[197] A broad range of both physical and chemical approaches have been used to synthesize alloy nanoparticles including molecular beams,[241] electrodeposition[239, 242], sonochemical reactions,[243]

chemical reduction,[234, 236] thrermal[237] and microwave[197] methods. Each method produces bimetallic nanoparticles with different compositions, sizes and shapes.

Catalysis is one important application for the use of both metallic and bimetallic nanoparticles. As previously mentioned, bimetallic nanoparticles often show enhanced catalytic acitivty than either of the pure metallic components. In this chapter, metallic and bimetallic nanoparticles, namely Pd, Ni, Co, PdNi and PdCo alloys, will be studied as nanocatalysts for CO oxidation.

8.2 Synthesis of metal nanoparticles

A signle-pot, microwave method was developed for the synthesis of three different metal nanoparticles: palladium, nickel and cobalt. Pd nanoparticle synthesis was studied as a starting point for the development of metal nanoparticle synthesis. In a typical synthesis, 1 mmol of Pd(II) acetylacetonate was dissolved in a mixture of 15 mL OAM and 0.32 mL OAC. The reaction mixture was heated in a hot oil bath with magnetic stirring to 110 °C and the temperature was maintained for one hour. Heating assists in dissolving the metal salt and the removal of water. During the entire heating process, nitrogen gas is bubbled through the solution to prevent the formation of metal oxide nanoparticles. After heating, the reaction mixture is cooled to 90 °C. In a separate test tube, 250 mg of borane tertbutylamine (BTB) is dissolved in 2 mL OAM. The BTB solution is added all at once to the Pd reaction mixture with stirring. Upon addition, the reaction mixture turns dark brown in color. The reaction mixture is then placed in a microwave tube that is purged with N_2 and sealed with a Teflon cap. MWI was applied for 10 min, which resulted in the solution turning darker and black in color. The solution remained sealed until cool to the touch. Following MWI, the precipitate was separated from the liquid phase by centrifugation in the presence of ethanol and dried at 80 °C overnight.

Nickel and cobat nanoparticles were synthesized by adapting this method. For the synthesis of Ni nanoparticles, 1 mmol of Ni(II) acetylacetonate ($Ni(acac)_2$) was reduced to Ni nanoparticles using 250 mg BTB. For the synthesis of Co nanoparticles, 1 mmol of Co(II) acetylacetonate ($Co(acac)_2$) was reduced to Co nanoparticles using 500 mg BTB and 15 min MWI. Complete reduction of $Co(acac)_2$ required a higher concentration of reducing agent (BTB) and longer MWI, which will be further discussed in more detail.

This method was extended to study the formation of Pd-based bimetallic nanoparticles. Pd-Ni and Pd-Co bimetallic nanoparticles were prepared by adapting this synthesis method to incorporate both metal salt precursors prior to reduction. For the synthesis of Pd-Ni, $Pd(acac)_2$ and $Ni(acac)_2$ were added to a mixture of OAC and OAM and the reaction was carried out as reported previously. Pd-Co bimetallic nanoparticles were prepared using $Pd(acac)_2$ and $Co(acac)_2$.

8.3 Characterization of metal nanoparticles

8.3.1 X-ray diffraction

XRD is a powerful tool for characterizing bimetallic nanoparticles because it provides information on crystallinity, lattice spacing and chemical composition.[241] Assuming that the lattice spacing of the two metals in the bimetallic system are distinctive, the degree of mixing is determined using the lattice spacing of the bimetallic system.[241] The crystallinity of the as synthesized metallic and bimetallic nanoparticles was characterized using XRD. First, the diffraction patterns of pure Pd and Ni nanoparticles (Figure 8.1) were examined. The measured patterns are indexed to the [111], [200] and [220] planes of the cubic crystal structures for Pd and Ni. The XRD results clearly indicate the absence of peaks that can be assigned to the corresponding metal oxides. No oxidation is observed by atmospheric oxygen, therefore,

indicating that the OAC and OAM mixture effectively caps the nanoparticle surface preventing oxidation.

XRD patterns of Pd-Ni nanoalloys prepared using 1:3, 1:1 and 3:1 molar ratios of $Pd(acac)_2$ to $Ni(acac)_2$ are displayed in Figure 8.1. In comparing the XRD patterns of the Pd-Ni nanoalloys, it is observed that the diffraction peaks of the nanoalloys are located between the diffraction peaks of pure Pd and Ni. This is emphasized for the [111] plane, which is displaced in Figure 8.1-b. The diffraction pattern for the Pd-Ni nanoalloy is not a sum of diffraction patterns of the individual components. There is no evidence of any pure metallic peaks, which indicates a binary nucleation process for complete nanoalloy formation. In order to prevent independent nucleation and growth, a high concentration of the strong reducing agent, BTB, was added in order to achieve co-reduction. The appearance of new peaks located in between those of the pure metal components and the absence of the diffraction peaks for the pure metals provide strong evidence for alloy nanoparticles.

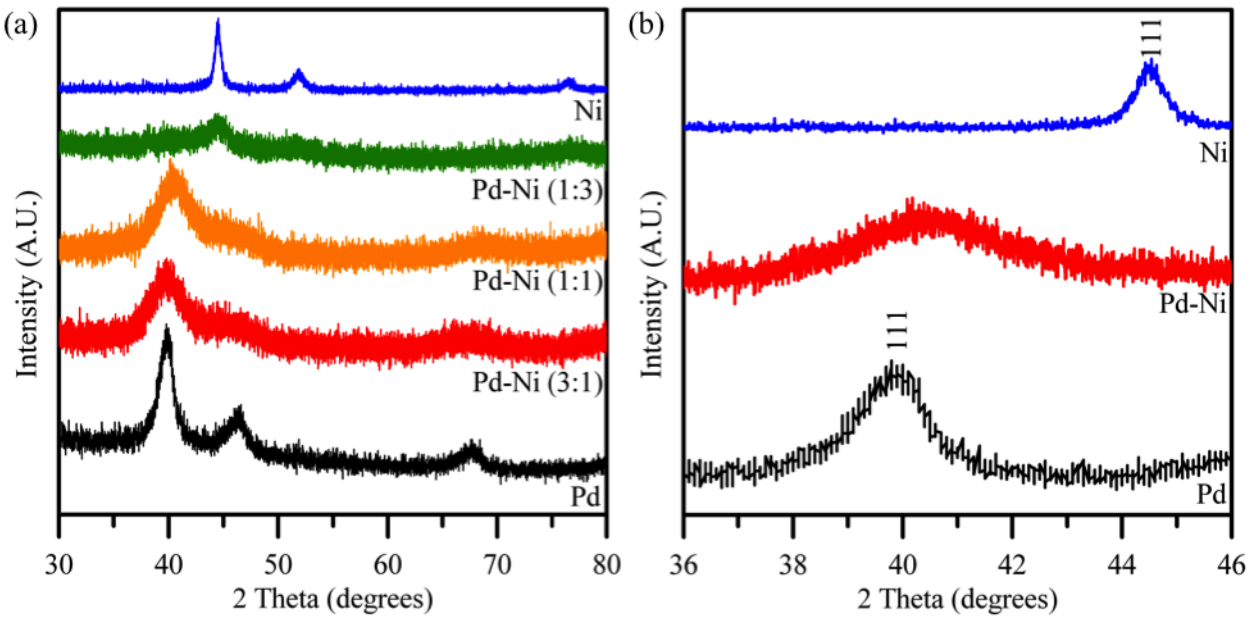

Figure 8.1. Powder XRD patterns of Pd, Pd-Ni, Ni nanoparticles.

Next, the crystallinity of Co and Pd-Co nanoparticles is studied. The XRD patterns of pure Co and Pd nanoparticles are displayed in Figure 8.2. The measured patterns are indexed to the [111], [200] and [220] planes of the cubic crystal structures for Pd and Co. The XRD results clearly indicate the absence of peaks that can be assigned to the corresponding metal oxides, similar to the previous results for Ni. This indicates that the mixture of OAM and OAC is effective towards capping the surface of Co nanoparticles as well.

Figure 8.2-a displays the XRD patterns of Pd-Co nanoalloys prepared using 1:3, 1:1 and 3:1 molar ratios of $Pd(acac)_2$ and $Co(acac)_2$. In comparing the XRD patterns of the Pd-Co nanoalloys, it is observed that the diffraction peaks of the nanoalloys are located between the diffraction peaks of pure Pd and Co. This is emphasized for the [111] plane, which is displaced in Figure 8.2-b Furthermore, the diffraction patterns of the Pd-Co nanoalloys show no evidence of any pure metallic peaks that indicate complete nanoalloy formation. The appearance of new

peaks located in between those of the pure metal components and the absence of the diffraction peaks for the pure metals provide strong evidence for alloy nanoparticles.

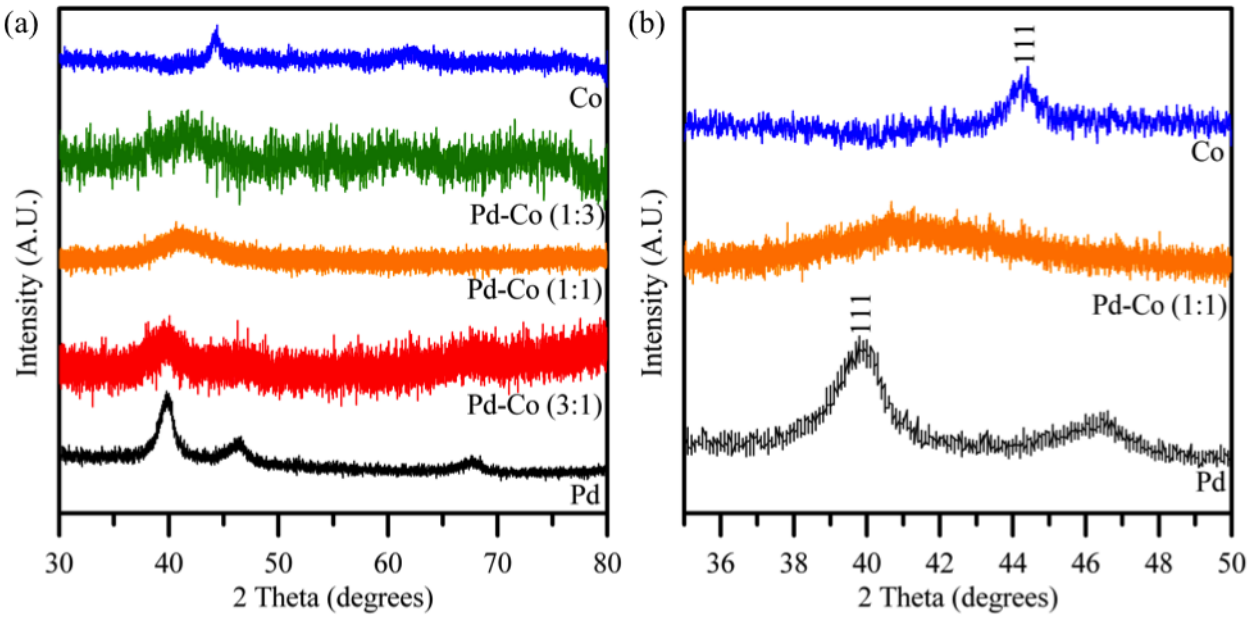

Figure 8.2. Powder X-Ray diffraction patterns of Pd, Pd-Co, Co nanoparticles.

$Co(acac)_2$ was more difficult to reduce compared to $Pd(acac)_2$ and $Ni(acac)_2$. A higher concentration of reducing agent, BTB, was required to completely reduce the $Co(acac)_2$ to Co nanoparticles compared to Pd and Ni nanoparticles. Insufficient BTB resulted in the formation of $Co(OH)_2$ rather than Co as shown in Figure 8.3. Therefore, Pd-Co nanoalloys were prepared using an increased amount of reducing agent, BTB, compared to Pd-Ni, which ensured coreduction and the formation of Pd-Co alloy.

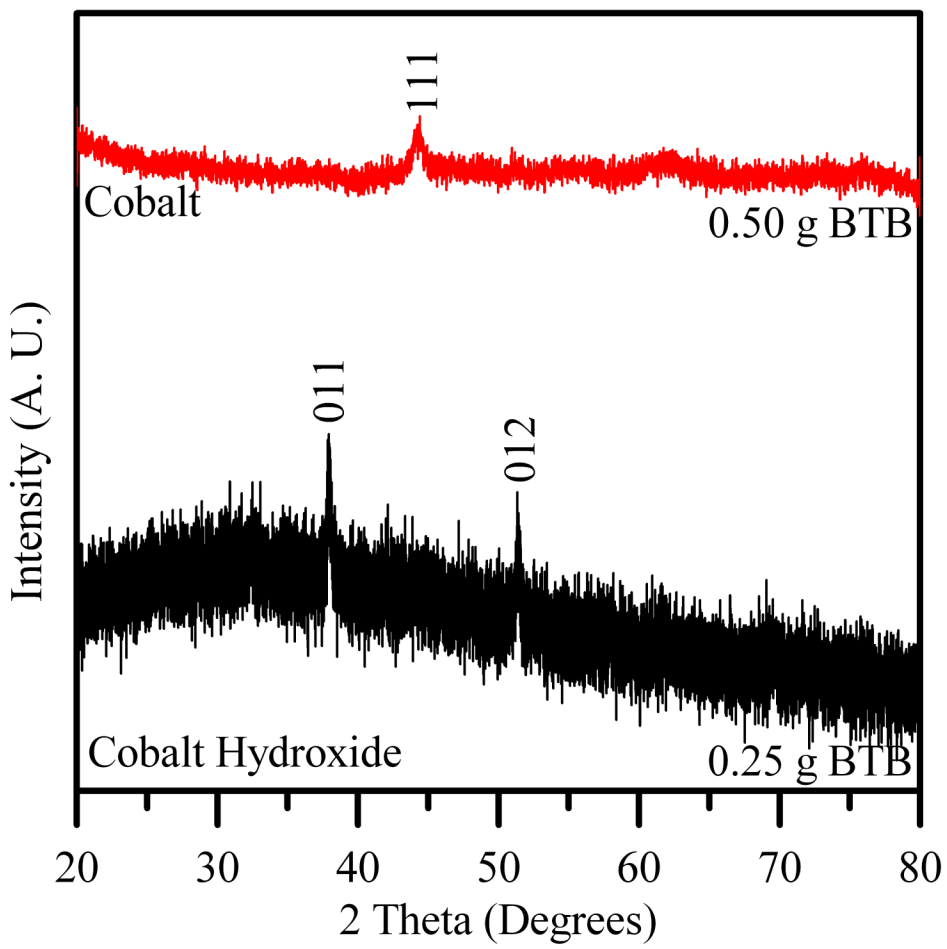

Figure 8.3. Powder X-Ray diffraction patterns of $Co(OH)_2$ and Co prepared using $Co(acac)_2$ and 0.25 and 0.50 g BTB, respectively.

8.3.2 Morphology

Nanoalloy morphology was studied using TEM. Figure 8.4 displays TEM images of Pd, Pd-Ni (1:1) and Ni nanoparticles prepared by MWI. By using a mixture of OAM, OAC and BTB, small, non-spherical Pd nanoparticles are formed. These particles appear to be agglomerates of small spherical nanoparticles. Both PdNi and Ni produce monodisperse spherical nanoparticles with average diameters of 5 and 13 nm, respectively. In our experiments, the metal ions are reduced by the BTB, and the OAM and OAC serve as the capping materials.

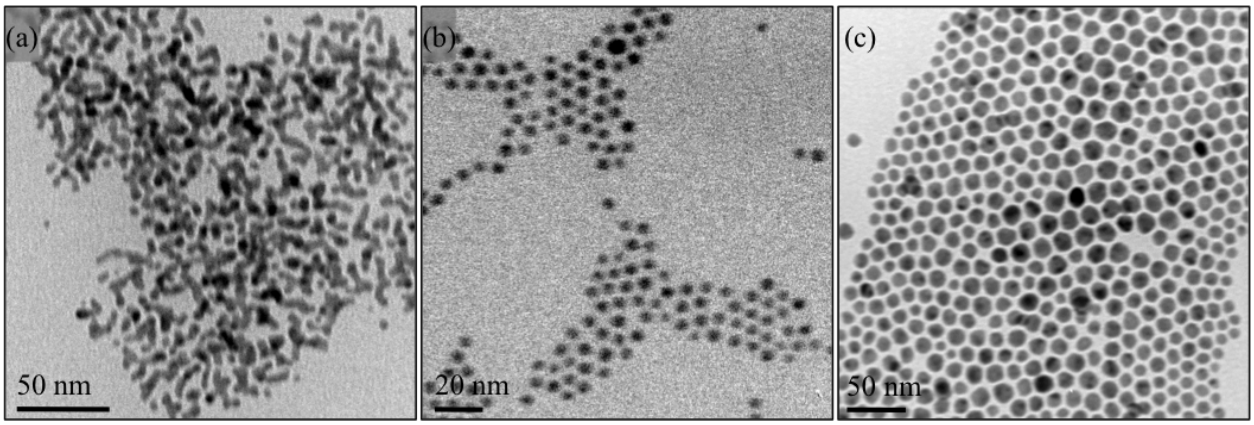

Figure 8.4 TEM of (a) Pd, (b) Pd-Ni, (c) Ni nanoparticles

Figure 8.5 displays TEM images of Pd, Pd-Co (1:1) and Co nanoparticles prepared by microwave. Pd-Co nanoparticles are monodisperse spherical nanoparticles with average diameter of 4 nm. However, Co produces larger, non-spherical particles with an average diameter of 17 nm. In comparing these results to the Pd-Ni nanoparticles, both bimetallic nanoparticles are small and spherical in morphology regardless of the non-spherical shape of the corresponding pure metallic nanoparticles.

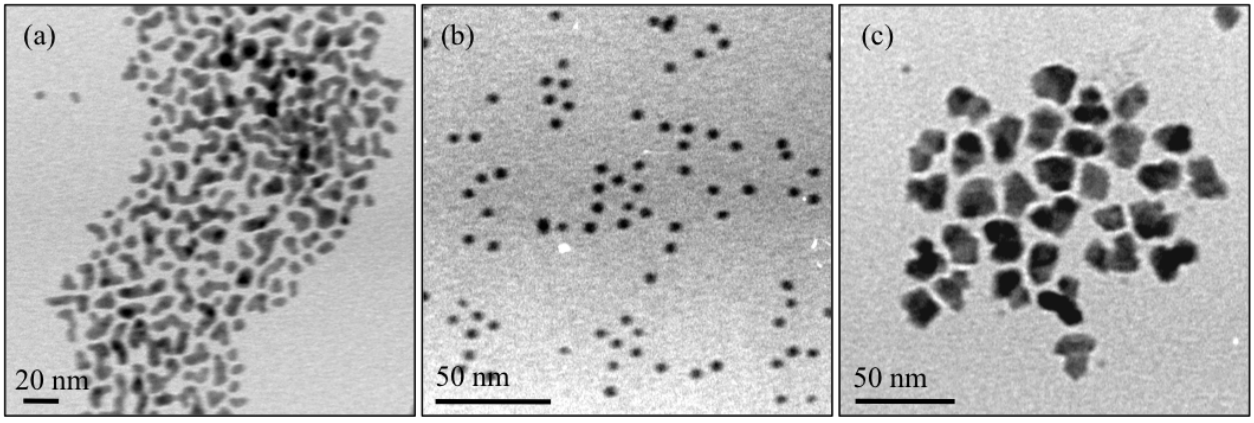

Figure 8.5. TEM of (a) Pd, (b) Pd-Co, (c) Co nanoparticles

8.4 Synthesis of metal nanoparticles supported on reduced graphene oxide

For the preparation of metal nanoparticles supported on graphene, two methods were studied. Figure 8.6 summarizes the synthetic strategies for the preparation of metallic

nanoparticles supported on RGO. Two approaches were studied for the preparation of metallic nanoparticles on RGO. The first approach (8.6-a) studies the simultaneous reduction of metal salt and GO using an *in situ* process. The second approach (8.6-b) studies the attachment of pre-synthesized metallic nanoparticles on RGO using a sonication method.

The first approach (8.6-a) studies the formation of metallic nanoparticles supported on RGO using an *in situ* process. Under these conditions, metal ions and GO are reduced simultaneously using MWI in the presence BTB and a mixture of OAC and oleylamine OAM. The reduction of GO using non-polar organic solvents including oleylamine has been previously reported.[206] GO has a high affinity for absorbing MWI and therefore, in the presence of GO, the reaction mixture rapidly heats up and there is significant local heating around the GO sheets in solution. Therefore, it is hypothesized that the nucleation and growth of the metallic nanoparticles are more likely to occur directly on the defects sites of the GO nanosheets. This hypothesis is further supported by the observation that the majority of the metallic nanoparticles are found directly adsorbed on the RGO nanosheets, as will be discussed in section 8.5.

The second approach (8.6-b) studies an *ex situ* process for preparing metallic nanoparticles supported on RGO. Under these conditions, metal ions are reduced using MWI in the presence of BTB and a mixture of OAC and OAM. After the metallic nanoparticles are formed, they are separated from the liquid phase and dried. The NP-RGO composites are formed by dispersing both metallic nanoparticles and RGO in hexanes using sonication. Following sonication there is good attachment between the organic capped nanoparticles and the RGO most likely attributed to strong interaction between the carbon capping agents and the RGO. *Ex stiu* processes are commonly used for the preparation of composite materials composed of metallic

nanoparticles on a support material because these methods allow for greater morphology control of the synthesis of the nanoparticles.

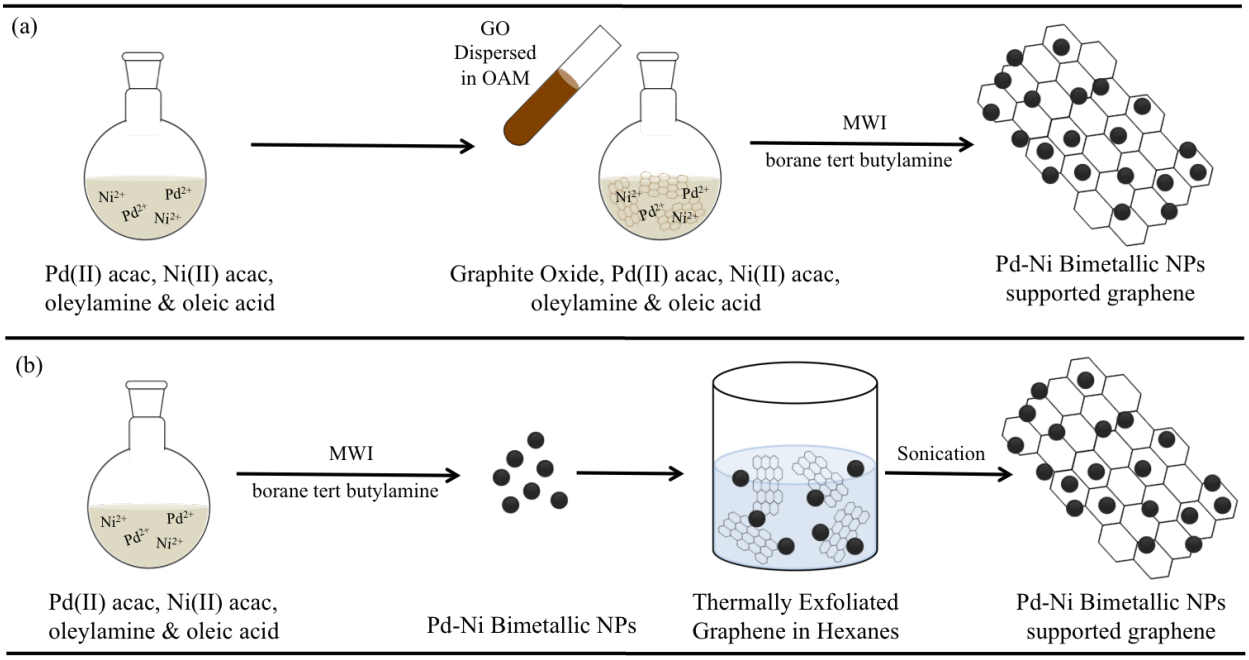

Figure 8.6. Schematic diagram summarizing synthetic strategies for the preparation of metallic nanoparticles supported on rGO.

As mentioned, both approached utilize GO as a starting material. GO was prepared from graphite powder following Hummers' method[203] by treatment with strong oxidizing agents ($KMnO_4$ in H_2SO_4), washing with water and drying. A complete preparation method for GO is given in Appendix A.

8.4.1 *In situ* synthesis of metal nanoparticle-RGO composites

GO (200 mg) is dispersed in 7 mL OAM by sonication for 4 hours. 0.5 mmol of $Pd(acac)_2$ was dissolved in 8 mL OAM and 0.32 mL OAC. The Pd reaction mixture was heated in a hot oil bath with stirring to 110 °C and the temperature was maintained for one hour to assist in dissolving and removal of water. During the heating process, N_2 is constantly being bubbled through the Pd reaction mixture. After heating, the reaction mixture is cooled to 90 °C. The GO

dispersion is then added to the Pd reaction mixture (adding prior to cooling would result in reduction of GO). In a separate test tube, 250 mg of BTB is dissolved in 2 mL OAM. The BTB solution is added all at once to the Pd-GO reaction mixture with stirring. MWI was applied to the reaction in an open round-bottom flask for 10 minutes. Following the microwave reaction, the precipitate was separated from the liquid phase by centrifugation in the presence of ethanol and dried at 80 °C overnight. Ni and Pd-Ni alloy nanoparticles supported on graphene were prepared using 0.5 mmol $Ni(acac)_2$ and 0.25 mmol of $Ni(acac)_2$ with 0.25 mmol of $Pd(acac)_2$, respectively. Similarly, Co and Pd-Co alloy nanoparticles supported on graphene were prepared using 0.5 mmol $Co(acac)_2$ and 0.25 mmol of $Co(acac)_2$ with 0.25 mmol of $Pd(acac)_2$, respectively. For both Co and Pd-Co alloy nanoparticles supported on grahene, 500 mg of BTB was used to ensure complete reduction of $Co(acac)_2$.

8.4.2 Sonciation (*ex situ)* synthesis of metal nanoparticle-RGO composites

GO prepared by Hummer's Method reduced using thermal exfoliation. In general, approximately 500 mg of GO is pressed into a pellet. The GO pellet is placed in a porcelain boat and loaded into a quartz tube (1 end open). The tube is under the flow of Argon, and the open end is connected to exhaust. The tube is inserted into a preheated tube furnace at 1200 °C for 2 minutes. Within in the first few second, light fluffy black powder is observed "floating" through the tube, which indicates the reduction of GO (thermally exfoliated graphene).

To prepare metal nanoparticles supported on graphene, 2.5 mg of preformed nanoparticles (prepared as described in section 8.2) and 10 mg of exfoliated graphene are dispersed in 15 mL of hexanes. The mixture was sonicated using bath sonication for 1 hour. It is expected that sonication results in binding of the metal nanoparticles to the RGO sheets. The

precipitate was separated from the liquid phase by centrifugation in the presence of ethanol and dried at 80 °C overnight.

8.4.3 Removal of organic ligands

In order to utilize the metal nanoparticles and nanoparticles-RGO composites, the OAM and OAC ligands are removed. Unsupported nanoparticles or composite materials are annealed under the flow of H_2 at 400 °C for 3 hrs. The nanoparticles are cooled to room temperature and CO oxidation catalysis is studied.

8.5 Characterization of metal nanoparticles supported on reduced graphene oxide

8.5.1 Raman spectroscopy of RGO

Raman spectroscopy was used to characterize the quality of RGO prepared using thermal exfoliation or MWI of GO. Few layer graphene typically exhibits a G band and D band. The Raman G band at ~1580 cm^{-1} is due to the doubly degenerate zone center E2g and is characteristic of the sp^2 carbon network.[205] The Raman D band at ~1350 cm^{-1} arises as a result of defects in the graphene structure and only appears in samples with a significant amount of defects or on the edges of pristine graphene sheets.[205] The ratio of the intensity of the Raman D and G bands is used to compare the relative number of defects in each sample. The Raman spectra of GO and RGO prepared through thermal exfoliation and MWI is displayed in Fig. 8.7. The ratio of intensities of the D band with respect to the G band increases slightly with the reduction of GO, from 0.96 to 1.0, which implies that the reduction using MWI in the presence of OAM leads to a higher number of defects in the graphene structure. For thermally exfoliated RGO, the ratio of intensities of the D band with respect to the G band slightly decreases, from 0.96 to 0.9. This decrease in intensity of the D band implies that fewer defects exist in RGO

prepared through thermal exfoliation. Thus, RGO prepared using MWI in the presence of OAM has a greater number of defect sites compared to RGO prepared using thermal exfoliation.

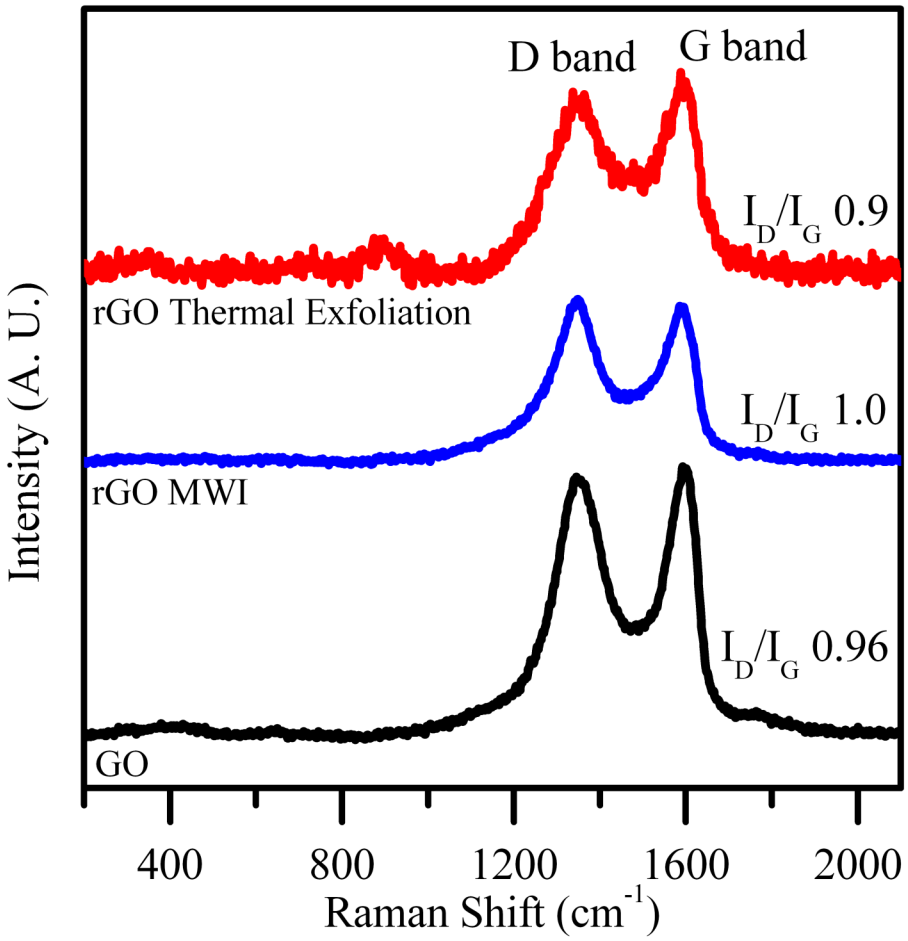

Figure 8.7. Raman spectra of GO, RGO prepared by MWI and RGO prepared by thermal exfoliation.

8.5.2 X-ray diffraction

The crystallinity of the Pd-RGO, Pd-Ni-RGO and Ni-RGO was studied using XRD and is displayed in Figure 8.8. These results show the corresponding [111] plane for Pd, Pd-Ni and Ni, indicating alloy formation in the presence of GO. These results imply that the addition of GO to the reaction mixture prior to MWI does not inhibit alloy formation. The absence of peaks corresponding to pure Pd and Ni in the Pd-Ni alloy provides strong evidence that a binary

nucleation mechanism persists in the presence of GO. Further, it is observed that the Pd-Ni and Ni peaks are broad, consistent with the formation of very small nanoparticles. Particle size will be further studied using TEM.

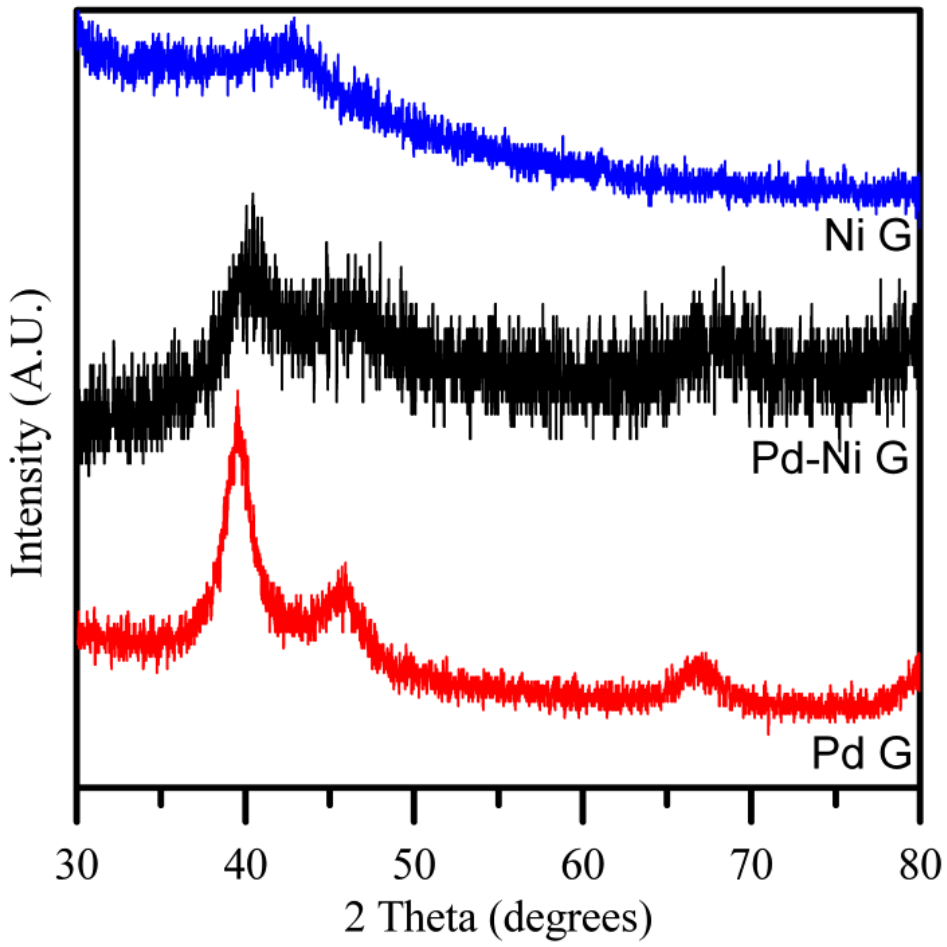

Figure 8.8 Powder X-Ray diffraction patterns of Pd-RGO, Pd-Ni- RGO and Ni- RGO.

8.5.3 Morphology

The morphology of the metal nanoparticles supported on RGO was studied. It was observed that the morphology of the resulting metallic nanoparticles supported on RGO is not affected by the addition of GO to the reaction mixture, and the metal nanoparticles maintain the same small, spherical shape when prepared alone. Figure 8.9 displays the TEM images of Pd (a-b), Pd-Ni (c), Ni (e), Pd-Co (d) and Co (f) supported on graphene prepared in situ. The *in situ*

method results in the formation of monodisperse spherical metallic nanoparticles supported on RGO sheets. It is expected that defects on the GO sheets act as nucleation sites for the formation of metal nanoparticles. The particles are not aggregated indicating that the metal nanoparticles are anchored on the RGO support, which provides strong evidence for the nucleation mechanism. Furthermore, the absence of free nanoparticles not attached to RGO indicates strong binding between the metallic nanoparticles and RGO.

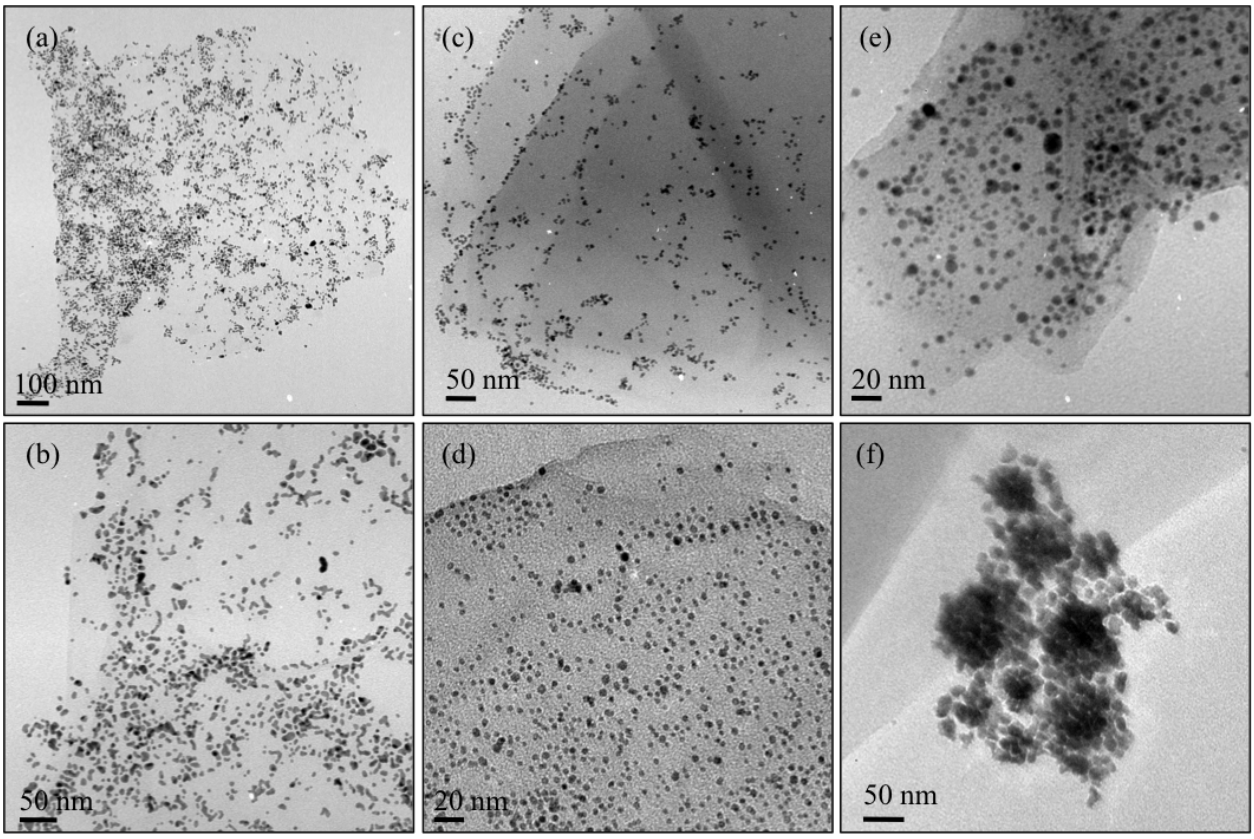

Figure 8.9. TEM of (a-b) Pd (c) Pd-Ni, (e) Ni, (d) Pd-Co and (f) Co nanoparticles supported on RGO prepared *in situ*.

The morphology of the metal nanoparticles supported on RGO prepared *ex situ* is also studied using TEM, as shown in Figure 8.10. The method uses preformed nanoparticles, and as expected the metal nanoparticles retain their original morphologies. There appears to be strong interaction between the OAM and OAC capped particles and the RGO sheets, which is indicated

by the heavy decoration and absence of free particles. This confirms that both methods result in metal nanoparticles anchored to RGO sheets.

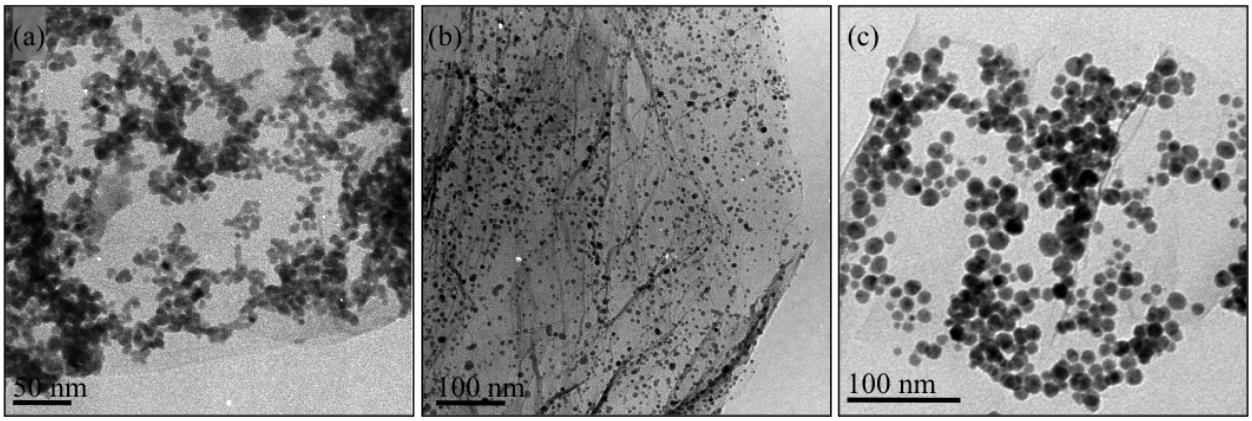

Figure 8.10 TEM of (a) Pd (b) Pd-Ni and (c) Ni nanoparticles supported on RGO prepared *ex situ*.

8.6 Catalytic CO oxidation

The catalytic activity for CO oxidation of the metallic and bimetallic nanoparticles supported on RGO prepared by MWI using both the *in situ* and *ex situ* approaches was studied. In all cases, samples of 29 wt % nanoparticles supported on RGO were considered. The capping agents were removed through the annealing process as described in section 8.4.3.

Figure 8.11 compares the CO conversion over pure, unsupported nanocatalysts prepared by the MWI method. It is clear that the Pd sample exhibits the highest activity with 50% and 100% conversions of CO to CO_2 at temperatures of 153 and 234 °C, respectively (Table 8.1). Unsupported Ni and Co show the lowest activity with 50% and 100% conversions at temperatures around 310 and 320 °C, respectively. The unsupported Pd-Ni and Pd-Co nanoparticles show similar catalytic activity to one another with 50% and 100% conversions at temperature around 300 °C and 315 °C, respectively.

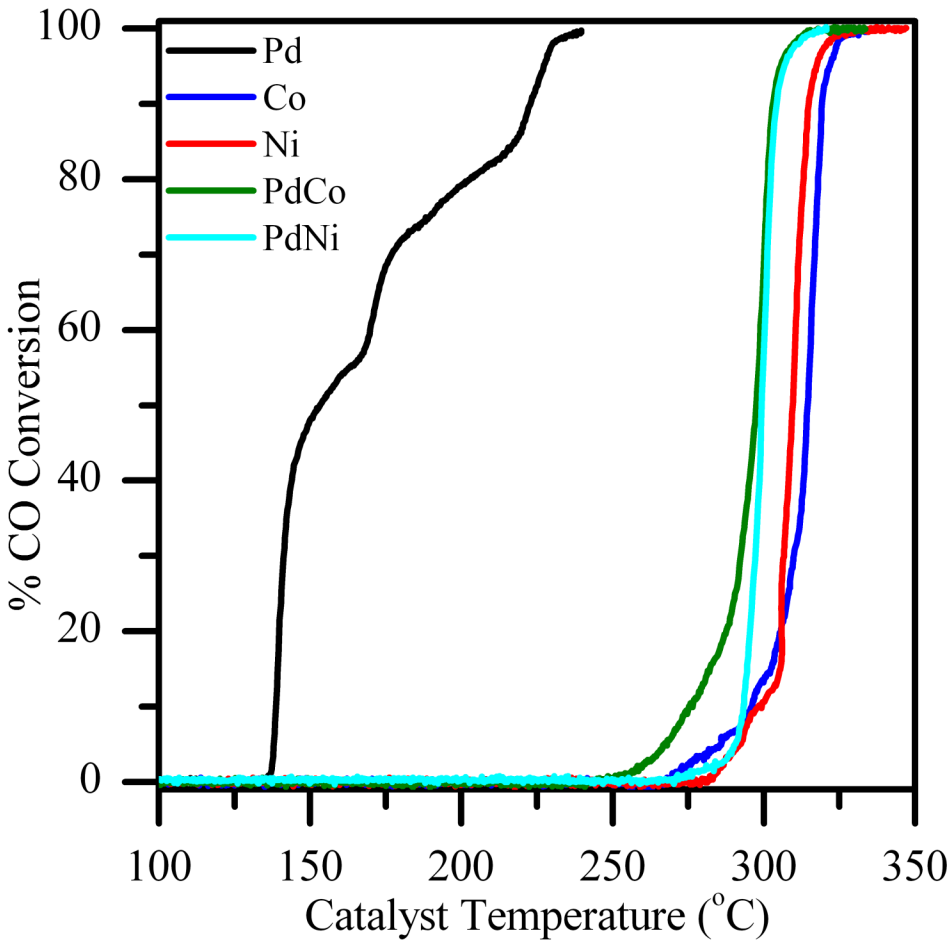

Figure 8.11. CO oxidation on different unsupported metal nanoparticles: Pd, Ni, Co and Pd-Ni, Pd-Co nanoalloys.

Upon supporting the metal nanoparticles on RGO, the nanoalloys show significant enhancement towards CO oxidation. First, the composites were prepared using the *in situ* method, which allows for simultaneous nanoparticle formation and graphene oxide reduction, were studied. In this case

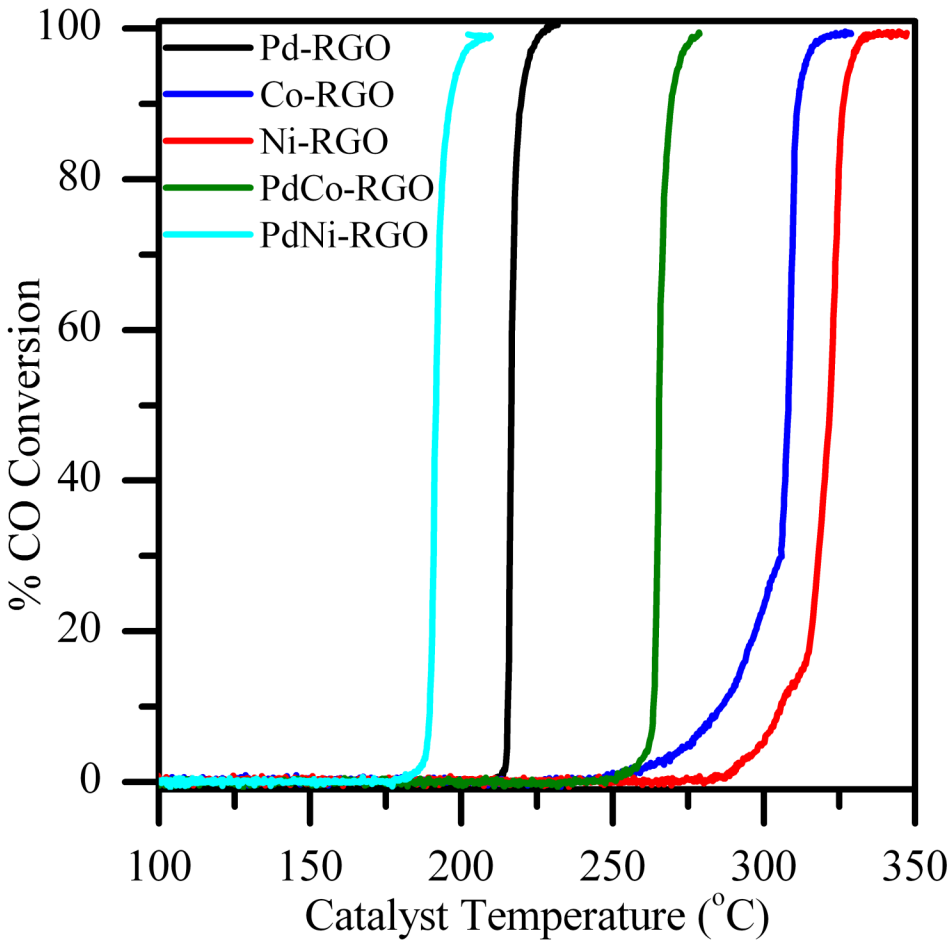

Figure 8.12 CO oxidation on different metal-RGO nanocomposites prepared by the *in situ* MWI method.

Next, the composites were prepared using the *ex situ* method in which preformed nanoparticles were attached to RGO through sonication were studied. Figure 8.13 compares the CO conversion over nanocatalysts supported on RGO prepared by the *ex situ* sonication method. It is clear that the Pd-Ni sample exhibits the highest activity with 50% and 100 % conversions of CO to CO_2 at temperatures of 229 and 263 °C, respectively (Table 8.1). The performance of the supported bimetallic alloys prepared by sonication is consistent with observed activity of the supported bimetallic alloys prepared in situ shown in Figure 8.12. The order of activity for composites prepared using sonication is consitstent with composites prepared *in situ*: PdNi

supported on RGO is highest, Pd supported on RGO is second highest and PdCo is third highest. The observed activity is conistently at a higheter temperature for the composites prepared by the sonication method in comparison with those prepared *in situ*, which implies an advantage to reducing metal precursors and GO simultaneously. This is interesting because many reports have focused on *ex situ* methods for supporting preformed nanoparticles on catalyst supports for catalysis applications due to synthetic challenges.

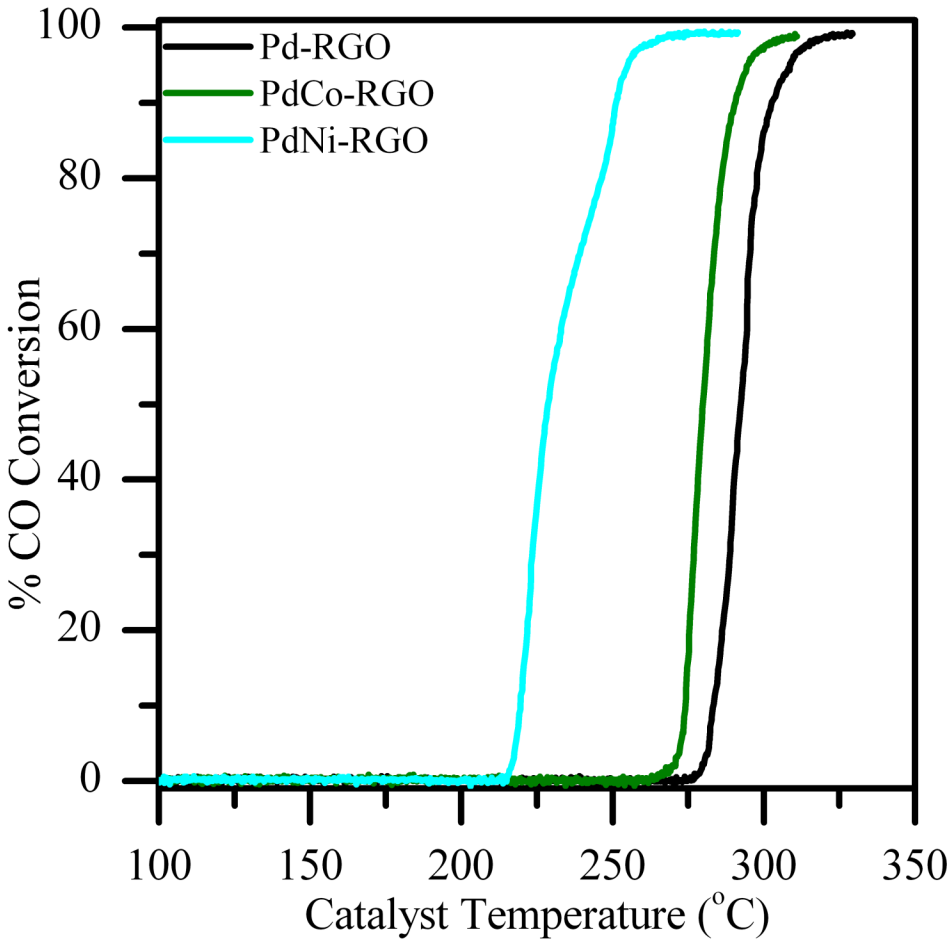

Figure 8.13 CO oxidation on different metal-RGO nanocomposites prepared by the sonication (*ex situ*) method.

Table 8.1 Temperatures for the CO oxidation over nanocatalysts.

Catalyst	Unsupported		Supported RGO *in situ*		Supported RGO *ex situ*	
	$T_{50\%}$ (°C)	$T_{100\%}$ (°C)	$T_{50\%}$ (°C)	$T_{100\%}$ (°C)	$T_{50\%}$ (°C)	$T_{100\%}$ (°C)
Pd	153	234	216	229	292	319
Co	314	325	308	322	-	-
Ni	310	322	322	335	-	-
PdCo	297	313	265	278	280	305
PdNi	299	314	192	206	229	263

8.7 Conclusions

This work demonstrates a simple MWI method for synthesis of a variety of metallic and bimetallic nanoparticles. The reduction of metal ions in the presence of a mixture of OAC and OAM with strong reducing agent BTB results in a binary nucleation process for the formation of alloy nanoparticles. The strong binding of OAC and OAM to the nanoparticle surface provides efficient surface capping, which prevents oxidation by atmospheric oxygen.

Furthermore, the same method can be used to synthesize metallic and bimetallic nanoparticles supported on RGO as catalysts for CO oxidation. GO has a high affinity for absorbing MWI, which results in local heating around the GO nanosheets. This local heating facilitates the reduction of metal precursors and the GO nanosheets act as heterogeneous surface sites for nucleation and growth of metallic nanoparticles. Preformed metallic and bimetallic nanoparticles are also supported on RGO nanosheets by sonication method. The results reveal that PdNi supported on RGO exhibits high activity for CO oxidation. The results reveal that PdNi supported on RGO exhibits high activity for CO oxidation. The nanocomposites prepared

by simultaneous reduction of metal ions in the presence of GO are consistently more active towards CO oxidation thatn those prepared using the sonication method.

Chapter 8: Conclusions

The work presented in this dissertation described the synthesis, characterization and photocatalytic activity of various ZnO-based nanomaterials. A simple one-pot MWI synthesis method for producing ZnO nanostructures with well-controlled morphologies was developed. ZnO nanostructures are formed by the rapid decomposition of zinc acetate using MWI in the presence of oleic acid and oleylamine, which results in nucleation of subsequent formation of ZnO hexagonal nanopyramids or nanorods depending on concentration. ZnO nanostructures are stabilized using a mixture of oleic acid and oleylamine, which selectively prevents the growth of ZnO nanostructures and directs the morphology. This is one of the first MWI methods avaialbe for a one-pot synthesis of ZnO nanostructures. One of the major benfits of this synthesis is that it uses only three reagents (zinc acetate, oleic acid and oleylamine), because the mixture of oleic acid and oleylamine acts as both stabilizing ligand and solvent. The simplicity of this method allows for it to be extended for incorporation other elements and functional materials for synthesis of doped-ZnO and ZnO-based nanocomposites, respectively.

Although oleic acid and oleylamine produce high quality, monodisperse nanostructures, they are only soluble in non-polar solvents such as toluene or hexanes. Through the use of ligand exchange with mercaptoundecanoic acid, ZnO nanostructures were transformed into water-soluble ZnO nanostructures. These water-soluble nanostructures were found to be effective

catalysts for the photodegradation of malachite green. The photocatalytic activity was improved by varying the morphology. ZnO nanorods with an average aspect ratio of 5 were found to be the most active pure ZnO photocatayst.

Various ways to enhance photocatalytic activity of ZnO nanostructures were studied by modifying this MWI method. Photocatalytic activity is enhanced through band gap modulation and the reduction of electron-hole recombination. Several approaches were studied, which included the incorporation of Au nanoparticles, N-doping of ZnO, supporting ZnO nanoparticles on reduced graphene oxide, and supporting N-doped ZnO on N-doped reduced graphene oxide.

The first system studied incorporated gold nanoparticles for the formation of Au-ZnO nanocomposites. In this system, the formation mechanisms of Au-ZnO nanocomposites were studied by starting with Au^{3+} and preformed Au nanoparticles. It was determined that, in both systems, Au nanocrystals act as heterogeneous nuclei for the nucleation and growth of ZnO nanopyramids, however, preformed Au nanoparticles result in a more narrow size distrubution of uniform Au-ZnO nanopryamids compared to Au^{3+}. Furthermore, this work provided direct evidence for the effect of Au nanocrystals on the assembly and growth for ZnO nanopyramids. The Au-ZnO nanopyramids may present improved performance in solar energy conversion and photocatalysis.

The second system studied were N-doped ZnO nanostructures, which are of increasing interest for both catalytic and electronic applications. Through modification of the MWI synthesis method to incorporate urea as a nitrogen source, a simple one-pot MWI synthesis method for N-doped ZnO was developed. This is one of very few wet synthesis methods for producing N-doped ZnO, and it is the only MWI synthesis method reported. This system was explored by adjusting the level of N-doping as well as the ZnO morphology by controlling the

urea and zinc acetate concentration, respectively. Furthermore, the charge carriers were characterized using Mott-Shottky measurement, which determined this approach yielded p-type ZnO.

The third system investigated using reduced graphene oxide as a catalyst support for ZnO nanostructures. ZnO nanoparticles supported on reduced graphene oxide nanosheets were synthesized *in situ* by adding GO to the reaction mixture prior to MWI. The RGO nanosheets resulted in increased reaction temperatures due to high microwave affinity and provided heterogeneous nucleation sites for nucleation and growth of ZnO nanoparticles. These nanocomposites are also transformed into water-soluble materials using the ligand exchange procedure. The ZnO-RGO nanocomposites show enhanced photocatalytic activity for the degradation of malachite green over the unsupported ZnO nanostructures. The enhanced activity is attributed to efficient charge transfer of the photogenerated electrons in the conduction band of ZnO to graphene.

By combining two approaches for enhancing photocatalytic activity, the final ZnO-based system studied was N-doped ZnO supported on N-doped RGO nanosheets. These nanocomposites were prepared using a simple combustion method through the decomposition of zinc nitrate and reduction of GO in the presence of urea. GO proved heterogeneous nucleation sites for ZnO, which resulted in well-defined N-ZnO nanoparticles supported on N-RGO nanosheets. The photocatalytic activity was enhanced 3-fold compared to both unsupported N-ZnO and pure ZnO supported on RGO. Therefore, this is a very promising system for possible enhancement towards solar energy conversion and other photocatalytic systems.

This work demonstrates the flexibility of this simple MWI approach, which can be tuned to sythesize various ZnO-based nanomaterials, which include N-doped ZnO, Au-ZnO, ZnO-

RGO and N-ZnO-RGO. The ability to use a single method for the preparation of a broad range of ZnO-based nanomaterials allows for the direct comparison of the photocatalytic activity of each system. Furthermore, this synthesis procedure could easily be extended to other ZnO systems and possibly other metal oxide systems. For example, the high photocatalytic activity of N-ZnO-RGO encourages approaches to study other systems that dope both the functional metal oxide and the carbon support.

A variety of future projects could be developed based off of the flexibility of this sysnthesis method and the success of enhancing photocatalytic activity. Since photocatalysis is an extremely important field, one might envision a multitude of different systems that could be developed trhough these studies. These might include the incorporation of other atoms such as boron or lithium into the ZnO nanostructures and their effect on photocatalytic activity. Co-doping of ZnO could also be explored, as it is well known that the addition of a second dopant may lead to increased stability. Further systems to study might include the incorporation of additional functional materials such as silver or pallaidum nanoparticles or carbon nanotubes. Other studies might focus the development of other synthesis methods that would make these systems water-soluble without the need for ligand exhange.

In addition to ZnO-based nanostructures, this dissertation also presents synthesis and characterization of metallic and bimetallic nanoparticles for CO oxidation. Metallic and bimetallic nanoparticles are prepared by reducing metal ions in the presence of a mixture of OAC and OAM with strong reducing agent BTB using MWI. This method results in a binary nucleation process for the formation of alloy nanoparticles. OAC and OAM bind strongly to the nanoparticles surface and prevent oxidation. The nanoparticles are supported on RGO using two methods: in situ by reduction of GO and sonication of preformed nanoparticles with RGO. PdNi

supported on RGO was determined to have the highest activity for CO oxidation. The nanocomposites prepared by simultaneous reduction of metal ions in the presence of GO are consistently more active towards CO oxidation thatn those prepared using the sonication method.

This dissertation presented an all-encompassing approach to understanding ZnO-based nanocatalysts from synthesis and characterization as well as catalytic activity. By understanding each step of the process, limitations and advantages at each step can assessed. This approach allowed for a more complete understanding of these systems.

References

1. Wang, Z. L. Zinc oxide nanostructures: growth, properties and applications *Journal of Physics-Condensed Matter* **2004,** 16, R829-R858.

2. Chang, J. F.; Kuo, H. H.; Leu, I. C.; Hon, M. H. The effects of thickness and operation temperature on ZnO : Al thin film CO gas sensor *Sensors and Actuators B-Chemical* **2002,** 84, 258-264.

3. Comini, E.; Faglia, G.; Sberveglieri, G.; Pan, Z. W.; Wang, Z. L. Stable and highly sensitive gas sensors based on semiconducting oxide nanobelts *Appl. Phys. Lett.* **2002,** 81, 1869-1871.

4. Lupan, O.; Emelchenko, G. A.; Ursaki, V. V.; Chai, G.; Redkin, A. N.; Gruzintsev, A. N.; Tiginyanu, I. M.; Chow, L.; Ono, L. K.; Cuenya, B. R.; Heinrich, H.; Yakimov, E. E. Synthesis and characterization of ZnO nanowires for nanosensor applications *Mater. Res. Bull.* **2010,** 45, 1026-1032.

5. Minne, S. C.; Manalis, S. R.; Quate, C. F. Parallel atomic force microscopy using cantilevers with integrated piezoresistive sensors and integrated piezoelectric actuators *Appl. Phys. Lett.* **1995,** 67, 3918-3920.

6. Hu, X.; Li, G.; Yu, J. C. Design, Fabrication, and Modification of Nanostructured Semiconductor Materials for Environmental and Energy Applications *Langmuir* **2010,** 26, 3031-3039.

7. Raula, M.; Rashid, M. H.; Paira, T. K.; Dinda, E.; Mandal, T. K. Ascorbate-Assisted Growth of Hierarchical ZnO Nanostructures: Sphere, Spindle, and Flower and Their Catalytic Properties *Langmuir* **2010,** 26, 8769-8782.

8. Huang, M. H.; Mao, S.; Feick, H.; Yan, H. Q.; Wu, Y. Y.; Kind, H.; Weber, E.; Russo, R.; Yang, P. D. Room-temperature ultraviolet nanowire nanolasers *Science* **2001,** 292, 1897-1899.

9. Kong, Y. C.; Yu, D. P.; Zhang, B.; Fang, W.; Feng, S. Q. Ultraviolet-emitting ZnO nanowires synthesized by a physical vapor deposition approach *Appl. Phys. Lett.* **2001,** 78, 407-409.

10. Zheng, M. J.; Zhang, L. D.; Li, G. H.; Shen, W. Z. Fabrication and optical properties of large-scale uniform zinc oxide nanowire arrays by one-step electrochemical deposition technique *Chem. Phys. Lett.* **2002,** 363, 123-128.

11. Ozgur, U.; Alivov, Y. I.; Liu, C.; Teke, A.; Reshchikov, M. A.; Dogan, S.; Avrutin, V.; Cho, S. J.; Morkoc, H. A comprehensive review of ZnO materials and devices *J. Appl. Phys.* **2005,** 98.

12. Bacaksiz, E.; Yilmaz, S.; Parlak, M.; Varilci, A.; Altunbas, M. Effects of annealing temperature on the structural and optical properties of ZnO hexagonal pyramids *J. Alloys Compd.* **2009,** 478, 367-370.

13. Herring, N. P.; AbouZeid, K.; Mohamed, M. B.; Pinsk, J.; El-Shall, M. S. Formation Mechanisms of Gold-Zinc Oxide Hexagonal Nanopyramids by Heterogeneous Nucleation using Microwave Synthesis *Langmuir* **2011,** 27, 15146-15154.

14. Mapa, M.; Gopinath, C. S. Combustion Synthesis of Triangular and Multifunctional ZnO1-xNx (x <= 0.15) Materials *Chem. Mater.* **2009,** 21, 351-359.

15. Zhou, X.; Xie, Z. X.; Jiang, Z. Y.; Kuang, Q.; Zhang, S. H.; Xu, T.; Huang, R. B.; Zheng, L. S. Formation of ZnO hexagonal micro-pyramids: a successful control of the exposed polar surfaces with the assistance of an ionic liquid *Chem. Commun.* **2005**, 5572-5574.

16. Yang, Y.; Guo, W.; Wang, X. Q.; Wang, Z. Z.; Qi, J.; Zhang, Y. Size Dependence of Dielectric Constant in a Single Pencil-Like ZnO Nanowire *Nano Lett.* **2012,** 12, 1919-1922.

17. Cheng, C. W.; Sie, E. J.; Liu, B.; Huan, C. H. A.; Sum, T. C.; Sun, H. D.; Fan, H. J. Surface plasmon enhanced band edge luminescence of ZnO nanorods by capping Au nanoparticles *Appl. Phys. Lett.* **2010,** 96, 071107-3.

18. He, H.; Cai, W.; Lin, Y.; Chen, B. Surface Decoration of ZnO Nanorod Arrays by Electrophoresis in the Au Colloidal Solution Prepared by Laser Ablation in Water *Langmuir* **2010,** 26, 8925-8932.

19. Liu, Z. F.; Zhang, Q. H.; Li, Y. G.; Wang, H. Z. Solvothermal synthesis, photoluminescence and photocatalytic properties of pencil-like ZnO microrods *J. Phys. Chem. Solids* **2012,** 73, 651-655.

20. Mahmood, K.; Park, S. B. Growth and conductivity enhancement of N-doped ZnO nanorod arrays *J. Cryst. Growth* **2012,** 347, 104-112.

21. Vayssieres, L. Growth of arrayed nanorods and nanowires of ZnO from aqueous solutions *Adv. Mater.* **2003,** 15, 464-466.

22. Wang, Z. L. Splendid One-Dimensional Nanostructures of Zinc Oxide: A New Nanomaterial Family for Nanotechnology *Acs Nano* **2008,** 2, 1987-1992.

23. Wang, X. D.; Zhou, J.; Lao, C. S.; Song, J. H.; Xu, N. S.; Wang, Z. L. In situ field emission of density-controlled ZnO nanowire arrays *Adv. Mater.* **2007,** 19, 1627.

24. Guo, Z.; Zhao, D.; Liu, Y.; Shen, D.; Zhang, J.; Li, B. Visible and ultraviolet light alternative photodetector based on ZnO nanowire/n-Si heterojunction *Appl. Phys. Lett.* **2008,** 93, 163501-3.

25. Greene, L. E.; Law, M.; Tan, D. H.; Montano, M.; Goldberger, J.; Somorjai, G.; Yang, P. General Route to Vertical ZnO Nanowire Arrays Using Textured ZnO Seeds *Nano Lett.* **2005,** 5, 1231-1236.

26. Greene, L. E.; Law, M.; Goldberger, J.; Kim, F.; Johnson, J. C.; Zhang, Y.; Saykally, R. J.; Yang, P. Low-Temperature Wafer-Scale Production of ZnO Nanowire Arrays *Angew. Chem. Int. Ed.* **2003,** 42, 3031-3034.

27. Rackauskas, S.; Mustonen, K.; Jarvinen, T.; Mattila, M.; Klimova, O.; Jiang, H.; Tolochko, O.; Lipsanen, H.; Kauppinen, E. I.; Nasibulin, A. G. Synthesis of ZnO tetrapods for flexible and transparent UV sensors *Nanotechnology* **2012,** 23.

28. Qiu, Y.; Yan, K.; Deng, H.; Yang, S. Secondary Branching and Nitrogen Doping of ZnO Nanotetrapods: Building a Highly Active Network for Photoelectrochemical Water Splitting *Nano Lett.* **2012,** 12, 407-413.

29. Choi, K.; Kang, T.; Oh, S. G. Preparation of disk shaped ZnO particles using surfactant and their PL properties *Mater. Lett.* **2012,** 75, 240-243.

30. Gargas, D. J.; Moore, M. C.; Ni, A.; Chang, S.-W.; Zhang, Z.; Chuang, S.-L.; Yang, P. Whispering Gallery Mode Lasing from Zinc Oxide Hexagonal Nanodisks *Acs Nano* **2010**.

31. Li, F.; Ding, Y.; Gao, P. X. X.; Xin, X. Q.; Wang, Z. L. Single-cystal hexagonal disks and rings of ZnO: Low-temperature, large-scale synthesis and growth mechanism *Angewandte Chemie-International Edition* **2004,** 43, 5238-5242.

32. Gao, P. X.; Wang, Z. L. Mesoporous polyhedral cages and shells formed by textured self-assembly of ZnO nanocrystals *J. Am. Chem. Soc.* **2003,** 125, 11299-11305.

33. Lao, C. S.; Gao, P. M.; Sen Yang, R.; Zhang, Y.; Dai, Y.; Wang, Z. L. Formation of double-side teethed nanocombs of ZnO and self-catalysis of Zn-terminated polar surface *Chem. Phys. Lett.* **2006,** 417, 358-362.

34. Kong, X. Y.; Wang, Z. L. Spontaneous polarization-induced nanohelixes, nanosprings, and nanorings of piezoelectric nanobelts *Nano Lett.* **2003,** 3, 1625-1631.

35. Kong, X. Y.; Ding, Y.; Yang, R.; Wang, Z. L. Single-crystal nanorings formed by epitaxial self-coiling of polar nanobelts *Science* **2004,** 303, 1348-1351.

36. Li, P.; Wang, D. S.; Wei, Z.; Peng, Q.; Li, Y. D. Systematic Synthesis of ZnO Nanostructures *Chemistry-a European Journal* **2013,** 19, 3735-3740.

37. Munoz-Hernandez, G.; Escobedo-Morales, A.; Pal, U. Thermolytic Growth of ZnO Nanocrystals: Morphology Control and Optical Properties *Crystal Growth & Design* **2009,** 9, 297-300.

38. Yang, M.; Sun, K.; Kotov, N. A. Formation and Assembly-Disassembly Processes of ZnO Hexagonal Pyramids Driven by Dipolar and Excluded Volume Interactions *J. Am. Chem. Soc.* **2010,** 132, 1860-1872.

39. Huang, A. S.; Caro, J. Controlled growth of zinc oxide crystals with tunable shape *J. Cryst. Growth* **2010,** 312, 947-952.

40. Tong, H.; Ouyang, S. X.; Bi, Y. P.; Umezawa, N.; Oshikiri, M.; Ye, J. H. Nano-photocatalytic Materials: Possibilities and Challenges *Adv. Mater.* **2012,** 24, 229-251.

41. Herrmann, J.-M. Heterogeneous photocatalysis: fundamentals and applications to the removal of various types of aqueous pollutants *Catal. Today* **1999,** 53, 115-129.

42. Yang, X.; Wolcott, A.; Wang, G.; Sobo, A.; Fitzmorris, R. C.; Qian, F.; Zhang, J. Z.; Li, Y. Nitrogen-Doped ZnO Nanowire Arrays for Photoelectrochemical Water Splitting *Nano Lett.* **2009,** 9, 2331-2336.

43. Kamat, P. V. Meeting the clean energy demand: Nanostructure architectures for solar energy conversion *J. Phys. Chem. C* **2007,** 111, 2834-2860.

44. Malato, S.; Fernandez-Ibanez, P.; Maldonado, M. I.; Blanco, J.; Gernjak, W. Decontamination and disinfection of water by solar photocatalysis: Recent overview and trends *Catal. Today* **2009,** 147, 1-59.

45. Nakajima, A.; Hashimoto, K.; Watanabe, T.; Takai, K.; Yamauchi, G.; Fujishima, A. Transparent superhydrophobic thin films with self-cleaning properties *Langmuir* **2000,** 16, 7044-7047.

46. Patil, A. B.; Patil, K. R.; Pardeshi, S. K. Enhancement of oxygen vacancies and solar photocatalytic activity of zinc oxide by incorporation of nonmetal *J. Solid State Chem.* **2011,** 184, 3273-3279.

47. Lv, T.; Pan, L.; Liu, X.; Lu, T.; Zhu, G.; Sun, Z. Enhanced photocatalytic degradation of methylene blue by ZnO-reduced graphene oxide composite synthesized via microwave-assisted reaction *J. Alloys Compd.* **2011,** 509, 10086-10091.

48. Xu, T.; Zhang, L.; Cheng, H.; Zhu, Y. Significantly enhanced photocatalytic performance of ZnO via graphene hybridization and the mechanism study *Applied Catalysis B-Environmental* **2011,** 101, 382-387.

49. Yang, Y.; Ren, L. L.; Zhang, C.; Huang, S.; Liu, T. X. Facile Fabrication of Functionalized Graphene Sheets (FGS)/ZnO Nanocomposites with Photocatalytic Property *Acs Applied Materials & Interfaces* **2011,** 3, 2779-2785.

50. Sobana, N.; Swaminathan, M. The effect of operational parameters on the photocatalytic degradation of acid red 18 by ZnO *Sep. Purif. Technol.* **2007,** 56, 101-107.

51. Gao, Y.; Pu, X.; Zhang, D.; Ding, G.; Shao, X.; Ma, J. Combustion synthesis of graphene oxide-TiO2 hybrid materials for photodegradation of methyl orange *Carbon* **2012,** 50, 4093-4101.

52. Bahnemann, D.; Bockelmann, D.; Goslich, R. Mechanistic studies of water detoxification in illuminated TiO2 suspensions *Solar Energy Materials* **1991,** 24, 564-583.

53. Chakrabarti, S.; Dutta, B. K. Photocatalytic degradation of model textile dyes in wastewater using ZnO as semiconductor catalyst *J. Hazard. Mater.* **2004,** 112, 269-278.

54. Chen, C. C.; Lu, C. S.; Chung, Y. C.; Jan, J. L. UV light induced photodegradation of malachite green on TiO2 nanoparticles *J. Hazard. Mater.* **2007,** 141.

55. Dawson, A.; Kamat, P. V. Semiconductor-metal nanocomposites. Photoinduced fusion and photocatalysis of gold-capped TiO2 (TiO2/Gold) nanoparticles *J. Phys. Chem. B* **2001,** 105, 960-966.

56. Diwald, O.; Thompson, T. L.; Goralski, E. G.; Walck, S. D.; Yates, J. T. The effect of nitrogen ion implantation on the photoactivity of TiO2 rutile single crystals *J. Phys. Chem. B* **2004,** 108, 52-57.

57. Fu, D.; Han, G.; Chang, Y.; Dong, J. The synthesis and properties of ZnO-graphene nano hybrid for photodegradation of organic pollutant in water *Mater. Chem. Phys.* **2012,** 132, 673-681.

58. Gaya, U. I.; Abdullah, A. H. Heterogeneous photocatalytic degradation of organic contaminants over titanium dioxide: A review of fundamentals, progress and problems *Journal of Photochemistry and Photobiology C-Photochemistry Reviews* **2008,** 9, 1-12.

59. Gopalakrishnan, K.; Joshi, H. M.; Kumar, P.; Panchakarla, L. S.; Rao, C. N. R. Selectivity in the photocatalytic properties of the composites of TiO2 nanoparticles with B- and N-doped graphenes *Chem. Phys. Lett.* **2011,** 511, 304-308.

60. Hariharan, C. Photocatalytic degradation of organic contaminants in water by ZnO nanoparticles: Revisited *Applied Catalysis a-General* **2006,** 304, 55-61.

61. Kajbafvala, A.; Ghorbani, H.; Paravar, A.; Samberg, J. P.; Kajbafvala, E.; Sadrnezhaad, S. K. Effects of morphology on photocatalytic performance of Zinc oxide nanostructures synthesized by rapid microwave irradiation methods *Superlattices Microstruct.* **2012,** 51, 512-522.

62. Kim, D.; Huh, Y. D. Morphology-dependent photocatalytic activities of hierarchical microstructures of ZnO *Mater. Lett.* **2011,** 65, 2100-2103.

63. Kumar, P. S. S.; Manivel, A.; Anandan, S. Synthesis of Ag-ZnO nanoparticles for enhanced photocatalytic degradation of acid red 88 in aqueous environment *Water Sci. Technol.* **2009,** 59, 1423-1430.

64. Kumar, P. S. S.; Raj, M. R.; Anandan, S.; Zhou, M. F.; Ashokkumar, M. Visible light assisted photocatalytic degradation of acid red 88 using Au-ZnO nanophotocatalysts *Water Sci. Technol.* **2009,** 60, 1589-1596.

65. Lakshmi, S.; Renganathan, R.; Fujita, S. Study on TiO2-mediated photocatalytic degradation of methylene-blue *Journal of Photochemistry and Photobiology a-Chemistry* **1995,** 88, 163-167.

66. Li, B.; Cao, H. ZnO@graphene composite with enhanced performance for the removal of dye from water *J. Mater. Chem.* **2010,** 21, 3346-3349.

67. Li, B.; Liu, T.; Wang, Y.; Wang, Z. ZnO/graphene-oxide nanocomposite with remarkably enhanced visible-light-driven photocatalytic performance *J. Colloid Interface Sci.* **2012,** 377, 114-121.

68. Li, P.; Wei, Z.; Wu, T.; Peng, Q.; Li, Y. Au-ZnO Hybrid Nanopyramids and Their Photocatalytic Properties *J. Am. Chem. Soc.* **2011,** 133, 5660-5663.

69. Liu, X.; Pan, L.; Lv, T.; Lu, T.; Zhu, G.; Sun, Z.; Sun, C. Microwave-assisted synthesis of ZnO-graphene composite for photocatalytic reduction of Cr(VI) *Catalysis Science & Technology* **2011,** 1, 1189-1193.

70. Lu, F.; Cai, W. P.; Zhang, Y. G. ZnO hierarchical micro/nanoarchitectures: Solvothermal synthesis and structurally enhanced photocatalytic performance *Adv. Funct. Mater.* **2008,** 18, 1047-1056.

71. Lu, W. W.; Liu, G. S.; Gao, S. Y.; Xing, S. T.; Wang, J. J. Tyrosine-assisted preparation of Ag/ZnO nanocomposites with enhanced photocatalytic performance and synergistic antibacterial activities *Nanotechnology* **2008,** 19.

72. Ray, A. K.; Beenackers, A. Novel photocatalytic reactor for water purification *AlChE J.* **1998,** 44, 477-483.

73. Yang, J. H.; Wang, J.; Li, X. Y.; Lang, J. H.; Liu, F. Z.; Yang, L. L.; Zhai, H. J.; Gao, M.; Zhao, X. T. Effect of polar and non-polar surfaces of ZnO nanostructures on photocatalytic properties *J. Alloys Compd.* **2012,** 528, 28-33.

74. Zhou, X.; Shi, T.; Zhou, H. Hydrothermal preparation of ZnO-reduced graphene oxide hybrid with high performance in photocatalytic degradation *Appl. Surf. Sci.* **2012,** 258, 6204-6211.

75. Mills, A.; LeHunte, S. An overview of semiconductor photocatalysis *Journal of Photochemistry and Photobiology a-Chemistry* **1997,** 108, 1-35.

76. Hoffmann, M. R.; Martin, S. T.; Choi, W. Y.; Bahnemann, D. W. Environmental applications of semiconductor photocatalysis *Chem. Rev.* **1995,** 95, 69-96.

77. Malik, P. K.; Sanyal, S. K. Kinetics of decolourisation of azo dyes in wastewater by UV/H2O2 process *Sep. Purif. Technol.* **2004,** 36, 167-175.

78. Sakthivel, S.; Neppolian, B.; Shankar, M. V.; Arabindoo, B.; Palanichamy, M.; Murugesan, V. Solar photocatalytic degradation of azo dye: comparison of photocatalytic efficiency of ZnO and TiO2 *Sol. Energy Mater. Sol. Cells* **2003,** 77, 65-82.

79. Graciani, J.; Nambu, A.; Evans, J.; Rodriguez, J. A.; Sanz, J. F. Au <-> N synergy and N-doping of metal oxide-based photocatalysts *J. Am. Chem. Soc.* **2008,** 130, 12056-12063.

80. Qin, H. C.; Li, W. Y.; Xia, Y. J.; He, T. Photocatalytic Activity of Heterostructures Based on ZnO and N-Doped ZnO *Acs Applied Materials & Interfaces* **2011,** 3, 3152-3156.

81. Akhavan, O. Photocatalytic reduction of graphene oxides hybridized by ZnO nanoparticles in ethanol *Carbon* **2011,** 49, 11-18.

82. Zhang, R.; Kerr, L. L. A simple method for systematically controlling ZnO crystal size and growth orientation *J. Solid State Chem.* **2007,** 180, 988-994.

83. Valerini, D.; Caricato, A. P.; Lomascolo, M.; Romano, F.; Taurino, A.; Tunno, T.; Martino, M. Zinc oxide nanostructures grown by pulsed laser deposition *Applied Physics a-Materials Science & Processing* **2008,** 93, 729-733.

84. Wang, X. D.; Song, J. H.; Wang, Z. L. Single-crystal nanocastles of ZnO *Chem. Phys. Lett.* **2006,** 424, 86-90.

85. Zhang, J. W.; Zhu, P. L.; Li, J. H.; Chen, J. M.; Wu, Z. S.; Zhang, Z. J. Fabrication of Octahedral-Shaped Polyol-Based Zinc Alkoxide Particles and Their Conversion to Octahedral Polycrystalline ZnO or Single-Crystal ZnO Nanoparticles *Crystal Growth & Design* **2009,** 9, 2329-2334.

86. Wahab, R.; Ansari, S. G.; Seo, H. K.; Kim, Y. S.; Suh, E. K.; Shin, H. S. Low temperature synthesis and characterization of rosette-like nanostructures of ZnO using solution process *Solid State Sciences* **2009,** 11, 439-443.

87. Zhang, Z. H.; Lu, M. H.; Xu, H. R.; Chin, W. S. Shape-controlled synthesis of zinc oxide: A simple method for the preparation of metal oxide nanocrystals in non-aqueous medium *Chemistry-a European Journal* **2007,** 13, 632-638.

88. Bilecka, I.; Elser, P.; Niederberger, M. Kinetic and Thermodynamic Aspects in the Microwave-Assisted Synthesis of ZnO Nanoparticles in Benzyl Alcohol *Acs Nano* **2009,** 3, 467-477.

89. Conner, W. C.; Tompsett, G. A. How could and do microwaves influence chemistry at interfaces? *J. Phys. Chem. B* **2008,** 112, 2110-2118.

90. Lidstrom, P.; Tierney, J.; Wathey, B.; Westman, J. Microwave assisted organic synthesis - a review *Tetrahedron* **2001,** 57, 9225-9283.

91. Henrich, V. E.; Cox, P. A., *The Surface Science of Metal Oxides*. Cambridge University Press: 1994.

92. Nicholas, N. J.; Franks, G. V.; Ducker, W. A. Selective Adsorption to Particular Crystal Faces of ZnO *Langmuir* **2012,** 28, 7189-7196.

93. Tsai, M. K.; Huang, C. C.; Lee, Y. C.; Yang, C. S.; Yu, H. C.; Lee, J. W.; Hu, S. Y.; Chen, C. H. A study on morphology control and optical properties of ZnO nanorods synthesized by microwave heating *J. Lumin.* **2012,** 132, 226-230.

94. Yin, H.; Casey, P. S.; McCall, M. J.; Fenech, M. Effects of Surface Chemistry on Cytotoxicity, Genotoxicity, and the Generation of Reactive Oxygen Species Induced by ZnO Nanoparticles *Langmuir* **2010,** 26, 15399-15408.

95. Albertsson, J.; Abrahams, S. C.; Kvick, A. Atomic Displacement, Anharmonic Thermal Vibration, Expansivity and Pyroelectric coefficient Thermal Dependences in ZnO *Acta Crystallographica Section B-Structural Science* **1989,** 45, 34-40.

96. Garcia-Martinez, O.; Rojas, R. M.; Vila, E.; de Vidales, J. L. M. Microstructural characterization of nanocrystals of ZnO and CuO obtained from basic salts *Solid State Ionics* **1993,** 63, 442-449.

97. Hu, Z. S.; Santos, J. F. H.; Oskam, G.; Searson, P. C. Influence of the reactant concentrations on the synthesis of ZnO nanoparticles *J. Colloid Interface Sci.* **2005,** 288, 313-316.

98. Jagadish, C.; Pearton, S. J., *Zinc Oxide Bulk, Thin Films and Nanostructures*. Elsevier: New York, 2006.

99. Djurisic, A. B.; Leung, Y. H. Optical properties of ZnO nanostructures *Small* **2006,** 2, 944-961.

100. Kaschner, A.; Haboeck, U.; Strassburg, M.; Kaczmarczyk, G.; Hoffmann, A.; Thomsen, C.; Zeuner, A.; Alves, H. R.; Hofmann, D. M.; Meyer, B. K. Nitrogen-related local vibrational modes in ZnO : N *Appl. Phys. Lett.* **2002,** 80, 1909-1911.

101. Du, G. T.; Ma, Y.; Zhang, Y. T.; Yang, T. P. Preparation of intrinsic and N-doped p-type ZnO thin films by metalorganic vapor phase epitaxy *Appl. Phys. Lett.* **2005,** 87, 213103.

102. Kerr, L. L.; Li, X. N.; Canepa, M.; Sommer, A. J. Raman analysis of nitrogen doped ZnO *Thin Solid Films* **2007,** 515, 5282-5286.

103. Woll, C. The chemistry and physics of zinc oxide surfaces *Prog. Surf. Sci.* **2007,** 82, 55-120.

104. Watts, J. F.; Wolstenholme, J., *An Introduction to Surface Analysis by XPS and AES*. John Wiley & Sons, Inc.: New York, 2003.

105. Chen, M.; Wang, X.; Yu, Y. H.; Pei, Z. L.; Bai, X. D.; Sun, C.; Huang, R. F.; Wen, L. S. X-ray photoelectron spectroscopy and auger electron spectroscopy studies of Al-doped ZnO films *Appl. Surf. Sci.* **2000,** 158, 134-140.

106. Hsieh, P. T.; Chen, Y. C.; Kao, K. S.; Wang, C. M. Luminescence mechanism of ZnO thin film investigated by XPS measurement *Appl. Phys. A* **2008,** 90, 317-321.

107. Stambolova, I.; Blaskov, V.; Shipochka, M.; Vassilev, S.; Dushkin, C.; Dimitriev, Y. Porous photocatalytically active ZnO films obtained from ethylcellulose modified solutions by spray pyrolysis *Mater. Chem. Phys.* **2010,** 121, 447-452.

108. Pavia, D. L.; Lampman, G. M.; Kriz, G. S.; Vyvyan, J. R., *Introduction to Spectroscopy*. Brooks/Cole Sengage Learning: Belmont, 2001.

109. Garnweitner, G.; Niederberger, M. Organic chemistry in inorganic nanomaterials synthesis *J. Mater. Chem.* **2008,** 18, 1171-1182.

110. Kamat, P. V.; Meisel, D. Nanoparticles in advanced oxidation processes *Current Opinion in Colloid & Interface Science* **2002,** 7, 282-287.

111. Katsumata, H.; Kawabe, S.; Kaneco, S.; Suzuki, T.; Ohta, K. Degradation of bisphenol A in water by the photo-Fenton reaction *Journal of Photochemistry and Photobiology a-Chemistry* **2004,** 162, 297-305.

112. Valerini, D.; Caricato, A. P.; Creti, A.; Lomascolo, M.; Romano, F.; Taurino, A.; Tunno, T.; Martino, M. Morphology and photoluminescence properties of zinc oxide films grown by pulsed laser deposition *Appl. Surf. Sci.* **2009,** 255, 9680-9683.

113. Matthews, R. W. Hydroxylation reactions induced by near-ultraviolet photolysis of aqueous titanium-dioxide suspensions *Journal of the Chemical Society-Faraday Transactions I* **1984,** 80, 457-471.

114. Neppolian, B.; Choi, H. C.; Sakthivel, S.; Arabindoo, B.; Murugesan, V. Solar/UV-induced photocatalytic degradation of three commercial textile dyes *J. Hazard. Mater.* **2002,** 89, 303-317.

115. Ollis, D. F., Solar-assisted photocatalysis for water-purification - issues, data, questions. In *Photochemical Conversion and Storage of Solar Energy*, Pelizzetti, E.; Schiavello, M., Eds. Kluwer Academic Publ: Dordrecht, 1991; pp 593-622.

116. Pirkanniemi, K.; Sillanpaa, M. Heterogeneous water phase catalysis as an environmental application: a review *Chemosphere* **2002,** 48, 1047-1060.

117. Vogel, R.; Hoyer, P.; Weller, H. Quantum-sized PbS, CdS, Ag2S, SB2S3, and Bi2S3 particles as sensitizers for various nanoporous wide-bandgap semiconductors *J. Phys. Chem.* **1994,** 98, 3183-3188.

118. Wang, J. C.; Liu, P.; Fu, X. Z.; Li, Z. H.; Han, W.; Wang, X. X. Relationship between Oxygen Defects and the Photocatalytic Property of ZnO Nanocrystals in Nafion Membranes *Langmuir* **2009,** 25, 1218-1223.

119. Yuan, J. Q.; Choo, E. S. G.; Tang, X. S.; Sheng, Y.; Ding, J.; Xue, J. M. Synthesis of ZnO-Pt nanoflowers and their photocatalytic applications *Nanotechnology* 21.

120. Zeng, H. B.; Cai, W. P.; Liu, P. S.; Xu, X. X.; Zhou, H. J.; Klingshirn, C.; Kalt, H. ZnO-based hollow nanoparticles by selective etching: Elimination and reconstruction of metal-semiconductor interface, improvement of blue emission and photocatalysis *Acs Nano* **2008,** 2, 1661-1670.

121. Bohle, D. S.; Spina, C. J. Cationic and Anionic Surface Binding Sites on Nanocrystalline Zinc Oxide: Surface Influence on Photoluminescence and Photocatalysis *J. Am. Chem. Soc.* **2009,** 131, 4397-4404.

122. de Moraes, S. G.; Freire, R. S.; Duran, N. Degradation and toxicity reduction of textile effluent by combined photocatalytic and ozonation processes *Chemosphere* **2000,** 40, 369-373.

123. Mohamed, M. B.; AbouZeid, K. M.; Abdelsayed, V.; Aljarash, A. A.; El-Shall, M. S. Growth Mechanism of Anisotropic Gold Nanocrystals via Microwave Synthesis: Formation of Dioleamide by Gold Nanocatalysis *Acs Nano* **2010,** 4, 2766-2772.

124. LaMer, V. K.; Dinegar, R. H. Theory, Production and Mechanism of Formation of Monodispersed Hydrosols *J. Am. Chem. Soc.* **1950,** 72, 4847-4854.

125. Wang, Z. L. Transmission electron microscopy of shape-controlled nanocrystals and their assemblies *J. Phys. Chem. B* **2000,** 104, 1153-1175.

126. Hong, W.-K.; Sohn, J. I.; Hwang, D.-K.; Kwon, S.-S.; Jo, G.; Song, S.; Kim, S.-M.; Ko, H.-J.; Park, S.-J.; Welland, M. E.; Lee, T. Tunable Electronic Transport Characteristics of Surface-Architecture-Controlled ZnO Nanowire Field Effect Transistors *Nano Lett.* **2008,** 8, 950-956.

127. Bao, J. M.; Zimmler, M. A.; Capasso, F.; Wang, X. W.; Ren, Z. F. Broadband ZnO single-nanowire light-emitting diode *Nano Lett.* **2006,** 6, 1719-1722.

128. Biswas, K.; Varghese, N.; Rao, C. N. R. Growth kinetics of nanocrystals and nanorods by employing small-angle X-ray scattering (SAXS) and other techniques *Journal of Materials Science & Technology* **2008,** 24, 615-627.

129. Dorfman, A.; Kumar, N.; Hahm, J. Nanoscale ZnO-enhanced fluorescence detection of protein interactions *Adv. Mater.* **2006,** 18, 2685.

130. Law, M.; Greene, L. E.; Johnson, J. C.; Saykally, R.; Yang, P. D. Nanowire dye-sensitized solar cells *Nature Materials* **2005,** 4, 455-459.

131. Zhang, J. P.; Zhang, L. D.; Zhu, L. Q.; Zhang, Y.; Liu, M.; Wang, X. J.; He, G. Characterization of ZnO : N films prepared by annealing sputtered zinc oxynitride films at different temperatures *J. Appl. Phys.* **2007,** 102, 114903.

132. Gautam, U. K.; Panchakarla, L. S.; Dierre, B.; Fang, X.; Bando, Y.; Sekiguchi, T.; Govindaraj, A.; Golberg, D.; Rao, C. N. R. Solvothermal Synthesis, Cathodoluminescence, and Field-Emission Properties of Pure and N-Doped ZnO Nanobullets *Adv. Funct. Mater.* **2009,** 19, 131-140.

133. Chavillon, B.; Cario, L.; Renaud, A.; Tessier, F.; Chevire, F.; Boujtita, M.; Pellegrin, Y.; Blart, E.; Smeigh, A.; Hammarstrom, L.; Odobel, F.; Jobic, S. P-Type Nitrogen-Doped ZnO Nanoparticles Stable under Ambient Conditions *J. Am. Chem. Soc.* **2012,** 134, 464-470.

134. Van de Walle, C. G. Hydrogen as a Cause of Doping in Zinc Oxide *Phys. Rev. Lett.* **2000,** 85, 1012-1015.

135. Cao, P.; Zhao, D. X.; Zhang, J. Y.; Shen, D. Z.; Lu, Y. M.; Yao, B.; Li, B. H.; Bai, Y.; Fan, X. W. Optical and electrical properties of p-type ZnO fabricated by NH3 plasma post-treated ZnO thin films *Appl. Surf. Sci.* **2008,** 254, 2900-2904.

136. Li, J.; Kykyneshi, R.; Tate, J.; Sleight, A. W. p-Type zinc oxide powders *Solid State Sciences* **2007,** 9, 613-618.

137. Minegishi, K.; Koiwai, Y.; Kikuchi, Y.; Yano, K.; Kasuga, M.; Shimizu, A. Growth of p-type zinc oxide films by chemical vapor deposition *Japanese Journal of Applied Physics Part 2-Letters* **1997,** 36, L1453-L1455.

138. Sato, Y.; Sato, S. Preparation and some properties of nitrogen-mixed ZnO thin films *Thin Solid Films* **1996,** 282, 445-448.

139. Zou, C. W.; Chen, R. Q.; Gao, W. The microstructures and the electrical and optical properties of ZnO:N films prepared by thermal oxidation of Zn3N2 precursor *Solid State Commun.* **2009,** 149, 2085-2089.

140. Varghese, N.; Panchakarla, L. S.; Hanapi, M.; Govindaraj, A.; Rao, C. N. R. Solvothermal synthesis of nanorods of ZnO, N-doped ZnO and CdO *Mater. Res. Bull.* **2007,** 42, 2117-2124.

141. Nickel, N. H.; Friedrich, F.; Rommeluere, J. F.; Galtier, P. Vibrational spectroscopy of undoped and nitrogen-doped ZnO grown by metalorganic chemical vapor deposition *Appl. Phys. Lett.* **2005,** 87, 211905.

142. Pan, Z. W.; Dai, Z. R.; Wang, Z. L. Nanobelts of semiconducting oxides *Science* **2001,** 291, 1947-1949.

143. Zeng, Y. J.; Ye, Z. Z.; Xu, W. Z.; Liu, B.; Che, Y.; Zhu, L. P.; Zhao, B. H. Study on the Hall-effect and photoluminescence of N-doped p-type ZnO thin films *Mater. Lett.* **2007,** 61, 41-44.

144. Lu, J. G.; Ye, Z. Z.; Zhuge, F.; Zeng, Y. J.; Zhao, B. H.; Zhu, L. P. p-type conduction in N-Al co-doped ZnO thin films *Appl. Phys. Lett.* **2004,** 85, 3134-3135.

145. Lu, J. G.; Zhang, Y. Z.; Ye, Z. Z.; Wang, L.; Zhao, B. H.; Huang, J. Y. p-type ZnO films deposited by DC reactive magnetron sputtering at different ammonia concentrations *Mater. Lett.* **2003,** 57, 3311-3314.

146. Obata, K.; Irie, H.; Hashimoto, K. Enhanced photocatalytic activities of Ta, N co-doped TiO2 thin films under visible light *Chem. Phys.* **2007,** 339, 124-132.

147. Ye, Z. Z.; Lu, J. G.; Chen, H. H.; Zhang, Y. Z.; Wang, L.; Zhao, B. H.; Huang, J. Y. Preparation and characteristics of p-type ZnO films by DC reactive magnetron sputtering *J. Cryst. Growth* **2003,** 253, 258-264.

148. Lu, J. F.; Zhang, Q. W.; Wang, J.; Saito, F.; Uchida, M. Synthesis of N-Doped ZnO by grinding and subsequent heating ZnO-urea mixture *Powder Technol.* **2006,** 162, 33-37.

149. Kumar, P. S.; Raj, A. D.; Mangalaraj, D.; Nataraj, D. Growth and characterization of ZnO nanostructured thin films by a two step chemical method *Appl. Surf. Sci.* **2008,** 255, 2382-2387.

150. Sieber, B.; Liu, H.; Piret, G.; Laureyns, J.; Roussel, P.; Gelloz, B.; Szunerits, S.; Boukherroub, R. Synthesis and Luminescence Properties of (N-Doped) ZnO Nanostructures from a Dimethylformamide Aqueous Solution *J. Phys. Chem. C* **2009,** 113, 13643-13650.

151. Hammarberg, E.; Prodi-Schwab, A.; Feldmann, C. Microwave-assisted polyol synthesis of aluminium- and indium-doped ZnO nanocrystals *J. Colloid Interface Sci.* **2009,** 334, 29-36.

152. Clavel, G.; Willinger, M. G.; Zitoun, D.; Pinna, N. Solvent dependent shape and magnetic properties of doped ZnO nanostructures *Adv. Funct. Mater.* **2007,** 17, 3159-3169.

153. Baxter, J. B.; Aydil, E. S. Nanowire-based dye-sensitized solar cells *Appl. Phys. Lett.* **2005,** 86, 053114.

154. Clark, D. E.; Sutton, W. H. Microwave processing of materials *Annu. Rev. Mater. Sci.* **1996,** 26, 299-331.

155. Zhu, Y. J.; Wang, W. W.; Qi, R. J.; Hu, X. L. Microwave-assisted synthesis of single-crystalline tellurium nanorods and nanowires in ionic liquids *Angewandte Chemie-International Edition* **2004,** 43, 1410-1414.

156. Loupy, A., *Microwaves in Organic Synthesis*. Wiley-VCH: Weinheim, 2002.

157. Uekawa, N.; Kajiwara, J.; Mochizuki, N.; Kakegawa, K.; Sasaki, Y. Synthesis of ZnO Nanoparticles by Decomposition of Zinc Peroxide *Chem. Lett.* **2001,** 30, 606-607.

158. Uekawa, N.; Mochizuki, N.; Kajiwara, J.; Mori, F.; Wu, Y. J.; Kakegawa, K. Nonstoichiometric properties of zinc oxide nanoparticles prepared by decomposition of zinc peroxide *PCCP* **2003,** 5, 929-934.

159. Gunstone, F. D.; Harwood, J. L.; Padley, F. B., *The Lipid Handbook*. Chapman and Hall: London, 1994.

160. Swern, D.; Parker, W. E. Application of urea complexes in the purification of fatty acids, esters, and alcohols. I. Oleic acid from inedible animal fats *Jour Amer Oil Chemists Soc* **1952,** 29, 431-434.

161. Wang, Z. Ten years' venturing in ZnO nanostructures: from discovery to scientific understanding and to technology applications *Chin. Sci. Bull.* **2009,** 54, 4021-4034.

162. Shan, F. K.; Kim, B. I.; Liu, G. X.; Liu, Z. F.; Sohn, J. Y.; Lee, W. J.; Shin, B. C.; Yu, Y. S. Blueshift of near band edge emission in Mg doped ZnO thin films and aging *J. Appl. Phys.* **2004,** 95, 4772-4776.

163. Joseph, M.; Tabata, H.; Kawai, T. p-type electrical conduction in ZnO thin films by Ga and N codoping *Japanese Journal of Applied Physics Part 2-Letters* **1999,** 38, L1205-L1207.

164. Sakai, K.; Kakeno, T.; Ikari, T.; Shirakata, S.; Sakemi, T.; Awai, K.; Yamamoto, T. Defect centers and optical absorption edge of degenerated semiconductor ZnO thin films grown by

a reactive plasma deposition by means of piezoelectric photothermal spectroscopy *J. Appl. Phys.* **2006,** 99, 043508.

165. Shtereva, K.; Tvarozek, V.; Netrvalova, M.; Sutta, P.; Novotny, I.; Pullmannova, A. Effect of Doping on the Optical and Structural Properties of ZnO Thin Films Prepared by RF Diode Sputtering *ECS Transactions* **2009,** 25, 65-72.

166. Tan, S. T.; Chen, B. J.; Sun, X. W.; Fan, W. J.; Kwok, H. S.; Zhang, X. H.; Chua, S. J. Blueshift of optical band gap in ZnO thin films grown by metal-organic chemical-vapor deposition *J. Appl. Phys.* **2005,** 98, 013505.

167. Diebold, U. The surface science of titanium dioxide *Surf. Sci. Rep.* **2003,** 48, 53-229.

168. Serpone, N.; Lawless, D.; Khairutdinov, R. Size Effects on the Photophysical Properties of Colloidal Anatase TiO2 Particles: Size Quantization versus Direct Transitions in This Indirect Semiconductor? *The Journal of Physical Chemistry* **1995,** 99, 16646-16654.

169. Kamat, P. V.; Dimitrijevic, N. M.; Nozik, A. J. Dynamic Burstein-Moss shift in semiconductor colloids *The Journal of Physical Chemistry* **1989,** 93, 2873-2875.

170. Burstein, E. Anomalous Optical Absorption Limit in InSb *Physical Review* **1954,** 93, 632-633.

171. Dong, G.; Zhang, M.; Zhao, X.; Yan, H.; Tian, C.; Ren, Y. Improving the electrical conductivity of CuCrO2 thin film by N doping *Appl. Surf. Sci.* **2010,** 256, 4121-4124.

172. Game, O.; Singh, U.; Gupta, A. A.; Suryawanshi, A.; Banpurkar, A.; Ogale, S. Concurrent synthetic control of dopant (nitrogen) and defect complexes to realize broadband (UV-650 nm) absorption in ZnO nanorods for superior photo-electrochemical performance *J. Mater. Chem.* **2012,** 22, 17302-17310.

173. Ye, J. D.; Gu, S. L.; Zhu, S. M.; Chen, T.; Hu, L. Q.; Qin, F.; Zhang, R.; Shi, Y.; Zheng, Y. D. The growth and annealing of single crystalline ZnO films by low-pressure MOCVD *J. Cryst. Growth* **2002,** 243, 151-156.

174. Bott, A. W. Electrochemistry of Semiconductors *Current Separations* **1998,** 17, 87.

175. Geim, A. K.; Novoselov, K. S. The rise of graphene *Nature Materials* **2007,** 6, 183-191.

176. Novoselov, K. S.; Geim, A. K.; Morozov, S. V.; Jiang, D.; Katsnelson, M. I.; Grigorieva, I. V.; Dubonos, S. V.; Firsov, A. A. Two-dimensional gas of massless Dirac fermions in graphene *Nature* **2005,** 438, 197-200.

177. Rao, C. N. R.; Sood, A. K.; Subrahmanyam, K. S.; Govindaraj, A. Graphene: The New Two-Dimensional Nanomaterial *Angewandte Chemie-International Edition* **2009,** 48, 7752-7777.

178. Allen, M. J.; Tung, V. C.; Kaner, R. B. Honeycomb Carbon: A Review of Graphene *Chem. Rev.* **2009,** 110, 132-145.

179. Geim, A. K. Graphene: Status and Prospects *Science* **2009,** 324, 1530-1534.

180. Goncalves, G.; Marques, P. A. A. P.; Granadeiro, C. M.; Nogueira, H. I. S.; Singh, M. K.; Gracio, J. Surface Modification of Graphene Nanosheets with Gold Nanoparticles: The Role of Oxygen Moieties at Graphene Surface on Gold Nucleation and Growth *Chem. Mater.* **2009,** 21, 4796-4802.

181. Kamat, P. V. Graphene-Based Nanoarchitectures. Anchoring Semiconductor and Metal Nanoparticles on a Two-Dimensional Carbon Support *J. Phys. Chem. Lett.* **2010,** 1, 520-527.

182. Scheuermann, G. M.; Rumi, L.; Steurer, P.; Bannwarth, W.; Muelhaupt, R. Palladium Nanoparticles on Graphite Oxide and Its Functionalized Graphene Derivatives as Highly Active Catalysts for the Suzuki-Miyaura Coupling Reaction *J. Am. Chem. Soc.* **2009,** 131, 8262-8270.

183. Siamaki, A. R.; Khder, A. E. S.; Abdelsayed, V.; El-Shall, M. S.; Gupton, B. F. Microwave-assisted synthesis of palladium nanoparticles supported on graphene: A highly active and recyclable catalyst for carbon-carbon cross-coupling reactions *J. Catal.* **2011,** 279, 1-11.

184. Banhart, F.; Kotakoski, J.; Krasheninnikov, A. V. Structural Defects in Graphene *Acs Nano* **2011,** 5, 26-41.

185. Kim, G.; Jhi, S.-H. Carbon Monoxide-Tolerant Platinum Nanoparticle Catalysts on Defect-Engineered Graphene *Acs Nano* **2011,** 5, 805-810.

186. Moussa, S.; Abdelsayed, V.; El-Shall, M. S. Laser synthesis of Pt, Pd, CoO and Pd-CoO nanoparticle catalysts supported on graphene *Chem. Phys. Lett.* **2011,** 510, 179-184.

187. Moussa, S.; Siamaki, A. R.; Gupton, B. F.; El-Shall, M. S. Pd-Partially Reduced Graphene Oxide Catalysts (Pd/PRGO): Laser Synthesis of Pd Nanoparticles Supported on PRGO Nanosheets for Carbon-Carbon Cross Coupling Reactions *ACS Catalysis* **2012,** 2, 145-154.

188. Williams, G.; Kamat, P. V. Graphene-Semiconductor Nanocomposites: Excited-State Interactions between ZnO Nanoparticles and Graphene Oxide *Langmuir* **2009,** 25, 13869-13873.

189. Yin, Z.; Wu, S.; Zhou, X.; Huang, X.; Zhang, Q.; Boey, F.; Zhang, H. Electrochemical Deposition of ZnO Nanorods on Transparent Reduced Graphene Oxide Electrodes for Hybrid Solar Cells *Small* **2010,** 6, 307-312.

190. Lin, Y.; Zhang, K.; Chen, W.; Liu, Y.; Geng, Z.; Zeng, J.; Pan, N.; Yan, L.; Wang, X.; Hou, J. G. Dramatically Enhanced Photoresponse of Reduced Graphene Oxide with Linker-Free Anchored CdSe Nanoparticles *Acs Nano* **2010,** 4, 3033-3038.

191. Zedan, A. F.; Sappal, S.; Moussa, S.; El-Shall, M. S. Ligand-Controlled Microwave Synthesis of Cubic and Hexagonal CdSe Nanocrystals Supported on Graphene. Photoluminescence Quenching by Graphene *J. Phys. Chem. C* **2010,** 114, 19920-19927.

192. Cuong, T. V.; Pham, V. H.; Chung, J. S.; Shin, E. W.; Yoo, D. H.; Hahn, S. H.; Huh, J. S.; Rue, G. H.; Kim, E. J.; Hur, S. H.; Kohl, P. A. Solution-processed ZnO-chemically converted graphene gas sensor *Mater. Lett.* **2010,** 64, 2479-2482.

193. Lee, J. M.; Pyun, Y. B.; Yi, J.; Choung, J. W.; Park, W. I. ZnO Nanorod-Graphene Hybrid Architectures for Multifunctional Conductors *J. Phys. Chem. C* **2009,** 113, 19134-19138.

194. Wu, J.; Shen, X.; Jiang, L.; Wang, K.; Chen, K. Solvothermal synthesis and characterization of sandwich-like graphene/ZnO nanocomposites *Appl. Surf. Sci.* **2010,** 256, 2826-2830.

195. Abdelsayed, V.; Panda, A. B.; Glaspell, G.; El-Shall, M. S., Nanoparticles: synthesis, stabilization, passivation, and functionalization. In *ACS Symposium Series 996*, Nagarajan, R.; Hatton, T. A., Eds. 2008; pp 225-247.

196. Herring, N. P.; Panda, A. B.; AbouZeid, K.; Almahoudi, S. H.; Olson, C. R.; Patel, A.; El-Shall, M. S., Microwave Synthesis of Metal Oxide Nanoparticles. In *Metal Oxide Nanomaterials for Chemical Sensors*, Carpenter, M. A.; Mathur, S.; Kolmakov, A., Eds. Springer: New York, 2013.

197. Abdelsayed, V.; Aljarash, A.; El-Shall, M. S.; Al Othman, Z. A.; Alghamdi, A. H. Microwave Synthesis of Bimetallic Nanoalloys and CO Oxidation on Ceria-Supported Nanoalloys *Chem. Mater.* **2009,** 21, 2825-2834.

198. Hassan, H. M. A.; Abdelsayed, V.; Khder, A.; AbouZeid, K. M.; Terner, J.; El-Shall, M. S.; Al-Resayes, S. I.; El-Azhary, A. A. Microwave synthesis of graphene sheets supporting metal nanocrystals in aqueous and organic media *J. Mater. Chem.* **2009,** 19, 3832-3837.

199. Panda, A. B.; Glaspell, G.; El-Shall, M. S. Microwave synthesis of highly aligned ultra narrow semiconductor rods and wires *J. Am. Chem. Soc.* **2006,** 128, 2790-2791.

200. Panda, A. B.; Glaspell, G.; El-Shall, M. S. Microwave synthesis and optical properties of uniform nanorods and nanoplates of rare earth oxides *J. Phys. Chem. C* **2007,** 111, 1861-1864.

201. Park, S.; Ruoff, R. S. Chemical methods for the production of graphenes *Nat. Nanotechnol.* **2009,** 4, 217-224.

202. Li, X. S.; Cai, W. W.; An, J. H.; Kim, S.; Nah, J.; Yang, D. X.; Piner, R.; Velamakanni, A.; Jung, I.; Tutuc, E.; Banerjee, S. K.; Colombo, L.; Ruoff, R. S. Large-Area Synthesis of High-Quality and Uniform Graphene Films on Copper Foils *Science* **2009,** 324, 1312-1314.

203. Hummers, W. S.; Offeman, R. E. Preparation of Graphitic Oxide *J. Am. Chem. Soc.* **1958,** 80, 1339-1339.

204. Liu, K. W.; Sakurai, M.; Liao, M. Y.; Aono, M. Giant Improvement of the Performance of ZnO Nanowire Photodetectors by Au Nanoparticles *J. Phys. Chem. C* **2010,** 114, 19835-19839.

205. Ferrari, A. C.; Meyer, J. C.; Scardaci, V.; Casiraghi, C.; Lazzeri, M.; Mauri, F.; Piscanec, S.; Jiang, D.; Novoselov, K. S.; Roth, S.; Geim, A. K. Raman spectrum of graphene and graphene layers *Phys. Rev. Lett.* **2006,** 97.

206. Liu, J.; Jeong, H.; Lee, K.; Park, J. Y.; Ahn, Y. H.; Lee, S. Reduction of functionalized graphite oxides by trioctylphosphine in non-polar organic solvents *Carbon* **2010,** 48, 2282-2289.

207. Yang, D.; Velamakanni, A.; Bozoklu, G.; Park, S.; Stoller, M.; Piner, R. D.; Stankovich, S.; Jung, I.; Field, D. A.; Ventrice, C. A., Jr.; Ruoff, R. S. Chemical analysis of graphene oxide films after heat and chemical treatments by X-ray photoelectron and Micro-Raman spectroscopy *Carbon* **2009,** 47, 145-152.

208. Sun, Y.; Riley, D. J.; Ashfold, M. N. R. Mechanism of ZnO Nanotube Growth by Hydrothermal Methods on ZnO Film-Coated Si Substrates *The Journal of Physical Chemistry B* **2006,** 110, 15186-15192.

209. Rao, C. N. R.; Matte, H. S. S. R.; Subrahmanyam, K. S.; Maitra, U. Unusual magnetic properties of graphene and related materials *Chemical Science* **2012,** 3, 45-52.

210. Cervantes-Sodi, F.; Cs√°nyi, G.; Piscanec, S.; Ferrari, A. C. Edge-functionalized and substitutionally doped graphene nanoribbons: Electronic and spin properties *Physical Review B* **2008,** 77, 165427.

211. Deifallah, M.; McMillan, P. F.; Cora, F. Electronic and Structural Properties of Two-Dimensional Carbon Nitride Graphenes *The Journal of Physical Chemistry C* **2008,** 112, 5447-5453.

212. Liu, H.; Liu, Y.; Zhu, D. Chemical doping of graphene *J. Mater. Chem.* **2011,** 21, 3335-3345.

213. Panchakarla, L. S.; Govindaraj, A.; Rao, C. N. R. Boron- and nitrogen-doped carbon nanotubes and graphene *Inorg. Chim. Acta* **2010,** 363, 4163-4174.

214. Late, D. J.; Ghosh, A.; Subrahmanyam, K. S.; Panchakarla, L. S.; Krupanidhi, S. B.; Rao, C. N. R. Characteristics of field-effect transistors based on undoped and B- and N-doped few-layer graphenes *Solid State Commun.* **2010,** 150, 734-738.

215. Ghosh, A.; Late, D. J.; Panchakarla, L. S.; Govindaraj, A.; Rao, C. N. R. NO2 and humidity sensing characteristics of few-layer graphenes *Journal of Experimental Nanoscience* **2009,** 4, 313-322.

216. Alver, U.; Zhou, W.; Belay, B.; Krueger, R.; Davis, K. O.; Hickman, N. S. Optical and structural properties of ZnO nanorods grown on graphene oxide and reduced graphene oxide film by hydrothermal method *Appl. Surf. Sci.* **2012,** 258, 3109-3114.

217. Lu, T.; Pan, L.; Li, H.; Zhu, G.; Lv, T.; Liu, X.; Sun, Z.; Chen, T.; Chua, D. H. C. Microwave-assisted synthesis of graphene-ZnO nanocomposite for electrochemical supercapacitors *J. Alloys Compd.* **2011,** 509, 5488-5492.

218. Luo, Q.-P.; Yu, X.-Y.; Lei, B.-X.; Chen, H.-Y.; Kuang, D.-B.; Su, C.-Y. Reduced Graphene Oxide-Hierarchical ZnO Hollow Sphere Composites with Enhanced Photocurrent and Photocatalytic Activity *J. Phys. Chem. C* **2012,** 116, 8111-8117.

219. Yoo, D.-H.; Tran Viet, C.; Van Hoang, L.; Nguyen Tri, K.; Kim, E. J.; Hur, S. H.; Hahn, S. H. Photocatalytic Performance of a Ag/ZnO/CCG Multidimensional Heterostructure Prepared by a Solution-Based Method *J. Phys. Chem. C* **2012,** 116, 7180-7184.

220. Zhang, Q.; Tian, C.; Wu, A.; Tan, T.; Sun, L.; Wang, L.; Fu, H. A facile one-pot route for the controllable growth of small sized and well-dispersed ZnO particles on GO-derived graphene *J. Mater. Chem.* **2012,** 22, 11778-11784.

221. Park, J. S.; Lee, J. M.; Hwang, S. K.; Lee, S. H.; Lee, H.-J.; Lee, B. R.; Park, H. I.; Kim, J.-S.; Yoo, S.; Song, M. H.; Kim, S. O. A ZnO/N-doped carbon nanotube nanocomposite charge transport layer for high performance optoelectronics *J. Mater. Chem.* **2012,** 22, 12695-12700.

222. Mou, Z.; Chen, X.; Du, Y.; Wang, X.; Yang, P.; Wang, S. Forming mechanism of nitrogen doped graphene prepared by thermal solid-state reaction of graphite oxide and urea *Appl. Surf. Sci.* **2011,** 258, 1704-1710.

223. Lin, Z. Y.; Waller, G.; Liu, Y.; Liu, M. L.; Wong, C. P. Facile Synthesis of Nitrogen-Doped Graphene via Pyrolysis of Graphene Oxide and Urea, and its Electrocatalytic Activity toward the Oxygen-Reduction Reaction *Advanced Energy Materials* **2012,** 2, 884-888.

224. Sun, L.; Wang, L.; Tian, C. G.; Tan, T. X.; Xie, Y.; Shi, K. Y.; Li, M. T.; Fu, H. G. Nitrogen-doped graphene with high nitrogen level via a one-step hydrothermal reaction of graphene oxide with urea for superior capacitive energy storage *Rsc Advances* **2012,** 2, 4498-4506.

225. Liu, J.; Zhang, T.; Wang, Z.; Dawson, G.; Chen, W. Simple pyrolysis of urea into graphitic carbon nitride with recyclable adsorption and photocatalytic activity *J. Mater. Chem.* **2011,** 21, 14398-14401.

226. Zou, X. X.; Li, G. D.; Wang, Y. N.; Zhao, J.; Yan, C.; Guo, M. Y.; Li, L.; Chen, J. S. Direct conversion of urea into graphitic carbon nitride over mesoporous TiO2 spheres under mild condition *Chem. Commun.* **2011,** 47, 1066-1068.

227. Zhang, Y. W.; Liu, J. H.; Wu, G.; Chen, W. Porous graphitic carbon nitride synthesized via direct polymerization of urea for efficient sunlight-driven photocatalytic hydrogen production *Nanoscale* **2012,** 4, 5300-5303.

228. Tabet, N.; Faiz, M.; Al-Oteibi, A. XPS study of nitrogen-implanted ZnO thin films obtained by DC-Magnetron reactive plasma *J. Electron. Spectrosc. Relat. Phenom.* **2008,** 163, 15-18.

229. Geng, D.; Yang, S.; Zhang, Y.; Yang, J.; Liu, J.; Li, R.; Sham, T.-K.; Sun, X.; Ye, S.; Knights, S. Nitrogen doping effects on the structure of graphene *Appl. Surf. Sci.* **2011,** 257, 9193-9198.

230. Li, X.; Wang, H.; Robinson, J. T.; Sanchez, H.; Diankov, G.; Dai, H. Simultaneous Nitrogen Doping and Reduction of Graphene Oxide *J. Am. Chem. Soc.* **2009,** 131, 15939-15944.

231. Wei, D.; Liu, Y.; Wang, Y.; Zhang, H.; Huang, L.; Yu, G. Synthesis of N-Doped Graphene by Chemical Vapor Deposition and Its Electrical Properties *Nano Lett.* **2009,** 9, 1752-1758.

232. Jiang, B.; Tian, C.; Pan, Q.; Jiang, Z.; Wang, J.-Q.; Yan, W.; Fu, H. Enhanced Photocatalytic Activity and Electron Transfer Mechanisms of Graphene/TiO2 with Exposed {001} Facets *J. Phys. Chem. C* **2011,** 115, 23718-23725.

233. Mappes, T.; Jahr, N.; Csaki, A.; Vogler, N.; Popp, J.; Fritzsche, W. The Invention of Immersion Ultramicroscopy in 1912-The Birth of Nanotechnology? *Angewandte Chemie-International Edition* **2012,** 51, 11208-11212.

234. Hu, Y.; Wu, P.; Yin, Y.; Zhang, H.; Cai, C. Effects of structure, composition, and carbon support properties on the electrocatalytic activity of Pt-Ni-graphene nanocatalysts for the methanol oxidation *Applied Catalysis B-Environmental* **2012,** 111, 208-217.

235. Li, Y.; Yu, Y.; Wang, J.-G.; Song, J.; Li, Q.; Dong, M.; Liu, C.-J. CO oxidation over graphene supported palladium catalyst *Applied Catalysis B-Environmental* **2012,** 125, 189-196.

236. Xu, Y.; Yuan, Y.; Ma, A.; Wu, X.; Liu, Y.; Zhang, B. Composition-Tunable Pt-Co Alloy Nanoparticle Networks: Facile Room-Temperature Synthesis and Supportless Electrocatalytic Applications *Chemphyschem* **2012,** 13, 2601-2609.

237. Liu, J.; Zhou, H.; Wang, Q.; Zeng, F.; Kuang, Y. Reduced graphene oxide supported palladium-silver bimetallic nanoparticles for ethanol electro-oxidation in alkaline media *Journal of Materials Science* **2012,** 47, 2188-2194.

238. Mazumder, V.; Sun, S. Oleylamine-Mediated Synthesis of Pd Nanoparticles for Catalytic Formic Acid Oxidation *J. Am. Chem. Soc.* **2009,** 131, 4588-+.

239. Usgaocar, A. R.; de Groot, C. H.; Boulart, C.; Castillo, A.; Chavagnac, V. Low power hydrogen sensors using electrodeposited PdNi-Si schottky diodes *Analytical Abstracts* **2012,** 170, 176-181.

240. Alonso, D. M.; Wettstein, S. G.; Dumesic, J. A. Bimetallic catalysts for upgrading of biomass to fuels and chemicals *Chem. Soc. Rev.* **2012**.

241. Ferrando, R.; Jellinek, J.; Johnston, R. L. Nanoalloys: From theory to applications of alloy clusters and nanoparticles *Chem. Rev.* **2008,** 108, 845-910.

242. Du, C. Y.; Chen, M.; Wang, W. G.; Yin, G. P. Nanoporous PdNi Alloy Nanowires As Highly Active Catalysts for the Electro-Oxidation of Formic Acid *Acs Applied Materials & Interfaces* **2011,** 3, 105-109.

243. Li, R.; Wei, Z.; Huang, T.; Yu, A. Ultrasonic-assisted synthesis of Pd-Ni alloy catalysts supported on multi-walled carbon nanotubes for formic acid electrooxidation *Electrochim. Acta* **2011,** 56, 6860-6865.

Appendix A

Preparation of Graphite Oxide by Hummer's Method

In a typical synthesis of graphite oxide, 2.5 g of sodium nitrate was dissolved in 115 mL of concentrated sulfuric acid in a 1 L Erlenmeyer flask using magnetic stirring. To help facilitate this process any lumps of sodium nitrate were broken up prior to addition to the sulfuric acid. Once the sodium nitrate was completely dissolved 5 g of graphite powder was added to the reaction mixture. The reaction mixture was placed in an ice bath and stirred until the dispersion reached 0 ºC. Next, 15 g of potassium permanganate was slowly and carefully added to the reaction mixture. This is an exothermic reaction and extreme care must be taken. The reaction flask is then removed from the ice bath and is heated to 35 ºC. The temperature is maintained, 35± 3 ºC, for 3 hours. After 3 hours, the solution is extremely viscous. Next, 230 mL of hot water is added to the flask, and the reaction is heated to 98 ºC for 30 min. Upon addition of water, the reaction mixture appears light brown in color. Next, 700 mL of hot water and 20 mL of 30 % hydrogen peroxide are added to the reation mixture, which results in a light golden color. The graphite oxide is then filtered using a fritted funnel and washed with at least 3 portions of hot water to remove salt impurities. Washing is an extremely important step when preparing graphite oxide for catalytic application, because the presence of residual salt impurities may contribute to catalyst poisoning.